Volume 66A
Number 4
July–Aug. 1962

Physics and Chemistry

U.S. DEPARTMENT OF COMMERCE

SECTION A

JOURNAL OF RESEARCH

NATIONAL BUREAU OF STANDARDS

Journal of Research

of the

National Bureau of Standards

A. Physics and Chemistry

JULY–AUG. • 1962

VOLUME • 66A

NUMBER • 4

Editor: C. W. Beckett

Associate Editors: D. D. Wagman
J. M. Richardson

Publication dates:
Feb. 1, Apr. 1, June 1, Aug. 1, Oct. 1, Dec. 1, 1962.

JOURNAL OF RESEARCH

The National Bureau of Standards Journal of Research reports research and development in the fields of activity shown at right. Also included from time to time are survey articles on topics closely related to the Bureau's scientific and technical program.

The Journal is published in four separate sections as follows:

A. Physics and Chemistry

Contains papers of interest primarily to scientists working in these fields. Issued six times a year. Annual subscription: domestic, $4.00; foreign, $4.75.

B. Mathematics and Mathematical Physics

Presents studies and compilations designed mainly for the mathematician and the theoretical physicist. Issued quarterly. Annual subscription: domestic, $2.25; foreign, $2.75.

C. Engineering and Instrumentation

Reports research and development results of interest chiefly to the engineer and the applied scientist. Issued quarterly. Annual subscription: domestic, $2.25; foreign, $2.75.

D. Radio Propagation

Reports work in radio propagation, upper atmospheric physics and communications. Issued six times a year. Annual subscription: domestic, $4.00; foreign, $4.75.

U.S. DEPARTMENT OF COMMERCE
Luther H. Hodges, Secretary

NATIONAL BUREAU OF STANDARDS
A. V. Astin, Director

Functions and Activities

The functions of the National Bureau of Standards are set forth in the Act of Congress, March 3, 1901, as amended. These include the development and maintenance of the national standards of measurement and the provision of means and methods for making measurements consistent with these standards; the determination of physical constants and properties of materials; the development of methods and instruments for testing materials, devices, and structures; advisory services to government agencies on scientific and technical problems; invention and development of devices to serve special needs of the Government; and the development of standard practices, codes, and specifications. The work includes basic and applied research, development, engineering, instrumentation, testing, evaluation, calibration services, and various consultation and information services. The Bureau also serves as the Federal technical research center in a number of specialized fields. The scope of activities of the National Bureau of Standards is suggested in the following listing of the divisions and sections engaged in technical work.

Washington, D.C.

Electricity. Resistance and Reactance. Electrochemistry. Electrical Instruments. Magnetic Measurements. Dielectrics. High Voltage.
Metrology. Photometry and Colorimetry. Refractometry. Photographic Research. Length. Engineering Metrology. Mass and Scale. Volumetry and Densimetry.
Heat. Temperature Physics. Heat Measurements. Cryogenic Physics. Equation of State. Statistical Physics.
Radiation Physics. X-ray. Radioactivity. Radiation Theory. High Energy Radiation. Radiological Equipment. Nucleonic Instrumentation. Neutron Physics.
Analytical and Inorganic Chemistry. Pure Substances. Spectrochemistry. Solution Chemistry. Standard Reference Materials. Applied Analytical Research. Crystal Chemistry.
Mechanics. Sound. Pressure and Vacuum. Fluid Mechanics. Engineering Mechanics. Rheology. Combustion Controls.
Polymers. Macromolecules: Synthesis and Structure. Polymer Chemistry. Polymer Physics. Polymer Characterization. Polymer Evaluation and Testing. Applied Polymer Standards and Research. Dental Research.
Metallurgy. Engineering Metallurgy. Microscopy and Diffraction. Metal Reactions. Metal Physics. Electrolysis and Metal Deposition.
Inorganic Solids. Engineering Ceramics. Glass. Solid State Chemistry. Crystal Growth. Physical Properties. Crystallography.
Building Research. Structural Engineering. Fire Research. Mechanical Systems. Organic Building Materials. Heat Transfer. Inorganic Building Materials. Metallic Building Materials.
Applied Mathematics. Numerical Analysis. Computation. Statistical Engineering. Mathematical Physics. Operations Research.
Data Processing Systems. Components and Techniques. Computer Technology. Measurements Automation. Engineering Applications. Systems Analysis.
Atomic Physics. Spectroscopy. Infrared Spectroscopy. Solid State Physics. Electron Physics. Atomic Physics.
Instrumentation. Engineering Electronics. Electron Devices. Electronic Instrumentation. Mechanical Instruments. Basic Instrumentation.
Physical Chemistry. Thermochemistry. Surface Chemistry. Organic Chemistry. Molecular Spectroscopy. Molecular Kinetics. Mass Spectrometry.
Office of Weights and Measures.

Boulder, Colorado

Cryogenic Engineering. Cryogenic Equipment. Cryogenic Processes. Properties of Materials. Cryogenic Technical Services.

Central Radio Propagation Laboratory

Ionosphere Research and Propagation. Low Frequency and Very Low Frequency Research. Ionosphere Research. Prediction Services. Sun-Earth Relationships. Field Engineering. Radio Warning Services. Vertical Soundings Research.
Radio Propagation Engineering. Data Reduction Instrumentation. Radio Noise. Tropospheric Measurements. Tropospheric Analysis. Propagation-Terrain Effects. Radio-Meteorology. Lower Atmosphere Physics.
Radio Systems. Applied Electromagnetic Theory. High Frequency and Very High Frequency Research. Modulation Research. Antenna Research. Navigation Systems.
Upper Atmosphere and Space Physics. Upper Atmosphere and Plasma Physics. Ionosphere and Exosphere Scatter. Airglow and Aurora. Ionospheric Radio Astronomy.

Radio Standards Laboratory

Radio Physics. Radio Broadcast Service. Radio and Microwave Materials. Atomic Frequency and Time-Interval Standards. Millimeter-Wave Research.
Circuit Standards. High Frequency Electrical Standards. Microwave Circuit Standards. Electronic Calibration Center.

Order all publications from the Superintendent of Documents
U.S. Government Printing Office, Washington 25, D.C.

Use of funds for printing this publication approved by the Director of the Bureau of the Budget (June 19, 1961).

JOURNAL OF RESEARCH of the National Bureau of Standards—A. Physics and Chemistry
Vol. 66A, No. 4, July–August 1962

Dielectric Properties of Semicrystalline Polychlorotrifluoroethylene

Arnold H. Scott, Donald J. Scheiber, Alexander J. Curtis, John I. Lauritzen, Jr., and John D. Hoffman

(April 2, 1962)

The dielectric properties of polychlorotrifluoroethylene (T_m=224 °C, T_g=52 °C) have been measured at temperatures between −50 and +250 °C, and at frequencies between 0.1 c/s and 8.6 kMc/s. Specimens of known crystallinities, ranging from χ=0.80 to χ=0.00 (pure liquid) were studied. Comprehensive tables of data are presented. The experimental techniques employed to measure the dielectric properties over these wide ranges of temperature, frequency, physical state, and sample type (disks, cylinders, and thin films), are discussed. The operation and calibration of the specimen holder, bridges, resonant circuits, and waveguide apparatus used are discussed in detail.

When the dielectric loss index, ϵ'', at 1 c/s is plotted as a function of temperature for a highly crystalline specimen (χ=0.80), where the crystallinity consists largely of lamellar spherulites, three distinct loss peaks are readily apparent. These peaks occur at about −40 °C (low-temperature process), 95 °C (intermediate-temperature process), and 150 °C (high-temperature process). The dielectric data are compared with the mechanical loss data obtained at 1 c/s by McCrum. Mechanical loss peaks at temperatures virtually identical to those in the ϵ'' versus T plot are found.

The *high-temperature* process is attributed to the presence of well-formed chain-folded lamellar spherulites. Some evidence points to the surfaces of the lamellae as the site of the loss mechanism. The high-temperature loss peak does not appear in resolved form in non-spherulitic specimens even when the crystallinity is high. The *intermediate-temperature* process originates in the normal supercooled amorphous phase, and is due to the complex dipole relaxation effects involving motions of large numbers of polymer chain segments that are associated with the onset of the glass transition at T_g=52 °C. As determined by $\overline{V}-T$ data, the glass transition temperature at T_g=52 °C that is associated with this relaxation effect does not shift appreciably with increasing crystallinity. The *low-temperature* dielectric loss process, which is active far below T_g, originates principally in the supercooled amorphous regions, and evidently corresponds to a fairly simple motion involving a small number of chain segments. This process tends to exhibit anomalous behavior in highly crystalline specimens, particularly at low temperatures.

A large dipolar contribution of the crystals to the static dielectric constant was observed. This contribution increased with increasing temperature, and corresponded to a very rapid dipole reorientation process ($\tau \sim 10^{-11}$ sec at 23 °C).

1. Introduction

Polychlorotrifluoroethylene, abbreviated here as PCTFE, has the chemical repeat unit

The molecular asymmetry of the repeat unit gives rise to a permanent dipole moment that subtends a right angle to the carbon chain axis.

Our original interest in investigating the dielectric behavior of this substance stemmed in large part from the fact that the polymer molecule possesses no side groups capable of independent orientation, such as complicate the investigation of certain other polymer systems. In PCTFE, one can be quite certain that any dielectric relaxation effects that are observed, whether originating in the crystalline or amorphous components, are to be attributed to motions involving portions of the polymer chain backbone.

The dielectric properties of PCTFE were investigated over a limited range of temperature and frequency by Reynolds, Thomas, Sharbaugh, and Fuoss [1] [1] in 1951. It was clearly established by them that the dielectric properties of low molecular weight PCTFE waxes were strongly affected when crystallization took place. A high molecular weight specimen was also studied, but the effect of changing degree of crystallinity was not investigated. Hartshorn, Parry, and Rushton [2], and Mikhailov and Sazhin [3], studied high molecular weight PCTFE and gave more extensive information on its dielectric properties. In these later studies, samples of varying but unknown degrees of crystallinity were investigated, so that only a qualitative connection could be established between degree of crystallinity and dielectric properties.

[1] Figures in brackets indicate the literature references at the end of this paper.

Hoffman and Weeks [4] have demonstrated a means whereby the degree of crystallinity of PCTFE over a wide range of temperature can be simply and accurately determined by measurements of the specific volume. This facilitates an attempt at a quantitative analysis of the dielectric data in terms of the degree of crystallinity.

The present investigation was undertaken to provide accurate dielectric data upon samples of known thermal history and degree of crystallinity over a wide temperature range (−50 to +250 °C), and a frequency range (0.1 to almost 10^{10} c/s) much broader than that studied by earlier investigators. From these data, an attempt can then be made to correlate the observed dielectric behavior with the degree of crystallinity and other variables. Special interest attaches to the identification of the contributions of the amorphous and crystalline phases to the dielectric behavior, and to differences in dielectric properties exhibited by specimens of nearly identical crystallinity prepared by different crystallization techniques.

The extension of the frequency range down to 0.1 c/s is made possible by the use of a low-frequency bridge described in detail elsewhere [5]. Nakajima and Saito [6] have reported measurements of the dielectric properties of PCTFE in the frequency range of 0.1 to 10^6 c/s in which a bridge of rather similar capabilities was used.

2. Specimens

2.1. Materials

All specimens used in this investigation were prepared from laboratory samples of Kel-F grade 300 polymer, which was supplied in sheet form by Dr. H. S. Kaufman. The number average molecular weight of the polymer was stated to be approximately 415,000. The equilibrium melting point of the crystals in the polymer is estimated to be 224±1 °C [7]. If the crystals are small, as is the case when they are formed at large or moderate subcooling, the observed melting point of a specimen will be somewhat lower, values ranging from 212 to 218 °C being commonly observed [7]. The normal glass transition in the amorphous component of this semicrystalline polymer is at 52 °C, as determined by the change of slope of volume-temperature curves [4].

2.2. Preparation of Specimens

The specimens employed in this investigation are divided into five categories determined by their degree of crystallinity and thermal history. The determination of the degree of crystallinity, χ, is given in section 2.4. In general, the specimen designations denote the degree of crystallinity of the material.

a. Specimen 0.80

The three specimens described below had degrees of crystallinity near $\chi=0.80$ and similar thermal histories. These specimens are therefore referred to jointly as "specimen 0.80." They were prepared from PCTFE that had been crystallized from the melt according to the procedure of Hoffman and Weeks [4]. The material was heated to 250 °C, which is well above the melting point, and then brought successively to temperatures of 200 and 190 °C, residing one day at each of these temperatures. The material was then maintained at 180 °C for three days, after which it was cooled to room temperature over a period of a few hours. Typical spherulitic crystallization occurs under these conditions. This cloudy-white material was then machined into a disk-shaped specimen, 4.2448 cm in diameter, which was called specimen 0.80A. Dielectric measurements were made upon specimen 0.80A using the Schering bridge and Q-meter described in appendix 6.3. Specimen 0.80B was then prepared from specimen 0.80A by machining the disk down to about 2.54 cm in diameter, the specimen diameter required by the re-entrant cavity described in appendix 7.1. Specimen 0.80B was employed in measurements involving the re-entrant cavity and the low-frequency bridge (0.1 to 200 c/s). The specimens employed in the microwave measurements were prepared by nearly the same procedure, and attained a degree of crystallinity of 78 percent.

The general method of crystallization described above is referred to as "crystallization from the melt" in the text.

The reader is cautioned that the name "specimen 0.80" is not intended to imply that the degree of crystallinity of the specimen always remains at $\chi=0.80$. As is discussed below, the degree of crystallinity of this specimen decreases appreciably when it is heated above about 175 °C.

b. Specimen 0.44

We refer here to two disk-shaped specimens of different diameters which were both 44 percent crystalline. They were prepared from bulk material about 2 mm thick which had been previously heated above the melting point to 250 °C, and then plunged into ice water. Specimen 0.44A was a disk 4.4033 cm in diameter. Specimen 0.44B was prepared by machining specimen 0.44A to a diameter of about 2.54 cm. Specimen 0.44A and 0.44B are jointly referred to as "specimen 0.44." These specimens had a slightly opalescent appearance, but were optically much clearer than specimen 0.80. The above technique is referred to in the text as "quench crystallization."

c. Specimen 0.12

This specimen was 12 percent crystalline. It was prepared from a thin film about 0.15 mm thick which had been pressed from the bulk material, heated to 250 °C, and plunged into ice water. The resultant thin film was optically clear.

In order to study the dielectric properties of nearly amorphous PCTFE at low temperatures, it

is necessary to resort to measuring quenched thin films rather than thick specimens. This is the case because between 120 and 170 °C there exists a temperature region in which extremely rapid crystallization takes place [7], and a thick specimen (say 2 mm thick) cannot be cooled rapidly enough through this region to prevent a significant amount of crystallization. A thin film having a large surface-to-volume ratio may be quenched more rapidly than the bulk material, thus achieving a lower degree of crystallinity. Such a weakly crystalline film will crystallize further if heated above approximately 60 °C.

d. Specimen 0.73

This specimen was prepared by annealing specimen 0.44B (quench crystallized bulk material) at 190 °C for two weeks. This increased the degree of crystallinity to $\chi=0.73$. It is important to note that this specimen was *not* crystallized directly from the melt as was specimen 0.80, but rather from a previously quenched specimen. This was done so that the dielectric properties of specimens with nearly the same high degree of crystallinity, but with crystals nucleated and grown under different conditions, might be compared. This crystallization process is referred to as the "quench→anneal" technique.

e. Specimen 0.0 (Liquid Phase)

By warming a disk specimen above $T_m=224$ °C, a body with no crystallinity ($\chi=0.00$) could be readily obtained. A specimen made in this way was studied up to 250 °C. Then by supercooling, the completely amorphous phase was studied down to about 200 °C. The onset of crystallization prevented measurements below this temperature.[2] Details of the methods used to obtain dielectric measurements on the liquid specimens, which tended to flow somewhat, are given in appendix 5.3.

Figure 1 shows the temperature dependence of the degree of crystallinity and the specific volume of the various specimens.

All the above mentioned specimens, with the exception of those used for the microwave measurements, and specimen 0.0, were machined or cut into disk shapes with areas and thicknesses determined by methods given below.

2.3. Determination of Dimensions of Disk Specimens

The area A^{23} at 23 °C was calculated from the average of several measurements of the specimen's diameter taken from various points on the circumference. A traveling microscope graduated to 0.0001 cm was employed for this purpose.

The average thickness of the specimen t^{23} at 23 °C was not directly measured but was calculated from

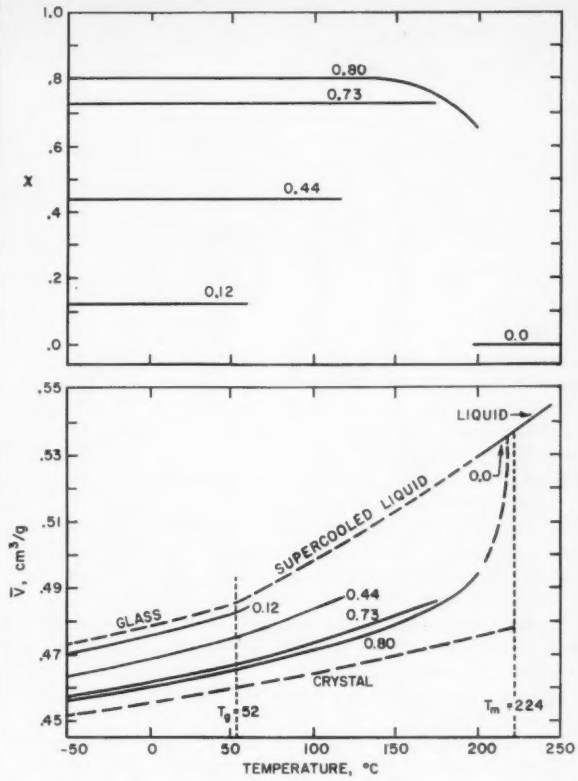

FIGURE 1. *Temperature dependence of the degree of crystallinity, χ, and the specific volume, $\overline{V}$, of the specimens.*

the equation

$$t^{23}=\frac{V^{23}}{A^{23}}=\frac{\overline{V}^{23}W_{air}}{A^{23}}, \tag{1}$$

where $\overline{V}^{23}$ is the specific volume at 23 °C, W_{air} the weight of the specimen in air, and V^{23} is the volume of the specimen at 23 °C. The specific volume employed in eq (1) was measured using the buoyancy technique. The specimen was weighed in air, and then in distilled water [3] at 23 °C (W_{water}). Given the density of the water, ρ_{water}, the specific volume was calculated from the equation

$$\overline{V}^{23}=\frac{W_{air}-W_{water}}{\rho_{water}W_{air}}. \tag{2}$$

A discussion of the accuracy of the measurements of A^{23} and t^{23} is given in appendix 5.1.e.

The above method of determining the average thickness of a specimen is distinctly superior to direct measurements using a micrometer, particularly for molded or machined specimens which have

[2] The rate of crystallization increases as the temperature is lowered below T_m. At 210 °C, the rate of crystallization from the supercooled liquid is altogether negligible, but below about 200 °C, the rate becomes high enough to interfere in the time required to measure ϵ' and ϵ''.

[3] Distilled water was selected as a suitable immersion fluid for PCTFE since the density of water is very well known and since the water absorption of PCTFE is unmeasurably small. A small quantity of wetting agent was added to the water to reduce surface tension. This affected the density of the water by no more than 10 ppm.

TABLE 1. *Physical characteristics of the disk and thin film specimens*

Specimen	Degree of crystallinity χ	Remarks	Specific volume at 23 °C, $\overline{V}^{23}$	Area, A^{23}	Thickness t^{23}	Vacuum capacitance C_v^{23}
			$cm^3\,g^{-1}$	cm^2	cm	pf
0.80A	0.80	Crystallized slowly from melt. Specimen highly spherulitic. Has white cloudy appearance.	0.4625	14.141	0.2315	5.408
0.80B			.4624	5.0523	.2309	1.937
0.44A	.44	Quench crystallized. Specimen contains no visible spherulites. Optically rather transparent.	.4711	15.228	.1840	7.328
0.44B			.4711	5.0658	.1832	2.448
0.73	.73	Crystallized by quench——→anneal method. Specimen contains no visible spherulites. Optically fairly transparent.	.4642	5.0561	.1750	2.558
0.12	.12	Prepared by rapid quenching of thin film. Optically transparent.	.4788	20.333	.01464	123.0

the usual slight surface irregularities. (The effect of such surface irregularities upon the dielectric measurements is considered in appendix 5.3.) In measuring a rigid material, a micrometer reads the *maximum* thickness of the material between its faces, and unless the two surfaces are perfect, the desired *average* thickness is not obtained. Using the specific volume method outlined above, the measurement "probe" consists of the liquid which establishes intimate contact with the surface, following its minute irregularities. Furthermore, if the material whose thickness is desired is somewhat soft, use of a micrometer tends to compress the specimen between its faces. Immersion in a liquid subjects the specimen only to very mild and uniform pressures.

The values of A and t at other temperatures are calculable from the change in specific volume with temperature, which has been previously measured [4].

Values of $\overline{V}^{23}$, A^{23}, t^{23}, and C_v^{23} for the specimens employed are given in table 1. Here C_v^{23} is the equivalent vacuum capacitance of the specimen at 23 °C expressed in pf.[4] C_v is given by

$$C_v^{23}=\epsilon_0\frac{A^{23}}{t^{23}}, \tag{3}$$

where ϵ_0 is the electric constant in the mks rationalized system ($\epsilon_0=8.854\times10^{-12}$ F/m,$=0.08854$ pf/cm).

After determining the above physical characteristics, the specimens were given conducting coatings. The planar surfaces of specimens 0.80A, 0.80B, 0.44, and 0.73 were given a conductive coating of evaporated gold, while silver conducting paint (silver 4922, manufactured by E. I. DuPont de Nemours and Co.) was applied to specimen 0.12.

2.4. Determination of χ

The degree of crystallinity of a specimen of PCTFE (defined here as the *mass* fraction crystallized) is at any temperature defined by the equation

$$\chi=\frac{\overline{V}_l-\overline{V}}{\overline{V}_l-\overline{V}_c}, \tag{4}$$

where $\overline{V}_l$ is the specific volume of the pure liquid (or glass), $\overline{V}_c$ is the specific volume of the pure crystal, and $\overline{V}$ the specific volume of the specimen in cm^3g^{-1}.

The values of $\overline{V}_l$ and $\overline{V}_c$ at 23 °C are 0.48175 and 0.45755 respectively [4]. One may then write for the degree of crystallinity at 23 °C

$$\chi=\frac{0.48175-\overline{V}^{23}}{0.0242}. \tag{5}$$

Using this formula, χ can be simply determined from the value of $\overline{V}^{23}$.

The value of χ remains constant with temperature as long as those temperature regions in which melting or further crystallization can take place are avoided. In order to avoid further crystallization of specimens 0.44 and 0.12, they were not heated above 118 and 60.6 °C, respectively.

Specimen 0.80, for which dielectric measurements were made up to 200 °C, underwent a significant amount of partial melting between 175 and 200 °C. (This partial melting is actually due to the complete melting out of the smaller crystals in the material.) In this region, the value of χ decreased, but the process was reversible as long as the specimen was brought down in temperature reasonably slowly. The temperature dependence of χ in this region is shown in figure 1. These curves were obtained from earlier work [4]. At 150, 175, and 200 °C, the value of χ for specimen 0.80 is 0.79, 0.75, and 0.65 respectively. In any analysis of the data in terms of χ, the variation of χ in this temperature range should not be negelected.

3. Experimental Results

The reader is referred to the appendix for discussion of the experimental details related to the specimen holder, bridges, Q-meter, re-entrant cavity, and waveguide apparatus employed in making the measurement of the loss index, ϵ'', and the real part of the relative dielectric constant, ϵ'.

The results of dielectric measurements are presented in both graphical and tabular form. The experimental points are shown on some of the plots to give an indication of the accuracy. From the

[4] 1 pf=1 picofarad=1 $\mu\mu$f.

TABLE 2. *Smoothed dielectric data for specimen 0.80*

If $\delta\epsilon'$ and $\delta\epsilon''$ represent the possible error in the values of ϵ' and ϵ'' reported below, then, when $f<100$ kc/s $\delta\epsilon'=0.15\%$ and $\delta\epsilon''=1\%$. When 100 kc/s $<f\leq 10$ Mc/s then $\delta\epsilon'=0.5\%$ and $\delta\epsilon''=5\%$.

Frequency \ Temperature	−50 °C		−35.5 °C		−25 °C		0 °C	
	ϵ'	ϵ'' x 10^4	ϵ'	ϵ'' x 10^4	ϵ'	ϵ'' x 10^4	ϵ'	ϵ'' x 10^4
0.1 c/s	2.597	360	2.653	264	2.684	187	2.740	100
.2	2.582	382	2.641	304	2.674	221	2.734	113
.5	2.559	389	2.621	355	2.661	279	2.727	139
1	2.540	378	2 604	391	2.647	326	2.721	160
2	2.522	355	2.584	415	2.631	370	2.713	189
5	2.500	312	2.558	423	2.605	421	2.702	239
10	2.486	279	2.539	410	2.586	449	2.690	298
20	2.474	243	2.519	380	2.565	457	2.675	364
50	2.461	198	2.498	326	2.538	426	2.651	445
100	2.454	167	2.485	282	2.520	382	2.629	488
200	2.447	145	2.473	240	2.503	335	2.604	511
500	2.438	126	2.461	190	2.485	269	2.571	487
1 kc/s	2.433	113	2.454	163	2.474	224	2.548	444
2	2.428	104	2.446	145	2.464	192	2.529	391
5	2.423	95	2.438	128	2.455	165	2.507	320
10	2.418	91	2.433	120	2.448	151	2.495	275
20	2.415	87	2.427	112	2.441	139	2.485	238
50	2.410	82	2.422	104	2.434	126	2.472	200
100	2.407	78	2.417	100	2.428	120	2.464	183
200	2.404	74	2.413	96	2.424	115	2.456	170
310	2.402	70	----	----	2.420	112	2.451	165
1 Mc/s	2.397	64	----	----	2.412	104	2.441	155
3.2	2.393	57	----	----	2.405	96	2.431	149
10	2.390	51	----	----	2.397	92	2.421	144

Frequency \ Temperature	23 °C		50 °C		75 °C		100 °C	
	ϵ'	ϵ'' x 10^4	ϵ'	ϵ'' x 10^4	ϵ'	ϵ'' x 10^4	ϵ'	ϵ'' x 10^4
0.1 c/s	2.772	53	2.798	26	2.832	61	2.862	58
.2	2.770	60	2.797	26	2.831	56	2.860	58
.5	2.765	75	2.796	30	2.827	50	2.858	58
1	2.762	88	2.794	34	2.824	45	2.856	58
2	2.758	105	2.793	38	2.821	40	2.854	59
5	2.751	133	2.791	49	2.818	35	2.849	60
10	2.746	162	2.788	59	2.816	33	2.846	61
20	2.737	197	2.785	72	2.815	35	2.842	63
50	2.725	257	2.781	100	2.812	44	2.838	65
100	2.714	315	2.777	130	2.810	54	2.835	66
200	2.700	387	2.772	175	2.808	67	2.832	68
500	2.672	490	2.760	267	2.804	95	2.828	70
1 kc/s	2.646	549	2.748	348	2.800	131	2.825	76
2	2.618	572	2.733	445	2.796	188	2.822	90
5	2.578	536	2.700	581	2.784	294	2.818	117
10	2.555	477	2.672	640	2.771	413	2.812	166
20	2.534	413	2.641	650	2.751	544	2.807	244
50	2.510	335	2.596	595	2.706	683	2.792	404
100	2.498	292	2.571	535	2.671	745	2.771	561
200	2.488	263	2.552	479	2.641	754	2.744	744
310	2.483	248	2.541	442	2.623	716	2.725	803
1 Mc/s	2.468	229	2.516	363	2.581	586	2.665	830
3.2	2.454	208	2.493	306	2.547	485	2.602	737
10	2.440	190	2.475	275	2.515	425	2.552	637
292	2.402	155	----	----	----	----	2.470	403
1 k Mc/s	2.388	155	----	----	----	----	----	----
3	2.375	165	----	----	----	----	----	----
8.6	2.360	180	----	----	----	----	----	----

Frequency \ Temperature	125 °C		150 °C		175 °C		200 °C	
	ϵ'	ϵ'' x 10^4	ϵ'	ϵ'' x 10^4	ϵ'	ϵ'' x 10^4	ϵ'	ϵ'' x 10^4
0.1 c/s	2.887	58	2.926	80	2.958	102	2.955	532
.2	2.886	57	2.923	78	2.956	66	2.946	330
.5	2.883	55	2.918	78	2.955	42	2.942	175
1	2.881	54	2.915	80	2.955	35	2.941	121
2	2.879	53	2.913	83	2.954	30	2.940	79
5	2.877	52	2.910	85	2.953	29	2.940	38
10	2.874	52	2.908	85	2.952	33	2.939	23
20	2.871	54	2.905	83	2.950	42	2.939	15
50	2.868	58	2.900	79	2.948	58	2.939	11
100	2.863	61	2.896	76	2.945	70	2.938	11
200	2.861	65	2.892	74	2.942	83	2.938	13
500	2.858	71	2.888	73	2.937	99	2.937	20
1 kc/s	2.854	77	2.885	72	2.932	111	2.937	28
2	2.852	82	2.882	74	2.927	137	2.935	40
5	2.846	92	2.878	82	2.919	119	2.933	58
10	2.842	104	2.875	92	2.913	116	2.930	73
20	2.839	127	2.871	107	2.908	113	2.927	89
50	2.832	187	2.865	131	2.902	123	2.920	111
100	2.825	277	2.860	175	2.898	142	2.916	127
200	2.814	432	2.854	243	2.892	171	2.913	146
310	2.808	552	2.848	314	2.887	214	2.909	158
1 Mc/s	2.757	826	2.823	608	2.867	421	2.900	246
3.2	2.688	920	2.768	821	2.825	793	2.882	518
10	2.610	873	2.700	1018	2.762	1090	2.849	1013
292	----	----	2.560	852	----	----	----	----

TABLE 3. *Smoothed dielectric data for specimen 0.44*

$\delta\epsilon'$ and $\delta\epsilon''$, the possible error in the values of ϵ' and ϵ'' reported below, are functions of the frequency and temperature.
When $T \leq 50$ °C and $f \leq 100$ kc/s then $\delta\epsilon' = 0.15\%$ and $\delta\epsilon'' = 1\%$.
When $T \leq 50$ °C and 100 kc/s $< f \leq 10$ Mc/s then $\delta\epsilon' = 0.5\%$ and $\delta\epsilon'' = 5\%$.
When $T > 50$ °C and $f \leq 100$ kc/s and $\delta\epsilon' = 0.6\%$ and $\delta\epsilon'' = 1.5\%$ and when $T > 50$ °C and 100 kc/s $< f \leq 10$ Mc/s then $\delta\epsilon' = 1\%$ and $\delta\epsilon'' = 6\%$.

Frequency \ Temperature	−50 °C		−36 °C		−24.5 °C		+0.5 °C	
	ϵ'	$\epsilon'' \times 10^4$	ϵ'	$\epsilon'' \times 10^4$	ϵ'	$\epsilon'' \times 10^4$	ϵ'	$\epsilon'' \times 10^4$
0.1 c/s	2.473	274	2.531	253	2.570	240	2.663	186
.2	2.459	289	2.518	278	2.560	264	2.654	203
.5	2.442	295	2.501	305	2.544	297	2.640	234
1	2.428	287	2.486	320	2.529	320	2.628	264
2	2.414	268	2.471	325	2.514	343	2.616	299
5	2.399	238	2.450	321	2.491	358	2.598	352
10	2.390	215	2.435	309	2.474	369	2.582	393
20	2.382	191	2.421	288	2.456	369	2.563	435
50	2.372	160	2.404	248	2.434	336	2.535	475
100	2.367	137	2.393	217	2.419	300	2.513	485
200	2.361	117	2.384	189	2.407	265	2.489	475
500	2.355	98	2.373	154	2.392	219	2.461	439
1 kc/s	2.351	86	2.367	130	2.384	190	2.442	400
2	2.347	75	2.361	110	2.376	165	2.426	356
5	2.344	65	2.354	93	2.368	134	2.406	292
10	2.341	61	2.351	85	2.363	115	2.395	247
20	2.338	58	2.348	78	2.358	100	2.384	210
50	2.335	54	2.344	73	2.352	87	2.373	170
100	2.333	51	2.340	69	2.348	81	2.366	147
200	2.331	48	2.338	66	2.344	79	2.361	127
310	2.330	46	----	----	----	----	2.357	118
1 Mc/s	2.326	41	----	----	----	----	2.349	95
3.2	2.324	36	----	----	----	----	2.340	82
10	2.321	30	----	----	----	----	2.334	73

Frequency \ Temperature	23 °C		50 °C		75 °C		100 °C		118 °C	
	ϵ'	$\epsilon'' \times 10^4$	ϵ'	$\epsilon'' \times 10^4$	ϵ'	$\epsilon'' \times 10^4$	ϵ'	$\epsilon'' \times 10^4$	ϵ'	$\epsilon'' \times 10^4$
0.1 c/s	2.755	119	2.837	64	2.888	89	2.955	162	2.992	89
.2	2.750	135	2.835	67	2.884	82	2.947	169	2.988	100
.5	2.741	160	2.831	75	2.879	75	2.937	170	2.983	118
1	2.734	188	2.828	85	2.876	71	2.930	166	2.977	132
2	2.725	219	2.824	98	2.872	68	2.922	159	2.971	145
5	2.712	268	2.818	124	2.867	65	2.913	148	2.961	163
10	2.700	317	2.811	149	2.864	68	2.907	142	2.953	174
20	2.686	375	2.804	183	2.861	73	2.900	136	2.945	179
50	2.662	452	2.793	248	2.856	89	2.892	127	2.935	181
100	2.640	513	2.782	306	2.853	116	2.887	123	2.928	176
200	2.615	573	2.770	383	2.848	138	2.880	121	2.919	170
500	2.577	628	2.742	518	2.839	200	2.875	127	2.909	162
1 kc/s	2.548	647	2.715	628	2.831	266	2.869	136	2.902	158
2	2.514	632	2.689	731	2.820	359	2.864	158	2.895	161
5	2.478	575	2.642	857	2.795	539	2.856	211	2.886	171
10	2.453	505	2.597	880	2.764	695	2.847	283	2.880	191
20	2.433	429	2.556	860	2.729	878	2.837	396	2.873	234
50	2.408	352	2.500	764	2.670	1018	2.810	634	2.859	347
100	2.394	301	2.465	670	2.618	1086	2.778	850	2.848	496
200	2.383	260	2.442	587	2.564	1076	2.728	1070	2.829	715
310	2.375	235	2.426	540	2.538	1040	2.693	1175	2.811	880
1 Mc/s	2.362	184	2.390	423	2.466	811	2.601	1207	2.727	1222
3.2	2.351	152	2.365	336	2.412	609	2.515	1050	2.620	1282
10	2.338	125	2.343	270	2.374	465	2.448	840	2.523	1178
292	2.316	80	----	----	----	----	2.352	386	----	----

smooth lines drawn through the points on such figures, the smoothed data presented in tables 2 to 5 [5] were obtained. The smoothed data are presented rather than the actual data in order to eliminate occasional points which are obviously excessively in error, as well as minimize the random effects of experimental error which arise from the limitations of the accuracy of the measuring apparatus. The experimental accuracy is discussed in detail in the appendix and is indicated in the legends of tables 2 through 6.

All the experimental loss index data have been corrected by subtracting out the loss component due to d-c resistance when this component exceeds 10^{-4}. The d-c resistance was determined by observing the current in the specimen after applying a d-c voltage. The d-c resistance (R_{dc}) was computed from readings obtained after the observable time effects had vanished. In some cases this involved times of about 10^3 sec. The loss component due to the d-c resistance was computed from the equation

$$\epsilon''_{dc} = (\omega C_v R_{dc})^{-1}. \quad (6)$$

where ω is 2π times f, the frequency. The low-frequency loss data are affected most by this component. Even so, at 0.1 c/s, ϵ''_{dc} was less than 10^{-4} for all specimens when the temperature was less than 100 °C. The loss data for specimen 0.44 required correction at 100 and 118 °C. Even at 118 °C, this correction was not required above 2 c/s, so that it scarcely altered the shape of the loss peak observed. Specimens 0.80 and 0.73 required correction only at temperatures at or above 175 °C. The loss data of the liquid specimen (200 to 250 °C), given in table 6,

[5] In addition to the data reported in tables 2 and 3, measurements were made on specimen 0.80 at 90, 112, 136, and 160° C and on specimen 0.44 at 105, 110, and 116° C. The above measurements extended from 0.1 to 200 c/s. These points were used to determine activation energies and are not given in the tables.

TABLE 4. *Smoothed dielectric data for specimen 0.12*

The accuracies in ϵ' and ϵ'' are about 1% and 3% respectively

Frequency \ Temperature	−36.5 °C		−24.3 °C		−3.1 °C		22.7 °C		39.3 °C		47.8 °C		60.6 °C	
	ϵ'	ϵ''	ϵ'	ϵ''	ϵ'	ϵ''	ϵ'	ϵ''	ϵ'	ϵ''	ϵ'	ϵ''	ϵ'	ϵ''
0.02 c/s	2.462	249×10⁻⁴	2.514	234×10⁻⁴	2.612	199×10⁻⁴	2.750	127×10⁻⁴	2.840	97×10⁻⁴	2.886	100×10⁻⁴	2.982	195×10⁻⁴
.1	2.436	286	2.488	280	2.592	248	2.739	156	2.830	114	2.877	101	2.968	159
.2	2.423	299	2.476	301	2.582	273	2.732	177	2.825	128	2.873	107	2.965	150
.5	2.405	316	2.458	336	2.565	318	2.722	212	2.818	148	2.867	121	2.959	146
1.0	2.391	320	2.442	355	2.550	352	2.712	251	2.812	180	2.861	143	2.954	150
2	2.378	310	2.427	362	2.535	385	2.701	293	2.803	215	2.855	167	2.949	157
5	2.361	294	2.406	370	2.511	430	2.684	353	2.791	265	2.845	211	2.941	171
10	2.349	278	2.390	368	2.492	462	2.667	415	2.779	321	2.837	252	2.933	197
20	2.336	253	2.374	348	2.470	480	2.648	476	2.765	387	2.826	308	2.925	224
50	2.322	220	2.355	320	2.441	491	2.621	560	2.743	484	2.808	399	2.913	283
100	2.313	196	2.342	290	2.419	488	2.595	622	2.721	582	2.791	497	2.900	345
200	2.306	169	2.331	255	2.398	465	2.566	667	2.694	674	2.768	595	2.885	422
500	2.298	134	2.317	213	2.371	413	2.524	702	2.651	784	2.731	754		
1 kc/s	2.292	117	2.309	181	2.354	373	2.492	699	2.614	862	2.696	880		
2	2.287	100	2.302	154	2.339	325	2.461	666	2.574	902	2.654	978		
5	2.282	84	2.294	126	2.323	261	2.423	598	2.518	899	2.593	1058		
10	2.278	72	2.289	107	2.313	220	2.398	526	2.478	860	2.545	1062		
20	2.275	64	2.285	92	2.305	184	2.377	452	2.441	782	2.499	1010		
50	2.272	54	2.280	76	2.296	144	2.355	362	2.400	646	2.443	874		
100	2.270	50	2.277	68	2.290	130	2.342	310	2.374	562	2.407	767		
200	2.269	46	2.275	62	2.286	115	2.330	260	2.354	448	2.378	659		

TABLE 5.—*Smoothed dielectric data for specimen 0.73*

$\delta\epsilon'$ and $\delta\epsilon''$ are the possible error in the values of ϵ' and ϵ'' reported below. When $f<100$ kc/s then $\delta\epsilon'=0.4\%$ and $\delta\epsilon''=1.4\%$ and when $f>100$ kc/s then $\delta\epsilon'=1.5\%$ and $\delta\epsilon''=6.5\%$

Frequency \ Temperature	−36.2 °C		23 °C		50.6 °C		75 °C		92.7 °C	
	ϵ'	ϵ'' x 10⁴	ϵ'	ϵ'' x 10⁴	ϵ'	ϵ'' x 10⁴	ϵ'	ϵ'' x 10⁴	ϵ'	ϵ'' x 10⁴
0.1 c/s	2.594	241	2.752	60	2.788	24	2.823	84	2.856	103
.2	2.584	278	2.749	68	2.787	25	2.819	76	2.851	100
.5	2.566	325	2.743	84	2.786	26	2.815	67	2.846	95
1.0	2.551	359	2.740	102	2.785	29	2.812	61	2.841	92
2	2.534	380	2.735	121	2.784	36	2.809	55	2.837	88
5	2.509	384	2.728	154	2.782	48	2.806	51	2.833	84
10	2.491	369	2.721	191	2.780	60	2.804	50	2.828	80
20	2.473	345	2.713	231	2.778	77	2.802	50	2.826	77
50	2.453	297	2.698	300	2.773	113	2.800	54	2.821	72
100	2.440	257	2.684	366	2.767	152	2.798	63	2.818	71
200	2.430	220	2.667	430	2.760	202	2.796	77	2.815	71
500	2.418	178	2.637	505	2.747	290	2.792	106	2.811	76
1 kc/s	2.410	154	2.613	544	2.734	382	2.787	144	2.806	88
2	2.404	137	2.586	562	2.715	488	2.782	205	2.803	105
5	2.397	121	2.550	521	2.681	607	2.769	324	2.798	149
10	2.392	111	2.524	468	2.649	667	2.754	448	2.792	227
20	2.387	103	2.506	414	2.616	680	2.730	597	2.781	337
50	2.381	95	2.484	341	2.573	630	2.686	727	2.758	530
100	2.376	90	2.468	298	2.544	560	2.649	776	2.729	674
200	2.371	87	2.454	270	2.523	495	2.611	775	2.693	801
320	2.367	85	2.446	254	2.508	458	2.588	745	2.665	864
1 Mc/s	2.360	80	2.426	224	2.477	382	2.545	640	2.598	855
3.2	2.352	76	2.410	202	2.452	315	2.508	532	2.550	727
10	2.344	74	2.395	187	2.432	270	2.479	445	2.512	633
45			2.379	169						
100			2.371	160						

Frequency \ Temperature	108.4 °C		123.9 °C		148.9 °C		174.5 °C	
	ϵ'	ϵ'' x 10⁴	ϵ'	ϵ'' x 10⁴	ϵ'	ϵ'' x 10⁴	ϵ'	ϵ'' x 10⁴
0.1 c/s	2.891	123	2.936	122	2.996	34	2.971	14
.2	2.885	121	2.930	126	2.992	42	2.970	12
.5	2.878	118	2.923	134	2.989	54	2.970	11
1.0	2.873	116	2.917	137	2.986	65	2.969	11
2	2.868	113	2.912	140	2.983	77	2.968	11
5	2.862	108	2.904	141	2.980	95	2.968	12
10	2.857	106	2.898	142	2.975	113	2.967	15
20	2.852	103	2.893	140	2.969	130	2.967	19
50	2.847	99	2.885	136	2.961	154	2.966	25
100	2.842	97	2.878	133	2.953	169	2.965	35
200	2.839	95	2.873	127	2.944	181	2.964	47
500	2.834	92	2.867	120	2.932	190	2.962	70
1 kc/s	2.830	91	2.862	116	2.923	190	2.958	94
2	2.826	97	2.856	114	2.915	186	2.953	125
5	2.821	120	2.849	121	2.905	178	2.942	170
10	2.817	154	2.844	132	2.897	175	2.933	198
20	2.811	209	2.839	152	2.888	175	2.924	211
50	2.799	340	2.831	223	2.879	188	2.909	221
100	2.784	490	2.825	319	2.872	227	2.901	228
200	2.761	686	2.809	469	2.865	295	2.894	267
320	2.741	802	2.795	608	2.857	380	2.888	311
1 Mc/s	2.675	945	2.744	930	2.831	690	2.871	493
3.2	2.603	910	2.676	1012	2.775	1000	2.832	847
10	2.545	825	2.600	965	2.702	1205	2.757	1180

TABLE 6. *Dielectric data for specimen 0.0* [a]

Time sequence	1			2			3			4		
Temperature	243.1 °C			219.5 °C [b]			244.2 °C			197.6 °C		
Frequency	ϵ'	$\epsilon''\times10^4$	$\epsilon''_{dc}\times10^4$	ϵ'	$\epsilon''\times10^4$	$\epsilon''_{dc}\times10^4$	ϵ'	$\epsilon''\times10^4$	$\epsilon''_{dc}\times10^4$	ϵ'	$\epsilon''\times10^4$	$\epsilon''_{dc}\times10^4$
20 c/s	2.514	120	263	2.574	55	128						
50				2.574	23	51						
100	2.514	22	53	2.574	11	26	2.568	36	91	2.633	3	12
200	2.513	11	26	2.574	6	13						
1 kc/s										2.633	2	1
10										2.633	6	
160										2.632	16	

[a] The accuracies of ϵ' and ϵ'' are about 0.5% and $\pm(1.5\%+1\times10^{-4})$ respectively. Values of ϵ'' given above were obtained by subtracting the indicated contribution of the d-c conduction (ϵ''_{dc}) from the measured value of the loss index.

[b] These specimens were in the supercooled liquid state.

required considerable correction, and the magnitude of the d-c component subtracted is included in table 6.

3.1. Data for Specimen 0.80. Nomenclature Used to Denote Loss Processes

Figures 2 and 3 show the frequency dependence of ϵ'' and ϵ', respectively, at the indicated temperatures for specimen 0.80. These plots illustrate the behavior with temperature of the most prominent loss process in the polymer.

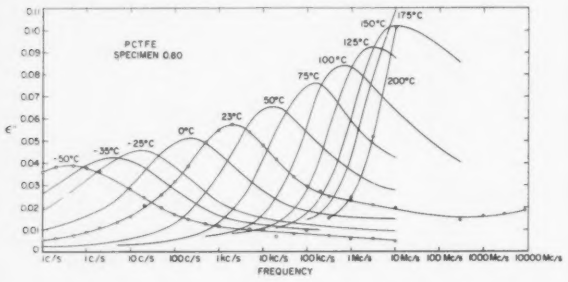

FIGURE 2. *Frequency dependence of the principal loss index peak in specimen 0.80 as a function of temperature.*

This peak corresponds to the low temperature peak on an ϵ'' versus temperature plot (see fig. 4).

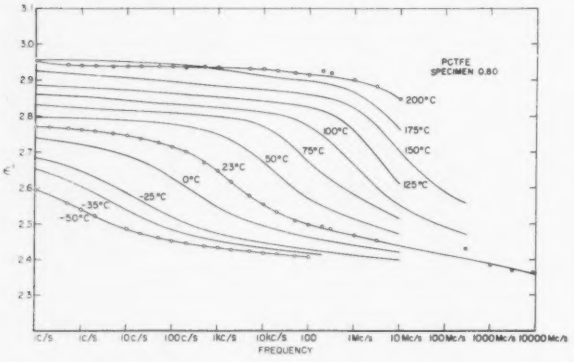

FIGURE 3. *Dielectric constant versus frequency for specimen 0.80 as a function of temperature.*

The loss process leading to the loss maximum evident in figure 2 will be called the *"low-temperature"* process, since on a plot of the loss index as a function of the temperature, T, at a constant low frequency, this effect occurs at temperatures lower than the other processes observed. Figure 4, in which ϵ'' at 1 c/s is plotted against T for the $\chi=0.80$ specimen, illustrates the scheme employed to name the loss processes observed in this polymer.

Considerable care will be taken in the paper to correlate and identify the loss peaks on the ϵ'' versus T plots, with the corresponding maximums (or other effects) in the appropriate ϵ'' versus log f plots. If a loss peak appears on an ϵ'' versus T plot, the underlying mechanism causing the peak will usually lead to a maximum or other discernible effect in an ϵ'' versus log f plot in the appropriate temperature and frequency range. In general, an analysis based on a study of both types of plot is more powerful than with just one or the other. It is emphasized that the nomenclature used to denote a process under discussion is based on the ϵ'' versus T plot (see fig. 4), irrespective of whether the process is manifested on an ϵ'' versus T plot or an ϵ'' versus log f plot.

Two other relaxation processes were observed in specimen 0.80. The first of these, on an ϵ'' versus

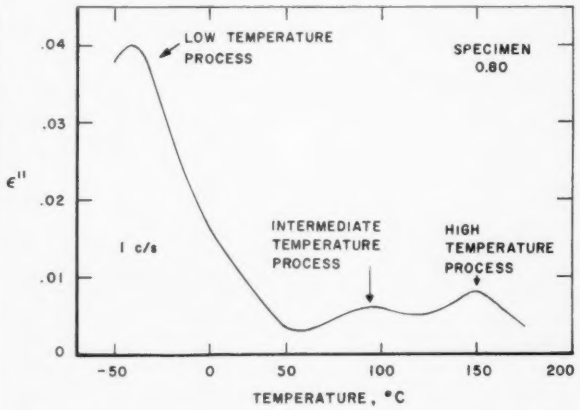

FIGURE 4. *ϵ'' versus temperature at 1 c/s for specimen 0.80.*

This illustrates the nomenclature scheme used to denote the loss processes.

log f plot (fig. 5), is most apparent in the temperature region between 75 and 125 °C at frequencies between 0.1 c/s and 10 kc/s. It is evident in figure 5 that a small loss maximum, partly obscured by other mechanisms, shifts from low frequencies on through the 10 c/s region to higher frequencies as the temperature is raised from 75 to 125 °C. This mechanism is the same as the one which leads to the clear-cut intermediate-temperature process peak when ϵ'' at a fixed (low) frequency is plotted as a function of temperature (fig. 4). Hence, this mechanism is denoted as the "*intermediate-temperature*" process.

The third relaxation process observed in the χ=0.80 specimen shows up quite clearly on both an ϵ'' versus log f plot and an ϵ'' versus T plot. The loss peak in the ϵ'' versus log f plot shown in figure 6 is easily seen at 150 and 175 °C, but at

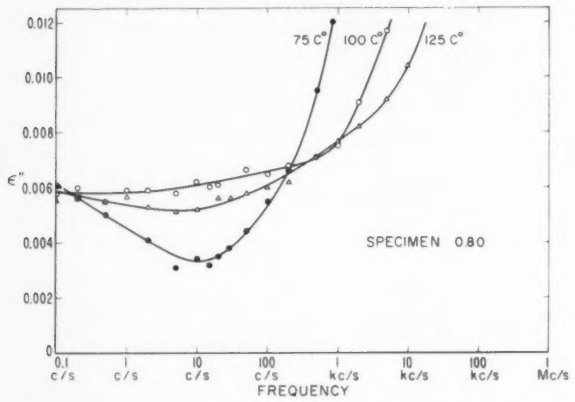

FIGURE 5. *Loss index versus frequency showing evidence for the intermediate-temperature loss process in specimen 0.80.*

Near 10 c/s, the loss is higher at 100 °C than at either 75 °C or 125 °C. This indicates that a small loss process traversed this region as the temperature increased. The loss mechanism causing this effect is the same as that which causes the intermediate temperature loss peak in figure 4.

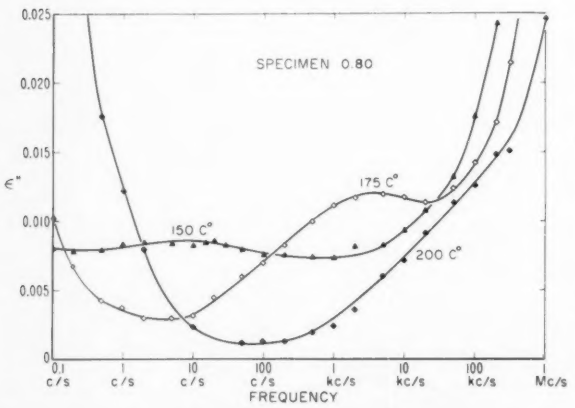

FIGURE 6. *ϵ'' versus frequency at various temperatures showing the high-temperature loss process in specimen 0.80.*

The loss process giving the maximum is the same as that which causes the high-temperature peak in figure 4.

The degree of crystallinity of specimen 0.80 changes at temperatures above 140 °C (see fig. 1). At 150 °C, 175 °C, and 200 °C the value of χ is 0.79, 0.75, and 0.65 respectively.

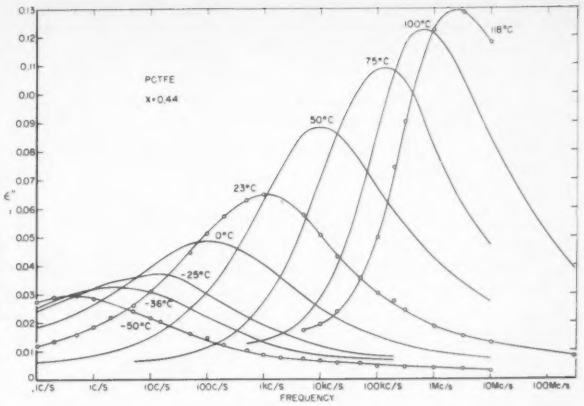

FIGURE 7. *ϵ'' versus frequency at various temperatures for specimen 0.44.*

This large loss peak is due to the low-temperature mechanism.

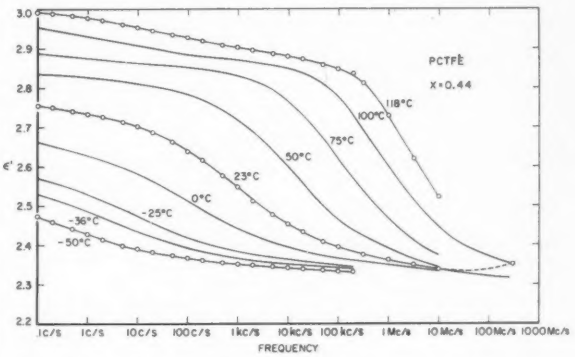

FIGURE 8. *Dielectric constant versus frequency for specimen 0.44.*

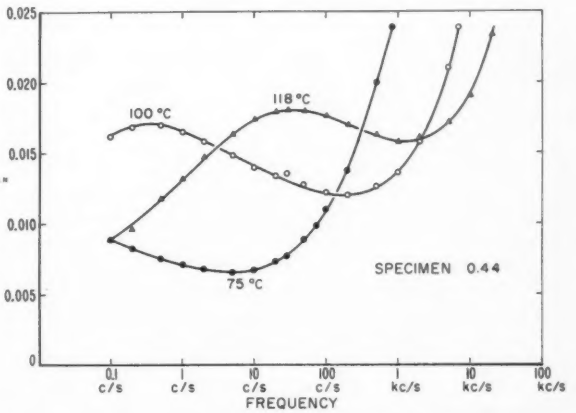

FIGURE 9. *Frequency dependence of the loss index of specimen 0.44 at high temperatures and low frequencies.*

The loss peak is mostly due to the intermediate-temperature mechanism, but contains some contribution from the high-temperature mechanism (*cf.* fig. 4).

200 °C it is obscured by the loss peak associated with the low- and intermediate-temperature processes. The mechanism leading to this loss peak is the same as that producing the high-temperature peak in the ϵ'' versus T plot (fig. 4). For convenience, this process, whether manifested in an ϵ'' versus T plot or an ϵ'' versus log f plot, is called the *"high-temperature"* mechanism.

3.2. Data for Specimen 0.44

The data for specimen 0.44 are presented in figures 7 and 8 where ϵ'' and ϵ' respectively are plotted as functions of log f at the indicated temperatures. From figure 7 it is apparent that the low-temperature relaxation process is active in this specimen.

Figure 9 shows the frequency dependence of the loss index in the high-temperature, low-frequency region. The loss index peak observed here is higher in magnitude than either the high-temperature process or the intermediate-temperature process evidenced in specimen 0.80. As will be discussed later, this loss peak is mostly due to an intermediate-

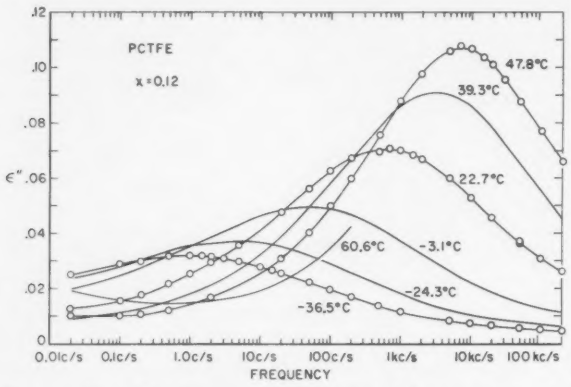

FIGURE 10. *The frequency dependence of the loss index for specimen 0.12 (thin film).*

These loss peaks are a result of the low-temperature process.

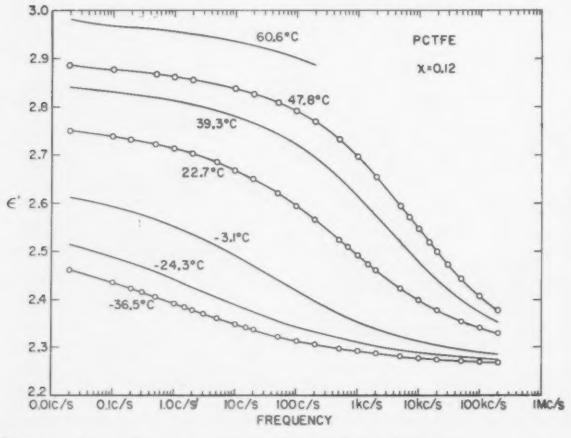

FIGURE 11. *Frequency dependence of the dielectric constant of specimen 0.12.*

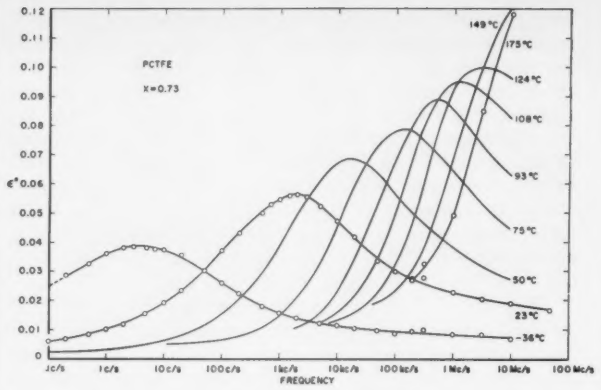

FIGURE 12. *ϵ'' versus frequency at various temperatures for specimen 0.73.*

The loss peaks are due to the low temperature mechansim.

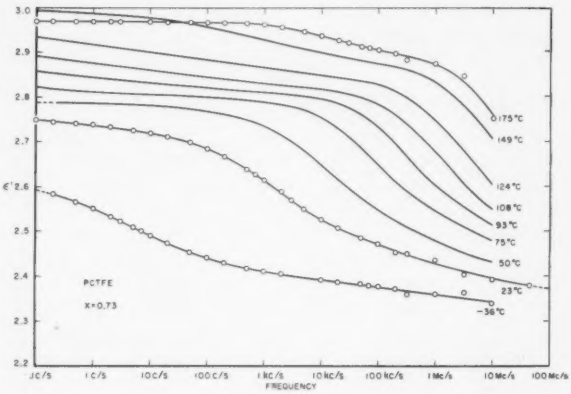

FIGURE 13. *The dielectric constant versus the frequency for specimen 0.73.*

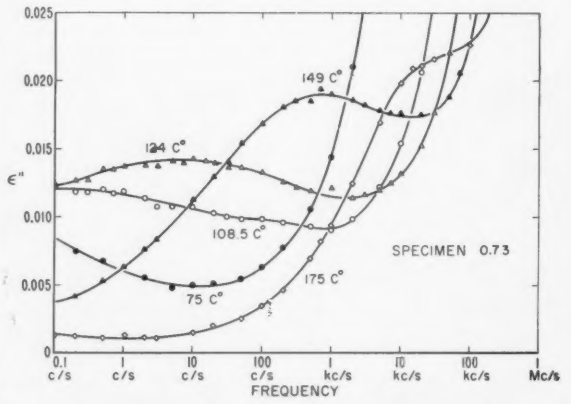

FIGURE 14. *The frequency dependence of ϵ'' for specimen 0.73 at high temperatures and low frequencies.*

The loss peaks are due to mixed intermediate and high temperature contributions (cf. fig. 4).

temperature mechanism of the type that appeared in the 0.80 specimen, but it evidently contains a contribution from the high-temperature loss mechanism. The peak in the ϵ'' versus log f plot that appears explicitly in figure 9 for $\chi=0.44$ is clearly substantially larger than that which exists (but which does not appear explicitly as a loss maximum in an ϵ'' versus log f plot) in the $\chi=0.80$ specimen (fig. 5).

3.3. Data for Specimen 0.12

Since this specimen was a thin film, special comments on the measurements are necessary. These are given in appendix 5.3. Broadly speaking, the error in the measurement of ϵ' and ϵ'' for the thin film is about ± 1 percent and ± 2 percent respectively. The measurements on the thicker disk-shaped specimens are subs antially more precise (see appendix, and footnotes in tables 2, 3, and 5).

Figures 10 and 11 show ϵ'' and ϵ' versus frequency for specimen 0.12. On an ϵ'' versus T plot, to be discussed later, the data on 0.12 exhibits the low-temperature process.

3.4. Data for Specimen 0.73

Figures 12 and 13 present ϵ'' and ϵ' versus frequency at the indicated temperatures for specimen 0.73. The loss peak in figure 12 is associated with the low-temperature peak on an ϵ'' versus T plot, and is rather similar in character to that evident in specimens 0.44 and 0.80.

The loss index of specimen 0.73 as a function of frequency for various temperatures between 75 and 175 °C is presented in detail in figure 14. Later, it will be shown by the use of an ϵ'' versus T plot at 1 c/s that this loss maximum results from "mixed" contributions from both the intermediate- and high-temperature mechanisms.

It is appropriate at this time to recall that specimen 0.73 was prepared by annealing a previously quenched bulk specimen at 190 °C until a high degree of crystallinity was achieved ("quench→anneal" technique). This was done in order to compare the dielectric properties of specimens with nearly the same high degree of crystallinity, but with crystals nucleated and grown under different conditions. The most striking difference between the dielectric properties of specimens 0.73 and 0.80 occurs in the high-temperature, low-frequency region. Comparison of figures 6 and 14, particularly the data obtained near 175 °C, demonstrates this difference most effectively. Figure 6 shows a loss peak maximum for specimen 0.80 ($\chi=0.75$/at 175 °C as noted in fig. 1) at 175 °C near 1.5 kc/s, while figure 14 shows a loss peak maximum for specimen 0.73 at 175 °C near 15 kc/s. The one-decade shift in the frequency location of this loss peak in the two specimens indicates that even though two specimens may have the same degree of crystallinity, their dielectric properties need not be identical. The cause of this effect will be discussed in section 4.1c.

3.5. Empirical Method of Estimating χ From the Dielectric Data

In order to correlate and compare the dielectric data of PCTFE presented here with results obtained previously by others, it is necessary to know approximately the degree of crystallinity of the specimens that they used. In many cases, the density of the specimen was not reported in the literature, so that this means of estimating the degree of crystallinity cannot be employed. However, at least a rough value of the degree of crystallinity can be obtained from the dielectric data itself.

To facilitate this determination, a convenient although crude crystallinity "scale" was obtained from our dielectric data on specimens of known χ. Comparison of our room-temperature data for specimens of various degrees of crystallinity showed that in the most commonly employed frequency region (about 50 c/s to 100 kc/s), the loss index at about 100 c/s exhibited the greatest dependence upon χ. The dependence of the 100 c/s values of ϵ'' and tan δ upon the degree of crystallinity is presented in figure 15. The degree of crystallinity of specimens employed in other dielectric investigations of PCTFE was estimated from the curves of figure 15. The results are given in table 7. In most cases, the

TABLE 7. *Estimated degree of crystallinity of PCTFE specimens used in other dielectric studies* [a]

Author	Specimen description	χ dielectric method	χ density method
Reynolds and coworkers [1]	"Kel-F" polymer	0.47	
Hartshorn and coworkers [2]	(1) cooled slowly from 250 °C	.60	
	(2) quenched from 210 °C	.54	
	(3) quenched from 250 °C	.40	
Mikhailov and Sazhin [3] [b]	(1) cooled slowly	0.65	
	(2) abruptly cooled	(~0.2)	
Nakajima and Saito [6]	(1) cooled slowly from melt	.52	0.48
	(2) quenched to room temperature.	.47	.46
	(3) quenched to −30 °C	(~0.3)	.43

[a] Except where noted, the values of χ (dielectric method) were estimated from the dielectric loss data using the crystallinity "scale" given in figure 15. The χ (density method) values were calculated from the densities (when given), using the crystallinity scale of reference [4].
[b] χ estimated from 23 ° C tan δ data at 50 c/s.

values of χ obtained by the dielectric method are compatible with the indicated thermal history of the specimen. However, the values of χ obtained for the "abruptly cooled" specimen of Mikhailov and Sazkin, and for the "quenched to −30 °C" specimen of Nakajima and Saito, appear to be lower than one would expect from the indicated thermal treatment *assuming* that bulk specimens were employed. (Nakajima and Saito used specimens 2 mm thick.)

Even with the most stringent quenching techniques we have been unable to attain such low values of χ except with thinner specimens. While the results in table 7 for the dielectric method doubtless give a rough picture of the range of χ used by other

investigators, it is clear that χ determinations based on ϵ'' or tan δ measurements on PCTFE must not be regarded as being a substitute for the more accurate density method.

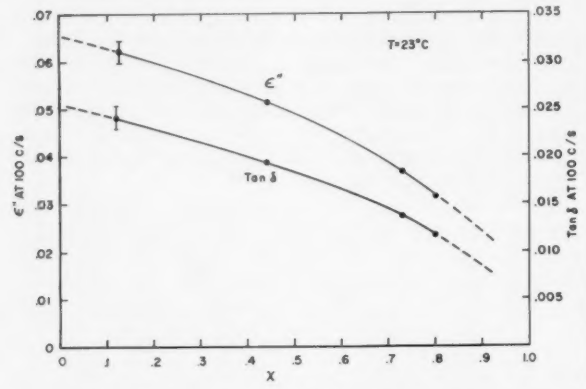

FIGURE 15. *The 100 c/s values of the loss index and tan δ at room temperature as a function of the degree of crystallinity.*

These data are intended to provide an approximate crystallinity scale for dielectric specimens where the specific volume has not been reported.

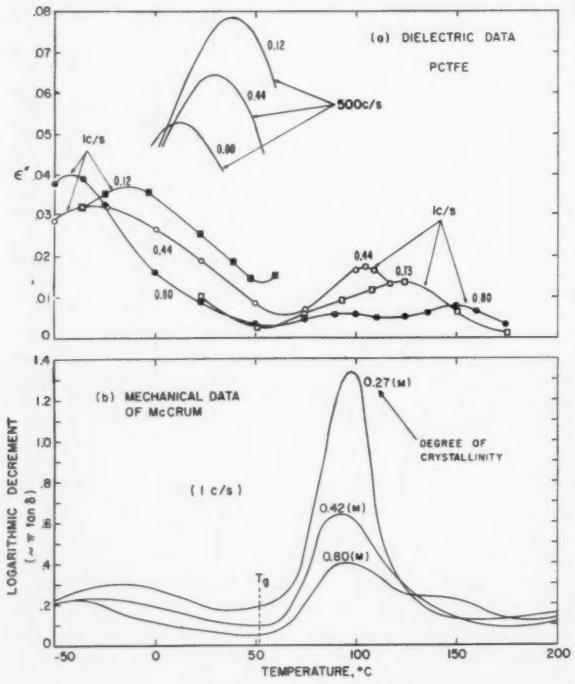

FIGURE 16. *Direct comparison between dielectric and mechanical loss data.*

a. The temperature dependence of the loss index at 1 c/s and 500 c/s for specimens of various crystallinities. b. The temperature dependence of the mechanical loss at 1 c/s for specimens of various crystallinities. The data at 1 c/s provide a direct comparison of the dielectric and mechanical data. The 500 c/s dielectric data illustrate the shift of the maximums with increasing f.

4. Interpretation of Results

4.1. The Intermediate- and High-Temperature Relaxation Processes

The principal objective of this section is to identify the phases in which the intermediate- and high-temperature loss processes originate, and to consider the nature of the relaxation phenomena in these phases. It will be demonstrated in section 4.4 that none of the dielectric loss peaks discussed are a result of Maxwell-Wagner polarization.

a. The Intermediate-Temperature Process

In discussing the intermediate-temperature loss process, use will be made of the dynamic mechanical loss data on PCTFE of McCrum [6] [8], who studied specimens of various degrees of crystallinity. Although others [9, 10, 11] have studied the dynamic mechanical properties of PCTFE, the data of McCrum are particularly valuable since he investigated specimens with a wide range of known crystallinities.

A useful type of plot in discussing the dielectric aspects of the intermediate-temperature loss process is shown in figure 16a, where ϵ'' is plotted as a function of temperature at 1 and 500 c/s for the various dielectric specimens. A graph of the mechanical loss data of McCrum, plotted as logarithmic decrement ($\simeq \pi \tan \delta$) versus temperature, also at 1 c/s, for samples of various degrees of crystallinity is shown in figure 16b.[7] The degree of crystallinity was calculated from specific volume data using eq (5).

Three mechanical loss peaks are evident in specimen 0.80(M)(χ=0.80). The intermediate-temperature peak is in general most pronounced and occurs at virtually the same temperature (95 °C) in all three specimens. The intermediate peak observed dielectrically in specimen 0.80 at 1 c/s also occurs near 95 °C. This suggests that the same molecular relaxational mechanism underlies both the mechanical and the dielectric intermediate-temperature loss peak. Since the magnitude of the mechanical intermediate-temperature peak is increased by increasing the fraction of the amorphous phase present (see fig. 16b), it seems reasonable to identify this peak tentatively as a property of the normal amorphous (supercooled liquid) component of the semicrystalline polymer. Further evidence supporting this identification will be presented shortly.

The intermediate peak in the dielectric data evidently decreases in magnitude as the fraction of the amorphous component decreases. (Compare 0.80 and 0.44 curves in fig. 16a). This decrease of intensity can be clearly discerned despite the fact there is evidently some "mixing" of the main intermediate component and a weaker high-temperature process

[6] The authors are deeply indebted to Dr. McCrum of the E. I. duPont de Nemours Company for making these data available to us prior to publication.

[7] Dr. McCrum has measured the logarithmic decrement (π tan δ) and the torsion modulus G, at 1 c/s using the torsion pendulum method at temperatures between −180 and +210 °C. Since no further mechanical loss maximums were observed below −50 °C and our dielectric data does not extend below −50 °C, only the π tan δ data above −50 °C are shown here.

component in specimen 0.44 which causes an upward shift of the characteristic temperature. (A detailed discussion of this shift is given in section 4.1c. The peak for 0.73, which was crystallized in a very different manner than 0.80, is so completely "mixed" and strongly shifted as to be of little value in the present comparison.) In any case, the relative intensities of the dielectric loss peaks at 1 c/s for 0.44 and 0.80 in the vicinity of 90 to 105 °C clearly suggest that the amorphous phase is the seat of the intermediate process.

It will now be demonstrated that the intermediate-temperature loss mechanism that appears at about 95 °C at 1 c/s in both the dielectric and mechanical data may reasonably be associated with the relaxational effects of the normal glass transition in the amorphous regions of the polymer at T_g=52 °C.

A typical property of the onset of the glass transformation in an entirely amorphous body is that the apparent heat of activation, ΔH^*, decreases rapidly as the temperature is increased above T_g. From the work of Williams, Landel, and Ferry (WLF) [12], this dependence of ΔH^* on temperature is given for many amorphous substances, including noncrystalline linear polymers, by the empirical expression

$$\Delta H^*(\text{cal/mole})=\frac{4.12\times10^3T^2}{(51.6+T-T_g)^2}, \qquad (7)$$

where T_g is the glass transformation temperature as determined from the break in a specific volume versus temperature ($\overline{V}-T$) plot. Ferry [13] has indicated that the constants in this expression may vary somewhat from one case to another, but eq (7) is still to be regarded as a fair representation of the general situation. The expression is valid between T_g and T_g+100 °K.

The apparent heat of activation was calculated from the data using the expression

$$\frac{-R\partial \ln f_m}{\partial(1/T)}=\Delta H^* \qquad (8)$$

where R is the gas constant, T the absolute temperature, and f_m the frequency of the maximum in an ϵ'' versus log f plot. In some cases, eq (8) was used over restricted temperature ranges to obtain ΔH^* as a function of temperature.

Figure 17 shows a plot of log f_m versus $1/T$.

Specimen 0.80 was the only specimen for which the maximum of the intermediate-temperature peak on an ϵ'' versus log f plot was sufficiently resolvable. The χ=0.44 specimen exhibits a peak mostly due to the intermediate process (figs. 9 and 16), but the shift of f_m with $1/T$ due to the intermediate component itself is not accessible.[8]

The apparent heats of activation associated with the intermediate-temperature process for the 0.80 specimen are given for two temperatures in table 8.

[8] An attempt was made to observe the intermediate-temperature process in specimen 0.12. Upon warming the film above about 60 °C, however, further crystallization took place. A loss peak (ϵ''_{max}=0.0243) was ultimately observed at 0.08 c/s at 92 °C. The degree of crystallinity of the specimen had by then increased to 0.34.

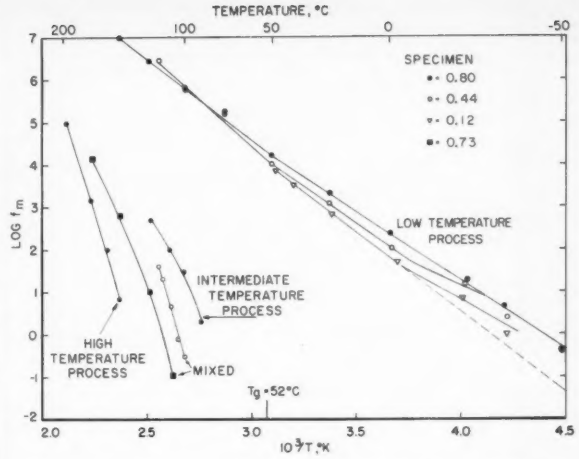

FIGURE 17. *Frequency of the maximums of the loss peaks, f_m, versus the reciprocal of the absolute temperature.*

The points were obtained from the ϵ'' versus log f plots.

TABLE 8. *Apparent heats of activation for the various dielectric relaxation processes* [a]

Specimen	χ	Temperature range	ΔH^*, kcal/mole
Low-temperature process			
0.80	0.80	−50 to 50 °C	14.6±5%
.44	.44	0 to 50 °C	15.8±5%
.12	.12	0 to 50 °C	16.7±5%
Resolved intermediate-temperature process			
0.80	0.80	Near 90 °C	67±20%
.80	.80	Near 120 °C	34±20%
Mixed-intermediate and high-temperature process			
0.73	0.73	Near 115 °C	95±20%
.73	.73	Near 160 °C	49±20%
.44	.44	100 to 118 °C	80±20%
Resolved high-temperature process			
0.80	0.79	Near 150 °C	91±20%
.80	.68	Near 190 °C	70±20%

[a] All heats of activation were calculated from data obtained from ϵ'' versus log f plots.

Despite the fairly large uncertainty, it is evident that ΔH^* decreases rapidly as the temperature is increased above T_g. (ΔH^* drops from 67 to 34).[9]

The temperature dependence of the apparent heat of activation for the intermediate-temperature process calculated using the dielectric data is in fairly good agreement with that calculated from the WLF expression, eq (7), with T_g=52 °C. This is illustrated in figure 18. The fact that some difference exists between the predicted and experimental values of ΔH^* in this case is not surprising, since

[9] While the experimental points determining the log f_m vs. $1/T$ curve for the intermediate process of specimen 0.80 (fig. 17) may possibly be fitted by a straight line, the curved line shown in figure 17 provides a far better fit of all the points. Furthermore, a curved line is to be expected in this case on the basis of experimental work of others [14, 48].

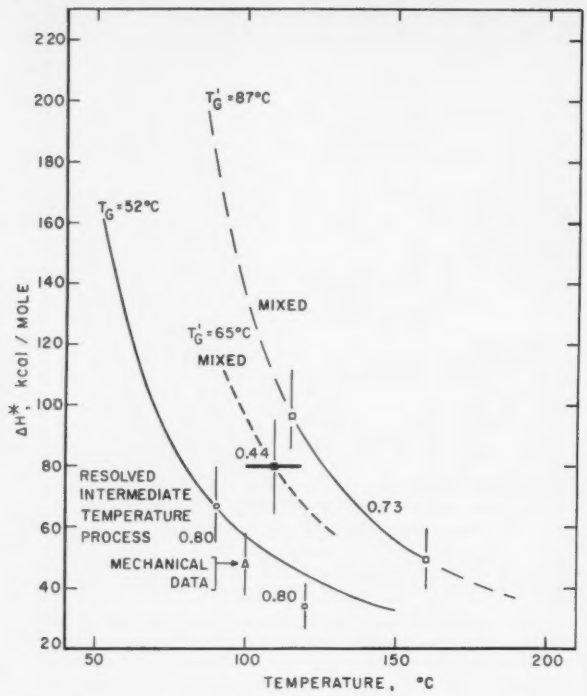

FIGURE 18. *The apparent activation energy of the intermediate-temperature process and mixed intermediate- and high-temperature processes versus the temperature.*

The curved lines were calculated from the WLF equation, using the indicated values for T_g or T_g'.

The points (except one) indicate the experimental dielectric data. The single mechanical point results from combining the 1 c/s data of McCrum [8] with the 3.3 c/s data of Schmieder and Wolf [9].

the accuracy with which ΔH^* is experimentally determined is rather low, and since the constants in eq (7) are not strictly universal.

Also shown in figure 18 is a single point calculated from the difference in location of the 1 c/s mechanical loss peak at 95 °C observed by McCrum, and the 3.3 c/s mechanical peak at 104 °C observed by Schmieder and Wolf [9]. Although this point was calculated from two different sets of data, and from a temperature rather than a frequency plot, it is consistent with the points obtained from the dielectric data for the intermediate-temperature process and falls fairly close to the curve calculated from eq (7).

The fact that the WLF expression is obeyed even approximately (with T_g=52 °C from $\overline{V}$–T data) for the resolved intermediate process indicates that this process is a relaxation effect that is premonitory to the glass transition that occurs at 52 °C.

Another indication that the intermediate process is associated with the glass transition is provided by the large change of modulus in the mechanical data in the general vicinity of the intermediate peak, especially in the less crystalline specimens. Strictly amorphous polymers show a similar large change of modulus.

When considered together, the facts outlined above lead to the definite conclusion that the intermediate-temperature process is indeed a bulk property of the amorphous (supercooled liquid) component of the polymer, and further, that this process is due to relaxation effects connected with the onset of the normal glass transition in these amorphous regions. The molecular phenomena leading to the intermediate-temperature process doubtless involve complex motions of a large number of polymer chain segments in the amorphous phase.

Saito and Nakajima [14] have experimentally demonstrated in the amorphous polymers they studied that the frequency of the loss index maximum for the relaxation peak associated with the glass transition lies between 10^{-2} and 10^{-3} c/s, when the temperature of the specimen is at the value of T_g determined from the break in the $\overline{V}$-T plot. Using a *linear* extrapolation of the log f_m versus $1/T$ data for the intermediate-temperature peak in specimen 0.80, one obtains T=57 °C when $f=10^{-2}$ c/s and T=47 °C when $f=10^{-3}$ c/s. The value of T_g (52 °C) does indeed lie between these temperatures. There are, however, several difficulties with this simple extrapolation in the case of PCTFE. The log f_m versus $1/T$ line is actually curved, and both of the above estimates of T are low in comparison with what is estimated using curvature (see below). The extrapolation is in any case rather long. Using an extrapolation with our best estimate of the curvature, it is estimated that $T=77\pm10$ °C for 10^{-2} c/s and $T=72\pm10$ °C for 10^{-3} c/s, both values being higher than the value T_g=52 °C obtained from $\overline{V}$-T data. While the above may be regarded as providing general though not conclusive support for our previous conclusion that the intermediate-temperature process is connected with the glass transition in the amorphous component, it is apparent that extrapolation to frequencies well below 10^{-3} c/s would be required to give a T value that corresponded to T_g from the $\overline{V}$-T data in the case of this semicrystalline polymer.

One possible explanation of the different f values (on a log f_m versus $1/T$ plot) that correspond to T_g, as measured by the $\overline{V}$-T method, in purely amorphous polymers ($f=10^{-2}$ to 10^{-3} c/s) on the one hand, and the amorphous component of semicrystalline polymers ($f\ll10^{-3}$ c/s) on the other, is that the T_g value from the $\overline{V}$-T data in an entirely amorphous polymer is considerably more time-dependent than it is in a semicrystalline polymer.

Saito and Nakajima have shown that T_g from $\overline{V}$-T data depends on the rate of measurement in purely amorphous polymers, being higher the more rapid the measurement [14]. Interestingly, the same authors have shown that T_g for a semicrystalline polymer, as measured by the $\overline{V}$-T method, is much less sensitive to the time scale of the measurement. (This accords with our experience on $\overline{V}$-T measurements of T_g with PCTFE). The implication is that the T_g value measured for a semicrystalline polymer by the $\overline{V}$-T method is lower and nearer the intrinsic (quite possibly time-independent) value than that of a corresponding purely amorphous polymer. One possible explanation of this is that it is a result of a size effect, the amorphous regions in semicrystalline polymers being quite small. In any event, it would appear that in semicrystalline systems, f values that are substantially less than 10^{-3} c/s may be more appropriate in estimating values of T for comparison with T_g values from $\overline{V}$-T data.

b. The High-Temperature Process

When clearly resolved on an ϵ'' versus T (dielectric) plot or a $\pi\tan\delta$ versus T (mechanical) plot, the high-temperature process peak appears at about 150 °C at 1 c/s (fig. 16). Notice that the resolved high-temperature peak appears only in the χ=0.80 specimens in both the dielectric and mechanical cases;

there is no indication of a resolved peak in specimen 0.73 (dielectric), which has practically the same degree of crystallinity at the temperature under consideration. Dielectric specimen 0.73 merely exhibits a single "mixed" high and intermediate peak. Further, no resolved high-temperature peak appears in mechanical specimens 0.27(M) or 0.42(M). This implies that the appearance of a resolvable high-temperature process not only involves the crystals in some way, but also depends on the manner in which the high crystallinity is achieved.

The crystallization in specimen 0.80 is of the typical lamellar spherulitic type. Large lamellar spherulites commonly appear in linear polymers crystallized from the melt under conditions of low to moderate supercooling such as was used in forming specimen 0.80 (section 2.2), and observations with a polarizing microscope fully confirm the existence of such objects in PCTFE specimens similar to 0.80 [15]. The milky-white appearance of specimen 0.80 is due to the scattering of light from these objects. Specimen 0.73, crystallized by the quench→anneal technique (sec. 2.2), is optically much clearer than 0.80, and contains no spherulites visible with a polarizing optical microscope. The same is true of specimen 0.44. The crystals (or spherulites) in 0.73 and 0.44 are evidently much smaller than in 0.80. In any case, it appears that the resolved high-temperature process evident in specimen 0.80 is closely associated with large and well-formed lamellar spherulites.

To an approximation sufficient for the present discussion, lamellar spherulites consist of stacks of chain-folded bladelike crystals (lamellae) that emanate from a central point (fig. 19). The long axes of the polymer molecules are essentially perpendicular to the two large flat faces of each blade, these faces containing the chain folds. In many cases, the lamellae are twisted as shown in figure 19. This twist leads to the beautiful bands that are seen in the optical extinction patterns of spherulites. The lamellae are commonly from 100 to 500A thick (distance between plane of chain folds), this thickness being larger the higher the crystallization temperature. A general theory of the formation of chain-folded lamellar spherulites has been given by Hoffman and Lauritzen [16].

If the high-temperature process were a "glass transition" type of effect, a break in the $\overline{V}$-T curve in the vicinity of about 120 °C would be expected. A careful examination of the $\overline{V}$-T curve of specimen 0.80 reveals no obvious break above the one at T_g=52 °C, though lack of sensitivity might possibly be the cause of its apparent absence. Also, the WLF expression with an elevated glass transition temperature (~118 °C) is not necessary to explain the apparent temperature dependence of ΔH^* for the resolved high-temperature process (table 8); the assignment of the constant value ΔH^*=80 kcal/mole provides an equally acceptable fit within the rather large experimental error. These observations, though not conclusive, are consistent with the proposal that the high-temperature process in PCTFE involves the crystal lamellae.

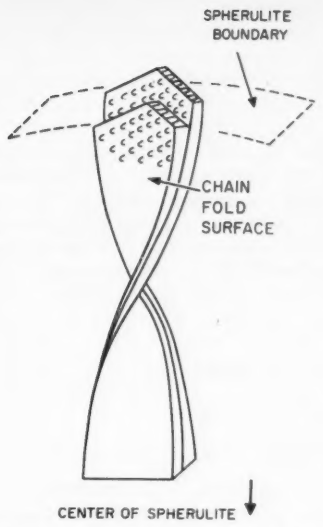

FIGURE 19. *Chain-folded lamellar structure in spherulites (schematic).*

There is some indication that the high-temperature process is not simply a property of the bulk crystalline phase.

If the high-temperature process were a bulk crystal property, it might be expected to appear in resolved form in specimen 0.73 with nearly the same intensity as it does in 0.80, whether or not the crystallization involved was of the well-formed lamellar spherulitic type. This is not the situation for the dielectric data. It may therefore be concluded that the high-temperature process is not a simple bulk property of the interior part of the crystals. This suggests that the high-temperature mechanism exhibited in resolved form by specimen 0.80 may involve the chain-folded surfaces of the lamellae. Crystal-size effects may be involved in shifting the high-temperature process to lower temperatures in 0.73, but this is not inconsistent with the general notion that lamellar surfaces or interlamellar surface interactions are involved. Also, the possibility exists that "abnormal" amorphous polymer contiguous to the crystal surfaces may be involved in the high-temperature process. This would place part of the cause of this process in the category of a lamellar-crystal–amorphous-phase interaction, but in a broad sense such an effect could still be regarded as a surface property.

In summary, the authors consider that a strong case exists for believing that the high-temperature process in its resolved form in PCTFE (specimen 0.80) is connected with the existence of well-formed lamellar chain-folded spherulitic structures. While it is not completely certain, some evidence suggests that the mechanism involves the surfaces of the lamellae.

Takayanagi has recently proposed that the high-temperature process, as observed in mechanical loss measurements in certain semicrystalline poly-

mers, is associated with chain-folded lamellar structures [17]. Resolved high- and intermediate-temperature peaks appear in the mechanical loss data of polyethylene and polyoxymethylene [18]. (These polymers also exhibit the low-temperature process).

A number of mechanisms can be proposed that might lead the crystals or their surfaces to exhibit dielectric and mechanical loss of the type observed in the high-temperature process. Broadly speaking, these mechanisms deal with motions of various types of surface (or other) defects in the lamellar crystals, motions of the chain folds, and interlamellar interactions, together with certain combinations of these concepts. However, the present experimental study does not point clearly to which if any of these ideas is correct, so no discussion of the various models is given.

c. Mixed Intermediate- and High-Temperature Processes

In figure 16a, it is seen that the dielectric loss peak that appears above 100 °C exhibits a large shift toward higher temperatures ($T \cong 105$ to $T \cong 125$ °C) as the degree of crystallinity increases from 0.44 to 0.73. Also, it is clear in the case of specimen 0.73 that only a single "mixed" peak appears, rather than two resolved peaks as in specimen 0.80. (Specimen 0.44 was not measured above 118 °C, but presumably has no resolved high-temperature process.) Recall again that specimens 0.44 and 0.73 do not contain large and well-formed spherulites, and that unlike 0.80, they were crystallized either during or subsequent to quenching.

The corresponding mechanical loss data for PCTFE plotted as $\pi \tan \delta$ versus T at 1 c/s do not exhibit such an obvious shift. Even when plotted as J'' (shear loss compliance) versus T, the loss peak shows no upward shift (within an error of about 5 °C) as χ is increased from 0.27 to 0.42. These specimens are similar to dielectric specimens 0.44 and 0.73 in being nonspherulitic,[10] and in exhibiting only a single "mixed" loss peak. All were crystallized by the "quench crystallized" or the "quench→anneal" technique.

The above-mentioned upward shift of a single dielectric loss maximum with increasing χ in quenched or quench→annealed specimens might seemingly be interpreted as a large and genuine increase in the glass transition of the amorphous phase that is induced by the presence of crystals. One objective of this section is to indicate that the large upward shift in the dielectric case is *not* indicative of an equally large increase of T_g as measured from $\overline{V}$-T curves. A simple alternative explanation of the shift of the dielectric loss peak is proposed, and the negligible shift in the mechanical case discussed. Also, further cause will be given for the necessity of distinguishing between polymers crystallized from the melt, where well-formed lamellar spherulites appear, and by the quench or quench→anneal technique, where in many cases obviously spherulitic crystallization does not arise. Brief mention is also made of crystallization in oriented systems.

The shift of the *apparent* glass transition, T_g', for dielectric specimens 0.44 and 0.73 implied by the ϵ'' versus log f data may be estimated by applying the WLF expression for ΔH^*. T_g' is taken as that temperature which provides the best fit of the observed temperature dependence of ΔH^* with the WLF expression (fig. 18). The WLF expression was originally proposed for purely amorphous materials rather than semicrystalline ones, so this use of it here must be viewed with caution. Nevertheless, it will be recalled that it applies reasonably well to the resolved intermediate component of 0.80. If there is "mixing" of the amorphous (intermediate) process and a crystal (high-temperature) process in 0.44 and 0.73, then only an apparent (T_g') value of the glass transition may be expected.

Regarding the normal amorphous material with $T_g = 52$ °C as the reference point, T_g' for specimen 0.44 by the WLF method apparently shifts by 65 °C − 52 °C = 13 °C, and the shift exhibited by 0.73 is 87 °C − 52 °C = 35 °C.

An analysis using the log f_m versus $1/T$ plots also implies that the apparent value of the glass transition associated with the "mixed" peaks increases as the degree of crystallinity increases from 0.44 to 0.73. This is evident in figure 17, where it is seen that for any given f value, T is higher for $\chi = 0.73$ than it is for 0.44. However, as noted in section 4.1a, it is not easy to get a close estimate of the value of the apparent glass transition in these cases because of the curvature, and the uncertainty of the f value that should be used.

The concept that these large differences represent a real upward shift in the glass transition of the magnitude indicated is not substantiated by careful measurements of the glass transition temperature from changes of slope in the $\overline{V}$-T curves. With an error of less than 5 °C, specimens 0.44, 0.73, and 0.80 exhibit the same T_g value on $\overline{V}$-T curves.[11]

It is therefore clear that the large upward shifts of the apparant glass transitions T_g' implied by the dielectric data are not to be regarded as real increases of the glass transition in the amorphous phase due to the presence of crystals. Recall also the fact that the mechanical data on specimens 0.27(M), 0.42(M), and 0.80(M) imply a small if not negligible increase of T_g with increasing χ. This is consonant with the $\overline{V}$-T measurements of T_g, which indicate a shift of between zero and about 5 °C for χ values between 0.44 and 0.80.

The disparity in the small if not negligible shift of T_g indicated by the mechanical and $\overline{V}$-T data on the one hand, and the large shift implied by the dielectric data on the other, can be explained at

[10] The use of the term "nonspherulitic" here means that no *large* well-formed spherulites visible with a polarizing optical microscope appear in the specimens. It is not intended to imply that numerous extremely small lamellar spherulites, or small and somewhat disoriented lamellae, may not exist in the specimens.

[11] The somewhat compressed scale employed in the $\overline{V}$-T curves of figure 1 does not show the break near 52 °C to great advantage. A more detailed presentation of data on specimens similar to 0.44 and 0.80 is given in reference [4] and clearly reveals the glass transition effect. The $\overline{V}$-T data for specimen 0.73 has not been previously published.

least in part as follows. Comparing dielectric specimen 0.80 and mechanical specimen 0.80(M) in figure 16, it is seen that the high-temperature peak in the dielectric case is slightly more prominent than the intermediate peak, while in the mechanical case it has a considerably lower relative intensity. If in some type of specimen the high-temperature peak shifts downward a certain number of degrees and "mixes" with the intermediate peak to form a single broadened peak, one would expect the maximum in this resultant single peak to occur at higher temperatures in the dielectric than the mechanical case because of the aforementioned relative intensity difference. This explanation is consistent with the large upward temperature shift of the single maximum in the "mixed" dielectric cases $\chi=0.44\rightarrow\chi=0.73$, and the corresponding much smaller shift in the mechanical case $\chi=0.27\rightarrow\chi=0.42$ (see fig. 16). A careful examination of the dielectric and mechanical data for these specimens, as compared with the 0.80 specimens, definitely suggests a downward temperature shift has occurred in the high-temperature mechanism in the nonspherulitic specimens. This downward shift in the high-temperature process may tentatively be ascribed to a crystal-size effect, much smaller and disoriented lamellae appearing in specimens 0.27(M), 0.42(M), 0.44, and 0.73 than in the typically lamellar spherulitic specimens 0.80 and 0.80(M).

The general question of the possible cause of a true shift of T_g due to increasing crystallinity is a most interesting one. As noted above, the actual upward shift in T_g of PCTFE specimens 0.44 and 0.73 is certainly not over about 5 °C as measured from $\overline{V}$-T data. Similarly, the mechanical data for 0.27 (M) and 0.42(M) imply the shift in the loss peak is not any larger than this, and quite possibly less.

Two effects could account for a true increase of T_g in the amorphous phase: (1) It has been shown by Gee and coworkers [19] that stress elongation (*circa* 250%) in an amorphous polymer can increase T_g as measured by the $\overline{V}$-T method by 1 to 7 °C, depending on the polymer. This shows that molecular orientation of the liquid phase could increase T_g somewhat. (2) Typical bundlelike crystallization, where one polymer molecule participates in many crystallites, might possibly occur to some extent in quenched specimens. This model is commonly considered to require a relatively marked increase of T_g as χ is increased.

Any relatively small shift (if it is in fact greater than zero) of the true value of T_g for PCTFE implied by the $\overline{V}$-T and mechanical loss data could be at least in part due to liquid orientation effects induced by the crystallization process. However, the small magnitude of the observed shift, 5 °C or less, does not seem consistent with the large shift that one would expect if specimens 0.27(M), 0.42(M), 0.44, and 0.73 possessed crystals constructed principally on the bundlelike pattern. In the chain-folded pattern of crystal growth, the molecular connections between the crystals (interlamellar links) will ordinarily be much less frequent than the number of intercrystalline links in the bundlelike system.

The above implies that the crystals in the quench crystallized and quench→annealed specimens (0.27(M), 0.42(M), 0.44, and 0.73) may be at least partly chain-folded in character. The chain-folded lamellae in such specimens are undoubtedly small in size and somewhat disorganized with respect to their mutual orientation, as compared to the situation in a well-formed lamellar spherulite. The 0.80 specimens contain large and well-formed lamellae with a substantial degree of chain folding.

It is considered to be of interest to comment briefly on what the present data and interpretation for the resolved high and intermediate peaks, and the single "mixed" high and intermediate peak in PCTFE, imply in the case of other polymers. A number of points are brought out that may prove useful in future investigations.

(1) It is clear that degree of crystallinity should not in all cases be expected to describe the specimen fully with respect to the high- and intermediate-temperature peaks. A case in point is the $\chi=0.80$ PCTFE specimen with resolved high and intermediate dielectric peaks, as compared with the $\chi=0.73$ specimen with a single "mixed" peak. Here the difference results ultimately from the different methods used to attain the high crystallinity, the $\chi=0.80$ specimen being typically lamellar spherulitic, and the 0.73 specimen possessing no large crystals. Entirely apart from suggesting that the high-temperature peak is associated with regular lamellar structures, these results suggest one reason why other polymers may in some cases exhibit but one "mixed" peak in the appropriate temperature range, rather than two resolved peaks. The present results on PCTFE show that the quench→anneal technique of crystallization leads to a single "mixed" dielectric loss process in the polymer. A similar result may be anticipated in other polymers, if large spherulites do not form during the quenching or annealing process.

The interesting work of Thompson and Woods [20] on nonspherulitic polyethylene terephthallate (PETP) filaments formed by quenching from the melt followed by annealing with crystallization appears to fit in this pattern, since only a single mechanical loss peak is observed. (Unfortunately the mechanical loss of highly spherulitic specimens of PETP crystallized from the melt at low undercooling has apparently not been studied. Such specimens may exhibit resolved high and intermediate peaks.) In contrast, polyethylene usually crystallizes very rapidly on cooling from the melt, rendering it difficult to avoid the formation of lamellar structures in specimens of ordinary size; this polymer commonly exhibits clearly resolved high- and intermediate-temperature loss peaks, as shown by Takayanagi [46]. However, by the use of stringent quenching techniques prior to annealing, Takayanagi has succedeed in supressing the high-temperature peak in a highly crystalline specimen of polyethylene to the point that only a single

(intermediate) peak is found [18]. These two types of result on polyethylene are highly reminiscent of our results on PCTFE with specimens 0.80 (spherulitic crystallized from melt) and 0.73 (nonspherulitic; quench→annealled).

(2) The appearance of but a single loss peak in the high–intermediate region may in some cases result simply from the fact that very little amorphous material is present in a highly crystalline specimen, causing only the high-temperature peak to appear. This condition was approached but by no means reached with PCTFE in $\chi=0.80$, but was evidently found by Takayanagi and coworkers in a very highly crystalline ($\chi=0.90$ to 0.94) specimen of linear polyethylene (Marlex 50) [17]. Less crystalline polyethylene specimens clearly exhibit both peaks.

(3) The relative insensitivity of T_g and related effects to degree of crystallinity exhibited by PCTFE may not obtain in other polymers, especially if other modes of crystallization are employed. For example, crystallization of highly oriented quenched fibers might lead to substantially more bundlelike character than the other methods. In this case, a single loss peak that shifted markedly with degree of crystallinity may be found which corresponded to a true increase of T_g as measured by the $\overline{V}$-T method. This may be at least a partial explanation of the large shifts (*circa* 40 °C) observed by Thompson and Woods with extruded filaments of PETP [20].

The dielectric data on PCTFE suggest that caution must be used in predicting true shifts in T_g when the intensity and crystal-size factors involved in "mixing" are the real causes of the shift of the loss maximums. The mechanical analog of this effect could easily arise in some polymers. In any case, the authors believe checking the actual shift of T_g by the $\overline{V}$-T method is a useful precaution against misinterpretation in such cases.

4.2. Dipolar Polarization and Large High-Frequency Contribution of the Crystals to the Dielectric Properties

One contribution of the crystals (or more likely their surfaces) to the dielectric properties has already been uncovered in PCTFE—the high-temperature mechanism. As will be seen shortly, the actual contribution of this effect to the dielectric constant is quite small. The principal objective of this section is to show that the crystals contribute another and generally much more prominent component to the static dielectric constant which is associated with a relaxation time that is extremely short. It will further be shown that this large high-frequency crystal contribution is a bulk property of the crystals.

It can be shown that the effective contribution of the dipole orientation polarization, $\langle P_\mu\rangle_{\text{eff}}$, to the static dielectric constant is given with sufficient accuracy by the expression

$$\overline{V}(\epsilon_s-\epsilon_\infty)\propto\langle P_\mu\rangle_{\text{eff}} \tag{9}$$

where $\overline{V}$ is the specific volume, ϵ_s the ultra-low-frequency (static) value of ϵ', and ϵ_∞ the limiting high-frequency value of ϵ'.[12] The quantity ϵ_∞ includes the contribution of electronic and atomic (infrared) polarization. The quantity $(\epsilon_s-\epsilon_\infty)$ is the increment of dielectric constant due to all the observed dipole orientation phenomena.

For the liquid specimen (0.0), ϵ_s was taken as the value of ϵ' as given in table 6, since at the high temperatures employed, about 200 to 250 °C, the relaxation effects occurred at frequencies much higher than were used in the measurements. The value of ϵ_s for the other specimens was obtained by extrapolation of the data on a Cole-Cole plot (ϵ'' versus ϵ') [21] to the abscissa on the low-frequency side of the curve. Some typical Cole-Cole plots are shown in figure 20.

In theory, ϵ_∞ can also be determined by extrapolation of the Cole-Cole plot to the abscissa of the high-frequency side of the curve. In practice however, this method of obtaining ϵ_∞ could be applied with high accuracy only at the lowest temperatures where many points fall close to ϵ_∞. The values of ϵ_∞ employed at other temperatures were calculated from the most reliable low-temperature value obtained from a Cole-Cole plot ($\epsilon_\infty=2.30$, $T=-50$ °C, specimen 0.44, shown in fig. 20a) using the Gladstone-Dale equation [22].[13]

$$R_{G-D}=\text{constant}=(n-1)\overline{V}=(\sqrt{\epsilon}_\infty-1)\overline{V}. \tag{10}$$

In using this equation the assumption is made that the atomic or electronic polarizability of a molecular constituent is not seriously affected by whether the constituent lies in the amorphous or the crystalline regions.

The behavior of $\overline{V}$ $(\epsilon_s-\epsilon_\infty)$ as a function of temperature for the various specimens is shown in figure 21. One of the most striking features of figure 21 is the fact that $\overline{V}$ $(\epsilon_s-\epsilon_\infty)$ for specimen 0.80 at 200 °C ($\chi=0.65$) is considerably higher than the 200 °C point on the line showing the typical dipolar liquid behavior of specimen 0.0. This marked increase in $\langle P_\mu\rangle_{\text{eff}}$ above the liquid value when the crystals form in the system near T_m strongly suggests that the crystalline phase makes quite a large contribution to the dipolar polarization. It will be demonstrated shortly that this is correct.

In order to identify at least a major part of this proposed crystal polarization, recall that in figure 2 the 23 °C loss index data of specimen 0.80 gave a strong indication of a loss peak at microwave frequencies. The existence of this peak is also borne out by the data of Hartshorn, Parry, and Rushton [2]. It is this high-frequency loss process that leads

[12] Fröhlich has shown on very general grounds that $\langle P_\mu\rangle_{\text{eff}}=(4\pi N/3)(\overline{mm}^*/\overline{kT})=(\epsilon_s-\epsilon_\infty)\overline{V}/f$ where f is the slowly varying function $(2\epsilon_s+\epsilon_\infty)/3\epsilon_s$ [23]. The quantity $\overline{mm}^*$ gives the magnitude of the square of the effective dipole moment resulting from orientation of dipoles, including short range interactions.

[13] Carr and Zimm [24] found that eq (10) applies more accurately to the estimation of the square of the index of refraction ($\epsilon_\infty=n^2$) as a function of density than the Lorentz-Lorenz, or various other expressions. The results for ϵ_∞ at other temperatures would have differed but little if the Lorentz-Lorenz expression, $[(n^2-1)/(n^2+2)]\overline{V}=R_{\text{L-L}}$, had been employed.

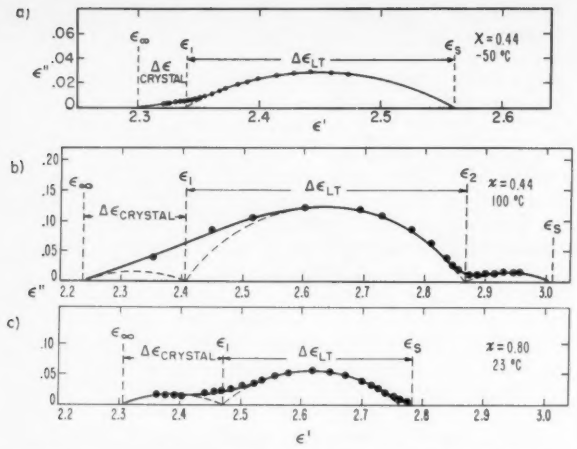

FIGURE 20. *Typical Cole-Cole plots of the dielectric data.*

to the high-frequency contribution in the room-temperature Cole-Cole plot for specimen 0.80. This contribution is labeled $\Delta\epsilon_{crystal}$ in figure 20c. (Justification for this identification is given below.) The microwave data are those near $\epsilon'=2.35$. The magnitude of $\Delta\epsilon_{crystal}$ was calculated from the Cole-Cole plots for the other specimens at various temperatures as the difference $\epsilon_1-\epsilon_\infty$ (see fig. 20b). Here ϵ_1 is the value of ϵ' at which a circular arc, which fits the data for the "low-temperature" or the main loss peak over the major part of its range, intercepts the abscissa on the high-frequency side. The value of ϵ_∞ was determined from eq (10). In all cases except the room-temperature data of specimen 0.80, where microwave data revealed the resolved process, $\Delta\epsilon_{crystal}$ manifested itself simply as a "tail" or asymmetry on the high-frequency side of the main arc. (See data at 100 °C for $\chi=0.44$ in fig. 20b). $\Delta\epsilon_{crystal}$ does not include the small crystal contribution of the high-temperature process.

The contribution of $\Delta\epsilon_{crystal}$ to $\overline{V}(\epsilon_s-\epsilon_\infty)$ obtained in the above manner for the various specimens is shown in figure 22 over the temperature range where the determination is considered reliable. The behavior of $\overline{V}\Delta\epsilon_{crystal}$ with temperature is in all cases that typical of a crystalline phase which is becoming more disordered with increasing temperature, i.e., $d(\overline{V}\Delta\epsilon_{crystal})/dT$ is positive. Furthermore, the value of $\overline{V}\Delta\epsilon_{crystal}$ for any specimen is directly proportional to the degree of crystallinity to within the experimental error. The value of $\overline{V}\Delta\epsilon_{crystal}$ extrapolated to the pure crystal is also shown in figure 22.

We therefore conclude that the very high-frequency process shown in the 23 °C ϵ'' versus log f data of figure 2, and which gives rise to $\Delta\epsilon_{crystal}$ on the Cole-Cole plots, is a bulk crystal property, and further, that the increase in $\overline{V}(\epsilon_s-\epsilon_\infty)$ upon crystallizing a specimen from the melt is due chiefly to the dipole orientation polarization of the crystals formed. The contribution $\overline{V}\Delta\epsilon_{crystal}$ may not be

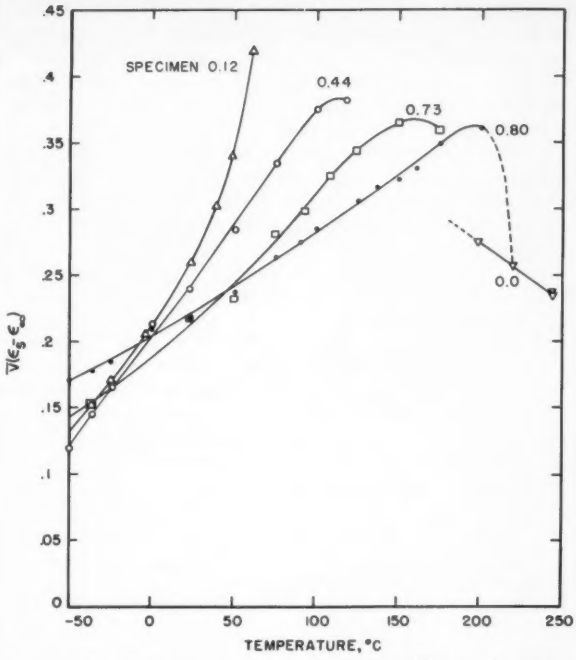

FIGURE 21. *The temperature dependence of* $\overline{V}(\epsilon_s-\epsilon_\infty)\cong(P_\mu)_{eff}$ *for the various specimens.*

$(P_\mu)_{eff}$ is nearly proportional to $\overline{V}(\epsilon_s-\epsilon_\infty)$, where $\overline{V}$ is the specific volume in cm^3/g, and $(\epsilon_s-\epsilon_\infty)$ is the increment of dielectric constant due to the total dipolar relaxational polarization.

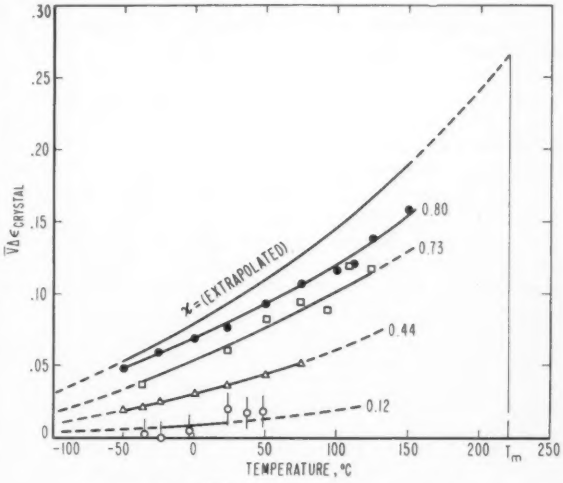

FIGURE 22. $\overline{V}\Delta\epsilon_{crystal}$ *versus the temperature.*

The curves indicate that $(\overline{V}\Delta\epsilon_{crystal})$ is directly proportional to χ, and justifies identifying the corresponding relaxational phenomena as a bulk property of the crystalline phase.

the sole crystal contribution to $\overline{V}(\epsilon_s-\epsilon_\infty)$, but it certainly is by far the largest one at most temperatures.

The work of Reynolds and coworkers [1] on the dielectric properties of low molecular weight PCTFE (mol wt=980) lends support to our finding that the crystals of PCTFE exhibit strong dipolar orientation

polarization and that this crystal polarization leads to a high-frequency "tail" or asymmetry in the data on a Cole-Cole plot. These authors were able to observe a relaxation peak in the pure liquid phase above the crystal melting point of their low molecular weight polymer. On a Cole-Cole plot, these data gave a regular circular arc with no evidence of a high-frequency "tail." Upon cooling the specimen and allowing crystals to form, the value of the static dielectric constant rose to surprisingly high values ($\epsilon_s \cong 8$). Furthermore, the dielectric data taken with the crystals in the system yielded a Cole-Cole plot with a sizeable "tail" or asymmetry on the high-frequency side.

From the standpoint of the ϵ'' versus T plots at 1 c/s, the crystal polarization found above does not lead to a loss peak in the observed temperature range. Its critical frequency even at 23 °C is around 10^{10} c/s, and this critical frequency almost certainly does not fall near 1 c/s even at −50 °C. The crystal relaxation peak on an ϵ'' versus T plot at 1 c/s would probably appear in the general vicinity of −100 °C or below, and be quite small because of the greatly diminished value of $\Delta\epsilon_{crystal}$ at such low temperatures (see fig. 22).

The crystal polarization process is somewhat unusual in two respects. First, the relaxation time associated with it is extremely short ($\tau \sim 10^{-11}$ sec at 23 °C), indicative of a low free energy of activation, and second, the polarization is rather strong, increasing to a value comparable to that of the normal liquid just below the melting point. Molecular reorientation of simple polar chain molecules about the long molecular axis leading to dielectric polarization and loss is a well known phenomenon [25, 26], but a rotation *en bloc* of large sections of the polymer chain of this type is probably not the sole cause of the high-frequency process in PCTFE. In a rigid single-axis rotator, only the component of the dipole moment perpendicular to the chain axis contributes to the orientation polarization. The chain of PCTFE is believed to possess a spiral twist [27] with a repeat distance of roughly 15 A. Whether the chain be syndiotactic or isotactic, this structure necessitates that the resultant dipole moment of a long section of chain (regarded as being rigid) would have only a very small component normal to the chain axis due to vectorial cancellation. The "rigid rod" model with spiral twist thus does not seem capable of explaining the high polarization observed, even if free intermolecular rotation about the long axis is assumed. Also, such a model would probably tend to suggest a longer relaxation time than is found experimentally. The latter is especially the case where chain folds exist at the ends of the chain elements. (In PCTFE crystallized at 180 °C the lamellae are roughly 300 A thick [28].)

One possible explanation of the high polarization and the short relaxation time is that the electric field distorts individual sections of the spirally twisted chain in the crystal, causing a local untwisting that leads to a large local dipole moment which then gives rise to dipolar polarization. The energy and geometry of one particular type of local uncoiling of a helical chain is a crystal has been considered by Reneker [29] in terms of point defects. He has concluded in the case of the polyoxymethylene chain, which has a spiral twist superimposed on a larger helix, that the local uncoiling of the larger helix would have a low energy of activation (about 2 kcal/mole), since such local uncoiling can be accomplished with only a slight disruption of the surrounding lattice. It is not clear whether this particular type of uncoiling could occur in PCTFE, since a detailed knowledge of the structure is lacking. Nevertheless, some type of local uncoiling or untwisting of the polymer chain seems the best possibility to explain the magnitude and rapidity of the dipolar polarization observed for the crystalline phase. The increase in dipolar polarization with increasing temperature observed in PCTFE is consistent with this suggestion.

If the above proposal is correct, one would expect that other polymers with spirally twisted molecules might exhibit a high-frequency crystal relaxation. For example, crystalline polyoxymethylene may prove to exhibit a high-frequency crystal relaxation process similar to that found in PCTFE in the microwave region.

4.3. The Low-Temperature Relaxation Process

The frequency dependence of the low-temperature relaxation process in specimens of various crystallinities and at various temperatures has been presented in figures 2, 7, 10, and 12. This loss process is from a dielectric standpoint the most prominent in PCTFE, and leads to the large low-temperature peak when the data are plotted on an ϵ'' versus temperature plot as shown in figure 16a.

An estimate of the contribution of this low-temperature process to $\langle P_\mu \rangle_{eff}$ can be established by dealing with the results obtained from the Cole-Cole plots such as those in figure 20. If $\overline{V}\Delta\epsilon_{crystal}$ (fig. 22) is subtracted from the value of $\overline{V}$ $(\epsilon_s - \epsilon_\infty)$ (fig. 21) for each of the specimens, the curves shown in figure 23a are obtained. These curves represent the sum of the contributions of the low-, intermediate-, and high-temperature processes to $\langle P_\mu \rangle_{eff}$. The dashed line marked "χ=0 extrapolated" represents an estimate of the behavior of the pure normal amorphous phase. This is based both upon an extrapolation of the high-temperature pure liquid points, and the curve for specimen 0.12 at lower temperatures. The behavior of the hypothetical pure amorphous phase of PCTFE depicted by this dashed line features a maximum between 50 and 100 °C which is readily apparent even in the 0.44 (56 percent amorphous) specimen. (It should be recalled that direct measurement of the dielectric properties of a completely amorphous specimen would be impossible between about 50 and 200 °C because rapid crystallization would occur).

If from the Cole-Cole plots one estimates the magnitude of the contribution of the high- and intermediate-temperature processes to $\overline{V}(\epsilon_s - \epsilon_\infty)$ and subtracts this contribution (shown in fig. 23b) from

the appropriate curves of figure 23a, then one obtains the curves shown in figure 23c.

The curves in figure 23c represent the contribution, $\overline{V}\Delta\epsilon_{LT}$, of the low temperature process in the various specimens to $\langle P_\mu \rangle_{eff}$. The $\chi=0$ dashed line represents our best estimate of the contribution of the low-temperature process in the pure normal amorphous phase to $\langle P_\mu \rangle_{eff}$. At low temperatures, this line is based on a simple extrapolation of the $\chi=0.12$ data. *The general appearance of the $\chi=0$ line in figure 23c between −50 and +150 °C leaves little doubt that a totally amorphous specimen of PCTFE would exhibit a prominent low-temperature process effect.* The $\chi=0.44$, $\chi=0.12$, and $\chi=0$ (extrapolated) lines clearly indicate that some type of dielectrically active molecular motions exist in the amorphous phase of the polymer far below the ordinary glass transition at $T_g=52$ °C.

The line indicated as $\chi=1$ (extrapolated) in figure 23c will be discussed subsequently.

Further evidence can be cited that shows that the amorphous phase makes a large contribution to the low-temperature effect. The low-temperature process gives rise to the main broad arc of width $\Delta\epsilon_{LT}$ when the dielectric data are placed on a Cole-Cole plot, as shown in figure 20. As mentioned earlier, Reynolds and coworkers [1] obtained similar Cole-Cole plots of their data on low molecular weight PCTFE waxes. Their work supports our belief that the amorphous phase makes a large contribution to the low-temperature process. Their Cole-Cole plot for the pure liquid phase consists of a simple arc. The arc component persists also in their semicrystalline specimens measured at lower temperatures. Furthermore, their log f_m versus $1/T$ plot (derived from the loss peaks which gives rise to the arc in the Cole-Cole plot for the semicrystalline specimen) gives a straight line that passes through the point obtained from the loss data of the pure liquid above the melting point. This demonstrates that the low-temperature process is controlled chiefly by molecular motions in the amorphous phase of low molecular weight PCTFE. The apparent heat of activation of the relaxation process they observed was 19 kcal/mole, which is quite similar to the value of 17.4 kcal/mole obtained by us for the low-temperature process as extrapolated to $\chi=0$ (see below).[14]

a. Effect of Crystallization on the Low-Temperature Process. Anomalous Behavior at High Crystallinity

The principal seat of the low-temperature process in moderate or weakly crystalline specimens has been clearly established above as the amorphous component. The objective of this section is to indicate the nature of the complications introduced into the low-temperature effect by high crystallinity.

One manifestation of the effect of crystallinity on the low-temperature process is a large shift of the maximums with χ in the π tan δ (mechanical) and ϵ'' (dielectric) versus T plots shown in figure 16. The temperature of the maximum, T_{max}, of the low-temperature process at 1 c/s is given in table 9 as a function of χ. It is seen that there is a close correspondence between T_{max} in the dielectric and mechanical cases, and that T_{max} falls as χ increases. By a simple extrapolation, it is readily estimated that T_{max} is −10 °C for $\chi\rightarrow 0$ and −45 °C for $\chi\rightarrow 1$.

Correspondingly, figure 17 shows that in the temperature interval from 0 to +50 °C the frequency of the maximum of the low-temperature process, at constant temperature, increases as χ increases.[15] Mikhailov [3] has observed a similar shift.

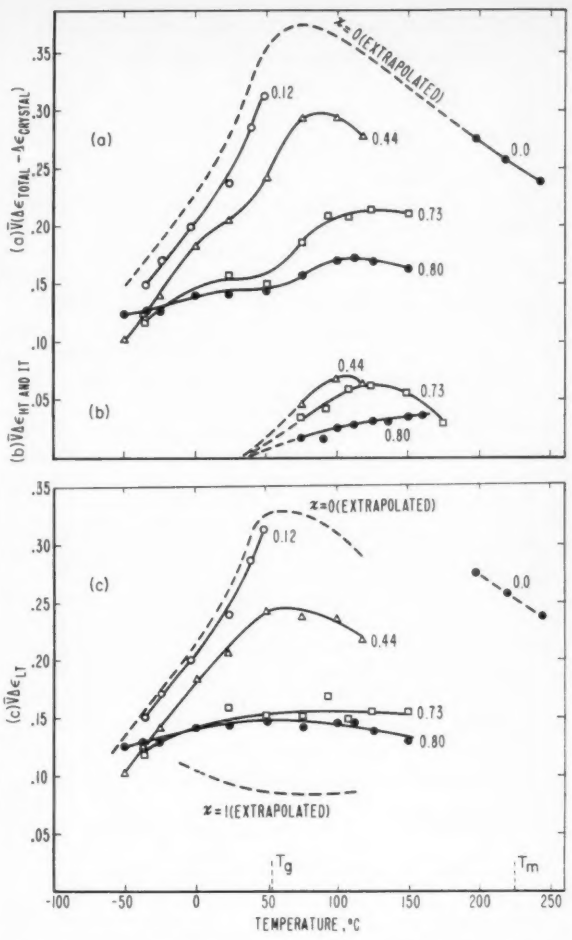

FIGURE 23. *Resolution of the components of the dipolar contributions to* $\overline{V}(\epsilon_s-\epsilon_\infty)\cong\langle P_\mu\rangle_{eff}$.

a. The total value $\overline{V}(\epsilon_s-\epsilon_\infty)$ less the crystal contribution, $\overline{V}\Delta\epsilon_{crystal}$.
b. The contribution of the high- and intermediate-temperature processes to $\overline{V}(\epsilon_s-\epsilon_\infty)$.
c. The contribution of the low-temperature processes to $\overline{V}(\epsilon_s-\epsilon_\infty)$.

[14] Reynolds and coworkers tentatively associated the arc portion of the Cole-Cole plots to the crystals, but we believe the revised interpretation given above is the correct one. There is however, agreement on the general fact that the crystals contribute to the dipolar polarization.

[15] In figure 17 the small change of slope in the log f_m versus $1/T$ plot of the low-temperature process near 50 °C is probably attributable to secondary effects connected with the glass transition. Above 75 °C, however, the maximum lies in the more inaccurate Q-meter measurement range so that the apparent change in slope could possibly arise from error in locating f_m.

TABLE 9. *Temperature at the loss maximum of the low-temperature process observed by dielectric and mechanical methods at 1 c/s*

χ	T_{max}	
	Dielectric	Mechanical
0.12	−13±5 °C	----------
.27	----------	−18±5 °C
.42	----------	−30±5 °C
.44	−30±5 °C	----------
.80	−41±5 °C	−40±5 °C

The activation energy for the low-temperature dielectric process shows a slight dependence of χ, as indicated in table 8. The activation energy is larger for the case $\chi \to 0$ ($\Delta H^* = 17.4$ kcal/mole) than for the case $\chi \to 1$ ($\Delta H^* = 13.5$ kcal/mole).

Perhaps the most obvious manifestation of the effect of crystallinity on the low-temperature process is the excess polarization denoted by the dashed line marked $\chi = 1$ (extrapolated) in figure 23(c). The implication is that the abnormality resides mostly in the highly crystalline specimens. The fact that $\chi = 1$ (extrapolated line) is well above the abscissa is not a result of an accumulation of experimental errors. In figure 24, it is readily apparent that the high-frequency crystal relaxation is widely separated from the main loss peak at 23 °C. The area under the main loss peak in figure 24 (as extrapolated to $\chi = 1$) leads to the anomalous contribution to $\overline{V}\Delta\epsilon_{LT}$ at $\chi = 1$ (extrapolated) shown in figure 23c.[16] It follows that the high-frequency crystal relaxation process is *not* responsible for the anomalous contribution to the low-temperature process at high χ.

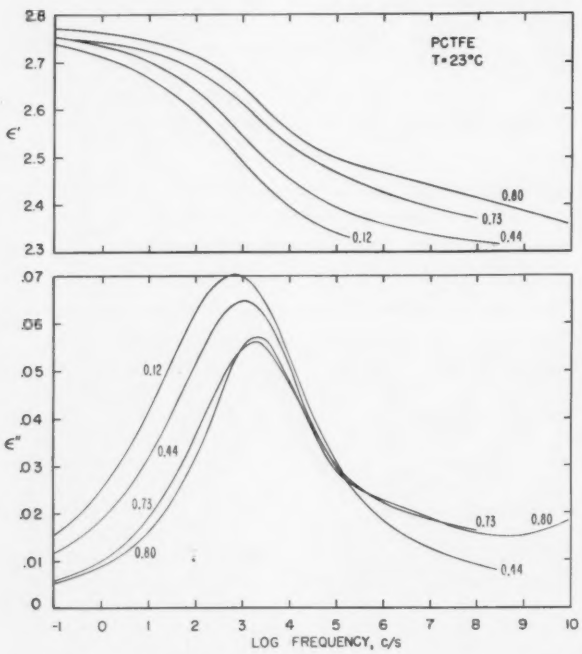

FIGURE 24. *Comparison of ϵ'' and ϵ' versus frequency curves at 23 °C for specimens of different crystallinities.*

The large loss peak near 10^3 c/s is due to the low-temperature mechanism. The contribution near 10^{10} c/s is due to the high-frequency crystal mechanism.

It is of importance to indicate that a similar anomaly does not occur, at least in such pronounced form, in all semicrystalline polymers. In a similar analysis of the low-temperature process in polyvinyl alcohol (PVA), Ishida, Takada, and Takayanagi [30] found that $\epsilon_s - \epsilon_\infty$ depended linearly on the fraction of amorphous material between $\chi = 0.37$ and 0.58, and extrapolated to zero for $\chi \to 1$. This crystalline polymer is atactic, and the dipoles in the extended chain configuration are not spirally arranged about the carbon chain axis as in PCTFE.

No completely satisfactory explanation of the origin of the anomalous contribution to $\overline{V}\Delta\epsilon_{LT}$ at high χ in PCTFE has been found. It could be due to a heretofore hidden contribution of the crystals. If so, the crystals would have to be highly disordered, and give a contribution to $\overline{V}\Delta\epsilon_{LT}$ that is nonlinear with χ. Conceivably, the crystal phase involved may be a bundlelike (non-folded) one, consisting of shorter chains segregated out as the chain-folded lamellae form from the longer molecules. Alternatively, the anomalous contribution of $\overline{V}\Delta\epsilon_{LT}$ for $\chi \to 1$ may be an abnormality induced into the amorphous phase by the presence of a large fraction of lamellar crystals. The present data are incapable of clearly indicating which, if any, of these explanations is correct.

None of the interesting peculiarities exhibited by the highly crystalline PCTFE specimens at low temperatures detract from the concept that the low-temperature process in its unperturbed form is basically a property of the amorphous component of the polymer.

b. Nature of the Molecular Mechanism

The overall heat of activation, ΔH^*, of the low-temperature process, according to table 8, centers around 15.6 kcal/mole. For the case $\chi \to 0$, it is 17.4 kcal/mole. Furthermore, this value is essentially independent of temperature. Both the low value of ΔH^* and its insensitivity to temperature indicate that the responsible molecular motion corresponds to dipole orientation over a fairly simple barrier system. It seems clear that only a relatively small number of chain segments can be directly involved. A kinking or "jump rope" motion in the amorphous phase involving but a few chain segments would suffice to explain the effects noted experimentally. The activation barrier that the dipoles involved must surmount in order to orient would in this case originate partly from hindered rotation in the chain itself, and partly from hindrances due to nearest neighbors. The large contribution to $\langle P_\mu \rangle_{eff}$ by the low-temperature mechanism is consistent with the proposed type of motion in a molecule with dipoles rigidly attached at a right angle to the main chain backbone.

[16] The mechanical loss data in figure 16 also indicate that extrapolation to $\chi = 1$ will not remove the low-temperature peak.

c. The low-Temperature Process and the Glass Transition

The observation that the low-temperature process in PCTFE is mainly a result of motions in the amorphous (glassy) phase is especially significant in view of the fact that it shows that rapid molecular motions persist far below the usual glass transition at T_g=52 °C. This cannot possibly be ascribed to independently rotatable side groups in the case of PCTFE. The results obtained here clearly imply that the purely amorphous phase of a polymer with dipoles rigidly attached at a right angle to the main chain backbone exhibit a bimodal set of relaxation times. The long set "freezes out" at 1 c/s above T_g and must involve complex long-range motions of sizeable parts of the molecules (intermediate-temperature process). The shorter set freezes out far below T_g at 1 c/s, and corresponds to a simpler motion involving a much smaller number of chain segments (low-temperature process). These two relaxation processes (or loss peaks) themselves are not properly termed "transitions," and we have avoided this usage. However, some type of transition may underlie one or both of the relaxation effects.

The intermediate-temperature process foretells the transition supercooled liquid→glassy state at T_g=52 °C. In some respects, the low-temperature process in a largely amorphous specimen may be regarded as denoting the onset of a "transition" within the glassy state. However, it is not known from the present work whether the "freezing out" of the low-temperature process would lead to a break in the $\overline{V}$–T curve similar in general character to that at T_g=52 °C associated with the intermediate-temperature process. Extrapolation of the log f_m versus $1/T$ plot for specimen 0.12 (fig. 17) to 0.01 c/s gives T=−60 °C. Interestingly, Baccaredda and Butta [31] have found a break in their sound velocity versus temperature data on PCTFE at −58 °C (as well as at +48 °C) in a 51 percent crystalline specimen. Such breaks in sound-velocity data often occur at the same temperature as breaks in $\overline{V}$–T data or specific heat data.

4.4. Maxwell-Wagner Polarization

Before giving the summary of the interpretation, it will be shown that none of the relaxation effects observed were due to Maxwell-Wagner polarization.

Reynolds and coworkers [1] suggested that since semicrystalline PCTFE consists of a two-phase system, some of the observed relaxation effects may have resulted from Maxwell-Wagner polarization. Nakajima and Saito [6] rejected this mechanism on the grounds that the observed d-c conductivity of neither phase is large enough to give any effect in their measurement region. Since the present work extends the measurements on the two phase system up to 200 °C, where higher d-c conductivities were observed, it is necessary to reinspect the problem.

Since the resistivity increases as the specimen is crystallized, we shall regard the crystals as nonconducting regions imbedded in a semiconducting matrix—the amorphous phase. We shall apply the equations developed by Wagner [32] to describe the dielectric properties of a composition consisting of a low concentration of spheres of one material dispersed through a matrix of another material. Wagner's equation is applied despite the facts that (a) we have no assurance that the crystals are spherical and, as is pointed out by Sillars [33], the crystal shape can alter the results appreciably, (b) we are extending it to a much higher concentration of spheres than Wagner visualized. Wagner's equation predicts a Debye-type loss peak (after the d-c conductivity effect is subtracted out). The peak has a relaxation time τ and an associated change in dielectric constant $\Delta\epsilon$ given by

$$\tau=\frac{3\epsilon_0\epsilon'\rho}{(2+q)} \tag{11}$$

and

$$\Delta\epsilon=\frac{3q(1-q)\epsilon'}{(2+q)^2}. \tag{12}$$

Here ϵ' is assumed to be nearly the same for the two phases, ρ is the resistivity of the amorphous matrix in ohm-cm, q is the volume fraction of crystals ($q\cong\chi$). From the observed resistivity of the specimen, ρ_s, the resistivity of the matrix, ρ, can be computed from the equation [32],[17]

$$\rho=\rho_s\frac{2(1-q)}{2+q}. \tag{13}$$

At 200 °C, ρ_s for specimen 0.80 was 7×10^{15} ohm-cm. Therefore, ρ is about 2.5×10^{15} ohm-cm. Substituting into eqs (11) and (12) we find τ=760 sec and $\Delta\epsilon$=0.3. A Debye-type loss peak is therefore predicted at a frequency of about 2×10^{-4} c/s, with a peak height of 0.15. A relaxation process of this nature would not detectably affect the data even at 0.1 c/s. Therefore, Maxwell-Wagner polarization is not responsible for the relaxation processes occuring at higher frequencies or at lower temperatures. In only one case was an appreciable conductivity effect noted in a crystalline specimen after the measured d-c contribution to ϵ'' had been subtracted. In the 175 and 200 °C data for specimen 0.80 shown in figure 6, a large upswing is seen in ϵ'' at the lowest frequencies. This was identified as being principally a conductivity effect and was not taken as indicating a true relaxation mechanism. In any event, this conductivity does not lead, through the Maxwell-Wagner effect, to the loss peaks at higher frequencies shown in figure 6.

If the crystals are assumed to be ellipsoids with a high axial ratio (corresponding electrically to individual lamellae) the proposed Maxwell-Wagner effect would occur at a frequency still lower than that calculated using the spherical approximation.

Equation (11) shows that τ is proportional to ρ, the resistivity of the amorphous matrix. In this connection, it is of interest to note that the resistivity of a specimen decreases considerably while the

[17] The applicability of the equation $\rho_s=\rho(2+q)/(2-2q)$ to the present situation was roughly checked. Crystallizing a specimen of PCTFE at 200 °C to a degree of crystallinity near 0.57 resulted in an increase in the resistivity to 2.7 times the value of the liquid ($\rho_s=(2.7)\rho$). Equation (13) with q=0.57, predicts $\rho_s=(2.99)\rho$, which is in reasonable agreement with the experimental observation.

specimen is maintained near or above 200 °C. If thermal degradation (or indeed any other mechanism) reduces the resistivity sufficiently, the predicted Maxwell-Wagner peak will move sufficiently far into the measurable frequency spectrum to combine with or mask the true relaxation peaks. This did not occur in the present study.

4.5. Summary of Interpretation

In the main, the high-, intermediate-, and low-temperature processes uncovered in PCTFE are consistent with an emerging pattern of the dielectric and mechanical behavior of semicrystalline polymers whose chains possess no independently rotatable side groups. A summary giving the important results concerning these mechanisms is given in table 10.

It is useful at this point to mention the nomenclature used by certain other authors in dealing with the specific mechanisms and phases involved in these three effects. Takayanagi calls the resolved high-temperature process in polyethylene, polyoxymethylene, and isotactic polypropylene "α_c", and attributes it to the effect of chain-folded lamellar structures [17, 18] as we have shown in the case of PCTFE. The resolved intermediate temperature process in the same polymers is denoted "α_a" by Takayanagi, and attributed to relaxations in the amorphous phase, as shown here for PCTFE. The present work on PCTFE establishes a clear relation between the relaxation effects associated with the intermediate-temperature process and the $\overline{V}-T$ glass transition at $T_g=52$ °C. The low-temperature process is called the "β" process in comparable polymers by Takayanagi. The present work shows that it is principally a result of the amorphous phase in PCTFE. On no account should the low-temperature process in the amorphous phase of the type of polymers mentioned above, which have no independently rotatable side groups, be confused with the relaxation effect that occurs in the amorphous phase of polymers that possess independently rotatable side groups, such as poly(methyl methacrylate). This latter effect is also often called "β'" [34, 35], but is to be distinguished from the "β" process in polymers without rotatable side groups.

The present work on PCTFE provides insight into the circumstances that allow the intermediate and high temperature processes to appear as two resolved peaks on the one hand, and as one "mixed" peak on the other. Two resolved dielectric loss peaks appear in specimens of high χ crystallized from the melt that contain well-formed lamellar spherulites; a single "mixed" dielectric peak appears in an equally crystalline specimen crystallized without large well-formed spherulites prepared by the quench→anneal technique. Another interesting point clearly brought out by the work on PCTFE is that increasing the degree of crystallinity does not actually lead to a large true increase of T_g as measured by the $\overline{V}-T$ method or by mechanical loss measurements. The apparent increase of T_g implied by the dielectric data is a result of mixing and intensity factors. There is no reason to suppose that a phase clearly indentifiable as basically amorphous does not exist in semicrystalline specimens of PCTFE even at high χ.

TABLE 10. *Summary of results of analysis of dipolar relaxation and polarization effects in semicrystalline PCTFE*

Process	T_{max} for 1 c/s loss peak on ϵ'' versus T plot	Phase involved	Remarks
High-temperature	+150 °C	Chain-folded lamellar crystalline	Appears in resolved form only in highly crystalline spherulitic specimens. $\Delta H^* \cong 80$ kcal/mole. Probably involves lamellar surfaces or interlamellar interactions.
Intermediate-temperature	+95 °C	Normal amorphous	Relaxation effect associated with onset of normal glass transition at $T_g=52$ °C. ΔH^* follows WLF relation with $T_g=52$ °C. Mechanism involves complex motions of many chain segments in amorphous regions.
Low-temperature (normal component)	−10 °C (extrapolated to $\chi=0$)	Normal amorphous	Relaxation effect in amorphous phase associated with short-range reorientation of a few chain segments over fairly simple barrier system (kinking or "jump rope" type motions). $\Delta H^*=17.4$ kcal/mole. Leads to most prominent loss peak observed.
Low-temperature (abnormal component)	−45 °C (extrapolated to $\chi=1$)	Abnormal amorphous or disordered crystal	Appears most prominently in highly crystalline specimens, mixes with normal component. $\Delta H^*=13.5$ kcal/mole. A high degree of orientational disorder is indicated.
High-frequency crystal polarization	Not observed at 1 c/s in temperature range studied. May appear below −50 °C	Crystalline	Bulk property of crystals. Relaxation time very short ($\tau \sim 10^{-11}$ sec at 23 °C). Mechanism may involve untwisting of spiral chain structure. Polarization increases with temperature, becomes comparable to liquid polarization near T_m. ΔH^* unknown, but probably small.

The fact that dielectrically active relaxation effects are observed both above and below the nominal glass transition temperature in the amorphous phase implies that a flexible right-angle dipole polymer liquid (with no independently rotatable side groups) can possess a bimodal distribution of relaxation times. The longer time set "freezes out," near or above T_g, depending upon the frequency, and consists of complex modes of relaxation involving a large number of polymer segments. The shorter time set involves more simple and localized motions which persist at temperatures far below $T_g=52$ °C in the case of PCTFE.[18]

An interesting and unusual feature of the present work on PCTFE is the proof of the existence and description of a large bulk crystal polarization effect associated with a very fast dipolar reorientation process. The loss process is so rapid that the corresponding maximum on an ϵ'' versus log f plot is not quite reached even at 8.6 kMc/s at 23 °C.

[18] If the side group constituting the right-angle dipole rigidly attached to the main chain backbone is large, the simple localized motion leading to the low-temperature process may be subdued or moved to higher temperatures. In such a case, the low-temperature process and the intermediate-temperature process might merge and become indistinguishable. However, this did not occur in PCTFE or the other semicrystalline polymers mentioned above.

This process may appear in other semicrystalline polymers in the microwave region. No large loss peak on an ϵ'' versus T plot at a fixed frequency due to this process was uncovered.

Maxwell-Wagner polarization is incapable of causing any of the loss peaks discussed.

5. Appendix. Micrometer Specimen Holder, Measurement Techniques, and Accuracy of Results for 0.01 c/s to 10 Mc/s

5.1. Introduction

During the course of our investigation of the dielectric properties of PCTFE and other polymeric materials, a number of problems relating to apparatus and measurement techniques were encountered and solved. Doubtless many of these problems were noted and adequately dealt with in various ways by other investigators, but the fact remains that such useful details are rarely published. The object of appendixes 5, 6, and 7 is to give an account of the experimental details in a form that will provide maximum usefulness to workers dealing with other systems, and which at the same time deals specifically with the measurements on the PCTFE specimens used in this research.

In this appendix, the following items are covered:

(a) The construction of the micrometer specimen holder used to make dielectric measurements on rigid disk specimens between 0.01 c/s to 10 Mc/s, and at temperatures ranging from −40 to +500 °C. (Descriptions of the two bridges and the Q-meter used with this specimen holder are given in appendix 6.)

(b) Methods used to compute ϵ' and ϵ'' for rigid disk specimens, such as PCTFE 0.80, 0.73, and 0.44, in the micrometer specimen holder.

(c) Analysis of accuracy of results on rigid disk specimens.

(d) Addition of a guard ring to the specimen holder, and the use of this device to measure ϵ' and ϵ'' for deformable materials such as the liquid specimen of PCTFE, 0.0. Also given are details of the experimental procedure, methods of calculation of results, and an analysis of the accuracy.

(e) Modifications of technique used to obtain ϵ' and ϵ'' for thin films (such as PCTFE 0.12) with the micrometer holder. Included here is a special analysis of the effect of surface irregularities in the film, and the effect of surface electrodes.

5.2. Micrometer Specimen Holder

a. Design Requirements

Most of the electrical measurements were made using a two-terminal sample holder which had been designed for use at temperatures from about −40 to +500 °C.[19] The substitution method was employed. The holder was designed so that it would have the following features: (a) Low differential thermal expansion so that there is a minimum of warping in the holder, and so that the spacing between the electrodes can be readily measured at all temperatures. (b) Low dielectric loss in the holder at all temperatures. (c) A means of controlling and accurately measuring the spacing between the electrodes. (d) A means of reproducibly connecting and disconnecting the holder from the two-terminal measuring circuit. (e) Series resistance and inductance should be sufficiently low that the holder may be reliably operated up to 10 Mc/s. A slight modification described later by which the holder may be operated in a three-terminal manner makes it possible to extend the frequency at the lower end to 0.01 c/s using a three-terminal low-frequency bridge [5].

b. Description of Holder

The holder was designed according to the principles given by Hartshorn [36], which eliminate the edge capacitance from the determination of capacitance, and which is a modification of the holder described by Baker [37]. The design is such that the electrodes can be placed in a furnace with controls for separating the electrodes and measuring the spacing between them outside the heated space. A view of this holder is given in figure 25. A schematic diagram of the holder is given in figure 26.

The upper electrode, **C,** is attached to a movable frame consisting of three metal rods, a ceramic disk at the top, and two brass plates, all clamped together to form a rigid framework. This framework moves only in a vertical direction guided by six guide wheels, **O,** which can also be adjusted to center the two electrodes. The wheels are attached to a fixed framework of rods and clamping plates. This fixed framework is rigidly attached to the supporting transite plate, **F,** and supports the silver base plate, **E.** The vertical position of the movable frame and electrode is controlled by the thumb nut, **K.** The position of the movable frame and electrode with respect to the fixed framework is measured by a micrometer screw, **L.** A pulley and counterweight system has been installed (not shown) which reduces the compressive force which the movable upper electrode and framework apply to the specimen when resting on it.

The movable electrode is electrically connected by a silver wire to the silver base plate, **E,** and thus to the stainless steel tube which forms the grounded terminal of the holder. For three-terminal operation with the low-frequency bridge this wire is disconnected from the movable electrode. Electrical contact between the electrode and the appropriate terminal of the low-frequency bridge [5] is established by plunging a brass rod tipped with a phosphor-bronze spring contactor downward through the oven into the hole in the upper electrode ordinarily containing a thermocouple. Electrical insulation between the upper movable electrode and ground is provided by the ceramic disk supporting the electrode. For operation at temperatures above 150 °C it was found desirable to place thin mica washers between all metal to ceramic contacts in order to increase the resistance to ground from the movable electrode.

The lower electrode, **D,** is mounted on a rod, **M,** that is held concentric with the thin-walled tube

[19] The design and construction of this holder was performed as a part of the research project on high-temperature-resistant polymers sponsored by the Ordnance Corps, Department of the Army.

which is welded to the silver base plate, **E.** The rod is axially centered and insulated by two Teflon disks [20] (see **P,** fig. 27). Vertical support is provided through three small fused silica rods, **U,** which pass through the upper Teflon disk. The rod and tube serve as terminals for the holder, and connection is made to the measuring instruments by means of rigid concentric leads, **J.** The silver cover, **B,** is lowered over the electrodes to form a complete electrostatic shield. Its high thermal conductivity helps to maintain uniform temperature in the holder.

Low differential expansion was obtained by constructing from the same material all members exposed to heat whose expansion contributes to vertical motion of the electrodes. Thus, the vertical rods, electrodes, and thin-walled tube are made from stainless steel. Stainless steel has a relatively low thermal conductivity, which is a desirable feature in

[20] Polytetrafluoroethylene, a product of E. I. DuPont de Nemours Co., Inc.

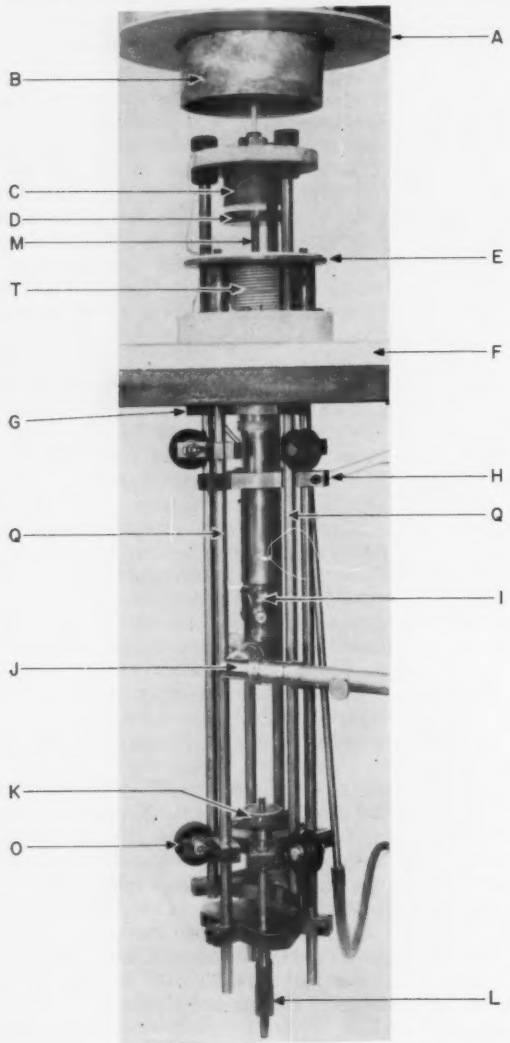

FIGURE 25. *Photograph of the specimen holder with the oven,* A, *and the silver cover,* B, *raised.*

A = Cylindrical oven
B = Silver cover of holder case
C = Movable electrode
D = Fixed, insulated electrode
E = Silver base of holder case
F = Transite support and base for oven
G = Clamping plate for movable frame
H = Clamping plate for fixed frame
I = Switch
J = Coaxial leads
K = Nut for supporting movable frame

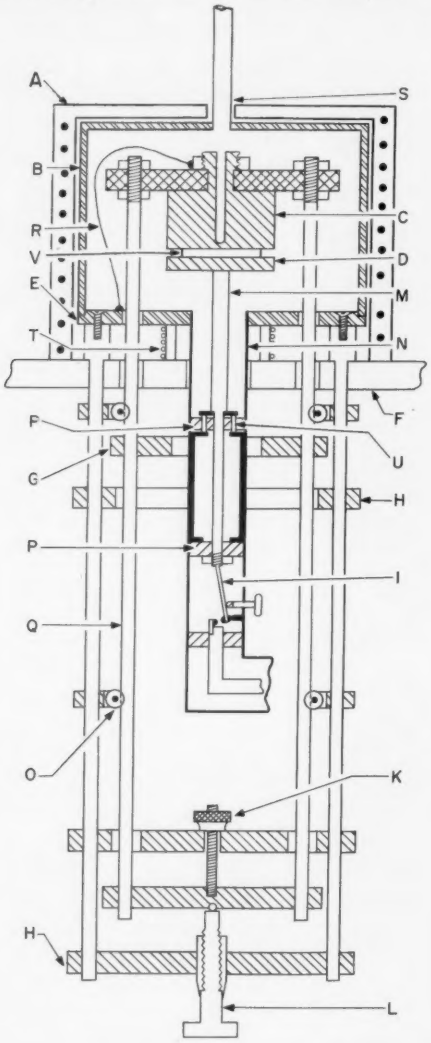

FIGURE 26. *Schematic of the specimen holder (not drawn to scale).*

L = Micrometer screw
M = Support rod for insulated electrode
N = Thin-walled tubing
O = Guide wheel
P = Teflon support washers
Q = Rod of movable frame
R = Flexible silver wire
S = Small tube to permit insertion of thermocouple
T = Heater coils
U = Fused silica rods
V = Disk specimen in measuring position

those parts of the holder which extend outside the electrode area. The differential expansion was determined by noting the micrometer reading at each temperature with the electrodes together. These values were used as corrections to the micrometer "zero" at the appropriate temperature. A further correction was made to compensate for the expansion of the segment of support rod which enters the heated area when the electrodes are separated.

Expansion of the movable framework perpendicular to the axis of the electrodes was nearly eliminated by making the top plate of the movable framework from Stupalith[21] ceramic, which had a very low coefficient of thermal expansion. The other horizontal plates of the movable framework are outside the heated space. As a result, the warping of the holder is negligible.

Spring washers were placed on the underside of the Stupalith disk so that it was firmly pressed against the upper nut of each of the vertical rods, regardless of the difference in expansion between the rods and the Stupalith. The shoulder of the upper electrode which was pressed against the Stupalith disk, was made large in order to seat the movable electrode firmly to the disk.

Low dielectric loss in the holder was achieved by using Teflon disks to insulate the high-potential electrode, and locating the disks outside of the oven. Because of thermal conduction in the tube and the rod, **M,** the upper insulating disk becomes heated to a temperature approaching 200 °C when the oven is at 500 °C. The electrical properties of Teflon remain sufficiently constant up to this temperature so that the heating of the Teflon disk had no effect on the operation of the holder. At 1 kc/s, over the entire temperature range, this holder has a loss tangent lower than the two-terminal variable air capacitor in the Schering bridge.

For operation above room temperature, heat is supplied by the oven, **A,** and the auxiliary heater, **T.** The auxiliary heater **T** is wound on a ceramic tube about 2 in. in diameter. A thermocouple attached to the silver base plate, **E,** is the sensing element to control the current in the auxiliary heater **T.** After some experimentation, the correct settings of the control temperature and of the currents in the two heaters can be determined such that thermal gradients anywhere in the specimen do not exceed 0.3 °C at any temperature up to 500 °C.

The temperature of the specimen is measured by a thermocouple located at the bottom of a hole drilled down the center of the upper electrode to within 1 mm of the lower surface. The thermocouple is inserted through the top of the oven, **A,** into this hole. The porcelain tube containing the thermocouple can be seen in figure 25 extending out of the hole.

A refrigerated head (not shown) replaces the oven, **A,** for operation down to about −40 °C. (By packing dry ice around the silver can, **B,** lower temperatures can be achieved, but the temperature control problem is then somewhat troublesome.) Temperatures between −40 and 0 °C are attained by supplying heat through a disk-shaped heater element (not shown) which rests on top of the silver can, **B.** A control thermocouple is also located in **B** near this heater. A flow of dried nitrogen gas is maintained in the holder to prevent the condensation of moisture at low temperatures, and to inhibit oxidation at all temperatures.

To assure accurate capacitance measurements using the substitution technique, a switch, **I,** was placed in the coaxial line. This switch consists of a spring contact, attached to the lower end of the rod, **M.** The spring switch is so constructed that its movable end is normally in contact with a grounded adjustable screw, projecting from the tubular shield. The switch is operated by a thumb screw having a Teflon tip which pushes the spring into contact with the center lead. The "open" and "closed" positions of the spring are fixed and highly reproducible thus assuring negligible error in the capacitance determination.

Though it was unnecessary in the present investigation, the stainless steel electrodes were electroplated to prevent their oxidation when operating in air near 500 °C. (Such oxidation would introduce a resistance in series with the specimen.) Gold plated over nickel appeared to be excellent, but with continued use at the high temperatures, the gold color slowly disappeared. The surface remained sufficiently conducting, however, so that no appreciable errors were introduced.

The opposing surfaces of the electrodes were lapped optically flat to within a few wavelengths of light before they were plated. After being plated they were again lapped to remove the unevenness of the plating. After assembly, the surfaces of the electrodes were made parallel by adjusting the nuts above and below the Stupalith disk.

Modification of this holder to incorporate a guard ring is discussed in appendix 5.3a.

c. Preparation of Disk Specimens for Measurement

Specimen stock was carefully selected to be free of foreign matter and voids. After determination of the radius r and thickness t of the disk specimens, they were carefully wiped, and cleaned if necessary. Care was taken to use no materials in cleaning which sorbed into the specimens. (In the case of PCTFE, warm water with detergent was found entirely satisfactory.) After rinsing and thoroughly drying, evaporated gold electrodes were applied *in vacuo.* Enough gold was applied (sometimes in several stages) to give an edge-to-edge resistance of less than 0.2 ohm as measured with point contacts. This assured that resistance effects due to the gold coatings would not affect the loss measurements even up to 10 Mc/s. Such evaporated gold electrodes adhered well to the specimens. The specimens were always flat enough so that very numerous contacts between the electrodes and the gold specimen coating were assured when the specimen was in the holder.

The position of the disk specimen, **V,** in the micrometer holder is shown in figure 26. The specimen radius is kept less than the electrode radius by

[21] Stupalith 2417, a product of Stupakoff Ceramic Manufacturing Co.

an amount $2t$, so that the edge capacitance will be unaffected by the presence of the specimen, and to assure that the specimen is in the uniform field region.

d. Method of Computing the Dielectric Constant and Loss Index (Disk Specimens)

In all measurements of the dielectric constant of PCTFE specimens 0.80, 0.44, and 0.73 using this holder, the following method was used to calculate ϵ' from the capacitance measurement. (The procedures used for specimen 0.12 and 0.0 are given in appendixes 5.4 and 5.3 respectively).

First, the capacitance of the empty holder, C_H, is measured as a function of electrode separation, t_H. For two-terminal measurements using the General Radio 716–C bridge or the Boonton Q-meter, the capacitance C_H includes all capacitance beyond the coaxial switch. In this case, C_H consists of the sum of C_L (fixed lead capacitance), C_a (direct capacitance between the electrodes, $\epsilon_0\epsilon'_N A_H/t_H$),[22] and C_e (inter-electrode "edge" capacitance). For three-terminal measurements using the low-frequency apparatus C_H is the sum of C_a and C_e only.

If C_p represents the equivalent parallel capacitance of the specimen then the dielectric constant ϵ' of the material can be computed from the ratio C_p/C_v where C_v is the vacuum capacitance of the specimen, $\epsilon_0 A/t$ (see eq (3)). Assuming C_L and C_e to be unchanged by the presence of the specimen, the capacitance measured with the specimen in the holder, C_x, may be expressed as the sum of $C_p+C_H-C_A$, where C_A is $\epsilon_0\epsilon'_N A/t_H$, the capacitance across that area, A, of the electrodes now occupied by the specimen, but previously occupied by dry nitrogen. (With the electrodes of the holder in contact with the specimen, the electrode separation t_H will in general be slightly larger than the specimen thickness t.) The expression for ϵ' may be written:

$$\epsilon'=\frac{C_p}{C_v}=\frac{C_x-C_H+C_A}{C_v}=\frac{C_x-C_H}{C_v}+\frac{t\epsilon'_N}{t_H}\cong\frac{C_x-C_H}{C_v}+\frac{t}{t_H}.^{23} \tag{A-1}$$

The ratio t/t_H is always slightly less than unity. For specimens about 0.2 cm thick, t/t_H may be about 0.99. This departure from unity is due to slight surface irregularities resulting from warping or unevenness, and the thickness of the conductive coating applied to the specimen.

Equation (A–1) is applicable to measurements made at all temperatures provided the variation of C_H (at constant t_H) with temperature is known. It has been determined that C_H varies with temperature in such a way that the variation can be ascribed to the calculable change in electrode area.

The loss index is determined for the measured parallel resistance, R_p, of the specimen from the equation

$$\epsilon''=\frac{1}{\omega R_p C_v}. \tag{A-2}$$

[22] A flow of dry nitrogen gas is maintained in the specimen holder so that the relative dielectric constant of nitrogen, ϵ'_N, appears in the expression for C_a.

[23] The error introduced in eq (A–1) by setting ϵ'_N equal to unity is only 0.02% for the specimens considered, for which $\epsilon'\cong 2.5$ and $t/t_H\cong 1$. We shall therefore set ϵ'_N equal to unity in the following discussions.

e. Accuracy of Measurements of ϵ' for PCTFE Disk Specimens 0.80, 0.44, and 0.73

The following discussion is given in order to determine how accurately ϵ' may be measured using the micrometer holder and techniques described above. (From eq (A–2) we see that the accuracy of ϵ'' will be determined primarily by the accuracy with which R_p can be measured. This depends primarily upon the measuring instrument. The ability of the measuring instruments to measure R_p is discussed in appendix 6, and estimates of the accuracy of ϵ'' given there.)

The accuracy with which ϵ' may be determined depends upon a number of factors, as can be seen from eq (A-1). We shall now rewrite eq (A-1) in terms of the independent variables involved and compute $\delta\epsilon'$, the error in ϵ', from the equation

$$\delta\epsilon'-\sum\left|\frac{\partial\epsilon'}{\partial x_i}\,\delta x_i\right| \tag{A-3}$$

where the x_i are the independent variables and δx_i is the uncertainty in x_i.

Note that the accuracy of C_H (the capacitance of the empty holder at separation t_H) depends upon two factors—the accuracy with which the measuring device can measure capacitance, and the ability to reproducibly set the separation of the electrodes to t_H with the specimen removed. These two effects may be approximately separated by writing C_H as

$$C_H=\frac{\epsilon_0 A_H}{t_H}+(C_L+C_e). \tag{A-4}$$

Any error in t_H will be reflected in the term $\epsilon_0 A_H/t_H$ where A_H is the area of the holder's electrodes, while the error of the capacitance measuring device may be thought of as affecting the term (C_L+C_e), which is essentially independent of t_H.

Equation (A-1) may now be rewritten in the form:

$$\epsilon'=\frac{(C_x-C_L-C_e)V}{\epsilon_0 A^2}-\frac{A_H V}{t_H A^2}+\frac{V}{At_H}. \tag{A-5}$$

The independently measured variables are, V, the volume of the specimen; A, the area of the specimen; t_H, and $(C_x-C_L-C_e)$.

Since

$$\frac{\partial\epsilon'}{\partial V}=\frac{\epsilon'}{V}, \tag{A-6}$$

$$\frac{\partial\epsilon'}{\partial A}=\frac{1}{A}\left[\frac{V}{t_H A}-2\epsilon'\right],$$

$$\frac{\partial\epsilon'}{\partial(C_x-C_L-C_e)}=\frac{1}{C_v},$$

and

$$\frac{\partial\epsilon'}{\partial t_H}=\left(\frac{A_H}{A}-1\right)\frac{t}{t_H^2},$$

eq (A–3) becomes:

$$\delta\epsilon' = \epsilon' \frac{\delta V}{V} + \left(2\epsilon' - \frac{t}{t_H}\right)\frac{2\delta d}{d} + \frac{\delta(C_x - C_L - C_e)}{C_v} + \left(\frac{A_H}{A} - 1\right)\frac{t}{t_H}\frac{\delta t_H}{t_H}, \quad \text{(A–7)}$$

where d is the diameter of the specimen.

Since V was determined by the buoyancy technique, it is given by

$$V = \frac{W_{(\text{air})} - W_{(\text{water})}}{\rho_{(\text{water})}}.$$

We may write

$$\frac{\delta V}{V} = \frac{\delta W_{(\text{air})} + \delta W_{(\text{water})}}{V\rho_{(\text{water})}} + \frac{\delta\rho_{(\text{water})}}{\rho_{(\text{water})}}. \quad \text{(A–8)}$$

The balance employed is accurate to 0.0001 g, and the density of water may easily be obtained to an accuracy of 0.00002 g/cm^3, therefore $\delta W_{(\text{air})} = \delta W_{(\text{water})} = 0.0001$ g and $\delta\rho_{(\text{water})} = 0.00002$ g/cm^3. Since $\rho_{(\text{water})} \cong 1$ g/cm^3 we have,

$$\frac{\delta V}{V} = \frac{0.0002 \text{ cm}^3}{V} + 0.00002.$$

Although d could be measured to 0.0001 cm by the traveling microscope employed, in general the specimens were not perfectly cylindrical. The diameter of specimens 0.80, 0.44, and 0.73 varied from point to point by as much as 0.001 cm from their respective average values. Accordingly, δd is 0.001 cm.

t_H can be measured using a micrometer to an accuracy of at least 0.0002 cm, so that δt_H is 0.0002 cm.

We can now evaluate the accuracy of measurements of ϵ' performed on the specimens whose dimensions are given in table 1. Specimens 0.80A and 0.44A are quite similar in physical dimensions so that rough average values may be assigned for the quantities necessary to compute $\delta\epsilon'$ from eq (A–7) for these two specimens. The assigned values are: $\epsilon' = 3$, $t = t_H = 0.2$ cm, A = 14.5 cm^2, $C_v = 6.3$ pf, $d = 4.3$ cm, $V = 2.9$ cm^3, and for our 2-in.-diam electrodes $A_H = 20$ cm^2. Using these values, eq (A–7) gives

$$\delta\epsilon' = 0.00291 + \frac{\delta(C_x - C_L - C_e)}{C_v}. \quad \text{(A–9)}$$

The term $\delta(C_x - C_L - C_e)$ depends upon the accuracy of the capacitance measurement. In the case of the low-frequency bridge and the Schering bridge (described later) this is about (0.05%+0.002pf). $\delta\epsilon'$ then becomes

$$\delta\epsilon' = 0.00291 + \frac{0.011 + 0.002}{6.3} = 0.0050.$$

This uncertainty in the value of ϵ' (0.16 percent) is the maximum error of ϵ'. The probable error is of course smaller, since some of the factors may tend to cancel one other.

If the Q-meter is employed, the error in the capacitance measurement may be as high as 0.08 pf. For specimens 0.80A and 0.44A this gives

$$\delta\epsilon' = 0.00291 + 0.0127 \cong 0.016,$$

corresponding to a maximum error of 0.5 percent in ϵ'. The Q-meter is of course less accurate than the bridges employed at lower frequencies.

The error involved in measurements of ϵ' on specimens 0.80B, 0.44B, and 0.73 may be similarly calculated. These specimens have quite similar physical dimensions. Assuming that $\epsilon' = 3$, $t = t_H = 0.2$ cm, A = 5 cm^2, $C_v = 2.2$ pf, $d = 2.5$ cm, $V = 1$ cm^3, and $A_H = 20$ cm^2, we have from eq (A-7),

$$\delta\epsilon' = 0.00766 + \frac{\delta(C_x - C_L - C_e)}{C_v}. \quad \text{(A–10)}$$

If the low-frequency bridge or Schering bridge is employed we have:

$$\delta\epsilon' = 0.00766 + \frac{0.0066 + 0.002}{2.2} = 0.0116.$$

If the Q-meter is used,

$$\delta\epsilon' = 0.044.$$

From the above considerations it is apparent that the data obtained from specimens 0.80A and 0.44A are more accurate than the data from specimens 0.80B, 0.44B, and 0.73. In this regard we shall now indicate the frequency range over which dielectric measurements were made upon the various individual specimens. Measurements on specimens 0.80A and 0.44A were made using the Schering bridge and the Q-meter covering the frequency interval from 50 c/s to 10 Mc/s. These specimens were then cut down in diameter to form 0.80B and 0.44B, which were measured using the re-entrant cavity and the low-frequency bridge (0.01 to 200 c/s). The values of ϵ' obtained using the low-frequency bridge on these specimens have a possible error of about 0.4 percent, as compared to an error of 0.16 percent in the data taken on specimens 0.80A and 0.44A with the Schering bridge. Occasional discrepancies between the two sets of ϵ' data were then remedied by shifting the low-frequency data by a constant amount to match that from the Schering bridge in the region of overlap (50 to 200 c/s). Since both sets of data are internally consistent to much better than 0.1 percent, then the error in the resulting ϵ' values for specimens 0.80 and specimens 0.44 is about 0.16 percent in the frequency interval from 0.1 c/s to 100 kc/s. From 100 kc/s to 10 Mc/s the uncertainty may be as high as 0.5 percent.[24]

[24] A detailed comparison of the ϵ' values obtained by the two-terminal method for disk specimens described here, and three-terminal measurements on specimens of similar size, has been made in our laboratory on a number of materials with moderate to low dielectric constants. Several of these had properties resembling PCTFE. These results, carried out from 100 c/s to 100 kc/s, clearly show that the two- and three-terminal methods give ϵ' values that generally agree to within 2 parts in 1,000, the error being random. It is clear from this and similar studies at lower frequencies [5] that the results on the disk specimens of PCTFE are free from fringing effects.

At all temperatures the ϵ' data obtained on specimens 0.80A and 0.80B under the same experimental conditions agreed to within 0.01. The data taken on specimens 0.44A and 0.44B, while showing equally good agreement at temperatures below 50 °C, deviated by as much as 0.027, or about 1 percent at 118 °C. It is possible that these more amorphous specimens may have become distorted at these elevated temperatures due to the slight compressive force of the electrodes. In any event, average values are given in this temperature region so that the error may be as high as about 0.5 percent.

The accuracy of measurements of ϵ' for specimen 0.73 has been previously discussed. In this case occasional mismatches in ϵ' values obtained on the low-frequency bridge and on the Schering bridge were remedied by shifting both sets of data to their average value in the region of overlapping frequency. The maximum shift in ϵ' required to match the data at any temperature was 0.004 or about 0.1 percent. The maximum uncertainty was previously calculated as about 0.4 percent in the frequency interval from 0.1 c/s to 100 kc/s and about 1.5 percent from 100 kc/s to 10 Mc/s.

Measurements of the liquid specimen are discussed in appendix 5.3, while a detailed consideration of the accuracy of thin film measurements is given in appendix 5.4.

5.3. Measurements on Pure Liquid (Specimen 0.0). Three-Terminal Modification of Micrometer Holder

Above its melting temperature (224±1 °C, [7]) PCTFE is a very viscous liquid. Although gross deformation of the specimen did not take place in dielectric measurements up to 250 °C, there was sufficient change of the specimen's area due to deformation to cause some doubt as to the accuracy of the results obtained using the technique of measurement outlined in appendix 5.2. To remove this uncertainty in the area, the specimen holder was equipped with a guard ring. With this arrangement three-terminal measurements were made upon a specimen of PCTFE (specimen 0.0) whose diameter was greater than that of the inside diameter of the guard ring. Changes in the specimen's area became unimportant since the area involved in computing C_x was then the equivalent area of the guarded electrode [38].

a. Holder Modifications, Guard Ring

The following is a brief description of the modification of the specimen holder, previously discussed in section 5.1b.

A stainless steel guard ring was attached to the movable electrode by four 0.125-in.-diam sapphire rods which pass horizontally through the guard ring and into the guarded electrode at 90° intervals. The sapphire rods were fitted tightly into carefully machined holes and held the guard ring in place with good rigidity.

The gap width between the guarded and guard electrodes was 0.0499 cm. The guard ring was grounded through a silver wire.

The diameter of the fixed unguarded electrode was increased to match the outside diameter of the guard ring (6.46 cm) by attaching a stainless steel circular plate to the smaller fixed electrode. This plate was machined so that a large shoulder extends down over the edge of the smaller electrode, serving to center the plate accurately on the smaller electrode. The plate and smaller electrode are tightly held together by three screws which pass horizontally through tapped holes in the shoulder and bear against a groove on the side of the smaller electrode.

All metal parts are made of stainless steel and have been gold plated.

In order to increase the electrical resistance between the movable guarded electrode and the ceramic plate which supports it, fused silica washers and spacers have been installed between all areas of contact.

This guarded electrode arrangement has been used only up to 250 °C. There is no apparent reason, however, why it could not be employed up to 500 °C.

b. Experimental Procedures

The specimen employed (specimen 0.0) was a disk about 5.4 cm in diameter and 0.2 cm thick. No surface electrodes were applied, since after heating to 250 °C the specimen and electrodes made good adhesive contact.

The dielectric measurements were first made near 250 °C, then near 220 °C, then near 200 °C. Measurements at 200 °C, where the specimen is in the supercooled liquid state, must be made as rapidly as possible since crystallization will become noticeable after about an hour [7]. Furthermore, since degradation takes place after prolonged exposure to temperatures above the melting point, these measurements were performed as rapidly as possible and in a nitrogen atmosphere.

The imminence of crystallization at one thermal extreme and the possibility of degradation at the other, made it unwise to take the time to cover more than a limited portion of the frequency spectrum. Three-terminal measurements were made only between 20 and 200 c/s.

Knowing the capacitance, C_H, as a function of the electrode separation, t_H, from experiment, the dielectric constant can be computed from the measured capacitance, C_x, by the equation

$$\epsilon' = \frac{C_x}{C_H}. \tag{A-11}$$

c. Accuracy

The error involved in the determination of ϵ' is given by

$$\delta\epsilon' = \frac{\epsilon'}{C_x}\,\delta C_x + \frac{\epsilon'}{C_H}\,\delta C_H. \tag{A-12}$$

The quantity δC_H consists of two parts: (a) the bridge uncertainty ± (0.05%+0.002 pf) and (b) the error due to our uncertainty in the value of t_H

(0.0002 cm). Therefore

$$\delta C_H = 0.002 \text{ pf} + 0.0005\, C_H + C_H \frac{\delta t_H}{t_H}. \quad \text{(A–13)}$$

Since $C_H = 8.4$ pf and $t_H = 0.22$ cm this becomes

$$\delta C_H = (0.002 + 0.004 + 0.0076) \text{ pf} = 0.0136 \text{ pf} \quad \text{(A–14)}$$

Substituting this into eq (A–12), with $C_x \cong 22$ pf, and $\delta C_x = \pm(0.05\% + 0.002 \text{ pf})$ gives

$$\frac{\delta \epsilon'}{\epsilon'} = 0.0006 + 0.0016 = 0.0022. \quad \text{(A–15)}$$

Therefore the calculated percentage error is 0.22 percent.

This apparent accuracy will be achieved however, only under ideal conditions, in particular only if the specimen and the electrodes make perfect contact. Inspection of the surface of the specimen after removal from the holder [25] showed no signs of bubbles or irregularities, indicating that the contact with the electrodes was good. To be safe, however, the uncertainty in the values of ϵ' given in table 6 is stated as ± 0.5 percent.

5.4. Thin Film Measurements (Specimen 0.12)

It is difficult to determine the dielectric properties of thin films with high accuracy. The most accurate results appear to be obtained by using the liquid displacement technique. This involves computing the dielectric properties of the specimen from the change in capacitance and resistance which results when the film is placed between the plates of a test cell containing a nonsolvent liquid whose dielectric properties are known. A complete description of this method is given elsewhere [39]. For the present application such a procedure was not adopted since it would have substantially prolonged the experimental phase of this investigation. The measurements of thin films reported here were made using the specimen holder with the guard ring attached as described in sec. 5.2. Three-terminal measurements were made up to 200 c/s using the low-frequency bridge modified to measure higher values of capacitance and conductance. Two-terminal measurements were made between 50 c/s and 200 kc/s after shorting the guarded electrode to ground.

The specimen was cut from a quenched thin film to have a diameter greater than that of the holder's guarded electrode. A guarded specimen electrode (slightly smaller than that of the holder's), a guard ring, and an unguarded electrode were applied to the specimen with silver conducting paint. Evaporated gold was not used because it was feared that the specimen might be excessively heated at its surface and thus crystallize locally. (The series resistance of the conducting paint led to no perceptible anomalous behavior in the measured loss up to 200 kc/s.) The specimen's average thickness, $t = 0.01464$ cm, was determined using the buoyancy technique (sec. 2.3) before applying the surface electrodes.

a. Three-Terminal Measurements on Films

The basic equation used to compute the dielectric constant from the three-terminal measurements is:

$$\epsilon'_m = C_x / C_v, \quad \text{(A–16)}$$

where C_x is the measured three-terminal capacitance of the holder with the specimen between the electrodes and C_v is the vacuum capacitance computed using the specimen's average thickness and the area of the holder's electrodes. This equation, however, neglects several factors which require closer inspecton when thin films are considered.

Surface Irregularities. Surface irregularities or roughness may become an important consideration where thin films are concerned since there it leads to a proportionally greater percentage variation in the thickness of the specimen. The effect of such irregularities is treated below in an approximate manner.

Let the plane surface area of a disk-shaped specimen be divided by a grid coordinate system into n small areas, each with area ΔA. Assuming that the field in the dielectric is everywhere perpendicular to the plane of the faces, then the total parallel capacitance of the system, C_{pm}, becomes:

$$C_{pm} = \epsilon' \epsilon_0 \Delta A \sum_{i=1}^{n} \frac{1}{t_i}. \quad \text{(A–17)}$$

Here t_i is the separation between the faces at the ith segment of area.

The average thickness, t, determined by the bouyancy method is

$$t = \frac{1}{n} \sum_{i=1}^{n} t_i. \quad \text{(A–18)}$$

Since t_i may be written as

$$t_i = t + (t_i - t) = t\left[1 + \frac{t_i - t}{t}\right], \quad \text{(A–19)}$$

then if $1/t_i$ is expanded in a binomial series, C_{pm} becomes:

$$C_{pm} = \frac{\epsilon' \epsilon_0 n \Delta A}{t}\left(1 + \frac{1}{n}\sum_i \left[\left(\frac{t_i - t}{t}\right)^2 - \left(\frac{t_i - t}{t}\right)^3 + \ldots\right]\right) \quad \text{(A–20)}$$

Dropping cubed and higher order terms and letting $n\Delta A = A$ we have [26]

$$C_{pm} = C_p\left[1 + \left(\frac{\sigma}{t}\right)^2\right]. \quad \text{(A–21)}$$

[25] It was necessary to dip the electrode assembly into liquid N_2 in order to remove the specimen from between the electrodes. This severe thermal shock did no apparent damage to either the specimen or the electrodes. The sapphire rods holding the guard ring in place were removed prior to this thermal shock.

[26] Calculation of the effects of surface irregularities with eq (A–21) will lead to a lower limit to the actual capacitance. It will be sufficiently accurate provided the surface is reasonably smooth, possessing very few sharp discontinuities, and also provided the undulations of the surface have "wavelengths" considerably greater than the specimen's thickness.

Here C_p is the parallel capacitance of the specimen calculated using the average thickness and σ is the standard deviation from the average thickness defined as:

$$\sigma=\left[\frac{\sum_{i=1}^{n}(t_i-t)^2}{n}\right]^{1/2}. \qquad \text{(A-22)}$$

Dividing eq (A-21) by C_v gives

$$\epsilon'_m=\epsilon'\left[1+\left(\frac{\sigma}{t}\right)^2\right], \qquad \text{(A-23)}$$

where ϵ'_m is the apparent or measured dielectric constant and ϵ' is the true value. This result shows that surface irregularities will always give rise to an apparent increase in the dielectric constant. The extent of the increase is governed by the square of the ratio (σ/t) and will therefore be more significant the thinner the specimen.

A convenient method of roughly evaluating σ is through micrometer measurements. Assuming that N micrometer readings are taken over the surface of the specimen, then the standard deviation, σ_r, of these readings, t_m, from the true mean, t, is

$$\sigma_r=\left[\frac{\sum_{m=1}^{N}(t_m-t)^2}{N}\right]^{1/2}. \qquad \text{(A-24)}$$

Since in most cases, σ_r will be slightly greater than σ, use of σ_r in place of σ will set an upper limit for the effect of surface irregularities. This method is equally applicable to specimens whose surfaces are slightly tilted.

For specimen 0.12, on the basis of some forty micrometer readings, σ_r was found to be 0.00107 cm, so that $(\sigma_r/t)^2$ is 0.0053. Therefore, to correct for the effect of surface irregularities, the measured value of ϵ' was reduced by about 0.5 percent.

Effects of specimen electrodes. It is obvious that for very thin specimens the thickness of the guarded surface electrode painted on the specimen may become important. If this electrode is sufficiently thick, a slight fringing field will be set up at its edge, tending to increase the capacitance.

Since the surface electrodes were about 0.0048 cm thick, and the specimen's thickness was only 0.01464 cm, a calculation of the possible magnitude of this effect was made.

Adopting an equation of W. R. Smythe [40] to describe the situation at hand, it was found that the capacitance increase due to the edge of the painted electrode was only about 0.07 percent of the total capacitance.

A far more important effect than this is produced by the fact that the area of the painted guarded electrode was smaller by about 7.4 percent than the area of the guarded electrode of the specimen holder. This leaves an air gap between the specimen and the holder's electrode in the uncoated region. The effect of this air gap is to reduce the measured capacitance, or equivalently, to lower the calculated value of ϵ'.

A calculation showed that the measured value of ϵ' should be increased on the average 3.5 percent to compensate for this uncoated area. This correction is slightly dependent on ϵ' and this dependence was included in the calculated correction.

Summary. Surface irregularities can be corrected for by reducing ϵ'_m by 0.5 percent. The effects of the air film near the edge of the guarded electrode may be corrected for by increasing ϵ'_m by 3.5 percent. The small fringing capacitance from the edge of the painted guarded electrode may be compensated for by decreasing ϵ'_m by about 0.1 percent. Therefore, summing these, the true value of ϵ' is attained by increasing ϵ'_m by about 2.9 percent. The values of dielectric constant for specimen 0.12 reported in table 5 include these corrections. The accuracy of the reported values of ϵ' is estimated to be about ± 1 percent.

b. Two-Terminal Measurements of Films

As indicated earlier, two-terminal measurements on specimen 0.12 were made up to 200 kc/s by shorting the guarded electrode to ground. Corrections were applied to the two-terminal measurements to compensate for the same factors which influenced the three-terminal measurements discussed above. The corrections to ϵ' (about 7%) were larger, however, due to the air film near the specimen's edge. After correction, the two-terminal and three-terminal measurements in the region of overlapping frequencies agreed to within 1 percent. The two-terminal data, which contained larger corrections, were than shifted to match the presumably more accurate three-terminal data.

c. Corrections to ϵ''

By methods similar to those discussed in section 5.4a, the effects of the factors mentioned upon measurements of ϵ'' were calculated and corrected. The net correction to the three-terminal measurements of ϵ'' was about a 4.5 percent increase. Two-terminal measurements required corrections near 14 percent. The accuracy of the values in ϵ'' given in table 5 is about ± 3 percent.

6. Appendix. Impedance-Measuring Devices Covering 0.01 c/s to 10 Mc/s for Use with Micrometer Specimen Holder

Three different instruments were employed to measure the dielectric properties of the PCTFE specimens over the broad frequency range from 0.1 to 10^7 c/s with the micrometer specimen holder. The following sections give discussions of each of these instruments, including their accuracy. Estimates of the accuracy of the ϵ'' measurements are given special emphasis.

6.1. Ultra-Low-Frequency Bridge

The low-frequency bridge operates in the frequency range of 0.01 to 200 c/s. It measures parallel capacitances between 0 and 100 pf, and conductances between 10^{-9} and 10^{-15} mhos. Under suitable conditions accuracies of $\pm$(0.05 percent

+ 0.002 pf) in capacitance and about ±(1 percent + $3f \times 10^{-15}$ mhos) in conductance are achieved. (Here f is the frequency in c/s.) The dielectric constant, ϵ', of a material can therefore be determined to an accuracy proportional to that of the capacitance measurements. The loss index is measured to an accuracy of about $\pm(1\% + 5 \times 10^{-4}/C_v)$ where C_v is the equivalent vacuum capacitance expressed in pf.

The low-frequency bridge employed is similar to the bridge of Weingarten [41] which is described also by Heroux [42]. It is a three-terminal device, but it is unnecessary to balance a separate guard circuit. A complete description and demonstration of the capabilities of the low-frequency apparatus employed here is given elsewhere [5].

6.2. Schering Bridge

A modified General Radio type 716–C Schering bridge is employed in the frequency range of 50 c/s to 200 kc/s. The bridge was modified as follows. The 100- to 1100-pf variable capacitor was removed from the bridge and replaced by a dual range (25 to 110 pf and 250 to 1100 pf) variable capacitor. This modification allows greater accuracy in the measurement of both low capacitances and low conductances. The capacitor is equipped with an additional reduction gear and scale which allows one to measure capacitances to a precision of 0.001 pf on the low range.

The substitution method is employed. Capacitances may be measured on the low range to an accuracy of about ±(0.05 percent + 0.002 pf) once the measuring capacitor is calibrated. The loss index ϵ'' may be measured to an accuracy of about $\pm(2$ percent $+ 1 \times 10^{-3}/C_v)$ where C_v is in pf.

In order to realize the full capability of this apparatus in the measurement of capacitance it is necessary to use rigid coaxial leads to connect the bridge and specimen holder. This minimizes the small erratic capacitance changes due to small physical motions which may occur if flexible coaxial leads are employed.

Adequate sensitivity is provided by a tunable null indicator (Rhode and Schwarz Type UBM) with only 15 v applied to the bridge by the signal generator (Hewlett Packard, Model 200–C).

6.3. Q-Meter

In the frequency range of 100 kc/s to 10 Mc/s a Boonton Radio Corporation type 160–A Q-meter is employed. This instrument has been modified and is now equipped with a "ΔQ-meter" to facilitate more sensitive measurements on low values of parallel conductances. The ΔQ-meter also allows one to tune more accurately to the resonance peak.

Since we attempted to achieve accuracies greater than those which the instrument was designed to deliver, special mention of the calibration procedure employed is given here.

a. Calibration and Operation

First the parallel variable resonating capacitors are calibrated as follows. (All operations are best carried out with the Q-meter turned on and in warmed up condition.) The main capacitor is carefully set[27] on its lowest indicated value (30 pf). With the vernier capacitor carefully set to zero, the capacitance terminals are connected to the Schering bridge which is then balanced at a frequency near 1 kc/s. The frequency 1 kc/s is chosen so as to avoid inductive effects in the leads connecting the Q-meter and bridge. Now the setting of the main capacitor of the Q-meter is increased, carefully setting 5 pf higher on the scale. The change in actual capacitance required to rebalance the Schering bridge gives the capacitance change between these two settings. This procedure is then repeated at each 5-pf interval along the scale until the required range is covered. Thus a relative calibration of the main capacitor is achieved. The vernier capacitor (scale reads −3 to +3 pf) is similarly calibrated at each 0.1-pf setting.

With the resonating capacitors now calibrated at 1 kc/s we make the assumption that this calibration remains constant with frequency up to 10 Mc/s. The problem of series inductance and resistance in the leads to the sample holder will be discussed later. Before doing so however, let us first outline the operational procedure followed in measurements of unknown impedances.

The micrometer specimen holder (previously described) containing the specimen is connected to the Q-meter through rigid coaxial leads which should be as short as possible. With the switch **I** of figure 26 open, the Q-meter is roughly resonated at the selected frequency by suitable choice of the coil and by varying the main capacitance setting. Next the main capacitor is set to the nearest 5-pf calibration point and resonance achieved by adjusting the vernier. The Q reading is then recorded (Q_1) as well as the readings of the capacitors which when corrected and summed give a capacitance C_1. Now the switch **I** is closed. Resonance is restored by decreasing C. At resonance, with the unknown in, the Q reading (Q_2) is recorded as well as the corrected capacitance reading, C_2. The measured parallel capacitance to ground beyond the switch is simply $C_M = C_1 - C_2$ from which the dielectric constant of the unknown may be determined from eq (A–1) by setting $C_x = C_M$ (if lead inductance is neglected). The loss index of the unknown is given by

$$\epsilon'' = \frac{C_T}{C_v}\left(\frac{1}{Q_2} - \frac{1}{Q_1}\right), \qquad \text{(A-25)}$$

where C_T is the total capacitance required to resonate the coil at the operating frequency. (C_T may be determined separately.)

b. Accuracy

The accuracy with which capacitance can be measured is limited essentially by the accuracy with

[27] The Q-meter has been equipped with a device to eliminate the effect of parallax from the reading of the main capacitor. This device consists of a one inch length of ½-in.-o.d. polymethylmethacrylate (PMMA) rod which has been split and one-half mounted over the fiducial line of the capacitor. A fine line has been inscribed on the outer rounded surface of the PMMA section parallel to the fiducial line. With this device the capacitor can be set at calibrated values up to 100 pf to within ±0.01 pf.

which the main capacitor can be set to the calibrated 5-pf intervals. With care this setting is reproducible to ± 0.01 pf up to about 100 pf. Since the substitution method is employed the capacitance can be measured to an accuracy of about ± 0.02 pf.

One may compute the error in ϵ'' ($\delta\epsilon''$) using the general method of eq (A–3). Equation (A–25) in terms of independent variables becomes

$$\epsilon''=\frac{C_T}{C_v}\left(\frac{\Delta Q}{Q_1 Q_2}\right), \tag{A–26}$$

Here ΔQ, (Q_1-Q_2), is an independent variable since it is independently measured using the ΔQ-meter attachment. Neglecting the comparatively small uncertainty in C_v the following relationship is derived

$$\frac{\delta\epsilon''}{\epsilon''}=\frac{\delta Q_1}{Q_1}+\frac{\delta Q_2}{Q_2}+\frac{\delta C_T}{C_T}+\frac{\delta\Delta Q}{\Delta Q}. \tag{A–27}$$

The term $\delta C_T/C_T$ is in general about 1pf/100 pf. The remaining three terms all consist of two parts. One part is the calibration error of the appropriate voltmeter (either the Q- or ΔQ-voltmeter) which, in both cases, we assume is one percent. The other part is the resolution with which the voltmeters can be read. The Q voltmeter can be read to about ± 1 (full scale 250). The limit of resolution on the ΔQ-voltmeter is about ± 0.2 (full scale 50). Assuming that $Q_1 \cong Q_2 \cong 200$,

$$\frac{\delta\epsilon''}{\epsilon''}=0.05+\frac{0.2}{\Delta Q}. \tag{A–28}$$

Eliminating ΔQ by use of eq (A–26) and substituting the above approximate numerical values gives

$$\delta\epsilon''=\pm\left(5\%+\frac{5\times 10^{-4}}{C_v}\right), \tag{A–29}$$

where C_v is in picofarads.

c. Lead Corrections

Certain corrections due to series inductance and resistance become important at high frequencies.

A lead inductance L in series with the holder capacitance C_x gives rise to an apparent capacitance C_M which is given by the equation

$$C_M=\frac{C_x}{1-\omega^2 L C_x},$$

or

$$C_{Mx}\equiv C_M-C_x=\omega^2 L C_x C_M=\omega^2 L C_M{}^2/(1+\omega^2 L C_M). \tag{A–30}$$

Furthermore, a resistance R_s in series with the equivalent capacitance C_M gives rise to a loss tangent for the empty holder given by the expression

$$(\tan\delta)_e=\omega R_s C_M=\frac{C_T}{C_M}\left(\frac{1}{Q_2}-\frac{1}{Q_1}\right). \tag{A–31}$$

Defining $\Delta(1/Q)_e$ as the $(1/Q_2-1/Q_1)$ observed when the holder contains no sample, eq (A–31) may be rewritten as

$$\Delta\left(\frac{1}{Q}\right)_e=\frac{\omega R_s C_M^2}{C_T}. \tag{A–32}$$

Thus for a particular coil (C_T=constant), at a particular frequency, eqs (A–30) and (A–32) show that (C_M-C_x) and $\Delta(1/Q)$ are functions of C_M and that experimentally derived plots of (C_M-C_x) and $\Delta(1/Q)_e$ versus C_M can be used to correct for the effects of L and R_s. For convenience (C_M-C_x) is defined as C_{Mx}.

Graphs of C_{Mx} and $\Delta(1/Q)_e$ were obtained in the following manner. The capacitance C_x of the empty holder at a particular electrode separation was determined at 1 kc/s using the Schering bridge. The holder was then connected to the Q-meter and C_M and $\Delta(1/Q)_e$ determined at the desired frequencies. This procedure was then repeated at different electrode separations so that values of C_x covering the desired range were measured. Completion of the experiment outlined above yielded data from which C_{Mx} and $\Delta(1/Q)_e$ versus C_M curves were drawn.

The dielectric properties of a specimen were determined as follows. With the specimen in the holder C_M and $\Delta(1/Q)_M$ were determined. C_M is the change in capacitance required to reresonate the system after switching the holder out. $\Delta(1/Q)_M$ is the measured change in $1/Q$. From the appropriate calibration curve the value of C_{Mx} at the observed C_M was obtained. C_x was obtained from the equation

$$C_x=C_M-C_{Mx}. \tag{A–33}$$

The dielectric constant of the specimen is then given by eq (A–1).

The value of $\Delta(1/Q)_e$ at the observed value of C_M was obtained from the calibration curve. If R_{sx} is the series resistance of the specimen then the measured tan δ is given by the approximate relation,

$$\tan\delta_M=\omega C_M\left(R_s+R_{sx}\frac{C_p^2}{C_x^2}\right)=\frac{C_T}{C_M}\Delta\left(\frac{1}{Q}\right)_M. \tag{A–34}$$

where C_p is the parallel capacitance of the specimen. From eqs (A–31) and (A–34) it is easy to show that

$$\epsilon''=\left(\frac{C_x}{C_M}\right)^2\frac{C_T}{C_v}\left[\Delta\left(\frac{1}{Q}\right)_M-\Delta\left(\frac{1}{Q}\right)_e\right]. \tag{A–35}$$

In all the above equations it is assumed that tan δ of the specimen is sufficiently small so that the equivalent parallel and series capacitance of the specimen are nearly the same. Values of tan δ up to 0.1 fulfill this restriction reasonably well.

At frequencies above about 3 Mc/s these corrections become significant. The accuracy of the measurements is reduced in some cases because the magnitude of the correction approaches the specimen's contribution to the measured quantity. Measurements of capacitance may err by ± 0.08 pf. The accuracy of loss index measurements becomes roughly $\pm$ (7 percent + $0.001/C_v$) where C_v is in pf.

7. Appendix. High-Frequency Measurements (290 Mc/s to 8.6 kMc/s)

Two separate instruments were used to determine ϵ' and ϵ'' at high frequencies. These are briefly described below. The description of these devices has been separated from that of instruments employed at lower frequencies for the reason that the operating principle is quite different.

7.1. Re-entrant Cavity

Figure 27 shows a cross section of the re-entrant cavity used for the measurements at 290 Mc/s. It is similar in most respects to re-entrant cavities described previously by Parry [43], Works [44], and Reynolds [45]. One feature which distinguishes this instrument is the variable length of the cavity effected by means of a sliding short (**J** in the diagram). This feature allows more flexibility in the selection of sample size and resonant frequency than is possible in a cavity of fixed length. It also simplifies the capacitance calibration: The short is withdrawn to the uppermost end of the cavity where it is insulated from the upper conductor by a ceramic insulator **I**. In this configuration it is possible to measure the interelectrode capacitance as a function of the micrometer setting using a Schering bridge at 1 kc/s.

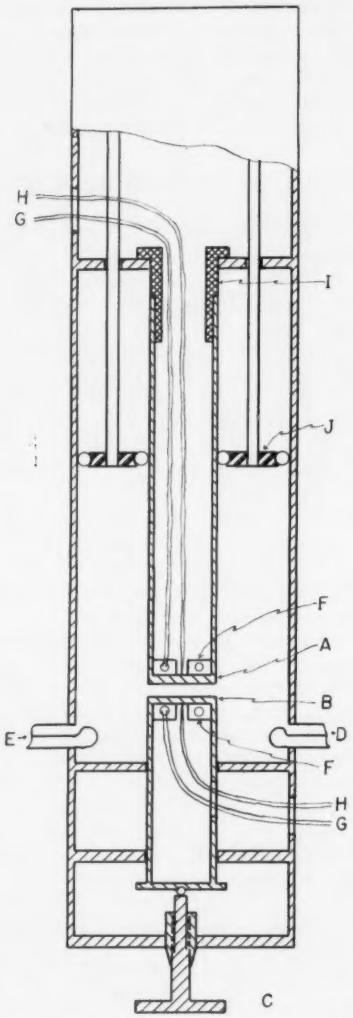

FIGURE 27. *The re-entrant cavity.*

A = Fixed electrode
B = Movable electrode
C = Micrometer screw
D = Input loop
E = Detector loop
F = Heater elements
G = Heater wires
H = Thermocouple wires
I = Ceramic insulator
J = Movable short

Measurements at temperatures above room temperature were achieved by means of heaters inside the ends of the electrodes. The end pieces could be maintained at temperatures up to 150 °C by separate control of the electrode heaters, **G**, using thermocouples, **H**, in each electrode. The interelectrode capacitance became somewhat uncertain at temperatures much above 150 °C due to thermal fluctuations along the supporting cylinders.

A block diagram of the cavity and the associated equipment is shown in figure 28. A Rollin Model 30A signal generator served as a signal source. As indicated, this signal was mixed with that from a low power signal generator operating within a few megacycles of the resonance frequency and the beat frequency was measured with a Collins radio receiver. Frequency changes of the driving generator were measured in this manner to an accuracy of 1 kc/s during the dielectric loss measurements as described below. A 1 kc/s modulation was applied to the signal source to facilitate detection. A bolometer and Hewlett Packard standing wave indicator (Model 415–B) were used for detection.

The measurements of dielectric constant and loss index were carried out in much the same manner as has been described by previous authors. The disk-shaped specimen (0.80B or 0. 44B) was placed between the electrodes which then maintained a slight pressure on the specimen. The sliding short

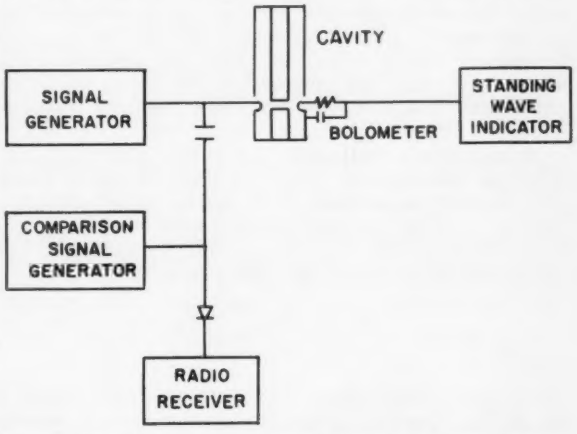

FIGURE 28. *Block diagram of the re-entrant cavity and ancillary equipment.*

was adjusted to achieve resonance after the generator had been set to the desired frequency. The electrode spacing was measured to an accuracy of about 1 μ. The sample was then removed and the electrode spacing readjusted to achieve resonance. From the calibration of the interelectrode capacitance it was possible to compute the capacitance of the sample and thus the dielectric constant.

Several methods have been described for measurements of the dielectric loss index. Essentially they are all one of two general types: in one case the Q of the empty cavity and the cavity with the sample in place are measured independently and thence the dissipation of the sample computed. An alternative method involves measurements of the Q of the empty cavity and the computation of the Q of the cavity with the sample from comparison of the voltage at reasonance for the two conditions. The Q of a resonant cavity can be measured by obtaining the shape of the resonance curve either by small changes in the capacitance of the cavity or by small change of the frequency of the driving generator. Due to the sliding short, the cavity could not be equipped with a vernier capacitor such as Reynolds [45] used, and the capacitance could only be changed by altering the electrode spacing. The Q of the empty cavity was so high that, in general, a change of interelectrode spacing of only a few microns was sufficient to achieve the half-resonance-voltage condition. Accurate determination of the Q of the empty cavity by this method was out of the question. Obviously this method could not be used when a sample was in the cavity fixing the interelectrode spacing. The frequency shift method was therefore used. The relation for computing the loss index is

$$\epsilon''=\frac{(dC/df)(\Delta f_2-\Delta f_1)}{C_r\sqrt{q-1}} \qquad \text{(A–36)}$$

in which the differential dC/df is determined by varying the electrode separation of the empty cavity (and thus the capacitance) by a small amount and observing the change in the resonance frequency over a narrow range near the frequency of the measurement. The quantities Δf_1, and Δf_2 are the frequency shifts from the resonant frequency for the empty and sample-loaded cavity required to observe a voltage $V_r/\sqrt{q}$ where V_r is the peak resonant voltage.

An alternate method of measuring dielectric loss, which is particularly suitable where the loss is small, involves the measurement of the ratio, $(V_1-V_2)/V_2$, where V_1 is the resonant voltage with the sample out and V_2 that with the sample in the cavity. The relationship for computing the loss is then

$$\epsilon''=\frac{(dC/df)\Delta f_1(V_1-V_2)/V_2}{C_r\sqrt{q-1}}. \qquad \text{(A–37)}$$

It is clear that where the difference $(\Delta f_2-\Delta f_1)$ is small, i.e., the loss is small, this technique improves the accuracy of the measurement. The detection system used in this work gave the voltage difference in decibels, which was conveniently converted by means of the expression

$$\frac{V_1-V_2}{V_2}=\left[\text{antilog}\left(\frac{db}{10}\right)\right]-1. \qquad \text{(A–38)}$$

Where suitable, these two methods of measurement gave loss values in close agreement, rarely differing by more than 2 percent.

The dielectric constants are estimated to be accurate to about 0.5 percent, the error being chiefly due to uncertainty of the interelectrode spacing of the empty cavity. The dielectric loss indexes are estimated to be accurate within 5 percent. In this case the errors are principally due to slight deviations from square law detection and variations in output level of the signal generator, particularly with small changes in frequency. Both these sources of error could undoubtedly be reduced, but it was believed that any real improvement in performance would require an unjustifiable amount of effort.

7.2. Microwave Apparatus

The dielectric properties of PCTFE at microwave frequencies were determined at room temperature (23 °C) with a Microwave Dielectrometer (Model 2), manufactured by Central Research Laboratories, Inc.

The principle of the Dielectrometer has been extensively discussed by Roberts, von Hippel, Westphal, and others [46, 47]. The instrument has a slotted, circular waveguide which may be operated at frequencies of 1, 3, and 8.6 kMc/s. At 8.6 kMc/s the waveguide is excited in the TE_{11} mode by reflex klystrons. At 1 and 3 kMc/s a center conductor is introduced so that the waveguide becomes a coaxial line, excited by klystrons in the TEM modes. One end of the waveguide is shorted, and the standing wave is measured by a precision traveling probe, which acts as a square law detector.

The introduction of a dielectric specimen, which fills the end of the waveguide and which presents plane faces perpendicular to the waveguide axis, establishes a new standing wave pattern. The traveling probe is used to determine the distance of the node from the shorted end, X_0, and to determine the distance between double power points, ΔX. This information, together with the length of the dielectric specimen, d, and the distance between nodes in the guide $\lambda/2$, is used to determine the propogation constant of the specimen, γ:

$$\frac{\tanh \gamma d}{\gamma d}=-\frac{\lambda}{2\pi d}\frac{\tan(2\pi X_0/\lambda)+j\dfrac{\sin(\pi\Delta X/\lambda)}{[1+\sin^2(\pi\Delta X/\lambda)]^{1/2}}}{1-j\dfrac{\sin(\pi\Delta X/\lambda)}{\sqrt{1+\sin^2(\pi\Delta X/\lambda)}}\tan\left(\dfrac{2\pi X_0}{\lambda}\right)}. \qquad \text{(A–39)}$$

Equation (A–39) is easily determined by transmission line theory [46]. After γ is determined we find the

dielectric properties from the equation [46]

$$\epsilon' - j\epsilon'' = \frac{(\lambda_c)^{-2} - \left(\frac{\gamma d}{2\pi d}\right)^2}{(\lambda_c)^{-2} + (\lambda)^{-2}}, \qquad \text{(A-40)}$$

where the cut off wavelength of the TE_{11} mode at 8.6 kMc/s is $\lambda_c = 43.43$ mm, while the cut off wavelength of the TEM modes at 1 kMc/s and 3 kMc/s is $\lambda_c = \infty$.

Small corrections due to the attenuation of the empty waveguide must be made to eqs (A–39) and (A–40) above. These corrections are described in the literature (see, e.g., Westphal [47].)

The accuracy of the measurements require that the specimen be accurately machined so that the end of the waveguide is filled snugly, with the plane faces perpendicular to the waveguide axis. Two circular cylindrical samples were made from stock of PCTFE. This stock had a specific volume of 0.4657 cm^3/g upon receipt. After a six-day heat treatment where the stock was held for extended periods at temperatures of 200, 190, 180, and 170 °C, the specific volume at 23 °C was decreased to 0.4629, which corresponds to a degree of crystallinity of 0.78 [4]. From this stock two right circular cylindrical specimens of 2.542-cm diam were machined with the plane faces accurately perpendicular to the cylindrical axis. The specimen which was used at 8.6 kMc/s had a length of 1.916 cm. The second specimen, used at 1 and 3 kMc/s, had a length of 3.179 cm, and had an accurately concentric center hole with a diameter of 0.950 cm to fit the coaxial center conductor of the instrument.

These specimens were then used for the determination of the dielectric constant and loss index at room temperature at frequencies of 1, 3, and 8.6 kMc/s. The results are included in table 2.[28]

[28] Because of the large samples that are required for the microwave apparatus, it was impossible to quench them to achieve a crystallinity as low as that of specimen 0.44.

8. References

[1] S. I. Reynolds, V. G. Thomas, A. H. Sharbaugh, and R. M. Fuoss, J. Am. Chem. Soc. **73,** 3714 (1951).
[2] L. Hartshorn, J. V. L. Parry, and E. Rushton, J. I.E.E. **100,** Pt. 11A, No. 3 (1953).
[3] G. P. Mikhailov and B. I. Sazhin, Soviet Phys. Tech. Phys. **1,** 1670 (1957). (Translated from Zhurnal Tekh. Fiziki.)
[4] J. D. Hoffman and J. J. Weeks, J. Research NBS **60,** 465 (1958).
[5] D. J. Scheiber, J. Research NBS **65C** (Eng. and Instr.), 23 (1961).
[6] T. Nakajima and S. Saito, J. Poly. Sci. **31,** 423 (1958).
[7] J. D. Hoffman, J. J. Weeks, J. Research NBS, **66A** (Phys. and Chem.), 13 (1961).
[8] N. G. McCrum (private communication).
[9] K. Schmieder and K. Wolf, Koll. Zeits. **134,** 149 (1953).
[10] A. K. Schulz, J. Chim. Phys. **53,** 933 (1956).
[11] K. H. Illers and E. Jenckel, Koll. Zeits. **165,** 84 (1959).
[12] M. L. Williams, R. F. Landel, and J. D. Ferry, J. Am. Chem. Soc. **77,** 3701 (1955).
[13] J. D. Ferry, Viscoelastic properties of polymers, J. Wiley & Sons, N.Y., (1961).
[14] S. Saito and T. Nakajima, J. Appl. Poly. Sci. **2,** 93 (1959).
[15] J. D. Hoffman and J. J. Weeks (manuscript in preparation).
[16] J. D. Hoffman and J. I. Lauritzen, Jr., J. Research NBS **65A** (Phys and Chem.), 297 (1961).
[17] M. Takayanagi, M. Yoshino, and K. Hoashi, J. Japan Soc. Testing Materials **10,** 418 (1961).
[18] M. Takayanagi, High polymers, Japan, **10,** 289 (1961) (In Japanese).
[19] G. Gee, P. N. Hartley, J. B. M. Herbert, and H. A. Lanceley, Polymer **1,** 365 (1960).
[20] A. B. Thompson and D. W. Woods, Trans. Faraday Soc. **52,** 1383 (1956).
[21] K. S. Cole and R. H. Cole, J. Chem. Phys. **9,** 341 (1941).
[22] J. H. Gladstone and J. Dale, Phil. Trans. 153, 317 (1863).
[23] H. Fröhlich, Theory of dielectrics, Oxford Univ. Press, London (1949). See Chapter 2.
[24] C. I. Carr, Jr., and B. H. Zimm, J. Chem. Phys. **18,** 1616 (1950).
[25] J. D. Hoffman, J. Chem. Phys. **20,** 541 (1952).
[26] J. D. Hoffman and B. F. Decker, J. Phys. Chem. **51,** 520 (1953).
[27] H. S. Kaufman, J. Am. Chem. Soc. **75,** 1447 (1953); H. S. Kaufman, Tech. Assoc. Pulp Paper Ind. **37,** 140 (1954).
[28] P. H. Geil (private communication).
[29] D. H. Reneker (private communication).
[30] Y. Ishida, Y. Takada, and M. Takayanagi, Kolloid Zeitschrift **168,** 121 (1960).
[31] M. Baccaredda and E. Butta, J. Poly. Sci. **44,** 421 (1960).
[32] K. W. Wagner, Archiv für Elecktrotechnik **2,** 371 (1914).
[33] R. W. Sillars, Inst. of E. E. **80,** 378 (1937).
[34] E. A. W. Hoff, D. W. Robinson, and A. H. Willbourn, J. Poly. Sci. **18,** 161 (1955).
[35] K. Deutsch, E. A. W. Hoff, and W. Reddish, J. Poly. Sci. **13,** 565 (1954).
[36] L. Hartshorn and W. H. Ward, Journal I.E.E. **79,** 597 (1936).
[37] E. B. Baker, Rev. Sci. Instruments **22,** 379 (1951).
[38] A.S.T.M. Standards, 1959 Supplement, Part 9, D–150, 7.(a) (1).
[39] A.S.T.M. Standards, 1959 Supplement, Part 9, D–150, Appendix III.
[40] W. R. Smythe, Static and Dynamic Electricity, 2d ed., ch. 6, McGraw-Hill, 1950.
[41] I. R. Weingarten, Annual Report of the Conference on Electrical Insulation, p. 53, 1955.
[42] L. Heroux, J. Appl. Phys. **29,** 1636 (1958).
[43] J.V.L. Parry, Proc. I.E.E. **98,** 303 (1951).
[44] C. N. Works, J. Appl. Phys. **18,** 605 (1947).
[45] S. I. Reynolds, General Electric Review, Sept. 1947.
[46] S. Roberts and A. von Hippel, J. Appl. Phys. **17,** 610 (1946).
[47] Dielectric Materials and Applications, ed. A. von Hippel, ch. 2, Distributed circuits, William B. Westphal. Published jointly by the Technology Press of MIT, and John Wiley & Sons, Inc., N.Y. (1954).
[48] P. F. Veselovskii and A. I. Slusker, Zhur. Tekh. Fiz. **25,** 939 and 1204, (1955).

(Paper 66A4–162)

JOURNAL OF RESEARCH of the National Bureau of Standards—A. Physics and Chemistry
Vol. 66A, No. 4, July–August 1962

Thermal Degradation of Fractionated High and Low Molecular Weight Polystyrenes[1]

S. L. Madorsky, D. McIntyre, J. H. O'Mara, and S. Straus

(April 16, 1962)

In previous work on the thermal degradation of polystyrene of average molecular weight of 230,000, carried out in a vacuum in the temperature range 318 to 348 °C, the rate curves exhibited distinct maximums when percentage loss of sample per minute was plotted as a function of percentage volatilization. These maximums correspond to a volatilization of about 35 to 45 percent and tend to flatten with decreased temperature of pyrolysis. A similar study of rates of thermal degradation at 307.5 °C has now been made on two groups of polymers: (1) low molecular weight, 24,000; 51,000; and 66,000; and (2) high molecular weight, 2,000,000; 2,250,000; and 5,000,000. Whole polymers and also fractions of narrow-range molecular weight were used. The rate curves for the 24,000 and 51,000 molecular-weight samples exhibit very high initial rates, but no maximums; the 66,000 sample showed a maximum at 45 percent volatilization. The rate curves for the 2,000,000, 2,250,000, and 5,000,000 molecular-weight samples exhibit a gradual rise up to about 25 percent volatilization; then, instead of forming maximums, they follow plateaus to about 50 percent volatilization. These plateaus are indicative of a zero-order reaction in the range that they cover, and the rates corresponding to them fit well on the Arrhenius activation-energy curve obtained previously for polystyrene samples at higher temperatures.

1. Introduction

The rates of thermal degradation of polystyrene in a vacuum have been studied extensively by Jellinek [1,2],[2] Madorsky [3,4], and Grassie [5,6]. However, the exact mechanism of degradation has been uncertain. The reaction does not follow a simple process of random initiation or end initiation. Instead, there appears to be a complex mechanism that has been explained by assuming random initiation, with a considerable amount of intramolecular and intermolecular transfer of free radicals, accompanied by unzipping at free-radical chain ends [7,8,9]. In addition to this, structural irregularities, so-called "weak links," in the backbone of the chains have been postulated to account for some of the degradation of the chains [1,2,5,6].

In the earlier studies on thermal degradation a polystyrene sample of molecular weight 230,000 (osmotic pressure) was pyrolyzed in the temperature range of about 330 to 400 °C. Curves of the rates of degradation in percent of original sample plotted as a function of percentage degradation exhibit maximums in the range of about 35 to 45 percent degradation [3]. These curves approach a horizontal line at decreased temperatures of degradation, as shown in figure 1. At 299.5 °C the middle portion of the rate curve approaches very closely a horizontal line [4], which is indicative of a zero-order reaction. Thus, although at the higher temperatures the mechanism of reaction is rather complicated, it seems to approach a zero-order at low temperatures. In order to elucidate this mechanism a series of experiments were carried out at relatively low temperatures, using polystyrene samples of high purity, fractionated and unfractionated, and of both high and low molecular weight.

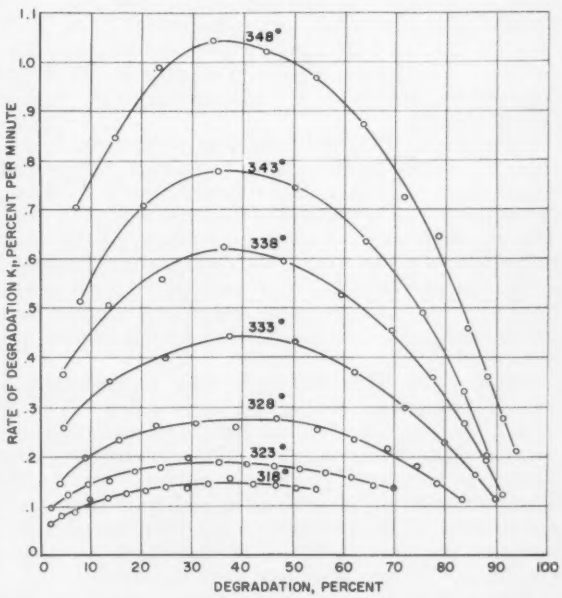

FIGURE 1. *Rates of thermal degradation of unfractionated polystyrene of molecular weight of 230,000.*

Rate of sample loss, K_1 is measured in percent of original sample. Figure is taken from references [3] and [4].

[1] This paper was presented at the 141st meeting of the American Chemical Society in Washington, D.C., March 20–29, 1962.
[2] Figures in brackets indicate the literature references at the end of this paper.

2. Apparatus and Experimental Procedure

In earlier studies on rates of thermal degradation of polymer a tungsten helical spring microbalance was used for the higher temperatures; in the present work an Elmic electronic microbalance was used because it was more suitable for measurements of the slower rates obtained at the relatively low temperature of 307.5 °C. This electronic balance automatically recorded the temperature and loss of weight of the sample, and could be operated for long periods of time without attention.

The experimental procedure using this balance has been described in detail [4]. A 4 to 5 mg sample of the polymer in a small platinum crucible was suspended from the arm of the balance enclosed in a glass housing. The system was evacuated to about 10^{-5} mm Hg. An electric furnace which was preheated to the required temperature was then raised around the glass housing for pyrolysis of the sample. A chromel-chromel constantan thermocouple directly under the crucible reached the operating temperature in about 15 min. Very little loss of weight occurred during the warming-up period. The thermocouple was precalibrated against a similar thermocouple placed in the crucible in contact with its bottom. The temperature was kept constant to within ± 0.2 °C by means of an electronic thermostat.

3. Materials

Eastman styrene, stabilized with *p-tert*-butylcatechol, was used in the preparation of the polymer. It was first washed with 7 percent NaOH, then with distilled water, and finally dried with $CaSO_4$. The dried monomer was distilled at 18 mm Hg. The purified dry monomer was degassed in a high-vacuum line and distilled into dilatometers. Two batches of polymers were prepared: polymer A and polymer B. No initiator was used for either of these two polymers.

Polymer A: This polymer was polymerized for a year at room temperature to about 50 percent conversion. The reaction mixture was poured into methanol. The precipitated polymer was then dried. The viscosity-average molecular weight of the whole polymer was 2,250,000. The fractionation was begun at a concentration of 0.5 percent of polymer in methyl ethyl ketone using isopropyl alcohol as a precipitant. Several fractions and subfractions were recovered.

Polymer B: This polymer was polymerized at 180 °C to about 30 percent conversion. The reaction mixture was poured into methanol and then precipitated with water. The viscosity-average molecular weight of the whole polymer was 51,000. Fractionation began with an initial concentration of 0.6 percent of the polymer in a methyl-ethyl ketone acetone mixture (1:1) using methanol as a precipitant. Twelve fractions were recovered.

Pertinent data on the unfractionated and fractionated materials used in this paper are shown in table 1. The molecular weights of these materials were determined by the viscosity method. The intrinsic viscosities were determined in benzene at 40 °C using an Ubbelohde viscometer. Molecular weights were calculated from the relation

$$[\eta]=1.00\times10^{-4}\cdot M_w^{0.75}$$

which is very close to the relation given by Flory [10] for the intrinsic viscosity and weight-average molecular weight of fractions of polystyrene.

TABLE 1. *Polystyrene samples used in pyrolysis*

Sample No.	Fraction	Mol. wt.
A-uf	Unfractionated	2,250,000
A-hf	High fraction	5,000,000
A-lf	Low fraction	2,000,000
B-uf	Unfractionated	51,000
B-hf	High fraction	66,000
B-lf	Low fraction	24,000

4. Experimental Work

4.1. Molecular Weight of Degraded Polymers

Samples of polystyrene fraction A-lf, molecular weight 2,000,000 (table 1), were pyrolyzed in a vacuum for various periods of time at temperatures ranging from 304 to 312 °C. The residues were dissolved in benzene and freeze-dried prior to determining their average molecular weight by viscosity and osmotic-pressure methods.

The viscosity method has been described above. The osmotic-pressure determinations were made in cyclohexane at 35 °C in Stabin osmometers using "never-dried" gel cellophane No. 600. Results of these pyrolysis experiments are shown in table 2. In figure 2 the results of molecular weight determinations of the residues by the viscosity and the osmotic-pressure methods for sample A-lf are compared with similar results obtained previously [3] using the osmotic-pressure method for an unfractionated thermally prepared polystyrene sample of molecular weight 230,000. The results indicate a rapid drop of molecular weight during the initial 10 percent loss of weight to about 70,000 to 80,000. This drop is similar for both the fractionated polystyrene of average molecular weight 2,000,000 and the unfractionated sample of molecular weight 230,000. Beyond 10 percent loss the drop is less drastic and the curve shows a tendency to level off at about 50,000 (osmotic-pressure molecular weight) for both polymers.

TABLE 2. *Molecular weights of degraded polystyrene fraction A-lf*

Temp.	Duration	Volatilization	M_v(visc.)	M_n(os. pr.)	M_v/M_n
°C	min	%			
304	180	1.3	335,000	200,000	1.68
312	240	5.7	168,000	98,600	1.70
310	660	16.6	90,500	61,100	1.48
304	960	41.0	65,000	36,600	1.78
310	1260	51.0	50,000	30,600	1.63
310	1500	61.0	41,000	25,600	1.60
Average					1.64

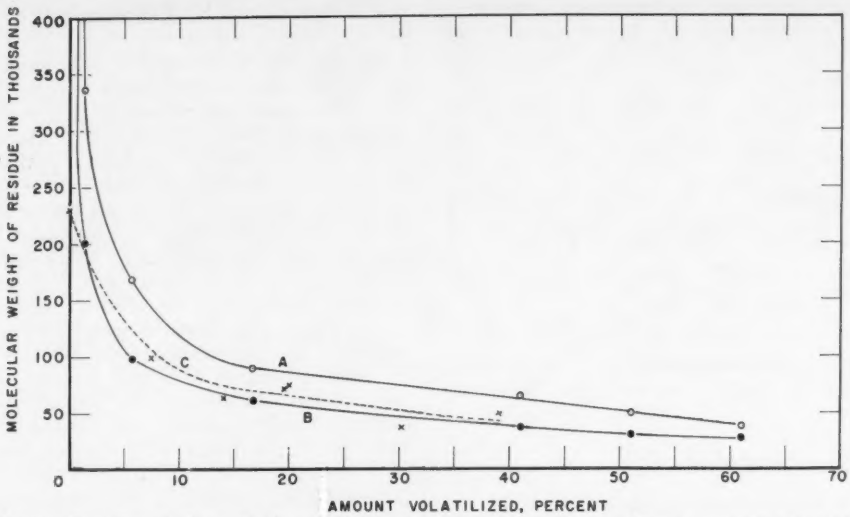

FIGURE 2. *Drop in the molecular weight of polystyrene, fraction A-lf, molecular weight 2,000,000*

A—by the viscosity method; B—by the osmotic-pressure method. Curve C is from earlier work [3], for unfractionated polymer, molecular weight 230,000 by the osmotic-pressure method.

4.2. Rates of Degradation

The whole polymers A and B, and their two fractions (table 1) were studied. Pertinent details of the rate experiments are shown in table 3. In figure 3 cumulative loss of weight, in percent of sample, is plotted as a function of time. Fractions A-hf and A-lf of 5,000,000 and 2,000,000 molecular weight, respectively, show the same pyrolysis curve. These high molecular-weight curves show inflexions and resemble those obtained previously for unfractionated, thermally prepared polystyrene, molecular weight, 230,000, and of two fractions from this polymer of molecular weights 106,000 and 584,000 [3].

TABLE 3. *Rates of degradation of polystyrene at 307.5 °C*

Sample No.	Mol. wt.	Duration	Volatilization	Max. rate
		hr	*%*	*%/min*
A-uf	2,250,000	30	73.0	0.0480
A-hf	5,000,000	30	62.5	.0450
A-lf	2,000,000	30	62.5	.0450
B-uf	51,000	22	74.0	[a].0555
B-hf	66,000	30	73.0	.0534
B-lf	24,000	22	73.0	.0690

[a] This rate corresponds to an inflection on the rate curve instead of to a maximum rate.

In figure 4 the rates, calculated from the curves in figure 3, are plotted in percent of sample volatilized per minute as a function of percentage volatilized. The high molecular weight polymers, both unfractionated and fractionated, show a gradual rise in rate up to about 25 percent loss, then there is a plateau extending to about 50 percent loss, followed by a drop in rate tending toward zero at 100 percent volatilization. The rate curve for B-hf fraction, 66,000 molecular weight, resembles those for the high molecular weight polymers, except that it does not have a plateau. The 24,000 B-lf fraction indicates a constant rate up to about 30 percent volatilization, followed by a drop toward 100 percent volatilization. The 51,000 B-uf sample starts at a very high rate and exhibits a pronounced inflexion between 40 to 45 percent volatilization, followed by a gradual decrease in rate.

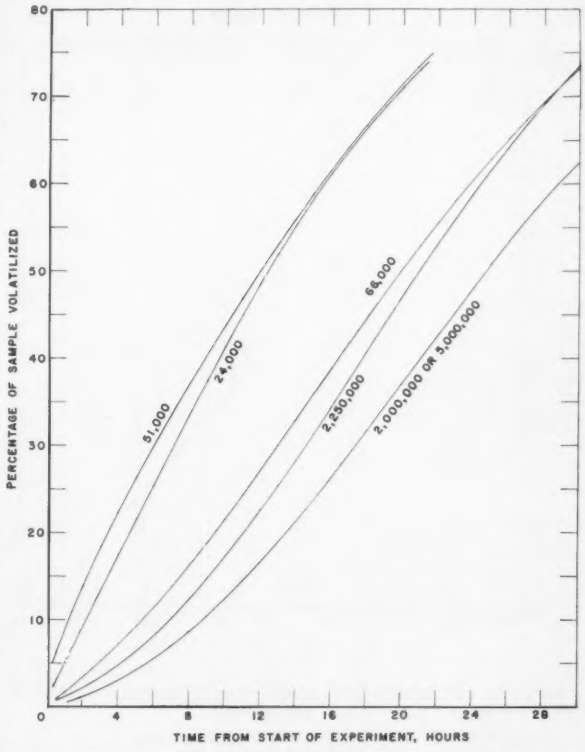

FIGURE 3. *Cumulative thermal degradation of polystyrene samples.*

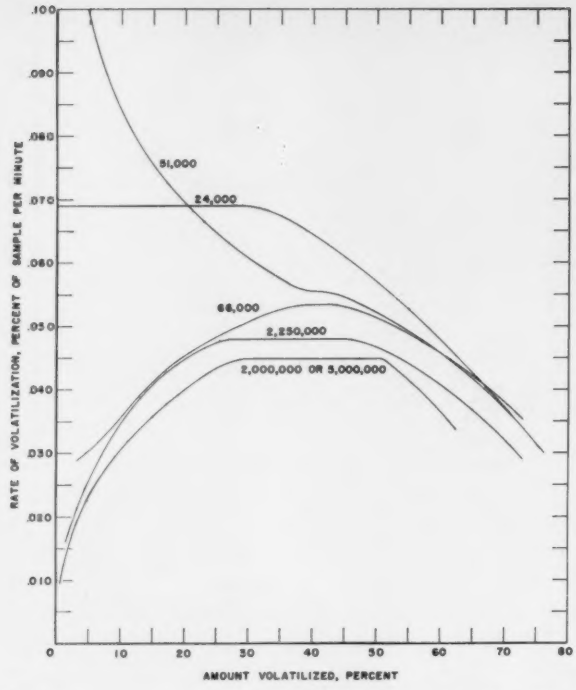

FIGURE 4. *Rates of thermal degradation of polystyrene samples.*

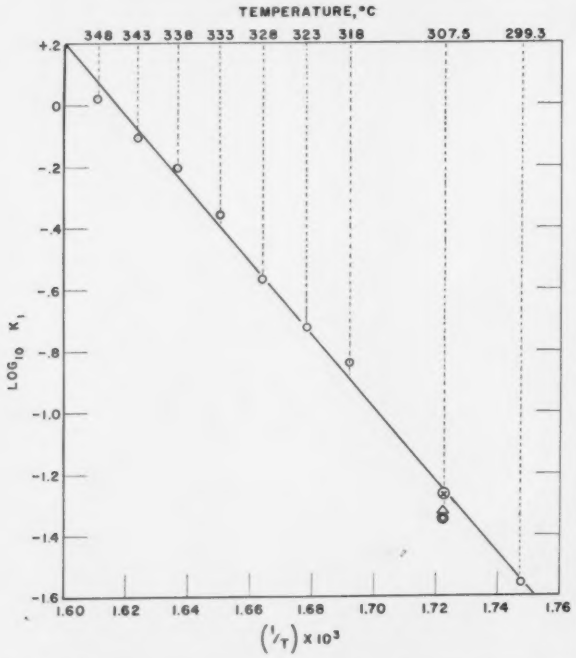

FIGURE 5. *Arrhenius plot for the rates of thermal degradation of polystyrene.*

○—Polystyrene molecular weight 230,000
⊗—Polystyrene sample B-hf
△—Polystyrene sample A-uf
◎—Polystyrene sample A-hf and A-lf

5. Discussion

As the high molecular weight polystyrene undergoes pyrolysis, its (M) drops rapidly during the first 5 to 10 percent loss of weight and stabilizes at about 40,000 to 60,000. The level of stabilization seems to be independent of the initial molecular weight or of the molecular distribution in the polymer species, provided the initial (M) is not below the stabilization level. The initial drop in molecular weight may be due partially to scissions at weak-link bonds caused by impurities in the polymers, but is mainly due to thermal scissions in the chain. This continues to a point where the drop in weight caused by random scissions is counter-balanced by the disappearance of smaller chains through unzipping, mainly into monomers. According to Staudinger and Steinhofer [11] and Madorsky and Straus [12], the degradation products from polystyrene consist of about 40 percent monomers, 20 percent dimer, 20 percent trimer, and some larger fragments. Unzipping takes place at free-radical chain ends, presumably as follows:

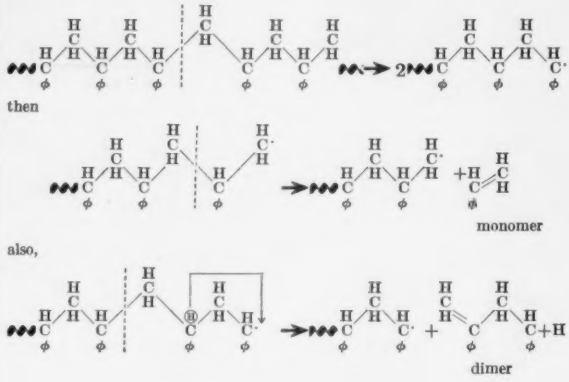

At this point stabilization sets in. Since loss here is mainly due to loss by unzipping at ends of chains, the rate is constant as long as the number of chain ends stays constant. This explains the plateau in the rate curves of the high molecular weight species. However, the average molecular weight drops gradually during this period, as is indicated in figure 2. Thus, as shown in figure 4, the portions of the rate curves from about 25 to 50 percent weight loss in the case of the three highest molecular weight samples point to a zero-order reaction. Beyond 50 percent volatilization a decrease in rate takes place due to a decrease in the number of chain ends. This is predicated on the assumption that in the range of conversion of 25 to 50 percent, the rate of disappearance of chain-ends by unzipping is equal to the rate of formation of new chain ends through random scission, while in the initial and final stages, the rate of disappearance of chains is respectively slower or faster than the rate of formation of new chain ends.

In the thermal degradation at 299.3 °C of unfractionated polystyrene of molecular weight 230,000, the rate curve shows a plateau in the range of about

20 to 50 percent volatilization [4]. However, at higher temperatures, 318 to 348 °C, the rate curves for this polymer show maxima instead of plateaus at about 35 to 45 percent volatilization [3]. This could be explained on the ground that with the rise in the temperature of pyrolysis the various reactions involved are speeded up and overlap so that the region of stabilization narrows down from a plateau to a peak.

Simha and Wall [8] predict, on theoretical grounds, the occurrence of maximums in the rate curves for the thermal degradation of polystyrene at about 25 percent degradation, in disagreement with the present and the earlier work.

Polystyrene fraction B-hf has a molecular weight (66,000) which is in the region at which stabilization occurs. Although the temperature of degradation is low enough for a plateau to occur, stabilization of molecular weight and of rate of loss of weight is of short duration and they begin to drop soon after stabilization sets in. As a result, the curve in figure 4 exhibits a maximum instead of a plateau. The whole polymer, B-uf, molecular weight 51,000, has apparently a large proportion of very short chains. The curve shows a high initial rate, followed by a short interval of stabilization at about 40 percent volatilization. From here on, this curve follows the same trend as the other curves. Low fraction B-lf, molecular weight 24,000, apparently has a narrow molecular weight distribution and is free from very short chain molecules. It decomposes initially in a manner of a zero-order reaction, but at a high rate, up to about 30 percent loss. Beyond this, the rate drops gradually due to the disappearance of some of the shorter molecules, while few scissions occur to compensate for the decrease in the number of chain ends.

Figure 5 represents an Arrhenius plot for the activation energy of the thermal degradation of polystyrene. The rate K_1 represents a rate of loss of weight in percent of the original sample per minute as a function of percentage volatilization. The points in this plot represent maximums of the rate curve shown in figure 1 for polystyrene of molecular weight 230,000, the peak of the rate curve shown in figure 4 for polymer fraction B-hf, and for the plateau rates in the same figure of polymer sample A-uf and its fractions, A-hf and A-lf. The slope of the curve indicates an activation energy of 55 kcal/mole. A similar value was obtained by plotting initial K_2 rates for polystyrene of molecular weight 230,000 [3, 4]. The initial K_2 rates were obtained by extrapolating to zero the degradation rates expressed in percent of residue per minute as a function of percentage volatilization.

6. References

[1] H. H. G. Jellinek, J. Polymer Sci. **3,** 850 (1948).
[2] H. H. G. Jellinek, J. Polymer Sci. **4,** 13 (1949).
[3] S. L. Madorsky, J. Polymer Sci. **9,** 133 (1952).
[4] S. L. Madorsky, J. Research NBS **62,** 219 (1959).
[5] N. Grassie and W. W. Kerr, Trans. Faraday Soc. **53,** 234 (1957).
[6] N. Grassie and W. W. Kerr, Trans. Faraday Soc. **55,** 1050 (1959).
[7] R. Simha and L. A. Wall, J. Phys. Chem. **56,** 707 (1952).
[8] R. Simha, L. A. Wall, and J. Bram, J. Chem. Phys. **29,** 894 (1958).
[9] S. Straus and S. L. Madorsky, J. Research NBS **65A** (Phys. and Chem.) 243 (1961).
[10] P. J. Flory, Principles of Polymer Chemistry, Cornell Univ. Press, p. 312, (1953).
[11] H. Staudinger and A. Steinhofer, Ann. Chemie **517**, 35 (1935).
[12] S. L. Madorsky and S. Straus, J. Research NBS **40,** 417 (1948).

(Paper 66A4–163)

JOURNAL OF RESEARCH of the National Bureau of Standards—A. Physics and Chemistry
Vol. 66A, No. 4, July–August 1962

Synthesis of 2-Propoxy-5-Methylbenzoic Acid [1]

Gerhard M. Brauer and Lester Simon

(April 3, 1962)

2-Propoxy-5-methylbenzoic acid has been synthesized by two routes from *p*-cresotinic acid. Synthesis of the ethyl ester of *p*-cresotinic acid, propylation to the ether, and subsequent hydrolysis of the ester proved to be the preferred route.

1. Introduction

The reactivity of various chelating agents with zinc oxide has been investigated in the course of work on the development of improved dental cements [1].[2] For this investigation there was needed an unsymmetrically disubstituted benzoic acid derivative that is liquid at room temperature.

From the few compounds that meet these specifications, 2-propoxy-5-methylbenzoic acid was selected. This compound has been reported [2] in a study of the effect of various alkoxy groups on the anomalous reactivity of *o*-alkoxyphenylmagnesium bromide Grignard reagents with carbon dioxide.

The synthetic route employed by Holmberg [2] in obtaining 2-propoxy-5-methylbenzoic acid did not appear to be well adapted for the preparation of the quantity needed because of the unavailability of the required intermediates as well as the formation, as a byproduct in the Grignard reaction, of a large amount of 2,2′-dipropoxy-5,5′-dimethylbenzophenone. Two other routes shown in figure 1 were therefore investigated; the second avoided tedious separation of intermediate products and gave a better yield.

[1] The research work was supported under an Office of Naval Research grant—contract ONR P. J.-NR 105-210.
[2] Figures in brackets indicate the literature references at the end of this paper.

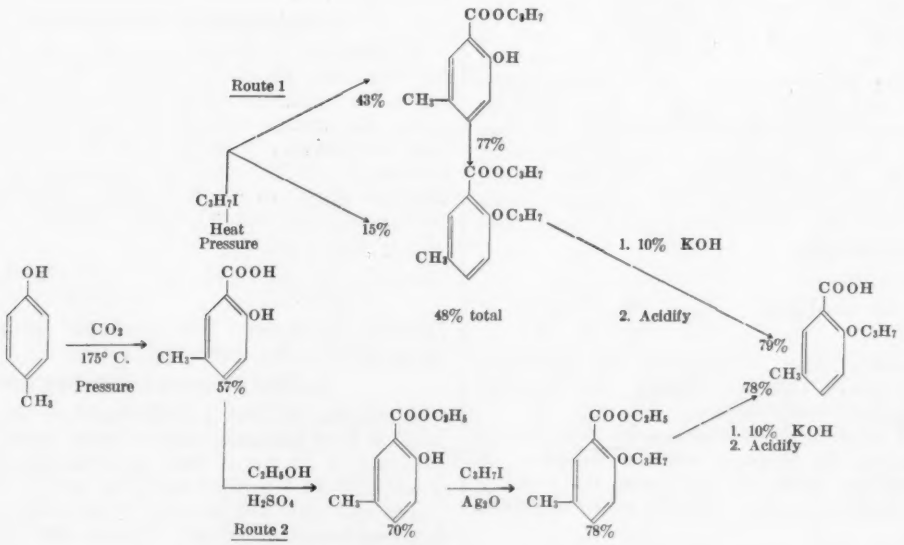

FIGURE 1. *Synthesis of 2-propoxy-5-methylbenzoic acid.*
(38% overall yield by route 1, 43% overall yield by route 2, based on *p*-cresotinic acid)

2. Experimental Procedure

2.1. Preparation of *p*-Cresotinic Acid

p-Cresotinic acid (2–hydroxy-5-methylbenzoic acid) was prepared by carbonation of *p*-cresol according to the procedure of Cameron, Jeskey, and Baine [3]. Dry, powdered potassium cresoxide was placed in a pressure bomb and carbon dioxide was admitted until a pressure of 10 atm was obtained. The bomb was heated for 24 hr at 175 °C and cooled; the material was then purified as described by Cameron et al.

2.2. Synthesis of 2-Propoxy-5-Methylbenzoic Acid (Route 1)

a. Propylation of *p*-Cresotinic Acid

In an 800-ml pressure bomb, a mixture of 52.9 g (0.35 mole) of *p*-cresotinic acid, 42 g (0.75 mole) of KOH, and 122 g (0.72 mole) of *n*-propyl iodide was heated overnight at 145 °C. The reaction mixture was dissolved in hot water, the solution was extracted with ether, and the ether solution was shaken with 5 percent aqueous NaOH. After evaporation of the ether, 45.0 g of liquid remained. Vacuum distillation of the residue gave two fractions.

Fraction 1, propyl 2-hydroxy-5-methylbenzoate, distilled at 77–79 °C/4 mm as a colorless liquid, bp 266–268 °C, n_D^{25} 1.5122, which gave a positive ferric chloride test for phenol.

Yield: 28.9 g (43%).
Anal: Calcd. for $C_{11}H_{14}O_3$: C, 68.02; H, 7.27.
Found [3]: C, 68.2 ; H, 7.4.

Infrared spectrum [4]: Absorption bands at the respective wavelengths indicate the presence of the following groups [4,5]: 3.16 μ, hydroxyl; 5.95 μ, ester carbonyl for salicylates; doublet at 6.15 μ and 6.24 μ, possible conjugation of the carbon-oxygen double bond with aromatic ring; 8.30 μ, phenol; and 12.11 μ, unsymmetrically trisubstituted benzene.

Fraction 2, propyl 2-propoxy-5-methylbenzoate, distilled at 100–108 °C/4 mm as a colorless liquid, bp 302 °C, n_D^{28} 1.5022, which gave negative tests with ferric chloride, Tollens' reagent, and 2,4-dinitrophenylhydrazine.

Yield: 12.2 g (15%).
Anal: Calcd. for $C_{14}H_{20}O_3$: C, 71.16; H, 8.53.
Found: C, 70.6; H, 8.4.

Infrared spectrum: The presence of the following groups is indicated: benzoyl, alkoxy, and unsymmetrically trisubstituted benzene.

The propyl ester of *p*-cresotinic acid (fraction 1) was converted to the propoxy ether as follows: A solution of sodium ethoxide, prepared from 2.8 g (0.125 equivalent) of sodium and 60 ml of absolute ethanol, and an excess (27.0 g, 0.159 mole) of propyl iodide were added to 24.2 g (0.125 mole) of the ester. The solution was refluxed until it was no longer alkaline to litmus. After evaporation of the ethanol under reduced pressure, the residue was dissolved in ether, and the solution was extracted with 5 percent aqueous NaOH. On concentration of the ether solution, there remained 22.7 g (77%) of propyl 2-propoxy-5-methylbenzoate, which, when purified by vacuum distillation, was identical in boiling point, n_D, and infrared absorption with fraction 2.

b. Hydrolysis of Propyl 2-Propoxy-5-Methylbenzoate

Ten grams of the sample in 35 ml of a 10 percent solution of KOH in 50 percent aqueous ethanol were refluxed for 4 hr, and the ethanol and propanol were removed by distillation. The residue was acidified with HCl and extracted with ether, and the ether extract was concentrated by evaporation. Vacuum distillation of the residue at approximately 4 mm yielded 6.5 g (79%) of 2-propoxy-5-methylbenzoic acid, bp 257 °C, n_D^{27} 1.527. Infrared spectrum confirmed the presence of –OH, COOH, ether, and unsymmetrically trisubstituted benzene groups.

2.3. Synthesis of 2-Propoxy-5-Methylbenzoic Acid (Route 2)

In order to avoid the tedious separation of the products of the propylation of 2-hydroxy-5-methylbenzoic acid, an improved synthesis of 2-propoxy-5-methylbenzoic acid was developed. The *p*-cresotinic acid is converted to the ethyl ester which is allowed to react with propyl iodide. The resulting ethyl 2-propoxy-5-methylbenzoate on hydrolysis gives 2-propoxy-5-methylbenzoic acid.

a. Ethyl 2-Hydroxy-5-Methylbenzoate

p-Cresotinic acid (13 g, 0.085 mole) was refluxed for 8 hr with 39 ml (0.67 mole) of absolute ethanol and a few milliliters of concentrated H_2SO_4 as a catalyst. The excess ethanol was distilled, and the ester was successively washed with water and 5 percent aqueous $NaHCO_3$, dried over anhydrous Na_2SO_4, and distilled at 94 to 95 °C/4 mm. The liquid had a boiling point of 235 °C, $n_D^{25}=1.5190$.

Yield: 10.8 g (70%).
Anal: Calcd. for $C_{10}H_{12}O_3$: C, 66.7; H, 6.73.
Found: C, 66.9; H, 7.0.

Infrared spectrum: The principal bands are the same as those for the propyl ester.

b. Ethyl 2-Propoxy-5-Methylbenzoate

A solution of 10.8 g (0.06 mole) of the ethyl ester n 21.6 g of benzene was refluxed overnight in the presence of 21.0 g of freshly precipitated, dry silver oxide and 32.4 g (0.19 mole) of propyl iodide. The liquid was decanted from the remaining solid, and the benzene was distilled off. The residue was extracted with ether, and the ether solution washed with 10 percent NaOH and dried. The liquid remaining after evaporation of the solvent distilled at 133 °C/6 mm

[3] Carbon and hydrogen analyses were done by E. Deardorff of the Standard Reference Materials Section, National Bureau of Standards.
[4] Infrared spectra were determined by Miss M. Katharyn Wharton, Applied Polymer Standards and Research Section, National Bureau of Standards.

The colorless liquid decomposed before reaching the boiling point, $n_D^{27}=1.5033$.

Yield: 10.4 g (78%).

Anal: Calcd. for $C_{13}H_{18}O_3$: C, 70.3; H, 8.16.
Found: C, 70.3; H, 8.1.

Infrared spectrum: The spectrum is very similar to that of the propyl ester. All absorption bands occur at approximately the same wavelengths as those found for the propyl ester.

c. Hydrolysis of Ethyl 2-Propoxy-5-Methylbenzoate

The procedure is similar to that described in route 1 for the hydrolysis of the propyl ester; 7.3 g of the ethyl ester was refluxed for 8 hr with 10 percent KOH in 50 percent ethanol.

Yield of purified product: 5.0 g (78%), $n_D^{27}=1.5269$.

Anal: Calcd. For $C_{11}H_{14}O_3$: C, 68.0; H, 7.3.
Found: C, 67.9; H, 7.5.

The infrared absorption spectra of the products obtained by routes 1 and 2 were identical.

The authors thank R. S. Tipson for valuable suggestions.

3. References

[1] Brauer, G. M., White, E. E., and Moshonas, M. G., J. Dental Res. **37,** 547 (1958).
[2] Holmberg, G. A., Acta Chem. Scand. **10,** 594 (1956).
[3] Cameron, D., Jeskey, H., and Baine, O., J. Org. Chem. **15,** 233 (1950).
[4] Spectra-structure correlation chart, The Perkin-Elmer Co., Norwalk, Conn.
[5] Bellamy, L. J., Infra-red Spectra of Complex Molecules, John Wiley & Sons, New York (1954).

(Paper 66A4–164)

JOURNAL OF RESEARCH of the National Bureau of Standards—A. Physics and Chemistry
Vol. 66A, No. 4, July–August 1962

The Gamma-Ray Distribution From Oriented Cerium-141

J. F. Schooley,[1] D. D. Hoppes, and A. T. Hirshfeld

(March 2, 1962)

The distribution of gamma-radiation emitted in the decay of Ce^{141} nuclei alined in neodymium ethylsulfate single crystals has been remeasured for temperatures as low as 0.0162 °K and has been found to be considerably more anisotropic than previously thought. The discrepancy is explained on the basis of preferential scattering of the plane-polarized radiation in the Dewar system. Similar measurements with Ce^{141} nuclei oriented in a polarized cerium ethylsulfate crystal have been made. The hyperfine constant for Ce^{141} in the neodymium ethylsulfate lattice is deduced as $A=0.0305\pm0.003$ cm^{-1}, and the $E2/M1$ ratio for the 145-kev gamma ray in Pr^{141} is $+0.068\pm0.008$.

1. Introduction

In order to use the gamma-ray distribution [1][2] $W(\theta)=1+\Sigma_\nu A_\nu f_\nu P_\nu(\cos\theta)$ from alined or polarized Ce^{141} as a secondary thermometer in experiments involving beta-ray distributions [2] or heat conduction in rare earth ethylsulfate crystals, we have reexamined this distribution experimentally. We find a considerably greater anisotropy than that reported by previous investigators [3, 4], and we find that scattering may offer an explanation for the discrepancy. Moreover, we are able to make an experimental determination of the hyperfine constants for cerium isotopes in concentrated neodymium ethylsulfate. Experiments with Ce^{141} in concentrated cerium ethylsulfate show that this system can produce almost total alinement when a small magnetic field is applied.

2. Experimental Procedure

2.1. General

The Ce^{141} used in this investigation was fission-product material which contained Ce^{144} and Pr^{144} as impurities. Conversion electron spectra observed with a thick-lens beta-ray spectrometer were used, together with data on the conversion coefficients [5], to find the contribution of the 134-kev Ce^{144} gamma-ray to the experimental spectrum of the 145-kev gamma-ray of Ce^{141}.

Approximately 1 microcurie of the activity was grown into each of four single crystals, each weighing 2 to 3 g. Two crystals contained only neodymium ethylsulfate and the activity. In another, 1 percent of the neodymium was replaced by stable cerium. The fourth crystal was concentrated cerium ethylsulfate. An inactive layer was grown around each crystal.

Although the experimental procedure used with the cerium ethylsulfate crystal was somewhat different from that used with the other specimens, the gamma-ray detectors and the counting procedures were the same in each case. Three gamma-ray detectors, usually utilizing 2 in. long by 2 in. diam NaI cylinders, were mounted in a horizontal array into which the Dewar assembly was swung after adiabatic demagnetization of the specimen. Each detector was monitored by a single-channel pulse height analyzer, whose output was switched at 1 min intervals from one to another of a pair of scalers. The output of one detector was also recorded by a 100-channel pulse height analyzer during the orientation period. After a counting time of from 3 to 10 min, the sample was warmed to the helium bath temperature in order to take a similar sampling of the isotropic radiation for normalization. The ratio of the "cold" to "warm" counting rates was then corrected for background, attenuation due to the finite solid angle subtended by the detector, and the gamma ray impurity.

2.2. Neodymium Ethylsulfate Host Crystals

The cryogenic apparatus used for the three neodymium ethylsulfate crystals has been described in detail by de Klerk and Hudson [6]; a useful modification has been the use of He^3 exchange gas, i.e. gas introduced to provide thermal contact between the sample and the pumped He^4 bath during the magnetization portion of the cycle. Pumping off the He^3 gas produced thermal isolation for demagnetization in approximately 3 min, an order of magnitude improvement over the use of He^4. Each crystal was mounted with the c-axis horizontal in order that the horizontal 22-kilogauss field could be applied for maximum cooling effect. The data of Meyer [7] were used to deduce the temperatures reached for the various values of magnetic field and bath temperature; in these runs, the final temperature varied between 0.1 °K and 0.016 °K. In general, two of the gamma-ray detectors were placed to receive radiation emitted parallel to the c-axis, and the third sampled radiation emitted perpendicular to this alinement axis. Warming of the specimen could be detected by change in the gamma-ray counting rate and by change in the paramagnetic susceptibility; there was, however, no systematic variation in the gamma-ray data during any counting period. Furthermore, the initial rate

[1] National Academy of Sciences—National Research Council Postdoctoral Resident Research Associate.
[2] Figures in brackets indicate the literature references at the end of this paper.

of warming from the lowest temperatures was difficult to assess by the mutual inductance bridge, since the perpendicular susceptibility appeared to change very little below 0.020 °K. For higher initial temperatures, the change in temperature during the "cold" counting period varied from about 5 percent at 0.026 °K to about 10 percent at 0.100 °K.

2.3. Cerium Ethylsulfate Host Crystals

The experimental arrangement in this case was dictated by the observation of Johnson and Meyer [8], indicative of an antiferromagnetic transition, that the adiabatic demagnetization process results in a minimum temperature of a cerium ethylsulfate specimen when the high initial field is reduced to 500 to 600 gauss, rather than to zero field. For an initial field of 22 kilogauss applied along the crystalline c-axis and a parallel residual field of 550 gauss, the final specimen temperature is calculated to be within the range 0.003 to 0.010 °K. In order to achieve optimum gamma-ray counting conditions in the present experiment, this residual field was supplied by a superconducting solenoid immersed in the helium bath. This coil consisted of 1,850 turns of 0.003 in. diam formvar-coated niobium wire, wound in two layers on the glass wall of the inner space of a light-guide cryostat designed for beta-ray distribution studies [9]. Since this solenoid produced a vertical field of no more than 1,700 gauss, it was necessary to use the large horizontal-field magnet for the initial field. In order to apply each field, in turn, along the crystalline c-axis, advantage was taken of the highly anisotropic g-values of cerium ethylsulfate [10]. The sample was suspended by a nylon thread passing horizontally through the crystal slightly above its center of gravity so that with zero applied field the c-axis was maintained vertical. Application of the 22-kilogauss field rotated the sample until the c-axis was horizontal. Upon demagnetization the crystal returned to the zero-field position, and it remained there when the solenoid was energized. The assembly was X-rayed under each of the above conditions to verify that the correct position was achieved.

As before, the gamma-ray counters were placed in a horizontal plane, which in this case corresponded to $\theta=90°$ for each. Contrary to the observations with the neodymium ethylsulfate samples, the gamma-ray counting rate changed noticeably during succeeding 1-min periods, necessitating an extrapolation of the "cold" counting rate to the time of demagnetization, approximately 1 min before the start of counting.

3. Results

The angular dependence of the gamma-ray intensity from cerium-141 alined in neodymium ethylsulfate was measured at approximately 0.0162 °K and found to be satisfactorily represented by the function

$$W(\theta)=1+(0.205\pm0.010)P_2(\cos\theta)$$
$$+(0.006\pm0.018)P_4(\cos\theta)$$

where θ denotes the angle between the axis of alinement (in this case the crystalline c-axis) and the direction of gamma-ray emission. The coefficient of $P_4(\cos\theta)$ relative to that of $P_2(\cos\theta)$ can be calculated approximately, given an estimate of f_2; this ratio, A_4f_4/A_2f_2, is calculated to be 0.024.

The temperature dependence of W(0°) for the neodymium ethylsulfate crystals is shown in figure 1. The data taken with the 1 percent cerium crystal could not be distinguished from that taken with the two essentially pure neodymium ethylsulfate crystals, and therefore it is also included in figure 1. The error flags denote the standard deviation of the mean of a number of 5 to 10 min counts at a given temperature. Overall, some one hundred such counts were made on the three samples. Corrections for detector solid angle, background, and cerium-144 impurity amounted to an average of 10 percent of A_2f_2. The temperature scale was derived from the data of H. Meyer [7] for a magnetic field applied parallel to the crystalline c-axis.

The data of Cacho et al., [3] were taken with low specific activity cerium-141, so that the sample corresponded almost exactly with the present 1 percent cerium crystal. Since A_2f_2 was plotted by them as a function of $1/T^*$, approximate corrections for the nonspherical shape of the specimen and for Meyer's T–T^* (sphere) relation have been made. The adjusted data, shown in figure 1, are in agreement with similar corrections made by Scurlock [11]. The triangular point in figure 1 represents the value of A_2 calculated from the experiments of Ambler, Hudson, and Temmer [4], using planar alinement of cerium-141 in cerium magnesium nitrate, multiplied by the f_2 deduced from the present experiments for the temperature 0.0166 °K.

An interesting feature of the gamma-ray distribution was the change in $W(\theta)$ with decreasing energy of the detected photon. The spectrum measured at 0.016 °K and an isotropic comparison spectrum taken 1 °K are shown in figure 2. $W(0°)$ was 1.205 ± 0.010 for photon energies between approximately 140 and 170 kev; between 140 and 125 kev, however, the intensity decreased uniformly until at 115 kev it reached a minimum value of 0.80 ± 0.04. Correspondingly, $W(90°)$ was 0.90 ± 0.01 at the photopeak energy, rising to a maximum of 1.10 ± 0.05 at approximately 115 kev. This reversal in the anisotropy at lower energies was demonstrated to be a scattering phenomenon by the use of a collimating system consisting of a 1 cm hole in a gold foil surrounding the vacuum jacket and tin-lined lead cones which were placed in front of the detector crystals. Multichannel analysis of the photon spectrum under these conditions showed no reversal of the anisotropy around 115 kev. It should be pointed out that most of the data shown in figure 1 were taken with single-channel analyzers and that, to avoid the attenuation due to this scattering effect, the discriminator thresholds were set at about 135 kev. This selection made the counting rate sensitive to small shifts in the pulse height, as is evidenced by the relatively large standard deviations shown on the data of figure 1.

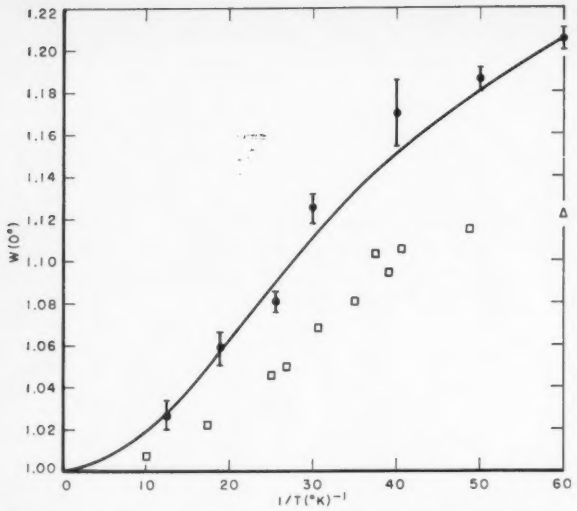

FIGURE 1. *The temperature dependence of* W(O°) *(which equals the quantity* $(1+A_2f_2)$ *in this case) for* Ce^{141} *in neodymium ethylsulfate.*

●, present data;
□, Cacho et al., [3];
△, calculated from data of Ambler, Hudson, and Temmer [4];
—, theoretical curve (see discussion sec. 4).

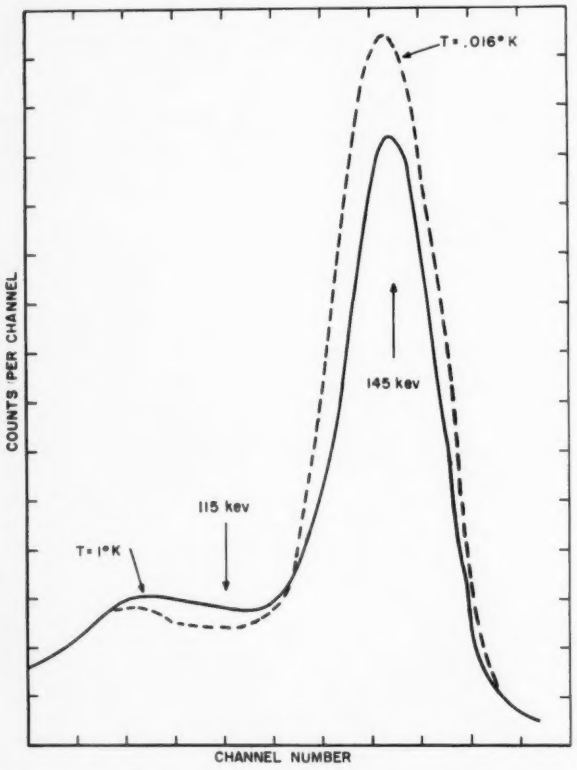

FIGURE 2. *The energy spectrum of gamma-radiation from* Ce^{141} *in neodymium ethylsulfate observed at* $\theta=0°$ *without collimation.*

—, isotropic spectrum taken at $T=1$ °K;
- -, spectrum taken at $T=0.016$ °K.

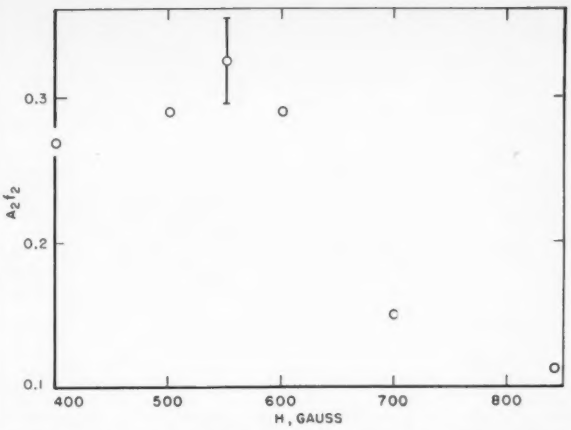

FIGURE 3. *The coefficient of* P_2 (cos θ) *for gamma-radiation from* Ce^{141} *oriented in cerium ethylsulfate, as a function of magnetic field applied parallel to the crystalline c-axis.*

The results of the cerium ethylsulfate experiments are illustrated in figure 3, in which the experimental A_2f_2 is plotted against applied field. The maximum value of A_2f_2 is seen to be about 0.325 ± 0.03. The corresponding magnitude of f_2 can be estimated, assuming the hyperfine interaction to be similar to that deduced for neodymium ethylsulfate as the host lattice, to be nearly 0.571, the value characteristic of complete alinement. The fact that $f_2 \leqq 0.571$ allows a lower limit of 0.508 to be placed on A_2. This limit A_2 was used in the analysis of the neodymium ethylsulfate data that follows.

4. Discussion

The change in sign of the experimental anisotropy at energies below about 130 kev can be accounted for by noting that the gamma-rays emitted from the alined cerium-141 are plane-polarized, and considering the effect of this polarization on subsequent scattering of the photons from the vacuum jacket and the Dewar walls (see fig. 4). With a typical (uncollimated) counting geometry the radiation de-

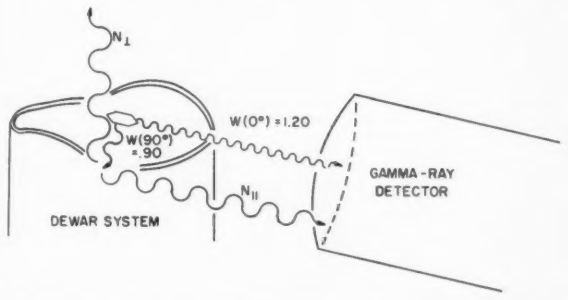

FIGURE 4. *Schematic diagram of source, Dewar system, and detector placed at* $\theta=0°$.

[Radiation emitted in the 0=90° direction and scattered by the Dewar system through an angle of 90° can impinge on the uncollimated detector. Indicated values of $W(0°)$ and $W(90°)$ are those observed at $T=0.016$ °K for the collimated beams.]

fined as $N_\parallel$ [12], taking the scattering medium as the Dewar system, could impinge directly upon the detector placed along the axis of alinement. A photon beam of 145 kev must be scattered through 90° in order to be degraded to an average energy of 115 kev according to the simple Klein-Nishina relation [13]; thus, without considering polarization of the gamma-rays, the ratio of "cold" to "warm" counting rates measured at 115 kev energy is seen to be less than unity. The (cold/warm) counting rate for the scattered beam identified as $N_\parallel$ in figure 4 would in fact be 0.90, but taking account of the detector solid angle and energy resolution raises this ratio to about 0.94. One can include the effect of preferential scattering of the radiation emitted at $\theta=90°$ due to it plane-polarized nature by use of the measurement of $N_\perp/N_\parallel=1.58$ at $T=0.025$ °K [3]. In this case the value of $N_\parallel$, normalized to unity for isotropic, unpolarized radiation, is 0.78 [12]. This is in agreement with the experimental measurement at that energy. It is seen that for photons losing more or less energy than those included in $N_\parallel$, the normalized intensity would be nearer unity, again in accord with experiment. A similar argument holds for measurements made with the gamma-ray detector placed to receive radiation emitted perpendicular to the c-axis.

The scattering phenomenon takes on particular significance in the present experiment because the small energy loss in 90° scattering places the "reverse anisotropy" region adjacent to the energy region of interest. Inclusion of some or all of this scattered radiation can be shown by multichannel analysis to reduce the measured value of A_2f_2 by a factor as high as 0.58. The discrepancy between the present data and that of the previous investigators [3] is of just this magnitude, and may in fact lie in the various gamma-ray pulse height analyzer settings. It might be pointed out that no attenuation factor for imperfections in the crystal lattice has been taken account of in the analysis of the present data. As was observed before, the presence of 1 percent cerium in the neodymium ethylsulfate crystal was found to have no measurable effect on the alinement results.

From the data taken with the cerium ethylsulfate crystal, $(A_2f_2)_{max}=0.32\pm0.03$. Since $f_2=0.571$ for complete alinement, $A_2\geq 0.30/0.57=0.52$. Assuming the zero-field Hamiltonian in neodymium ethylsulfate $\mathcal{H}=AS_zI_z+B(S_xI_x+S_yI_y)+CS_zT_z$, where T_z is the total spin component of the two nearest neighbor cerium ions [14] and where $B\sim 0.05\ A$, the energy levels and consequently the parameter $f_2(T)$ of the system can be calculated. From a comparison of the calculated temperature dependence of f_2 for for various values of the hyperfine parameter A with the experimental A_2f_2 curve, taken with the limit on A_2 deduced from the cerium ethylsulfate data, the hyperfine constant $A=0.0305\pm0.003$ cm^{-1}. If one assumes that $A=$(constant) μ_N/I, then using the value of the nuclear magnetic moment of Ce^{141} determined by Kedzie et al., [15] corrected by use of the more accurate value of $\langle r^{-3}\rangle$ due to Judd and Lindgren [16], one obtains the value 0.091 ± 0.01 for the constant. The constant thus calculated is somewhat larger than the value calculated by Haag et al., [17] on the basis of the theory of Elliott and Stevens, [18] for cerium ethylsulfate.

The value of f_2 calculated at $T\sim 0.0162$ °K is 0.414 ± 0.025; this number, taken with the experimental A_2f_2 at the same temperature yields for A_2 the value 0.495 ± 0.03. The calculated temperature dependence of A_2f_2 for $A_2=0.495$ and $A=0.0305$ cm^{-1} is shown in figure 1. Taking the attenuating effect due to the unobserved beta decay to be represented by the factor 0.97 [19], we find for the 145 kev gamma-ray of Pr^{141} an $E2$ to $M1$ mixing ratio [12] $\delta=+0.068\pm0.008$.

The authors wish to acknowledge the helpful suggestions of E. Ambler of the Cryogenic Physics Section.

NOTE: Since this paper was prepared, data on the gamma-ray distribution from Ce^{141} oriented in neodymium ethylsulfate has been noted in the thesis of J. N. Haag (UCRL 9872, September 29, 1961 (unpublished)). These data are in close agreement with the corresponding data of the present authors.

5. References

[1] See e.g., E. Ambler, Methods of nuclear orientation. Progress in Cryogenics, 1960 pp. 249, 265, and 268, $A_\nu=\frac{B_\nu}{f_\nu}\times$ weighted average of $U_\nu(L_\beta)\times F'_\nu(LI_fI_i)$, in the notation of this author. The U_ν give the attenuation due to a beta transition of multipolarity L_β, while the F'_ν involve the nuclear spins, vector coupling coefficients, and the gamma multipole mixing ratio, δ

[2] D. D. Hoppes, Technical Note #93, NBS Aug. 1961.

[3] C. F. M. Cacho, M. A. Grace, C. E. Johnson, A. C. Knipper, R. G. Scurlock, and R. T. Taylor, Phil. Mag. **46,** 1287 (1955).

[4] E. Ambler, R. P. Hudson, and G. Temmer, Phys. Rev. **97,** 1212 (1955).

[5] Nuclear Data Sheets, National Research Council, NRC 58–10–81 (National Academy of Sciences, Washington, D.C.)

[6] D. de Klerk and R. P. Hudson, J. Res. NBS **53,** 173 (1954).

[7] H. Meyer, Phil. Mag. **2,** 521 (1957).

[8] C. E. Johnson and H. Meyer, Proc. Roy. Soc. **A253,** 199 (1959).

[9] C. S. Wu, E. Ambler, R. W. Hayward, D. D. Hoppes, and R. P. Hudson, Phys. Rev. **105,** 1414 (1957); R. W. Hayward and D. D. Hoppes, IRE Trans. on Nuclear Science (IRE, New York, 1958) NS**5** No. 3.

[10] A. Bogle, A. H. Cooke, and S. Whitley, Proc. Phys. Soc. **A64,** 931 (1951).

[11] Private communication from C. E. Johnson to E. Ambler (1960).

[12] See, for example, E. Ambler Methods of nuclear orientation, Progress in Cryogenics, **1960,** p. 272.

[13] A. T. Nelms, NBS Circular 542, Aug. 28, 1953, p. 19.

[14] C. E. Johnson, J. F. Schooley, and D. A. Shirley, Phys. Rev. **120,** 2108, (1960).

[15] R. W. Kedzie, M. Abraham, and C. D. Jeffries, Phys. Rev. **108,** 54 (1957).

[16] B. R. Judd and I. Lindgren, Phys. Rev. **122,** 1802 (1961).

[17] J. N. Haag, C. E. Johnson, D. A. Shirley, and D. H. Templeton, Phys. Rev. **121,** 591 (1961).

[18] R. J. Elliot and K. W. H. Stevens, Proc. Rev. Soc. (London) **A215,** 437 (1952).

[19] R. W. Hayward, A. T. Hirshfeld, D. D. Hoppes, and R. S. Kaeser (to be published).

(Paper 66A4–165)

JOURNAL OF RESEARCH of the National Bureau of Standards—A. Physics and Chemistry
Vol. 66A, No. 4, July–August 1962

Light Source for Producing Self-Reversed Spectral Lines

Jack Sugar

(March 26, 1962)

A new light source has been developed which produces numerous self-reversed lines in both the first and second spectra of rare-earth elements. It consists of a pulsed arc discharge with a peak current of 75 amperes and an on-time of one millisecond per cycle. Resonance lines are nearly completely absorbed, and can be distinguished by this character. From spectrograms obtained with this light source, the ground states of Tb I and U II were determined, and those reported for Yb I, Yb II, Tm I, Tm II, and U I were confirmed.

1. Introduction

In atomic emission spectra, the presence of self-reversed spectral lines provides valuable information for the analysis of spectral structure. Because such lines generally arise from transitions to the ground state or to low-lying states of the atom, they may be used to deduce this important part of the energy level structure. In searching for regularities in a line-list containing tens of thousands of entries, as do those of most rare-earth elements, it is a great simplification to recognize a small group of lines which have energy levels in common.

In the past, at least three different light sources have been employed for observing the lines that are most readily absorbed or reversed; they are (1) the high-temperature furnace, (2) the underwater spark, and (3) the d-c arc.

(1) A. S. King developed the technique of obtaining atomic absorption lines by photographing a continuous spectrum which has passed through an electrically heated carbon tube containing metal vapor. An early example of his work is the description of the absorption spectrum of chromium [1].[1] However, as a result of the relatively low temperature limitation on the absorbing vapor, only very low-lying levels of the neutral atom, and in general no ionic levels, are sufficiently populated to produce absorption lines. Furthermore, metals with very high boiling points will not yield to this technique.

(2) Spectral phenomena observed when high-voltage condensed sparks are passed between metallic electrodes submerged in water have been investigated for more than half a century. It was found that the dissociation of water produces a continuum in which a small fraction of the spectral lines characteristic of the metal vapor are absorbed. An example of the application of this technique to the determination of atomic energy levels is the study of the underwater absorption spectra of the palladium and platinum triads by W. F. Meggers and O. Laporte [2]. The main difficulties with this technique arise from the presence in some spectral regions of absorption bands due to water molecules, the superposition of metallic spark lines in emission, and the total absence of absorption for certain metals, presumably because of instant oxidation.

(3) A d-c arc discharge with a current of several amperes nearly always produces self-reversal of the very strong lines in the spectrum of the electrode material by absorption in the sheath of cool vapor surrounding the discharge. The degree of self-reversal increases exponentially with the product of the intensity of the radiation and the number of absorbing atoms through which it passes [3].

The spectra of rare-earth elements are characteristically lacking in lines of outstanding high intensity. Therefore, they rarely contain self-reversed lines in the low-current arc. It has been found that by raising the current in the arc, one usually enhances self-reversal because of the increased rate of vapor production. This increases the density of absorbing atoms surrounding the discharge. A substantial rise in current, however, will generally melt the electrodes unless adequate cooling is provided. A convenient method for obtaining a cool, high-current arc is described in this paper.

2. Apparatus

A square current pulse of short duration and high ampereage may be obtained by discharging a delay line through a matching load impedance. This may be employed to produce a pulsed high-current arc by placing the electrode gap in series with the load. If a suitable pulse width and repetition rate is selected, the average current can be kept low enough so that no cooling is required to prevent the electrodes from melting.

A diagram of the electrical circuit used in this experiment is given in figure 1. A delay line consisting of five stages with a capacitance of 20 μf and an inductance of 500 μh per stage was charged to 400 v. The rotating shorting bar in series with the load was employed to close the output circuit,

[1] Figures in brackets indicate the literature references at the end of this paper.

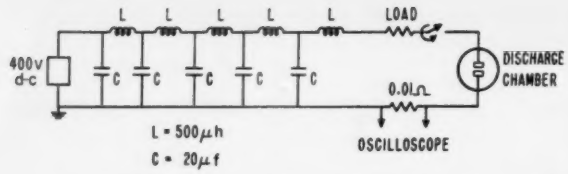

FIGURE 1. *Electrical circuit for obtaining pulsed arc discharge.*

discharging the delay line through the arc chamber. The proper load resistor was determined by observing the voltage waveform across the 0.01 ohm resistor with an oscilloscope. Too little resistance results in an oscillating discharge, while too much causes a distorted pulse shape. With the above circuit values, the load was about 2 ohms, and a square pulse of 75 amp peak and 1 msec duration was obtained.

A repetitive rate of 10 per second gave an average current of only 0.75 amp while providing a strong exposure in about 5 to 10 min in the wavelength range 2400 to 7000 A. The spectrograms were made with a Wadsworth mounting of a 4 x 2 in. concave grating having a 21 ft radius and 30,000 grooves per in.

The discharge chamber contained helium at a pressure of 1 atm. The operation of this arc in an inert atmosphere prevents the oxidation of metal vapor so that an absorbing layer can be maintained. Furthermore, the presence of highly energetic helium metastable atoms favors the production of metallic ions so that strong absorption is exhibited by these ions as well as by the neutral atoms.

A gap of about 2 mm was maintained between the electrodes.

3. Observations

The spectra of ytterbium, thulium, uranium, and terbium were obtained with the pulsed arc. Portions of each of these are shown in figure 2, where the self-reversed lines are indicated by a dot and the resonance lines of the neutral and singly-ionized atom are further designated by R_I and R_{II}, respectively. Numerous self-reversed lines appeared among the first spectrum lines of each of these elements and among the second spectrum lines of all but uranium, which contained only two. The resonance lines of the neutral atoms are clearly distinguished by their appearance as broad absorption lines against a continuous background.

3.1. Ytterbium

The first observations with this light source were made with ytterbium electrodes. Both the first and second spectra of this element have been extensively analyzed by W. F. Meggers, although only a small portion of the level structure has been reported[4].

Meggers compared these spectrograms with his Yb line-list and found that 23 lines of the first spectrum and 39 of the second spectrum were self-reversed. The highest level giving rise to self-reversed lines was at 19,710 cm^{-1} in Yb I and at 35,832 cm^{-1} in Yb II.

Figure 2 shows the characteristic appearance of resonance lines in the first and second spectra of ytterbium. Both have wide gaps in the center of the emission line, but the wings of the Yb I line at 3464 A are almost completely absorbed. This shape appears to be characteristic of first spectrum resonance lines and can serve as a means of identifying them. The width of the self-absorbed center of this line was about 0.5 A.

3.2. Thulium

The absorption spectrum of thulium has been observed by L. F. H. Bovey and W. R. S. Garton in an electric furnace operated at 2400 °C[5]. They found 88 absorbed lines in the wavelength range 2600 to 6000 A which they interpreted as belonging to Tm I. However, a comparison with the partial analysis of Tm II reported by Meggers[6] reveals that 23 of these belong to this spectrum.

The spectrum obtained with the pulsed arc in the wavelength range 2300 to 7000 A contained 120 self-reversed lines of Tm I and 126 of Tm II. In Tm I only the ^2F ground term and 16 higher levels have been reported by W. F. Meggers [6]. Every line which he designated as arising from a transition to the $^2F_{7/2}$ ground state gives the appearance of a broad absorption line. However, there were seven more lines with the same character which could not be paired with a second line whose wave number difference equals the ^2F interval. These have been classified by Meggers as originating from upper levels with $J=9/2$ and, as such, can only combine with the $^2F_{7/2}$ ground state.

The line at 3916 A is due to a transition to the $^2F_{5/2}$ level at 8771 cm^{-1} above the ground state. Although the absorbed center of the line is wide, the wings are strong and serve to distinguish these strongly self-reversed lines from the resonance lines.

The low $^3F_{4,3,2}$ and $^1F_3$ levels of Tm^+ (the ground state is $^3F_4$) were also found by Meggers [6]. Sixty-five self reversed lines of Tm II are classified, among which are all but four lines of intensity greater than 50. This is a verification that the lines are correctly assigned. Meggers accepted only those upper levels which combined with three low levels. By using the self-reversed lines, the analysis can confidently be extended to include upper levels which combine with only two low levels. Also, upper levels making only one combination with a ^3F level (because of the selection rule on J) can be confidently determined if the Zeeman pattern is correct and if the line is self-reversed.

3.3. Uranium

The spectrum of uranium in the range 2300 to 7000 A contained 100 self-reversed lines of U I and only 2 of U II. The absorbed central portions of the lines were much narrower than those of any of

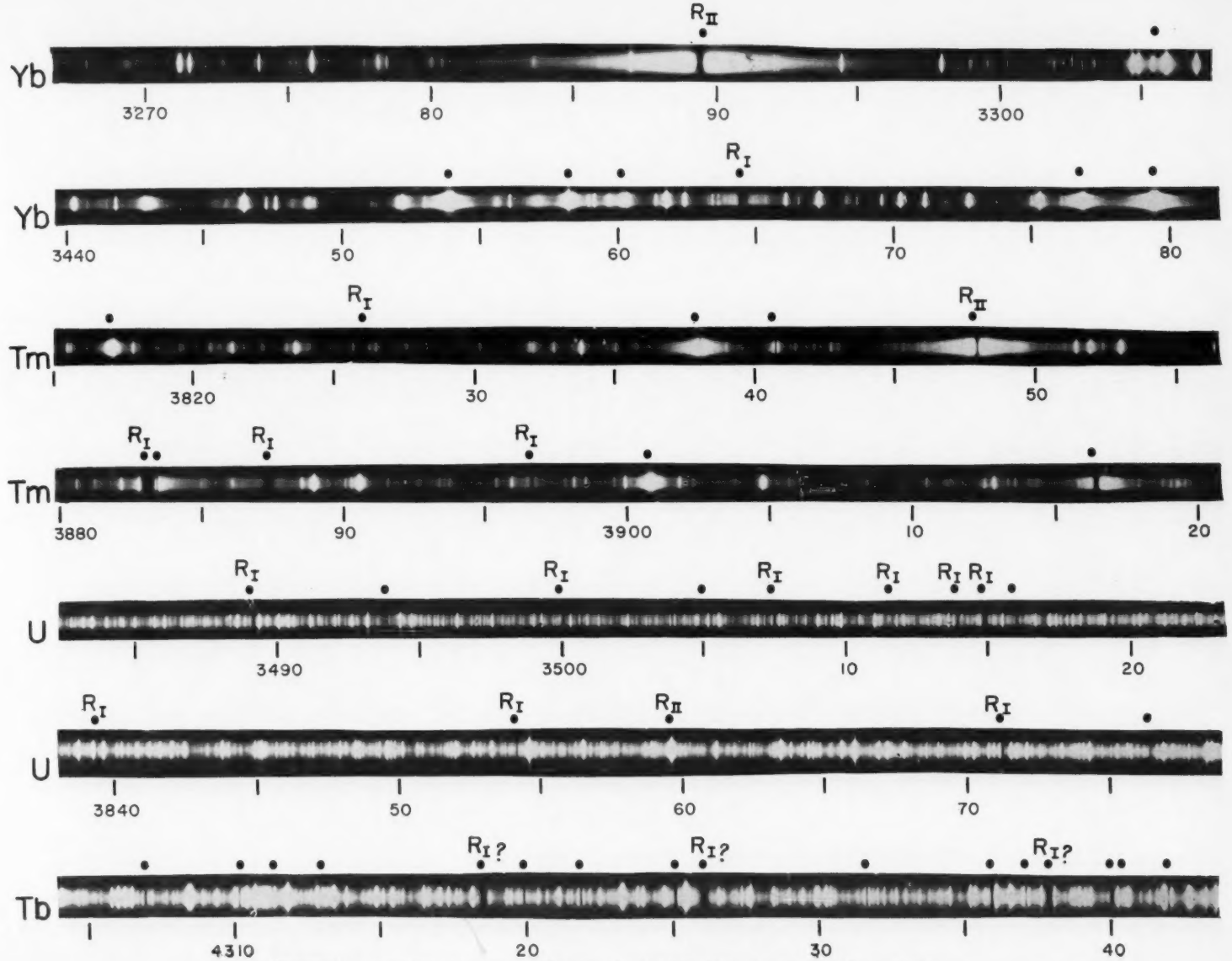

FIGURE 2. *Portions of spectra of* Yb, Tm, U, *and* Tb *obtained with pulsed arc discharge.*
Self-reversed lines are indicated by a dot. R_I and R_{II} are resonance lines of first and second spectra.

the other elements observed, although practically complete absorption of resonance lines was still present. None of these self-reversed lines classified by Kiess, Humphreys, and Laun [7] arise from transitions to levels higher than 3801 cm^{-1}. However, many self-reversed lines are not classified, including resonance-type lines.

Recently a few U I lines were observed in absorption with a King-type furnace by N. P. Penkin and S. E. Frish [8].

In U II, two independent sets of energy levels are known. Neither of these has been established as the lower group. A listing of the levels and classified lines is given in a paper by Van Den Bosch [9], in which the two groups are referred to as A and B.

The relative intensity tables of Meggers, Corliss, and Scribner [10] give the three leading strong lines of U II as 3859, 3854, and 3670 A with intensities 360, 180, and 160, respectively. The first and third of these are due to transitions in group B to levels at 289 and 915 cm^{-1}, and are the only self-reversed lines in U II. The second line arises from a transition to the lowest level of group A. Because self-reversal depends on the product of the radiation intensity and the population of the absorbing energy level [3] for lines of approximately the same wavelength, the lowest level of group A must be higher than the 915 cm^{-1} level of group B. The ground state of U II is therefore the $^4I_{9/2}$ level of the $5f^36s^2$ configuration in group B. No resonance lines of U II are self-reversed because they are too weak, the strongest having an intensity [10] of 120.

The relatively weak self-reversal of uranium lines reflects the high boiling temperature of this element compared with those of the lanthanide series.

3.4. Terbium

Aside from a preliminary proposal by P. F. A. Klinkenberg [11] no analysis of the terbium spectrum has been published, but J and g values for a group of Tb I lines have been reported by S. Davis [12]. This spectrum was observed with the present light source to see whether any of the lines exhibiting very wide self-reversal had been analyzed by Davis.

About 400 lines in the region from 2300 to 7000 A showed self-reversal. Three of these strongly resemble resonance-type lines, with the emission lines almost completely absorbed. They appear in figure 2 at 4318, 4326, and 4338 A. Only the line at 4338 A has been assigned J and g values: $g_1=1.331$ $g_2=1.397$, $J_1=15/2$, $J_2=13/2$.

In pure LS-coupling the g-value for a $^6H_{15/2}$ term is 1.333, and for a $^6G_{13/2}$ term is 1.385. The most probable lowest configuration of Tb I is either $4f^96s^2$ or $4f^85d6s^2$. These would yield the ground states $^6H_{15/2}$ and $^5H_{17/2}$, respectively, according to Hund's rule. The strong self-reversal and Zeeman observations for the 4338 A line indicate that the ground state of Tb I is $^6H_{15/2}$. Furthermore, the upper state should belong to the $4f^85d6s^2$ configuration since Davis reported no indication of hyperfine structure for this line, nor for the other two strongly self-reversed lines mentioned above. This suggests that the $6s$ shell is closed in both the upper and lower configurations.

This assignment is confirmed by Penselin and Schüpman [13] who observed the $^6H_{15/2}$ level by a magnetic resonance experiment, and obtained a g-value of 1.3225. Since they also detected other levels, they could not conclude that this is the lowest state of Tb I.

The other two resonance-type lines are probably transitions from the excited $^6H_{15/2}$ and $^6I_{17/2}$ levels.

4. Conclusion

An important need in the problem of analysis of rare-earth spectra is now satisfied by the development of a simple light source giving self-reversed lines. While the analysis can probably be done without it, the initial break into the level structure is much more easily obtained with such information. Because of the unique appearance of absorbed resonance lines in the light source under discussion, these observations can verify whether or not the ground state of an atom has been found. Also, the amount of self-reversal of lines of the same intensity was shown to be a valuable clue for determining which absorbing energy level is lower.

This light source also produced numerous self-reversed lines in the second spectra of most of the observed elements.

5. References

[1] A. S. King, Astrophys. J. **60,** 282 (1924).
[2] W. F. Meggers and O. Laporte, Phys. Rev. **28,** 642 (1926).
[3] R. D. Cowan and G. H. Dieke, Rev. Mod. Phys. **20,** 418 (1948).
[4] W. F. Meggers, J. Opt. Soc. Am. **50,** 1136 (1960).
[5] L. F. H. Bovey and W. R. S. Garton, Proc. Phys. Soc. **67,** 476 (1954).
[6] W. F. Meggers, Rev. Mod. Phys. **14,** 96 (1942).
[7] C. C. Kiess, C. J. Humphreys, and D. D. Laun, J. Research NBS **37,** 1 (1940) RP1729
[8] N. P. Penkin and S. E. Frish, Optika i Spek. **3,** 473 (1957).
[9] J. C. Van Den Bosch, Physica **15,** 503 (1949).
[10] W. F. Meggers, C. H. Corliss, and B. F. Scribner, Spectrochim Acta **17,** 1168 (1961).
[11] P. F. A. Klinkenberg, Physica **13,** 16 (1947).
[12] S. Davis, Astrophys. J. **132,** 486 (1960).
[13] S. Penselin and K. Schüpman, unpublished reference in article by Cabezas, Lindgren, and Marrus, Phys. Rev. **122,** 1797 (1961).

(Paper 66A4–166)

JOURNAL OF RESEARCH of the National Bureau of Standards—A. Physics and Chemistry
Vol. 66A, No. 4, July–August 1962

A Diamond Cell for X-ray Diffraction Studies at High Pressures

G. J. Piermarini and C. E. Weir

(April 5, 1962)

A high pressure X-ray powder camera has been constructed. The instrument has been found to be useful for routine X-ray work, using molybdenum radiation, to pressures of approximately 60 kilobars. Previously reported transitions have been observed in silver iodide, potassium iodide, bismuth, and thallium. The high pressure forms and lattice parameters were found to be: AgI—f.c.c. (NaCl type), $a_0=6.067$ A; KI—s.c. (CsCl type), $a_0=4.093$ A; Tl—f.c.c. (NaCl type), $a_0=4.778$ A; Bi structure not determined. These data confirm previous reports on the high pressure forms of AgI and KI. Data on Tl and Bi are apparently reported for the first time. The high pressure modifications were studied at the following approximate pressures which are not indicative of the point where the transition occurs: AgI—3.3 kilobars, KI—20 kilobars, Bi—28 kilobars, and Tl—60 kilobars.

The pressure limit to which the unit can be used successfully has not been ascertained. It is believed to be much higher than the pressures reported. The present instrument is capable of producing powder diffraction patterns of materials of relatively high scattering power, giving data to $2\theta=35°$. High background on the X-ray powder patterns is believed to arise from scattering by the diamonds. This background may obscure weak diffraction rings. This effect may be reduced by screening, monochromatization, and other improvements in experimental technique.

1. Introduction

There has beeen considerable interest in the structures of high pressure polymorphs ever since Bridgman's studies showed the frequency of occurrence of transitions at elevated pressures [1].[1] High pressure forms are not usually obtained by cooling at 1 atm, and in only a few instances appear to be obtainable in a metastable condition at 1 atm. McFarlan [2, 3] used this method of determining the X-ray structure of certain of the high pressure forms of ice. In general, it appears that the structures of the high pressure polymorphs can be studied only at high pressure. The first successful attack on this problem appears to have been made by Jacobs [4, 5] who obtained powder patterns of high pressure phases with a camera enclosed in the pressure vessel. He used helium gas as the pressure-transmitting fluid and a beryllium window to permit X-rays to enter the vessel. This method was used to a maximum pressure of 5 kilobars (1 bar$=10^6$ dynes cm^{-2}). The next marked advance appears to have been made by Lawson and his coworkers who constructed first a miniature beryllium pressure vessel [6] and later a miniature diamond pressure vessel [7]. The vessels were transparent to Mo K X-rays and the enclosed specimen could be studied. Using diamonds the maximum pressure attainable appears to have been approximately 30 kilobars. The diamond cell method was used by Jamieson [8, 9] for studies of high pressure polymorphs of geological interest. Jamieson later [10, 11] has reported a high pressure X-ray device using diamonds in an anvil-type squeezer. In this technique the flat specimen was loaded to a desired stress between two single crystal diamond pistons. This unit was designed to be mounted on the spindle of an X-ray diffractometer. A similar device is being studied by Adams [12]. Evdokimova and Vereshchagin [13] have used an externally supported beryllium pressure vessel to study the lattice parameters of strontium and barium to a maximum pressure of 15 kilobars.

Recently an infrared cell using diamonds in an anvil-type squeezer was developed in this laboratory [14] and used successfully for studies to pressures of 50 kilobars in a routine manner. The design of this cell has been modified to permit studies of X-ray powder diffraction patterns to pressures of at least 60 kilobars. This report describes the instrument and preliminary studies on a few materials of interest which serve to illustrate its range of application.

2. Apparatus

The high pressure X-ray camera is shown in cross section in figure 1. The unit contains a hardened steel entablature (E) and a piston (H) actuated by hydraulic pressure generated by means of an external hand pump and introduced through a fitting (M). The hydraulic liquid is confined to the small volume between the rubber O-rings (J) and exerts an axial thrust on the shoulder of the piston (H). The entablature (E) is supported by the thrust washer (C) and the cap (B) which screws on to the unit. Both the entablature and the piston are fitted with small brilliant-cut gem-quality diamonds (F) each weighing approximately 0.03 g (or 0.15 carats). The

[1] Figures in brackets indicate the literature references at the end of this paper.

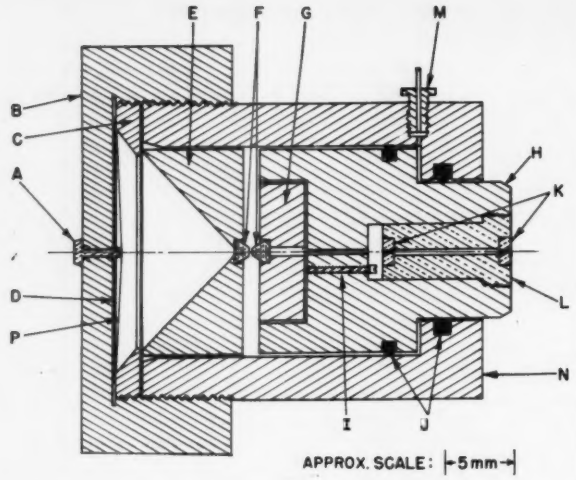

FIGURE 1. *Cross section of high pressure X-ray powder camera.*

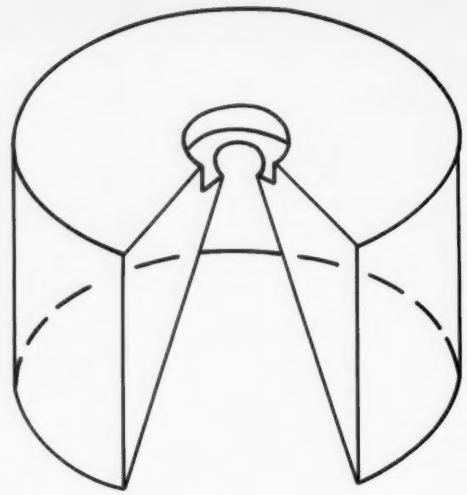

FIGURE 2. *Details of entablature.*

diamonds are seated on their table faces in small close-fitting recesses. The diamond in the piston is seated in a small cylindrical insert (G) which fits into the piston. The culets of both diamonds were ground off to produce small flat surfaces parallel to the tables. The flat-topped steel screw (I) in the piston is one of three such screws spaced 120° apart about the axial hole of the piston to facilitate alinement of the flat surfaces of the two diamonds when necessary. The X-ray beam enters through the collimating pinholes, 0.014 in. in diameter, which are contained in the brass inserts (K). The small axial hole in the piston (H) acts as a guard slit which eliminates diffraction lines originating in the pinholes.

In use zirconium-filtered molybdenum radiation traverses both diamonds and the film of powder compressed between the diamond surfaces. Diffraction rings from the powdered specimen diverge through the diamond in the entablature and are recorded on the film (D), placed inside the cap and held securely between cap and thrust washer. In all experiments the film is covered with a light-protective paper (P). A small beam stop (A) is inserted through the cap and secures the film at the center. The entablature is machined out to produce a conical surface of semivertex angle of approximately 45°.

From figure 1 it is apparent that the specimen is not located within the cone obtained by extending the inner conical surface of the entablature that is designed to serve as the exit aperture. The distance from the specimen to the apex of this cone for a given entablature, is determined by the thickness of the diamond. In these experiments the diamond is of such thickness that the specimen is always above the apex of the cone and the effective aperture is defined by the cone formed by the specimen and the aperture in contact with the diamond table surface. Under the experimental conditions used here, diffraction rings with $2\theta > 20°$ are not transmitted. Two solutions to this problem were attempted. First the diamond was made thinner thus bringing the specimen plane within the cone formed by extending the conical surface of the entablature. For low pressure work this was found to be useful. High pressures could not be obtained in this manner because of the reduction in the strength of the diamond. Second, a wedge was cut out of the entablature (see fig. 2). This permitted higher-angle rings to be diffracted through the wedge up to $2\theta \approx 35°$. However, a portion of the diamond seat and retaining wall were removed by this process, and at high stresses some lateral motion of the diamond was observed. A less radical procedure consisted in removing only a small portion of the diamond seat and leaving the girdle-retaining wall intact. By using a hardened steel entablature in this manner, measurements have been made to pressures of at least 60 kilobars with no evidence of motion of the diamond. The photographs under these circumstances show the higher angle rings as arcs while those of lower angle appear as complete circles. The complete rings permit centering the film for measurement of the diameters of the arcs.

In figure 1 it will be noted that the pressure must be released before the photographic film can be removed for processing. Another short-coming is associated with the inconveniently short specimen-to-film distance. Greater precision in the measurement of the diffraction-ring diameters can be achieved by increasing this distance. A bell-shaped film enclosure was made for optional use to permit locating the film at distances of from 30 mm to 75 mm from the specimen (see fig. 3). This closure (R) screws onto a modified cap (S) which is bored out to permit exit of the diffraction rings. The modified cap contains a thrust washer (T). A cylindrical spacer (U) provides a shoulder on which the film plate (V) containing the film (X) and light-protective paper (Y) rests. The film and paper are held fixed

by the taut beam stop (W) and film plate (V). This entire unit shown in figure 3 replaces the retaining cap (B) and thrust washer (C) shown in figure 1. To change the film the bell-shaped enclosure (R) is unscrewed from the retaining cap (S) and taken as a unit to the dark room. The film plate (V) is unscrewed from the bell-shaped housing. The film is removed from the film plate by unscrewing the beam stop (W). This arrangement permits repeated exposures at constant pressure, and also allows diffraction patterns to be obtained with different pressures without the necessity of releasing the pressure between runs.

Both arrangements have desirable characteristics. In this study the latter modification was usually preferred because the resulting larger X-ray powder pattern was easier to analyze. The error in the diffraction ring measurement was thereby reduced. Although the longer specimen-to-film distance increases accuracy, it also increases exposure time required 4-fold. The increased exposure time is undesirable because prolonged periods of high pressure on the specimen have been suspected of causing small cracks to develop in the pressure surface of the larger faced diamond. The cracks may have developed because of poor alinement of the two diamond pressure surfaces. Experience [14] has shown that better alinement reduces the cracking tendency and increases the useful life of the diamonds considerably. One set of diamonds with properly alined pressure surfaces, for example, was used daily for about a month to compress materials to pressures up to 30,000 bars before one of the diamonds developed very shallow cracks approximately 0.05 mm long. Even with these flaws the set of diamonds continued to perform satisfactorily. On continued use, however, the cracks increased in size and in the study of bismuth some material was forced into these cracks. The bismuth apparently was not removed by the cleaning technique employed, and as a result, in the subsequent study of potassium iodide at 20 kilobars, there was interference from bismuth in the X-ray powder pattern. This problem is considered further in the discussion of potassium iodide.

In all experiments pressures were generated by means of a commercial hand pump using oil as the hydraulic liquid. The pressure was measured with a bourdon-tube gage. A valve was mounted in the liquid line between the pump and the gage so that the pressure cell and gage could be isolated from the pump during exposures. The dimensions of the unit and the diamond surface areas are such that the hydraulic pressure is magnified by a factor of approximately 500. Thus to achieve a pressure of 60 kilobars on the specimen a liquid pressure of approximately 120 bars is required.

3. Method

The materials studied were silver iodide, potassium iodide, bismuth, and thallium. They were selected because: (1) the pressures at which their known transitions occur cover a wide range [1, 15], and (2) structural data on silver iodide and potassium iodide are available for comparison [4, 5, 9]. The materials were commercially available chemicals and were used in this study with no further purification. Silver iodide consisted initially of a mixture of the hexagonal and cubic forms and was converted predominantly to the metastable cubic form by grinding vigorously for about ½ hr [16].

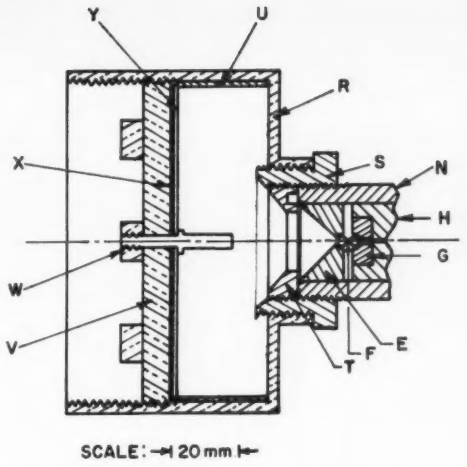

FIGURE 3. *Cross section of modified film enclosure.*

About 5 mg of the powdered material was placed on the face of the diamond in the fixed piston. The material on the surface of the diamond was tamped lightly with a spatula. Some adhered to the diamond face; the excess was removed. The small patch of material remaining on the diamond face served as the sample. The thallium specimen, however, was not prepared in this manner. Instead, a thin film of freshly sliced metal was placed between the two diamond pressure faces and quickly compressed to minimize contact with the air.

The entablature containing the specimen was inserted in the piston housing of the mounted and alined camera. The retaining cap containing the film, the light-protective paper, and the thrust washer was screwed on tightly. A pressure of 500 bars was slowly applied to the specimen to create a uniform film and also to bring all moving components into their proper positions. The pressure was reduced over a 5 min period to a value just greater than atmospheric pressure. By keeping a slight positive pressure on the specimen, all the moving components in the camera were properly positioned. The X-ray powder patterns of the low pressure phases were obtained under these conditions.

The X-ray powder patterns of the high pressure form were obtained as follows. After the low pressure pattern was obtained, new film was placed in the camera and the pressure was raised to a value approximately 20 percent above the transition pressure determined by Bridgman [1, 15] for the specimen being studied. The pressure was then reduced

slowly to a value slightly greater than the reported value for the transition. The reduction in pressure was carried out slowly over a period of 5 min. The high pressure powder pattern was then obtained.

It must be emphasized that there was no effort made to determine accurate transition pressures for these materials. The object was to determine if a transition could be detected by this technique, and what structurally significant crystallographic data could be obtained. The pressures were calculated from the fluid pressure, the force on the sliding piston, and the area of the smaller of the two diamond pressure surfaces.

The nature and accuracy of the pressures calculated from the load applied and the area of the smaller diamond surface have been discussed previously in connection with the infrared cell [14]. In the spectroscopic studies it was noted that the observed transition of sodium nitrite near 15 kilobars agreed with previously reported data within the experimental error. Additional experiments were performed to determine the initial appearance of the bismuth transition in the present apparatus. These studies showed that the transition was first noted between calculated pressures of 19.5 and 21.0 kilobars, values which are considerably lower than the pressure of approximately 25 kilobars reported by Bridgman [1]. The discrepancy between the spectroscopic and X-ray results has not been investigated but is believed to arise predominantly from errors arising in this work. Significant errors in pressure may be caused by the following factors: (1) The magnitude of the pressure gradients and the effect of the topography of the diamond surfaces on the gradients; (2) the effect of alinement errors on the pressure gradients; and (3) the effect of the film thickness and shear strength of the specimen. It is believed also that the effective area of the smaller diamond used here is somewhat less than the measured area because of departures of its surface from optical flatness.

The specimen-to-film distance was determined by calibration and also by measurement. In the calibration technique, a powder pattern obtained under the conditions specified above for the low-pressure phase study, was used to calculate the specimen-to-film distance using "*d*"- spacings obtained by Swanson et al., [17]. The calculated value, which differed only slightly from the measured value, was used in the interpretation of the powder patterns of the high pressure phases. A check on the specimen-to-film distance was made to determine if any permanent distortion occurred after application of high pressure. This was done by calibrating the instrument before and after high pressures had been applied. No significant change was observed. The diameters of the diffraction rings were measured to 0.05 mm with a hair-line type instrument. The incomplete rings were measured by a difference technique with reference to a complete inner ring.

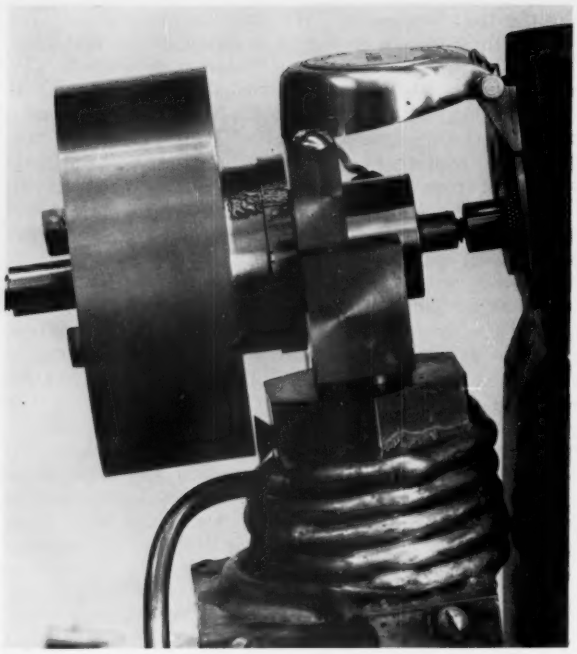

FIGURE 4. *Photograph of modified high pressure X-ray powder camera in operation.*

Silver iodide was studied using the original design of the instrument, which prevented film replacement unless the pressure on the specimen was released. For this arrangement a specimen-to-film distance of 16.13 mm was calculated. Using zirconium-filtered molybdenum radiation (45 kv and 20 ma), a film exposure of 1 hr was required for a satisfactory powder pattern. The remaining materials were studied with the modified instrument described earlier in this report. This camera had a 52.6 mm specimen-to-film distance and required an exposure of 4 hr with the same radiation source. A photograph of the latter instrument in operation is shown in figure 4.

4. Results

4.1. Silver Iodide

Two halves of X-ray powder patterns of silver iodide obtained with this camera are shown in figure 5. The left half refers to material studied at approximately 1 bar; the right half to material studied at approximately 3,300 bars. The two films were split and matched for easy comparison. Except for pressure the experimental conditions in both exposures were the same. Diffraction rings are clearly visible and a transition is quite apparent. This is expected because Bridgman [15] showed that silver iodide exhibits a transition at about 3,000

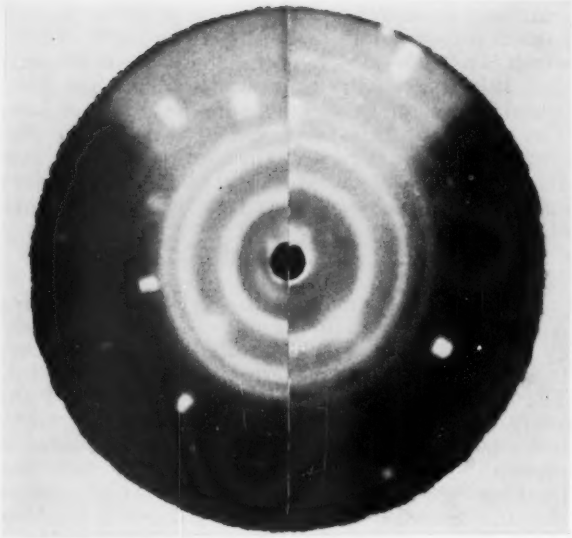

FIGURE 5. *Matched halves of X-ray powder patterns of* AgI (*left half,* AgI *at approx. 1 bar; right half,* AgI *at approx. 3.3 kilobars*).

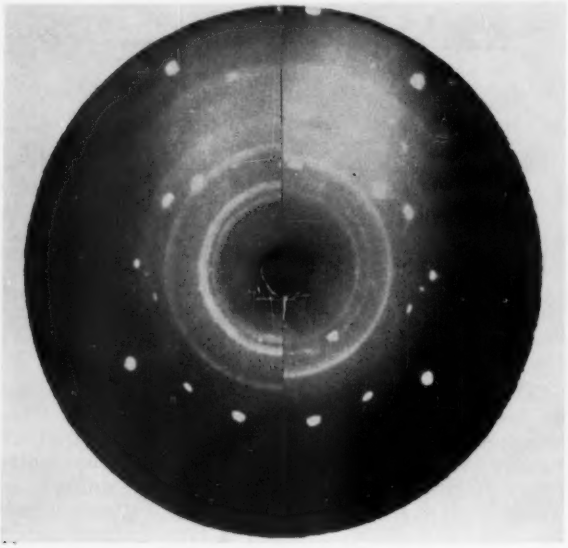

FIGURE 6. *Matched halves of X-ray powder patterns of* KI (*left half,* KI *at approx. 1 bar; right half,* KI *at approx. 20 kilobars*).

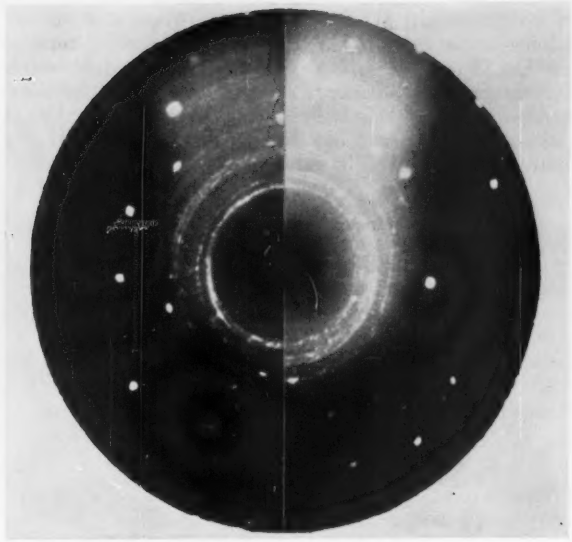

FIGURE 7. *Matched halves of X-ray powder patterns of* Bi (*left half,* Bi *at approx. 1 bar; right half,* Bi *at approx. 28 kilobars*).

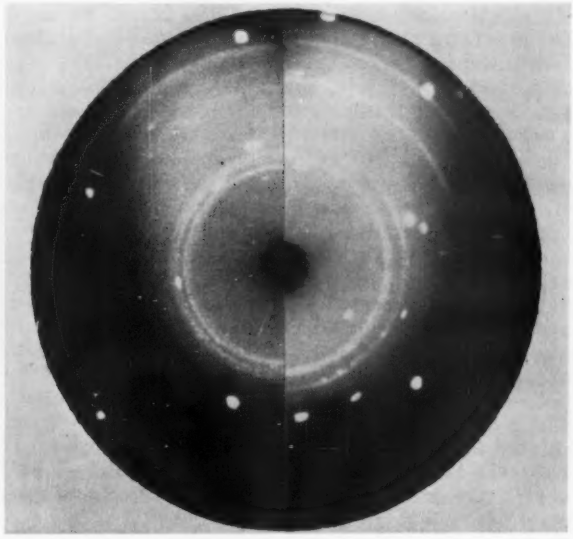

FIGURE 8. *Matched halves of X-ray powder patterns of* Tl (*left half,* Tl *at approx. 1 bar; right half,* Tl *at approx. 60 kilobars*).

bars. The incomplete rings are due to the wedge cut-out in the entablature. A close examination of the film indicates no evidence of low-pressure material contributing to the powder pattern on the right. It follows that the minimum pressure in the region penetrated by the radiation beam was less than approximately 300 bars below the calculated pressure. The importance of pressure gradients is recognized in determining the pressure on the specimen. The spots on the film are Laue spots originating from the two diamonds.

The six rings in the high pressure phase pattern were readily indexed as face-centered cubic (see table 1). The high pressure form has the halite-type structure containing 4 molecules per unit cell. Comparison of these results with those obtained by Jacobs [4] shows good agreement. His average lattice constant is 6.070 A. The calculated density

of silver iodide III based on the present 6.067 A lattice constant obtained at 3,300 bars is 6.98 g cm^{-3}. The total volume change calculated between 1 bar and 3,300 bars including the transition AgI—II→AgI—III is 18.5 percent. Using Bridgman's data [15] the corresponding volume change is estimated to be 18 percent.

TABLE 1.—*"d"-Spacings and lattice constants of AgI at approximately 3.3 kilobars*

hkl	*"d"*-Spacings, A	Lattice constant, A
200	3.031	6.062
220	2.158	6.103
222	1.764	6.110
400	1.507	6.028
420	1.352	6.046
422	1.241	6.080
Statistical average of lattice constant		6.067*
Standard deviation		0.015

*See appendix.

4.2. Potassium Iodide

According to Bridgman [15] potassium iodide which normally exists in the NaCl type structure exhibits a transition at about 17,850 bars. Figure 6 demonstrates the transition. The modified instrument using a larger specimen-to-film distance was employed. Therefore, the films are different in appearance from those shown in figure 5. There are weak lines in these patterns which cannot be brought out more clearly by longer exposure because of a disproportionate increase in background. This background is believed due to scattering from the two diamonds. Results from this study are shown in table 2. The high pressure form was readily indexed as simple cubic, that is, the CsCl type structure. Satisfactory agreement with Jamieson's results [9] is obtained. He reported an average lattice constant of 4.13 A at 20,800 bars. Using the 4.093 A value obtained in these studies, the calculated density for potassium iodide II at approximately 20 kilobars is 4.02 g cm^{-3}. A volume change of 22.2 percent is calculated for potassium iodide over the pressure range 1–20,000 bars including the transition KI—I→KI—II. A corresponding value of 20 percent is estimated from Bridgman's data [15].

TABLE 2.—*"d"-Spacings and lattice constants of KI at approximately 20 kilobars*

hkl	*"d"*-Spacing, A	Lattice constant, A
100	4.037	4.037
110	2.902	4.103
111	2.361	4.089
200	2.056	4.112
210	1.829	4.090
211	1.670	4.090
Statistical average of lattice constant		4.093*
Standard deviation		0.008

*See appendix.

A close examination of the high pressure powder pattern reveals a diffraction ring (second from center) which is not due to potassium iodide. It is believed that this ring is due to bismuth which had been forced into some small cracks in the diamond face. The ordinary means employed in cleaning the diamond faces did not remove the material. Later, new diamonds were prepared and studies on potassium iodide with these new diamonds showed no evidence of this ring.

4.3. Bismuth

Initial studies on bismuth revealed a complex X-ray powder pattern for the material at approximately 28 kilobars. This is demonstrated in figure 7. Due to its complexity the pattern could not be indexed. The *"d"*-spacings obtained from the film on the right are listed in table 3. Upon examination, one strongly suspects that the room pressure hexagonal form is present. This is entirely possible. The fact that bismuth exhibits two very close transitions, one at about 24 kilobars, and the other at about 27 kilobars adds to the problem [18]. Both high pressure forms could conceivably be present simultaneously. Consequently, no conclusions were drawn about the high pressure form of bismuth at 28 kilobars. Further work to solve this problem is contemplated.

TABLE 3. *X-ray powder data for* Bi *at approximately 28 kilobars*

Angle, 2θ, degrees	*"d"*-Spacing, A
12.40	3.284
13.72	2.969
14.38	2.833
15.83	2.561
17.10	2.385
18.40	2.218
20.60	1.983
22.45	1.823

4.4. Thallium

Thallium exhibits a transition reported at about 40 kilobars [19]. Figure 8 demonstrates the transition, showing the high pressure form at approximately 60 kilobars. This phase has apparently never before been observed by X-ray diffraction. Table 4 gives the analysis of the high pressure pattern. It was readily indexed as face-centered cubic. Based on the lattice constant 4.778 A, a density of 12.44 g cm^{-3} for thallium at about 60 kilobars was calculated. The total volume change calculated including the transition $Tl_{h.c.p.} \rightarrow Tl_{f.c.c.}$, is 5.0 percent. The corresponding volume change based on Bridgman's data [19] is estimated to be 10 percent.

The results of this study corroborate two predictions which have been made for the high pressure form of thallium. Based on the correlation of thermodynamic data at one atmosphere with high pressure equilibria, Kaufman [20] has predicted a face-centered cubic structure for thallium. A similar prediction has been made by Parthe [21] using a space-filling concept.

TABLE 4. *"d"-Spacings and lattice constants of* Tl *at approximately 60 kilobars*

hkl	"d"-Spacing, A	Lattice constant, A
111	2.731	4.730
200	2.391	4.782
220	1.689	4.776
311	1.442	4.783
222	1.383	4.791
Statistical average of lattice constant		4.778*
Standard deviation		0.008

*See appendix.

5. Appendix

It is desirable to weight the data statistically to obtain a more significant value of the lattice parameter. This is particularly important in these experiments because the diffraction rings are limited to low angles. The following method was used to determine the average lattice parameter and its standard deviation:

If r represents the radius of a given ring, D the specimen to film distance, and 2θ the diffraction angle, then when

$$r<D \text{ (as in these experiments) } \sin\theta\approx\frac{r}{2D}. \quad (1)$$

If the experimental error in measurement is ϵ, then $\epsilon_{\sin\theta}=\frac{\epsilon_r}{2D}$, where the subscripts denote the quantities to which the error refers. The error in the radius measurement is not a function of r.

The Bragg relationship for the spacing including the error term is, $\sin\theta=\frac{\lambda}{2d}+\frac{\epsilon_r}{2D}$, where d is the interplanar spacing and λ the wavelength.

For the cubic system, this may be written in terms of the lattice parameter, a_0, and the Miller indices, h, k, l, as

$$2D\sin\theta=\frac{D\lambda\sqrt{h^2+k^2+l^2}}{a_0}+\epsilon_r. \quad (2)$$

(Paper 66A4–167)

Equation (2) contains a relationship between the two variables $2D\sin\theta$ and $D\lambda\sqrt{h^2+k^2+l^2}$ representing a line through the origin of slope $1/a_0$. The best value of a_0 was determined by least squares and the standard deviation by well-known methods (for example, see p. 42 of "Statistical Methods for Chemists" by W. J. Youden, John Wiley & Sons, New York, N.Y., 1951).

The authors are indebted to the Institute of Geophysics of the University of California at Los Angeles for the use of their facilities in the preliminary developments of the X-ray camera. In particular, the assistance and advice of L. H. Adams and W. Hoffman are greatly appreciated. The authors are also indebted to J. Mandel of the National Bureau of Standards staff for advice on the statistical evaluation of the lattice parameters.

6. References

[1] P. W. Bridgman, The physics of high pressure (G. Bell & Sons Ltd., London, 1952) ch. VIII.
[2] R. L. McFarlan, J. Chem. Phys. **4,** 60 (1936).
[3] R. L. McFarlan, J. Chem. Phys. **4,** 253 (1936).
[4] R. B. Jacobs, Phys. Rev. **54,** 325 (1938).
[5] R. B. Jacobs, Phys. Rev. **54,** 468 (1938).
[6] A. W. Lawson and N. A. Riley, Rev. Sci. Instr. **20,** 763 (1949).
[7] A. W. Lawson and T. Y. Tang, Rev. Sci. Instr. **21,** 815 (1950).
[8] J. C. Jamieson, Z. Krist. **107,** 65 (1956).
[9] J. C. Jamieson, J. Geol. **65,** 334 (1957).
[10] J. C. Jamieson, A. W. Lawson, and N. D. Nachtrieb, Rev. Sci. Instr. **30,** 1016 (1959).
[11] J. C. Jamieson, in "Progress in very high pressure research" (Proceedings of an international conference held at Bolton Landing, Lake George, New York, June 13–14, 1960, John Wiley & Sons, Inc., New York, N.Y., 1961).
[12] L. H. Adams (private communication).
[13] V. V. Evdokimova and L. F. Vereshchagin, Soviet Physics Solid State. English Translation **2,** 1539 (1961).
[14] C. E. Weir, E. R. Lippincott, A. Van Valkenburg, and E. N. Bunting, J. Research NBS **63A,** 55 (1959); Spectrochim. Acta **16,** 58 (1960).
[15] P. W. Bridgman, Proc. Amer. Acad. of Arts and Sci. **76,** 1 (1945).
[16] N. H. Kolkmeijer and J. W. A. van Hengel, Z. Krist. **88,** 317 (1934).
[17] H. E. Swanson et al., Standard X-ray diffraction powder patterns, NBS Cir. 539, Vol. 1–10.
[18] F. P. Bundy, Phys. Rev. **110,** 314 (1958).
[19] P. W. Bridgman, Phys. Rev. **60,** 351 (1941).
[20] L. Kaufman, Acta Met. **9,** 896 (1961).
[21] E. Parthé, Z. Krist. **115,** 1/2. 52 (1961).

JOURNAL OF RESEARCH of the National Bureau of Standards—A. Physics and Chemistry
Vol. 66A, No. 4, July–August 1962

Thermal Conductivity of Gases. I. The Coaxial Cylinder Cell[1]

Leslie A. Guildner

(April 13, 1962)

By combining appropriate geometric configuration and mathematical analysis with improved measuring techniques, the cell constant of a coaxial cylinder thermal conductivity cell was determined within 0.1 percent.

An analysis of the rate of heat transfer in such a cell showed a way to treat the data so that the error contribution of experimental deviations from idealized conditions is kept small. The principal considerations are:

1. That heat transport by convection is significantly large in a dense gas. This transport was analyzed mathematically from basic principles. The agreement of experimental results with the analysis indicated that the expressions are valid and that the convective heat transport could be accounted for with little more error than was involved in the precision of the heat transfer measurements.

2. That the heat transfer in a vacuum corresponds to the heat transfer by radiation and solid contacts in the presence of a gas. The uncertainty was that associated with the accuracy of determining the vacuum values.

3. That other effects were small enough to be computed and corrected for without increasing the uncertainty of the values of the thermal conductivity.

1. Introduction

The coaxial cylinder thermal conductivity cell, with large diameter of inner cylinder relative to the conductivity gap width, is one of the forms of apparatus often used to determine the thermal conductivity of gases. Over a period of several years, refinements were made in the design of a cell, in the analysis of heat transfer, in measurement techniques and in the treatment of the data. It is the purpose of this paper to set forth a summary of considerations which are applicable to measurements with a cell of this general type.

The heat guards at the ends of a coaxial cylinder cell can be designed so that the geometric form of the conductivity gap is simple. It is then possible to make a reliable mathematical analysis of the heat transfer by conduction. Consistent with a nearly exact mathematical analysis, special techniques were used for measuring the cell dimensions with improved accuracy.

At sufficiently high gas densities, convective heat transport becomes significant in a coaxial cylinder cell. When the axis of the cell is vertical, the heat transport by convection can be analyzed from basic principles. This analysis indicates the proper measurements to be made and the required treatment of the data.

Other effects which should be accounted for—asymmetry of the heat flow, radiation from the emitter and conduction through the mounting pins, and the temperature gradient in the body of the metal—are considered. The significance of these effects will be clearer after understanding some of the details of a cell, which will be described in the next section.

2. Apparatus

The cell shown in figure 1 was made of silver. It consisted of an emitter *EM*, surrounded by a receiver *RE*. The emitter was located by seven Pyrex pins

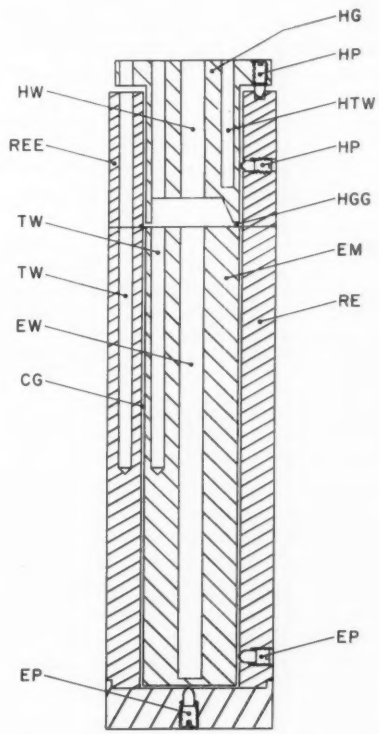

FIGURE 1. *Vertical cross section of coaxial cylinder cell.*

[1] This work was performed at the Massachusetts Institute of Technology and sponsored by Project SQUID, which is supported by the Office of Naval Research, Department of the Navy, under contract Nonr 1858(25) NR-098-038. Reproduction in full or in part is permitted for use of the United States Government.

637358—62——5

EP, one on the axis at the bottom, three spaced uniformly around the receiver near the bottom, and three (not shown) similarly spaced near the top. Electrical energy was supplied to the emitter by a heater in the heater well *EW*. The heater was made from Nichrome ribbon uniformly wound on a machined Grade "A" "Lava" form. The temperature or the temperature difference was measured by thermocouples inserted in the thermocouple wells *TW* of the emitter and receiver. The junctions were at two levels in the receiver and emitter, one level being midway along the emitter close to the bottom of the wells, and the other level just below the top of the emitter. The thermocouples were installed between the wall of the well and an inserted rod of silver. The thermocouple wires were insulated by thin sheets of mica, and they were packed tightly in the thermocouple wells.

A heat guard *HG* provided a continuation of the conductivity gap *CG*. It was positioned by six Pyrex pins *HP*, three spaced uniformly around the side and three around the top. The top pins were adjusted so that the width of the heat guard gap *HGG* was equal to the width of the conductivity gap. The heat guard temperature was maintained as close as possible to the temperature of the emitter, by introducing electrical energy from a heater in the heat guard heater well *HW*. The temperature was measured by a thermocouple whose junction was placed near the bottom of the heat guard thermocouple well *HTW*.

The leads from the emitter heater and the emitter and receiver thermocouples passed through the heat guard or the corresponding portion of the receiver, the receiver extension *REE*. (The receiver extension surrounding the heat guard was separate to facilitate assembly.) The thermocouple leads were insulated with mica and in order to improve heat transfer were held against the walls of the thermocouple wells, by means of a split rod of silver, which was wedge shaped.

The mounting pins were made in three parts: a Pyrex rod, 3 mm in diameter with a 60° included angle conical point, a pure aluminum holder, and a silver screw. The lengths of Pyrex and aluminum were chosen such that their composite expansion was close to that of silver over the temperature range 0 to 400 °C.

The dimensions of this cell, although not essential to the discussion in this paper, are used for illustration, and were approximately:

Conductivity gap	0.068 cm
Heat guard length	3.8 cm
Emitter diameter	2.2 cm
Emitter length	11.4 cm.

The dimensions should be chosen so that $\Delta r/\bar{r} \leq 0.1$. The length of the emitter should be sufficient for 90 or 95 percent of the heat transfer to take place radially, and the length of the heat guard should be enough to reduce unaccountable heat loss from the emitter satisfactorily. The choice of the size of the conductivity gap represents a compromise. On the one hand, a narrow gap makes the ratio of the heat transfer by conduction large relative to the heat transfer by radiation and also very effectively makes the relative heat transport by convection small. On the other hand, when the gap is made too narrow, the uncertainty in the value of the cell constant is increased. The choice of dimensions will depend upon the objectives of the investigation.

3. The Cell Constant

3.1. Mathematical Treatment

We can obtain the cell constant from the assumption that the rate of heat transfer, $\dot{q}$, is proportional to the temperature gradient and the surface area. In the steady state, we can integrate the temperature gradient over the region of heat flow, so that $q=CK\Delta t$, where C is the cell constant, K is the thermal conductivity, and Δt is the temperature difference across the region in the steady state condition.

The principal terms of the cell constant can be evaluated by considering the radial heat flow across a section of length l of an infinite coaxial cylinder and the linear heat flow across a circular section of radius r_1 of two infinite parallel plates at the bottom. The determination of an accurate cell constant requires that recognition be made of the additional heat flow which takes place at the heat guard gap and at the bottom corner of the emitter. If both the conductivity gap, Δr, and the heat guard gap are small compared to the radius of the emitter, r_1, the conductivity gap and adjacent portion of the heat guard gap can be treated as if planar. In figure 2, the relaxation solution for the gas isotherms near the heat guard shows that the perturbing effect of the gap has practically vanished within two gap widths in any direction. Therefore, it is proper to employ the Schwarz-Christoffel transformation which is valid for an infinite cell. The transformations for both the heat guard gap and the bottom corner are given in Carslaw and Jaeger, [1][2] pp. 444 and 445. In an analogous manner to the solution for the bottom corner given on pp. 453–454, the correction terms for the heat guard gap may be found. On the assumption that the heat flow over the length of the cell takes place as if unperturbed, the deviations may be combined as a factor times half the heat guard gap, which is to be added to the length of the cell. If the heat guard gap is equal to the conductivity gap, Δr, the added length is [3]

$$c_2=0.923\ \Delta r/2.$$

The bottom corner of the emitter adds a term to the cell constant of $2\pi r_1 \times 0.559$ for equal conductivity gaps on the sides and bottom. Thus, the total rate of heat transfer by gas conduction is

$$\dot{q}=K\left[\frac{2\pi(l+c_2)}{\ln r_2/r_1}+\frac{\pi r_1^2}{\Delta r}+2\pi r_1 \times 0.559\right]\Delta t \qquad (1)$$

where r_2 is the inner radius of the receiver. The

[2] Figures in brackets indicate the literature references at the end of this paper.
[3] See appendix 1.

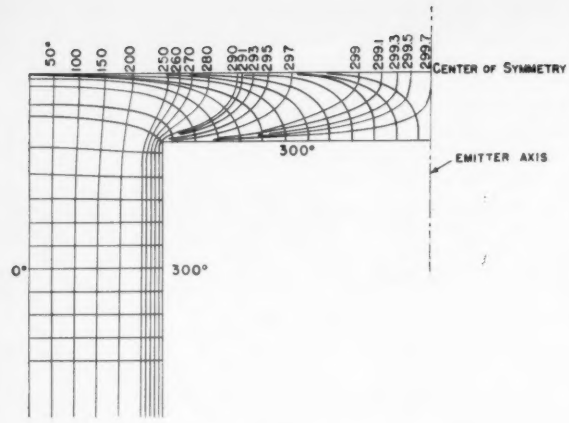

FIGURE 2. *Relaxation solution of the heat guard gap.*

cell constant is

$$C=\pi\left[\frac{2(l+c_2)}{\ln r_2/r_1}+\frac{r_1^2}{\Delta r}+1.118r_1\right]. \qquad (2)$$

From eq (2), we find 99.4 percent of the heat transfer from the cell illustrated in figure 1 is accounted for by the two principal parts: 94.9 percent by radial heat flow, 4.5 percent by linear heat flow. The transfer from the heat guard gap amounts to 0.25 percent, and the transfer from the bottom corner amounts to 0.33 percent.

3.2. Measurement of Receiver and Emitter Radii

Both to increase the flow of heat by conduction and to reduce the heat transferred by convection, the conductivity gap should be kept as small as will permit the accurate determination of the cell constant. For the case of $\frac{\Delta r}{r_1}\ll 1$, the rate of heat transfer by conduction from a section of length l of an infinite coaxial cylinder is $\dot{q}=\frac{2\pi\bar{r}Kl\Delta t}{\Delta r}$ within a relative error of $\frac{1}{3}\left(\frac{\Delta r}{2\bar{r}}\right)^2$, or 0.03 percent for $2\bar{r}=2.2$ cm and $\Delta r=0.068$ cm. The equation serves to emphasize that for the same error in the cell constant two orders of higher accuracy of length measurements are required to determine the conductivity gap, than the radii themselves.

The measurements of the two radii were made with a super-micrometer as measurements of two outer diameters, the one directly, the other by use of a "falling probe." If a "probe" is allowed to fall by its own weight, as shown in figure 3, the gap between the probe and the outer cylinder can be calculated from the air flow [2]. In an annulus formed by two coaxial cylinders of radius r_p and r_2, length L, and gap $m=r_2-r_p$, the volume of gas of viscosity η flowing in time θ with a difference of pressure

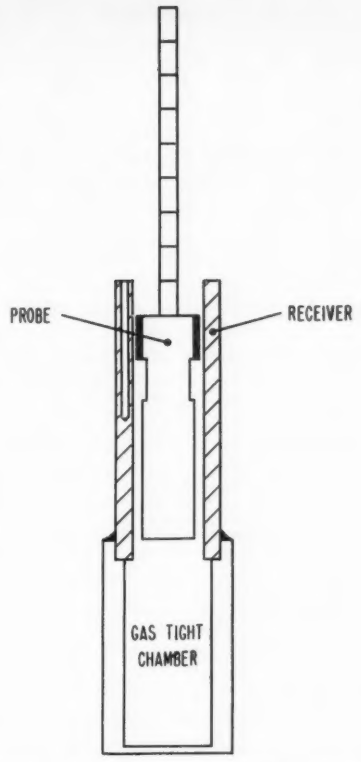

FIGURE 3. *Falling probe device for inner diameter measurement.*

$\Delta p=p_1-p_2$ and average pressure $\bar{p}$ can be expressed within a relative error of $\frac{m^2}{60\,r_p^2}$ as

$$\Delta V=\frac{\pi\bar{p}\Delta pg\bar{r}m^3\theta}{6\eta p_2 L}.$$

$\bar{r}=(r_p+r_2)/2$ and p_2 is the atmospheric pressure.

With the volume expressed as the probe displacement

$$m^3=\frac{6\eta p_2 r_2^2\Delta lL}{g\bar{p}\Delta p\bar{r}\theta} \qquad (3)$$

where g is the gravitational constant and Δl is the distance of fall in time θ.

The average inner radius of the receiver is determined by adding the gap, m, to the radius of the probe, r_p. The determination of the gap, m, was precise within 2.5×10^{-5} cm.

The measurement of $2r_p$ was precise within 2.5×10^{-5} cm, as well as $2r_1$, the outer diameter of the emitter. The sum of $m+r_p$ for varying m was consistent within 2.5×10^{-5} cm. Thus with differences of radius between receiver and emitter as small as 0.06 cm, the length of Δr was determined to an accuracy within 0.1 percent.

4. Convection

In general, the hydrodynamical equation for nonturbulent flow of a fluid of velocity $\bar{v}$, viscosity η, pressure p, and density ρ is (div η grad) $\bar{v}$=grad $p-\rho g$, where g is the acceleration of gravity [3]. For two infinite vertical plates at uniform temperatures $t_0-\Delta t/2$ and $t_0+\Delta t/2$, the equation reduces to

$$\eta \frac{d^2 v_z(x)}{dx^2}=(\rho-\bar{\rho})g.$$

The axes are taken with the origin at the midpoint between the planes. The x-axis is normal to the planes, the y-axis is horizontal, and the z-axis is vertical. The average density, $\bar{\rho}$ is the density at $x=0$.

If the separation of the planes is Δr, $t(x)=t_0+\frac{x\Delta t}{\Delta r}$ and

$$\rho=\bar{\rho}[1-\alpha(t-t_0)]=\bar{\rho}-\frac{\bar{\rho}\alpha x\Delta t}{\Delta r}, \text{ where } \alpha=-\frac{1}{\bar{\rho}}\left(\frac{\partial \rho}{\partial t}\right)_p.$$

Since $v=0$ when $x=-\frac{\Delta r}{2}$ and $x=\frac{\Delta r}{2}$,

$$v(x)=\frac{\alpha\bar{\rho}g\Delta t x}{6\bar{\eta}\Delta r}[\Delta r^2/4-x^2] \tag{6}$$

In a closed system, the circulation takes place as a single stream, reversing direction at the top and bottom. Conservation of mass requires a term second order in Δt which does not affect the heat transport by more than 1 percent for actual measurement, hence it was neglected.

The heat transported per unit horizontal distance is

$$\dot{q}=c_p\int_{-\Delta r/2}^{\Delta r/2} v(x)\rho(x)\Delta t(x)dx=\frac{\Delta r^3 g}{720}\frac{\alpha\rho^2 c_p\Delta t^2}{\eta}$$

where c_p is the specific heat capacity and the average density is indicated without the bar. The horizontal distance in the cell is very nearly $2\pi\bar{r}$. Then the rate of heat transport per degree is

$$\dot{q}/\Delta t=\frac{2\pi\bar{r}\Delta r^3 g}{720}\frac{\alpha\rho^2 c_p\Delta t}{\eta}. \tag{7}$$

If the total heat transfer is studied as a "conductivity," $\dot{q}/C\Delta t$, a portion is due to convection, which may be written as

$$K_{\text{conv}}=\frac{\dot{q}_{\text{conv}}}{C\Delta t}=\frac{2.6\times10^{-6}\alpha\rho^2 c_p\Delta t}{\eta}. \tag{8}$$

The value 2.6×10^{-6} combines the constants of eq (7) and the value of the cell constant C for the cell of figure 1.

The neglect of terms of higher order in Δt for $\rho(x)$ affects K_{conv} detectibly near the critical point of CO_2. When $\Delta t<5$ deg C, these terms need not be considered for other measurements to be reported.

Engineering investigations of convection have been analyzed by use of several correlating functions. It may seem at times as if serious discrepancies exist when the correlation is extended to inappropriate conditions. Let us consider three dimensionless quantities:

(1) The Grashof-Prandtl product

$$\text{Gr}\cdot\text{Pr}=\frac{g(\Delta r)^3\alpha\rho^2 c_p\Delta t}{\eta K}; \tag{9}$$

(2) The Grashof number

$$\text{Gr}=\frac{g(\Delta r)^3\alpha\rho^2\Delta t}{\eta^2};$$

(3) The Reynolds number

$$\text{Re}=\frac{\rho\bar{v}x_0}{\eta},$$

where the average velocity $\bar{v}=\frac{(\Delta r)^2\alpha\rho g\Delta t}{192\eta}$ and $x_0=\Delta r/2$.

Then

$$\text{Re}=\frac{g(\Delta r)^3\alpha\rho^2\Delta t}{384\eta^2}. \tag{10}$$

Thus the Grashof number and the Reynolds number are functionally the same for a gas in a vertical gap. Within the range of pressure and temperature such that the Eucken factor, $K/\eta c_v$, is a constant and that $\gamma=c_p/c_v$ is a constant, the Grashof-Prandtl product and the Reynolds number will serve equally well for the correlation of laminar convective effects.

The ratio of K_{conv} to K_{gas} can be found by dividing eq (8) by K_{gas}, and is functionally $(\Delta r/l)$ (Gr·Pr). It can be seen from eq (8)/K_{gas} that the criterion of Kraussold, that convection is insignificant[4] for Gr·Pr$<$1000, leads to different error limits depending upon $\Delta r/l$. For the cell of figure 1, Gr·Pr=1000 involves a relative heat transfer by convection of 8×10^{-3}.

Representing a ratio of the heat transport of convection to conduction, Gr·Pr is a logical correlating function for heat transport by laminar convection. Over the range of variables that eq (9)/eq (10) is a constant, either will serve as a criterion for the initiation of turbulent convection. Near the critical point, however, $c_p\to\infty$ and $\gamma\to\infty$. Since the Eucken factor does not vary greatly, Gr·Pr can become enormous while the Reynolds number remains small. The Reynolds number depends upon the velocity resistance per se, and it is the fundamental quantity, not Gr·Pr, which should be used as the criterion for initiation of turbulent flow.

The purpose of this section is to demonstrate how the data can be treated to give the heat transfer by thermal conduction alone. Measurements must be made under conditions of laminar flow. For CO_2, Onsager and Watson [4] have shown that with

[4] Worse yet is the statement that convection does not exist for Gr·Pr$<$1,000. The author hopes this idea will take its place with the phlogiston theory!

apparatus of the planar, vertical type, turbulence commences at a value of the Reynolds number of about 25. Often it is clear that $Re<<25$. If there is uncertainty, the Δt for transition from laminar to turbulent flow should be determined experimentally. At constant pressure and constant average gas temperature, eq (8) indicates that $\dot{q}/\Delta t$ versus Δt is linear for laminar flow. By straight line extrapolation of $\dot{q}/\Delta t$ versus Δt to zero Δt, the heat transport by convection is eliminated.

The essential requirements of eq (8) are confirmed by the results. The heat transport correlates well versus $\frac{\alpha\rho^2 c_p \Delta t}{\eta}$. The $\dot{q}/\Delta t$ versus Δt extrapolations are linear within the precision of the data, except for very large values of eq (8) where second order effects may be detectible. The values of Δt calculated from eq (10) (indicated by an asterisk on some extrapolation isotherms in the next paper) are in satisfactory accord with the experimental measurements.

5. Asymmetry of the Heat Flow

5.1. Coaxial Centering

If the emitter is not centered perfectly the geometrical factor of $\ln r_2/r_1$ should be replaced by $\cosh^{-1}[(r_2^2+r_1^2-d^2)/2r_1r_2]$, where d represents the displacement of the two axes. For the cell of figure 1, an error of 7×10^{-4} cm in the centering would make a difference of only one part in 100,000 in the cell constant.

5.2. Heat Loss From the Bottom of the Emitter

The cell with a single heat guard loses heat on the bottom as well as on the sides. With a uniform heater winding this leads to an asymmetric temperature distribution, which becomes larger as the gas thermal conductivity becomes larger. A reasonable approximation permitting mathematical treatment assumes uniform heat flow from the center heater to the emitter, no heat flow on the heat guard end, and the heat flow across the conductivity gap proportional to the temperature difference. The solution for this problem is

$$-K_{Ag}\Delta t/2\dot{q}=h\sum\frac{\pm\sqrt{\alpha_n^2+h^2}\cos(\alpha_n z)\phi_0(r;n)}{\alpha_n^2([\alpha_n^2+h^2]l+h)\phi_1(a;n)}$$

where $h=AK$, A is the total exterior surface area, K is the thermal conductivity of the substance in the gap, and K_{Ag} the thermal conductivity of silver.[5]

$$a\leq r\leq b$$

$$0\leq z\leq l$$

$$\phi_0(r;n)=I_0(r\alpha_n)[\alpha_n K_1(b\alpha_n)-hK_0(b\alpha_n)]+K_0(r\alpha_n)[\alpha_n I_1(b\alpha_n)+hI_0(b\alpha_n)]$$

$$\alpha_n\phi_1(a;n)=\left(\frac{\partial\phi_0}{\partial r}\right)_{r=a}=I_1(a\alpha_n)[\alpha_n K_1(b\alpha_n)-hK_0(b\alpha_n)]-K_1(a\alpha_n)[\alpha_n I_1(b\alpha_n)+hI_0(b\alpha_n)]$$

and the α_n are the ordered positive roots of $h=\alpha_n\tan(\alpha_n l)$. The value of $\sqrt{\alpha_n^2+h^2}$ is taken positive or negative in accord with the sign of $\sin\alpha_n l$.

The functions I_0, I_1, K_0, and K_1 are Bessel functions of complex argument. The result shows that the average temperature of the emitter is not at the center but at

$$z=0.66l \text{ for } K=5.95\times10^{-5},$$

$$z=0.675l \text{ for } K=5.95\times10^{-4},$$

$$\text{and } z=0.697l \text{ for } K=11.90\times10^{-4}.$$

Conductivities calculated from the average of the top and center temperatures must be increased by the factor indicated in figure 4. This factor is accurate enough that usually no significant error is involved, and could be reduced by adding measurement of the temperature difference at the bottom of the cell.

6. The "Blank" and Conduction of Pins

When the cell is evacuated, the heat transferred by radiation and by conduction of the pins can be treated as a measurement of a "conductivity," called a "blank." The present cell had a blank at 0 °C of 0.138×10^{-5} cal cm^{-1} sec^{-1} deg C^{-1}, about 4 percent of the conductivity of CO_2 at the same temperature and 1 atm pressure. It was estimated that no more than half of the heat transfer of that blank was due to conduction of the pins.

It was assumed that the conductivity of a gas could be found by deducting the blank from the value of the apparent conductivity for zero temperature difference. However, the blank may not adequately represent the heat transfer in the presence of a gas for the following reasons:

(1) The conduction of heat across the pin-emitter interface may increase in the presence of a gas.

(2) The temperature distribution in the pins may perturb the heat transfer in the gas significantly.

In the first case, if the pressure of the pins against the emitter is high enough, the effect of the gas on the conduction across the contact interface is negligible. Ascoli and Germagnoli [5] showed that the temperature difference across a steel-aluminum interface with 8 μin. finish became nearly constant in a vacuum once the pressure of contact reached 100 kg/cm^2. For N_2 at 1 atm, the temperature difference across the interface with the same heat flux became nearly constant at 50 kg/cm^2 contact pressure, and at 100 kg/cm^2 was equal within experimental error to the corresponding vacuum value. Boeschoten and Van Der Held [6] found three times the heat conduction in the presence of 1 atm of helium as in a vacuum at 35 kg/cm^2 contact pressure. The inference from the preceding investigation is that at 100 kg/cm^2,

[5] If the cell were made of another material, the corresponding thermal conductivity would be used in place of K_{Ag}.

the ratio would be 1.5/1. Rough surfaces approach the behavior of smooth surfaces as the contact pressure is increased. These measurements were performed upon a steel-aluminum interface rather than a Pyrex-silver interface used in the present apparatus. However, the ability of silver to conform to the harder surface of Pyrex is at least as great as for aluminum to conform to steel. The pins were forced into the silver sufficiently that indentations 0.003 to 0.005 in. deep were made in the emitter, which is to say with sufficient force to exceed 1500 kg/cm², the tensile strength of silver. The Pyrex pins were held in an aluminum sleeve such that the composite expansion of the two materials approximately matches the expansion of the cell material from 0 to 400 °C. Consequently the centering of the emitter and the contact pressure between the pin and the emitter should be maintained over the temperature range. Hence it can be expected that gases of low conductivity caused an insignificant change in the rate of transfer of heat through the pins. In helium, the uncertainty in pin conduction should not exceed 0.1 percent of the gas conduction.

The additional heat transfer through the gas, which arises because the temperature distribution in the pins does not follow the radial gradient, can be evaluated by relaxation methods, and leads to the result that an 18 percent increase of conduction for the area of the surface occupied by the base of the pin will be observed when the conductivity of the gas is 10 percent that of Pyrex. The area occupied by the bases of seven pins was 0.4 percent of the total surface area of the receiver so that at a gas conductivity of 3×10^{-4} cal cm^{-1} sec^{-1} deg C^{-1} an increase of conduction of 0.07 percent will be observed. If the conductivity of the fluid reached the value of Pyrex, the pins would have no effect on the temperature gradient, and at low values of gas conductivity, the effect is about the same as at a conductivity of 3×10^{-4} cal cm^{-1} sec^{-1} deg C^{-1}.

7. Radial Temperature Gradient in the Emitter and Receiver

A correction, in general small, must be made for the fact that the thermocouples are placed in the body of the emitter and receiver. This is a power series of $K_{corr}=K_{meas}\ [1+aK_{meas}+(aK_{meas})^2+\ .\ .\ .]$ of which only the first corrective term is large enough to be significant. For the dimensions of the silver conductivity cell in figure 1, $a=10.70$ cm sec deg C/cal.

8. Discussion of Other Cells

There are only a few forms of thermal conductivity cells suitable for accurate absolute determinations of the thermal conductivity of gases. The "hot wire" cell is an extreme case of a coaxial cylinder cell, with a small radius of the emitter, but the cell constant cannot be determined with the accuracy possible for a larger radius of emitter. The heat transfer analysis is complicated, and in a dense gas convection is difficult to control because of the large temperature gradient near the wire.

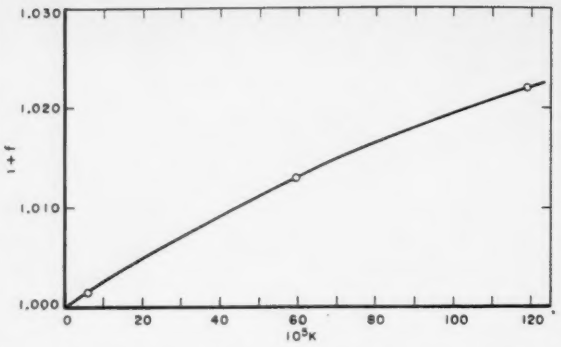

FIGURE 4. *Correction to the conductivity for asymmetric heat flow.*

A coaxial cylinder cell with heat guards at both ends would not have the end heat flow which requires the corrections given in figure 4. However, there is an uncertainty in the results due to a possible heat flow between the emitter and heat guards. When the emitter is suspended or held in place by sleeve or rod connections with the heat guards (as is customary for this design), the increased conduction possible by a slight difference in temperature between the emitter and guards will increase significantly the uncertainty of the thermal conductivity determination. The uncertainty is reduced if the thermal conductivity is relatively large, and if the emitter-receiver temperature difference is large. In order to avoid these restrictions, the suspension method could probably be modified.

In principle the flat plate cell, with an emitter and guard above the receiver, should not be affected by convection. In dense gas, there is good possibility that many such cells have had significant convection transfer from "chimneys," but that no special measurements were made to check. However, by proper design, it can be expected that convection difficulties would be eliminated. The cell constant can be determined with about the same accuracy as for the coaxial cylinder cell, but instability of the flat plate cell alinement affects the cell constant directly. By contrast, a change of the coaxial cylinder cell alinement affects the cell constant comparatively little.

9. Conclusions

By use of a heat guard and receiver extension which extends the conductivity gap of a coaxial cylinder, the conduction across the gap can be expressed accurately. In combination with special measuring techniques involving a "falling probe," the value of the cell constant can be obtained to an accuracy within ±0.1 percent.

The coaxial cylinder cell must be used with the axis vertical in order to permit analysis of convective heat transport. It was deduced mathematically and found experimentally that the apparent conductivity is affected by laminar convection linearly with the temperature difference. The temperature difference which causes the Reynolds number, eq (10), to be

25 defines the highest temperature difference for which laminar flow can be expected. The effects of convection can be eliminated by extrapolating the apparent conductivity versus the temperature difference to zero temperature difference, provided the measurements lie in the range of laminar flow.

For high accuracy, corrections must be made to the data for asymmetry of heat flow, perturbation of the temperature gradient by the mounting pins, and the temperature gradient in the emitter and receiver. Of course, the rate of heat transfer in a vacuum is deducted. There has now been sufficient quantitative measurement to show that the radiation and pin transfer should remain constant within 0.1 percent in the presence of a gas.

Of the various types of cells used for measuring the thermal conductivity of gases, the coaxial cylinder cell and the flat plate cell offer the most promise of accurate results.

10. References

[1] H. S. Carslaw and J. C. Jaeger, Conduction of heat in solids, 2d Ed., Oxford Univ. Press, London, 1959.
[2] W. H. MacAdams, Heat transmission, 2d Ed., McGraw-Hill Book Co., Inc., New York, 1942.
[3] R. C. Jones and W. H. Furry, Rev. Mod. Phys. **18,** 151 (1946).
[4] L. Onsager and W. W. Watson, Phys. Rev. **56,** 474 (1939).
[5] A. Ascoli and E. Germagnoli, Energia Nucleare **3,** 113 (1956).
[6] F. Boeschoten and E. F. M. Van Der Held, Physica **23,** 37 (1957).

11. Appendix

Given the conductivity gap h and heat guard gap $2k$.[6] We identify the points, $A\ B\ C\ D\ E\ F\ G\ H$ in the complex z-plane. These points are transformed in the t-plane by the Schwarz-Christoffel transformation, which is

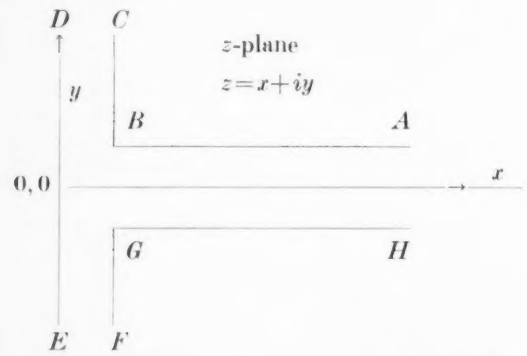

$$z=-iC\left\{\frac{\sqrt{1-a^2}}{2a}\ln\frac{[t+a][1-at+\sqrt{(1-a^2)(1-t^2)}]}{[t-a][1+at+\sqrt{(1-a^2)(1-t^2)}]}+\sin^{-1}t\right\}+\pi\frac{C\sqrt{1-a^2}}{2a};$$

$$C=2k/\pi; \qquad a^2=k^2/(h^2+k^2).$$

[6] Note that the symbolism is that of Carslaw and Jaeger, and in general should not be identified with the symbolism of the rest of the paper.

Points A, H, C, D, E, and F are assumed to lie at infinity in the z-plane. Corresponding values of the points are shown for the t-plane.

t-plane
$t=\zeta+i\xi$

A	B	C,D	$0,$	0	E,F	G	H
$-\infty$	-1	$-a$	0	0	a	1	∞

By use of the conformal mapping function

$$\pi w=\ln(t+a)/(t-a)$$

the points in the z-plane are transformed to the indicated points in the w-plane.

w-plane
$w=\mu+iv$

C	$A,$	H	F
$-\infty$	0	0	∞
D	0	0	E
$-\infty-i$	$0,-i$		$\infty,-i$

Thus in the w-plane, heat flow between two infinite parallel plates can be studied.

If the heat flow to $w=u-i$ is studied, this corresponds to the heat flow to $DE=-iy$ in the z-plane. By substituting $\pi w=\ln\left(\frac{t+a}{t-a}\right)$ and $w=u-i$, $z=-iy$,

$$-iy=-ih(u-i)-\frac{ih}{\pi}\ln\frac{[1-at+\sqrt{(1-a^2)(1-t^2)}]}{[1+at+\sqrt{(1-a^2)(1-t^2)}]}$$

$$-\frac{2ik}{\pi}\sin^{-1}t+h.$$

For u (and y) large, $t\to+a^-$

$$y=hu+\frac{h}{\pi}\ln(1-a^2)+\frac{2k}{\pi}\sin^{-1}a.$$

The heat transport to DE per unit width per unit temperature difference is, in the w-plane, Ku (where K is the thermal conductivity of the medium).

$$Ku=K\left(\frac{y}{h}-\frac{1}{\pi}\ln[1-a^2]-\frac{2k}{\pi h}\sin^{-1}a\right).$$

Thus, there are two corrective terms to be added to the normal term y/h for the steady heat flow between two planes distant h apart. For the case that the heat guard gap ($2k$) is equal to the conductivity gap (h)

$$a^2=1/5.$$

Where the conduction is regarded as unperturbed along FG and BC, we can get a relative correction to the normal term for infinite plates over the distance of the heat guard gap by taking $y=2k=h$. Then

$$Ku=K\left(1-\frac{1}{\pi}\ln\left[1-a^2\right]-\frac{1}{\pi}\sin^{-1}a\right)$$

or we may add a length to the emitter equal to one half the heat guard gap times the factor in parenthesis, i.e.,

$$c_2=k\left(1-\frac{1}{\pi}\ln\left[1-a^2\right]-\frac{1}{\pi}\sin^{-1}a\right)$$

$$=k(1-0.0766)=0.9234k.$$

(Paper 66A4-168)

JOURNAL OF RESEARCH of the National Bureau of Standards—A. Physics and Chemistry
Vol. 66A, No. 4, July–August 1962

Thermal Conductivity of Gases. II. Thermal Conductivity of Carbon Dioxide Near the Critical Point[1]

Leslie A. Guildner

(April 13, 1962)

The thermal conductivity of CO_2 has been measured in a coaxial cylinder cell as a function of pressure over a range of temperatures from 3.66 to 75.26 °C. Particular attention was given to the measurements from 1 to 9 deg C above the critical temperature at pressures closely spaced to include the critical density.

The thermal conductivity of $CO_{2(g)}$ near the critical point is very large compared to one atmosphere values around room temperature. At 1 deg C above the critical point the thermal conductivity reaches a maximum at the critical density. This maximum is greater than the maxima at higher temperatures. At 75.26 °C, 44 deg C above the critical temperature, little unusual increase at the critical density was observed.

The rate of heat transport by convection in the critical region is also very large. This problem was studied carefully in order that the temperature differences used were restricted to the region of laminar flow, and that appropriate extrapolation procedures were used to find the rate of heat transfer by thermal conduction alone.

Also, at densities and temperatures away from the critical region, new thermal conductivity values were obtained.

1. Introduction

Despite a conveniently accessible critical temperature of about 31.045 °C and a moderate critical pressure of about 72.85 atm, the transport phenomena in the critical region of carbon dioxide have received little attention. The viscosity of carbon dioxide has been measured by the oscillating disk method [1][2] and by capillary flow [2]. The thermal conductivity of carbon dioxide has been measured "in the critical region," [3] but in the range of density, $0.35<\rho<0.60$ g/cm^3, no measurements have been reported. Furthermore, other investigations have similarly failed to include the density range within 0.1 g/cm^3 of the critical [4] or have been at too high a temperature to demonstrate any characteristic behavior [5]. This paper describes a thermal conductivity investigation, emphasizing the region $32<t<40$ °C and $0.4<\rho<0.55$ g/cm^3 but including a wider range of both temperature and density.

2. Experimental Description

Thermal conductivities of CO_2 were determined as functions of its pressure, average gas temperature and temperature difference. Following the design and considerations given in Paper I [6], a coaxial cylinder cell of 99.9 percent pure silver had a cell constant $C_t=C_{23}\,\varphi\,(t)$, where $C_{23}=1.207_3\times10^3$ cm at 23 °C and the relative thermal expansion of silver is $\varphi(t)=[1+0.1862\times10^{-4}(t-23°)+7.4\times10^{-9}(t-23°)^2]$ with t in °C. The cell and surrounding stainless steel container were maintained at a temperature constant to ±0.001 deg C in an oil bath of the Beattie-Collins type [7], regulated by a proportionating thyratron circuit [8]. The temperature was obtained on the international scale using a platinum resistance thermometer and Mueller bridge, both carefully calibrated.

In order to make them stable, the Chromel-P Alumel thermocouples used to measure the temperature difference were annealed in an atmosphere of CO_2 for 205 hr at 500 °C. As a further protection from parasitic emfs from strain, non-uniformity of composition and non-uniform temperature at the junction with copper outside the system, the thermocouple wires were welded to gold and the junctions tempered—brought into good thermal contact—at a "lava block" below the top of the constant temperature bath. (See fig. 1.) The leads of one reference junction, maintained at 0 °C in an ice bath, were brought into the cell-container. Gold leads were welded to the reference thermocouple leads also, and the gold-thermocouple junctions were tempered in the same tempering block as the other gold-thermocouple junctions. After emerging from the cell, the contact between each gold lead and its copper lead was made in thermal contact with a large copper block which was well insulated thermally. The leads of each thermocouple junction, by extension with a gold and then a copper intermediary, were wired into a set of switches, in such a way that all pair combinations were possible.

As part of the lead tempering, it was necessary to provide a portion of the gold thermocouple lead wires with a constant temperature environment. The use of some device such as the "heater" shown in figure 1 was necessary, particularly if the gas was at high enough pressure to be liquefied in the gas lead

[1] This work was performed at the Massachusetts Institute of Technology and sponsored by Project SQUID, which is supported by the Office of Naval Research, Department of the Navy, under contract Nonr 1858(25) NR-098-038. Reproduction in full or in part is permitted for any use of the United States Government.

[2] Figures in brackets indicate the literature references at the end of this paper.

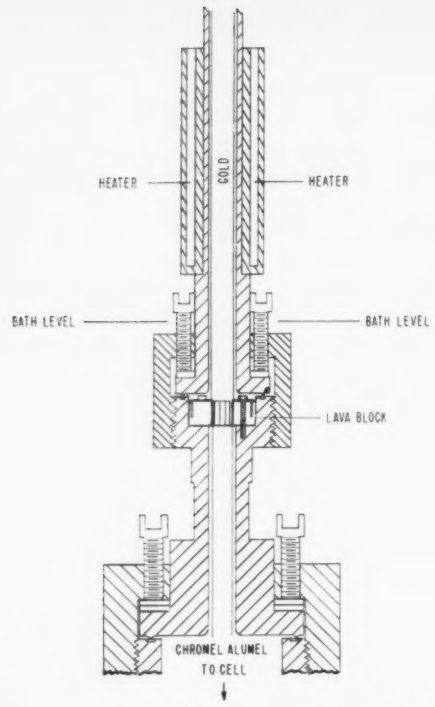

FIGURE 1. *Heater and lava block tempering station for thermocouple leads.*

above the cell. This heater was controlled so as to produce a constant temperature excess Δt above the bath temperature. With CO_2 at 75 °C bath temperature it was found necessary to use different Δt values, depending upon the pressure, but it proved true that the minimum value which made the thermocouple voltages steady gave constant calibration results.

Electromotive forces of the thermocouples were determined by potentiometric measurement, on an instrument with dials reading directly to single microvolts. The range was extended to hundredths of microvolts by galvanometer deflections. The sensitivity for the temperature difference readings was 31.4 mm/μv with a reading error of 0.1 mm. The potentiometer was calibrated both absolutely and for proportionality in 1947, fourteen years after its construction, and was recalibrated for proportionality during the course of the measurements. The power was also determined by potentiometric measurements with voltage divider networks, where all components had been carefully calibrated.

Carbon dioxide, available as liquid in tanks at 99.5 percent[3] purity, was first passed, in the gaseous phase, through a magnesium perchlorate drying tube and then frozen at liquid nitrogen temperatures. After vacuum pumping for several hours, the residual pressure was reduced to 0.3 percent of its original value, then indicating residual contamination of the O_2 and N_2 impurity of <0.001 percent. The CO_2 pressures were measured on a dead-weight piston gage, calibrated against the vapor pressure of CO_2 at 0 °C [9], with calibrated weights.

Pressures were controlled by a special regulator system to about 1 part in 100,000.

[3] Pure Carbonic Co. states the impurities of the gas used as 0.342% N_2, 0.086% O_2, and 0.072% H_2O.

3. Measurements

To permit the specification of density near the critical density as accurately as possible, the pressures for conductivity measurements were selected at average gas temperatures of 32.054, 34.721, 40.089, and 75.260 °C, because these are the temperatures of the pVT isotherms of Michels and Michels [10], and Michels, Blaisse, and Michels [11]. From these pVT data and the determinations of Wentorf [12], the value of $\rho=0.474$ g/cm^3 was assumed for the critical density. At lower pressures and also in the liquid state, the values of density were derived from equations of state. Other conductivity measurements covering a large density range were made at about 3.7, 26, 31, and 36 °C.

To permit extrapolation of the apparent conductivity to that at zero temperature difference, two sets of triplicate measurements of the top and middle emitter-receiver difference thermocouples were made at three different Δt's in the ratio of 1: 2: 4 with constant average gas temperature. When conditions permitted, a maximum temperature difference of about 5 deg C was considered optimal. In some cases near the critical point, however, the danger of turbulent flow made it desirable that the maximum temperature difference be only 0.025 deg C.

When experimental conditions made it uncertain whether turbulent convection existed, exploratory measurements were made to locate a possible transition from laminar to turbulent flow. If it was found, the determinations for extrapolations were made for temperature differences less than that which produced turbulence.

The blank was measured at two temperatures at the beginning of the investigation. The stability and reproducibility of the blank was shown by repeating the measurements toward the end of the work.

With no power input in the cell, there should be no difference in temperature between the emitter and receiver, but appreciable difference thermocouple emf's were still found to exist. In general, within the range of 0 to 75 °C, these "residual" or "parasitic" voltages were less than ± 1 μv and they were fairly stable. They might have been due to heat flows to the cell, or to strain and variation of composition of leads in the temperature gradient between the cell and room temperature. In any case the parasitic emf's amounted to a "zero calibration" and they were deducted from the measurements when the emitter was heated. The importance of this procedure was emphasized for measurements near the critical point, where some of the net emf's for the temperature difference were less than the parasitic emf.

4. Results

4.1. Treatment of Data

The principal data obtained for a determination of the apparent conductivity were

(1) The emf across the voltage divider of the emitter heater, V_{em}.
(2) The emf across the voltage divider of the standard resistor, V_{std}.
(3) The emf of the emitter-receiver difference thermocouples, $\Delta V_{\Delta t}$.
(4) The emf of the emitter-heat guard difference thermocouple.
(5) The emf of the receiver-ice thermocouple.
(6) The weights for the deadweight gage measurement of pressure.
(7) The platinum thermometer resistance for the bath temperature.

Items (5) and (6), together with calibrations, allowed a specification of the pressure and temperature of the gas. Items (4) and (7) permitted maintenance of required experimental conditions. The apparent thermal conductivity obtained from a set of measurements is defined as $K_{app}=\frac{\dot{q}}{C_t\Delta t}$. Now $\dot{q}$, the power, is the product of the emf's of the emitter and standard resistor times a number representing the calibrated factors for the voltage dividers, divided by the resistance of the standard resistor. The temperature difference, Δt, is obtained from the emf's of the emitter-receiver difference thermocouples, $\Delta V_{\Delta t}$, divided by the calibrated value of dE/dt for Chromel-P Alumel at the average temperature. Thus

$$K_{app}=\frac{\dot{q}}{C_t\Delta t}=\left(\frac{V_{em}V_{std}}{\Delta V_{\Delta t}}\right)D_{23}\left(\frac{dE}{dt}\Big/\phi(t)\right). \quad (1)$$

This requires

$$D_{23}=\frac{0.23885X}{C_{23}R_{std}}=1.321_{96}\times10^{-11}\ \text{I. T. cal cm}^{-1}\ \text{sec}^{-1}\ (\mu\text{v})^{-2}$$

where X is the appropriate factor for the voltage dividers. The results in this paper are expressed with heat units in I.T. calories, based on the conversion 1 absolute joule=0.23885 I.T. calories. At constant average gas temperature, dE/dt and $\varphi(t)$ are constant. The only variables of eq (1) for an isotherm, therefore, are the emf measurements. The computations are greatly reduced by processing the emf product to obtain the value extrapolated to zero difference thermocouple emf. If we put

$$\Psi=\frac{V_{em}V_{std}}{\Delta V_{\Delta t}},$$

the coordinates of the extrapolations are Ψ versus $\Delta V_{\Delta t}$. Corrections were made to Ψ for small deviations from the steady state. The heat flow between emitter and heat guard, if the temperature difference was not zero, was determined as a function of the conductivity and corrections applied. A linear change in the rate that power was supplied to the emitter required a correction to represent a steady state measurement. It was obtained from $K_{corr}=K_{app}+\frac{2\alpha C_p}{C_t}$, where α is the relative rate of change of the heating current, C_p is the heat capacity of the emitter and C_t is the cell constant. Usually these corrections were insignificant and for no measurements did the total correction exceed 0.2 percent. When Ψ is extrapolated to zero $\Delta V_{\Delta t}$ to give Ψ_o, the corresponding K_{app} is $(K_{app})_o$. Corrections for the assymetric temperature distribution, $f(K_{app})_o$, the perturbation of heat flow by the pins, $-7\times10^{-4}(K_{app})_o$, and the temperature gradient in the emitter and receiver, $10.70(K_{app})_o^2$, were made as $\Sigma\delta K=(f-7\times10^{-4})(K_{app})_o+10.70(K_{app})_o^2$. Finally, the blank was deducted to arrive at the conductivity of the gas, $K=(K_{app})_o-\text{blank}+\Sigma\delta K$.

4.2. Calibrations of a Reference Thermocouple, Extrapolations of Ψ Versus $\Delta V_{\Delta t}$ and Calculation of K

The reference thermocouple was installed so it could be calibrated against a platinum resistance thermometer in the bath. Values of the emf versus t were obtained by repeated measurements at 5 deg temperature intervals. The curve of dE/dt versus t for Chromel-P Alumel (fig. 2) was obtained by numerical differentiation. Small adjustments, up to one part in 2,000, were made and compensated for

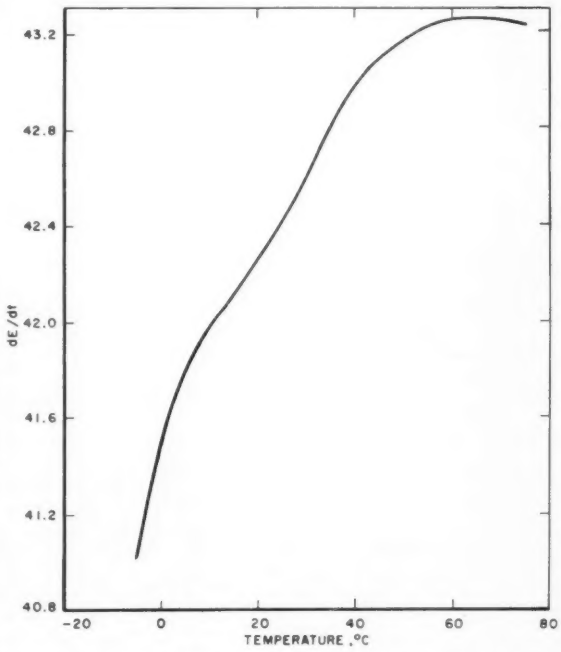

FIGURE 2. *dE/dt(μv/deg C) for Chromel-P Alumel thermocouples from 0 to 75 °C.*

in the adjoining values. The integrated values for E checked the calibration values of 745.3, 1691.15, and 3202.6 μv within 0.1 μv at 18, 40, and 75 °C, and within 0.2 μv of 2208.2 μv at 52 °C.

Sample data and the calculated Ψ are shown in table 1 for one point on curve 5, figure 3, for $\Delta V_{\Delta t}=$ 38 μv. Residuals have been deducted. They were about +0.045 μv for upper em-rec, and −0.250 μv for lower em-rec difference thermocouples.

Extrapolations exhibiting the change in slope typical of the increase of heat transport by turbulent convection are shown in lines 1, 2, 3, 4, and 5 of figure 3. X on the lines 2, 3, 4, and 5 indicates the calculated value of $\Delta V_{\Delta t}$ for the Reynolds number Re=25. A part of a typical low-pressure extrapolation, line 6, is shown for comparison.

A summary of all the results is presented in table 2.

Column 3 gives the highest emf of the difference thermocouples used in the extrapolations. Column 4 gives the emf of the difference thermocouples for the transition to turbulence. $D=D_{23}/\varphi(t)$.

The isotherms of K versus ρ in the region of critical density are presented graphically in figure 4. The detail of the isotherms at 3.662, 26.00, 30.90, 36.24, and 41.22 °C for $\rho<0.20$ g/cm³ are shown in figure 5.

TABLE 1. *Potentiometer measurements for thermal conductivity of* $CO_{2(g)}$

t=75.26 °C, p=178.2 atm

Time	$\Delta V_{\Delta t}$ em-rec		Ave $\Delta V_{\Delta t}$	V_{std}	V_{em}	10^{-5} Ψ	10^{-5} ΨAve	$(\Delta V_{\Delta t})$ Ave
	upper	lower						
2.00 P	38.261	38.224	38.244	3008.27	3736.46	2.939	2.939	38.23
2.30 P	38.284	38.209	38.247	3007.61	3735.68	2.938		
2.55 P	38.203	38.174	38.189	3006.68	3734.47	2.940		
4.30 P	38.198	38.137	38.168	3005.01	3732.08	2.938	2.937	38.15
4.45 P	38.147	38.100	38.124	3003.22	3730.20	2.939		
5.00 P	38.168	38.144	38.156	3001.83	3728.36	2.933		

The data are typical for $\Delta V_{\Delta t}\geq$ 25 μv where the average deviation was ±0.1%.

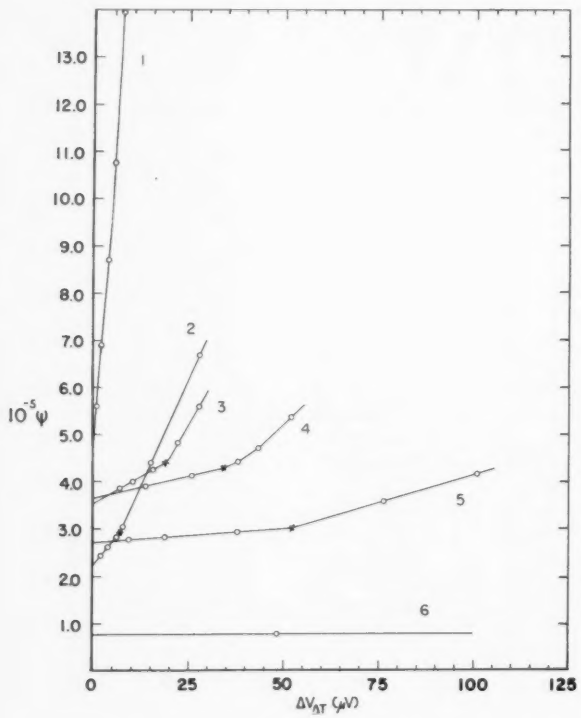

FIGURE 3. *Extrapolation curves showing change to turbulent convection.*

(1) t=34.721 °C, p=79.13 atm; (2) t=32.054 °C, p=72.51 atm; (3) t=25.99 °C, p=68.71 atm; (4) t=25.99 °C, p=75.85 atm; (5) t=75.26 °C, p=178.2 atm; (6) t=41.22 °C, p=2.31 atm.

TABLE 2. *Summary of results*

P (atm)	ρ (g/cm³)	Max Δt Extrap (μv)	Turb Δt (μv)	$10^{-5}\Psi_0$ (μv)	$(K_{app})_0$	$\Sigma\delta K$	K	Probable error (%)
					10^5cal cm^{-1} sec^{-1} deg C^{-1}			
3.662 °C; D=1.3224×10^{-11}; dE/dt=41.76μv/deg C; 10^5 blank=0.140								
2.10	0.0041	230	.....	.....	3.670	0.001	3.53	0.7
18.3	.0409	270	.....	.....	4.039	.003	3.90	.7
36.3	.0997	230	.....	.....	5.143	.003	5.01	.7
44.2	.89	90	.....	.....	26.30	.216	26.4	.7
56.6	.91	88	.....	.....	26.98	.239	27.1	.7
26.00 °C; D=1.3219×10^{-11}; dE/dt=42.48 μv/deg C; 10^5 blank=0.155								
2.18	0.0036	230	.....	.....	4.044	0.003	3.89	0.5
31.16	.0685	195	.....	.....	4.694	.003	4.54	.5
56.9	.1696	64	70	.....	6.819	.006	6.67	.6
68.7	.73	16	18	3.515	19.91	.122	19.9	1.0
75.9	.76	26	35	3.641	20.45	.132	20.4	0.8
30.90 °C; D=1.3218 ×10^{-11}; dE/dt=42.65 μv/deg C; 10^5 blank=0.160								
2.18	0.0036	228	.....	.....	4.138	0.003	3.98	0.5
30.82	.0651	130	.....	.....	4.755	.003	4.60	.5
57.6	.1607	67	80	.....	6.520	.005	6.37	.5
31.31 °C; D=1.3218 ×10^{-11}; dE/dt=42.66 μv/deg C; 10^5 blank=0.160								
77.70	0.652	13	16	3.495	19.71	0.120	19.7	1
32.05$_4$ °C; D=1.3217×10^{-11}; dE/dt=42.68 μv/deg C; 10^5 blank =0.161								
72.51	0.300	6	7	2.295	12.95	0.051	12.8	1.5
74.29	.398	1	.....	5.475	30.88	.303	31	6
74.49	.4482	1	.....	10.03	56.58	1.001	57	7
74.56	.4758	2.3	.....	12.16	68.59	1.439	70	8
74.62	.498	1.1	.....	8.720	49.19	0.812	50	7
74.99	.553	1.7	2.1	4.923	27.77	.245	28	6
75.90	.600	2.6	3.4	3.800	21.44	.144	21.4	4
79.67	.650	7	.....	3.476	19.61	.120	19.6	2
34.72$_1$ °C; D=1.3217×10^{-11}; dE/dt×42.79 μv/deg C; 10^5 blank=0.164								
78.18	0.400	4	5.3	3.630	20.53	0.132	20.5	3
79.13	.474	4	4.5	4.570	25.85	.213	25.9	3
80.46	.550	7	.....	3.545	20.05	.123	20.0	2
36.24 °C; D=1.3216 ×10^{-11}; dE/dt =42.81 μv/deg C; 10^5 blank =0.166								
2.18	0.0036	233	.....	.....	4.256	0.003	4.09	0.5
30.2	.0614	188	.....	.....	4.820	.003	4.66	.5
57.55	.1490	140	.....	.....	6.335	.006	6.18	.4

TABLE 2. *Summary of results*—Continued

P (atm)	ρ (g/cm³)	MaxΔt Extrap (μv)	Turb Δt (μv)	$10^{-5}\psi_0$ (μv)	$(K_{app})_0$	$\Sigma\delta K$	K	Probable error (%)
					10^5cal cm^{-1} sec^{-1} deg C^{-1}			
40.08$_7$ °C; D=1.3215×10^{-11}; dE/dt=42.99 μv/deg C; 10^5 blank=0.170								
85.81	0.400	6	----------	2.707	15.38	0.072	15.3	2
88.91	.474	2	----------	2.941	16.71	.087	16.6	4
91.85	.550	9	10.5	3.142	17.85	.099	17.8	1.5
40.10$_7$ °C; D=1.3215 ×10^{-11}; dE/dt=42.99 μv/deg C; 10^5 blank=0.170								
124.9	0.737	32	40	3.493	19.84	0.122	19.8	0.5
195.2	.840	95	----------	4.089	23.23	0.170	23.23	.3
41.22 °C; D=1.3215 ×10^{-11}; dE/dt=42.99 μv/deg C; 10^5 blank=0.171								
2.31	0.0040	200	----------	----------	4.332	0.003	4.16	0.5
57.69	.1412	140	----------	----------	6.160	.006	6.00	.4
73.79 °C; D=1.3207×10^{-11}; dE/dt=43.04 μv/deg C; 10^5 blank=0.206								
2.31	0.0036	200	----------	----------	4.969	0.003	4.77	0.5
75.26 °C; D=1.3207 ×10^{-11}; dE/dt=43.22 μv/deg C; 10^5 blank =0.207								
150.7	0.474	40	42	2.306	13.16	0.052	13.01	0.6
178.2	.575	38	50	2.739	15.63	.075	15.50	.5
300.0	.770	30	50	3.659	20.89	.137	20.8	.5

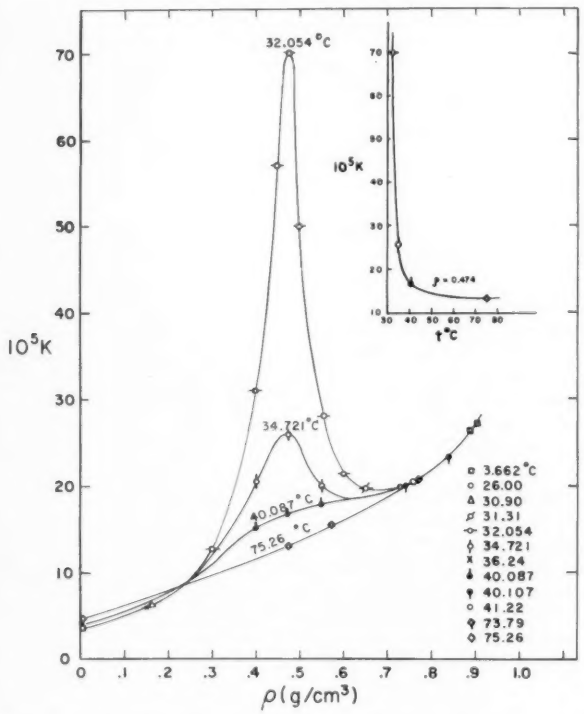

FIGURE 4. *Thermal conductivity of CO_2 in the region of the critical point.*

(K in units of cal cm^{-1} sec^{-1} deg C^{-1}, ρ in g cm^{-3})

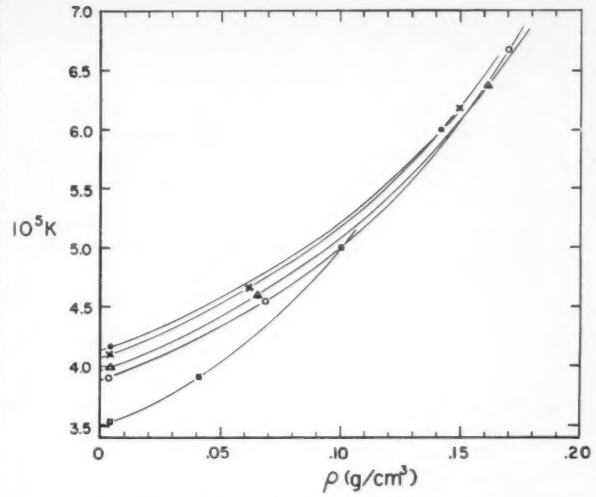

FIGURE 5. *Thermal conductivity of CO_2(g) at low densities from 3.66 to 41.22 °C.*

(K in units of cal cm^{-1} sec^{-1} deg C^{-1}, ρ in g cm^{-3})
Same key as figure 4.

5. A Study of Convection for the 32.054 °C Isotherm

The maximum temperature difference, which can exist before the onset of turbulence, becomes smaller as the crtical conditions are approached. Since there is a loss of precision at very small temperature differences, it may not be possible to determine by experiment whether extrapolations of measurements close to the critical point are entirely in the laminar range. Thus, the extrapolations for 32.054 °C average gas temperature at 0.398, 0.448, 0.4758, and 0.498 g/cm³ density, shown in figure 6, might include one or more points involving turbulent heat transport.

The temperature difference for the transition to turbulent flow can be evaluated by calculating that value of Δt for which the Reynolds number equals 25. From paper I, $\mathrm{Re}=-\frac{g(\Delta r)^3}{384}\left(\frac{\partial\rho}{\partial t}\right)_p\frac{\rho\Delta t}{\eta^2}$. The evaluation of some of these quantities near the critical point is tenuous, so the results of calculations are only approximate. For instance, without a careful study leading to a reliable equation of state, $\left(\frac{\partial\rho}{\partial t}\right)_p$ must have an uncertainty of 5 to 10 percent. It was found that $\left(\frac{\partial p}{\partial t}\right)_\rho$ is very nearly constant from 31.185 to 34.721 °C for a given ρ, hence $\left(\frac{\partial\rho}{\partial t}\right)_p$ was evaluated from $\left(\frac{\partial\rho}{\partial t}\right)_p=-\left(\frac{\partial\rho}{\partial p}\right)_t\left(\frac{\partial p}{\partial t}\right)_\rho$. The experimental values of the viscosity of CO_2 vary even more. At 31.10 °C and 0.504 g/cm³ Michels, Botzen, and Schuurman reported η to be 76×10^{-5} poise. On

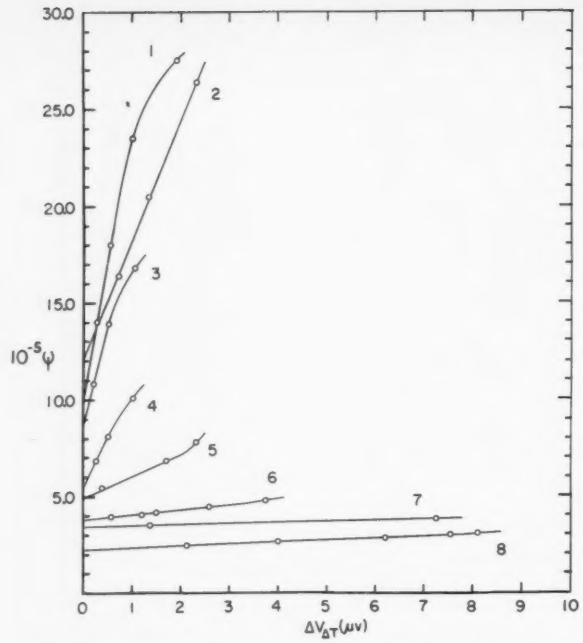

IGURE 6. *Extrapolation curves near the critical density for the 32.054 °C isotherm.*

(1) ρ=0.4482 g cm^{-3}; (2) ρ=0.4758 g cm^{-3}; (3) ρ=0.498 g cm^{-3}; (4) ρ=0.398 g cm^{-3}; (5) ρ=0.553 g cm^{-3}; (6) ρ=0.600 g cm^{-3}; (7) ρ=0.650 g cm^{-3}; (8) ρ=0.300 g cm^{-3}.

the other hand, at 31.14 °C and 0.502 g/cm^3, Naldrett and Maass reported η to be 37.91×10^{-5} poise, or almost exactly one-half as much. In table 3 one set of values of Δt for transition to turbulence is given for the viscosities reported by Michels, Botzen, and Schuurman, and another set for the viscosities reported by Naldrett and Maass.

Table 3 shows at least two points on every extrapolation line except for ρ=0.4758 are within the limits of temperature difference for laminar convection. For values of viscosity reported by Naldrett and Maass, the calculations show that turbulence can be expected only when Δt is greater than the maximum used in the extrapolations for ρ=0.300, ρ=0.398, and ρ=0.553. For the largest temperature difference, the heat transfer would include turbulence at ρ=0.448 and ρ=0.498 but not for the two smaller temperature differences. However, the rate of heat transfer at the highest temperature difference at ρ=0.4482 or ρ=0.498 is too low even to be linear with other points. At ρ=0.4758, (approximately the critical density), according to the calculation only the lowest temperature difference is within the limits of laminar flow. This is remarkable if true, since the slope of the extrapolation at ρ=0.4758 is less than that at ρ=0.4482 or ρ=0.498, hardly a manifestation of turbulence.

The values of viscosity reported by Naldrett and Maass show no unusual increase at the critical density. The only significant uncertainty, then, in the correct values of the viscosity is between those values and higher values. If the higher values of viscosity reported by Michels, Botzen, and Schuurman are used, the calculated temperature difference for transition to turbulence is greater than the temperature differences used in the extrapolations at all densities except the critical density.

The usefulness of these considerations is that one must conclude, even from a very conservative evaluation, that the important part of the extrapolations are based on measurements made under conditions of laminar flow.

6. Discussion

At low pressures, the measurements were made so that the temperature difference indicated by the thermocouple emf $\geq 25\mu$v. This allows Ψ_0 to be determined with an uncertainty of about ±0.1 percent, as a combination of uncertainty in the individual values and the uncertainty introduced by the extrapolation. The value of D is uncertain by ±0.1 percent because of uncertainty in mechanical measurements for the cell constant. The dE/dt for the Chromel-P Alumel thermocouples is considered to be uncertain by ±0.1 percent also.

The blank was difficult to determine, and initial determinations, shortly after beginning the conductivity measurements, varied by ±5 percent.

Determinations made at the conclusion of measurements agreed with the initial values within that variation. The uncertainty of the blank is insignificant for values of $10^5 K \geq 10$ cal cm^{-1} sec^{-1} deg C^{-1} relative to the other errors, but at 3.7 °C it contributes ±0.2 percent for $10^5 K$=3.5.

TABLE 3. *Temperature difference for transition to turbulent flow at 32.054 °C near the critical density*

ρ g/cm^3	0.300	0.398	0.4482	0.4758	0.498	0.553
p atm	72.51	74.29	74.49	74.56	74.62	74.99
$(\partial p/\partial t)_\rho$ atm/deg C	1.07	1.45	1.63	1.70	1.80	2.06
$(\partial\rho/\partial p)_t$ g/(cm^3 atm)	0.0273	0.175	0.360	0.399	0.300	0.088
$-(\partial\rho/\partial t)_p$ g/(cm^3 deg C)	.0292	.254	.587	.678	.540	.181
$10^5\eta$ (poise) (Michels, Botzen, and Schuurman)	25	38	50	52	55	52
Δt for transition to turbulence						
Calculated (μv)	9.5	1.9	1.3	1.1	1.5	3.6
Experimental (μv)	7.6	>1	>2	>2.3	>1.1	2.1
Extrapolation interval	6	1	1	2.3	1.1	1.7
$10^5\eta$ (poise) (Naldrett and Maass)	25	28.5	34.7	37	37.9	39
Δt for transition to turbulence						
Calculated (μv)	9.5	1.1	0.6	0.55	0.73	2.05

The 3.66 °C isotherm was the first to be measured. It is considered that the reliability of the data improved with experience, hence a larger estimated uncertainty for this isotherm is given in table 2 than for other measurements under comparable conditions.

The uncertainty of the values near the critical point is considered to be primarily due to lack of reproducibility of the small emf's of the difference thermocouples. Measurements at 0.25 μv were precise within ± 5 percent (i.e., ± 0.0003 deg C). At least 12 emf measurements are included in the value of a 0.25 μv point.

The curvature of the extrapolations for $\rho = 0.45$, 0.50 and 0.55 g/cm^3 may be unaccounted for mathematically because of the neglect of second order terms, in the expression for K_{conv}. The importance of the second order terms decreases as Δt decreases, hence the isotherms should approach linearity as $\Delta t \to 0$.

There could be an appreciable error in interpolation of densities on the 32.054 °C isotherm of the pVT measurements of Michels, Blaisse, and Michels. The values of density stated in table 2 are adjusted from the nominal values of 0.40, 0.45, 0.476, 0.50, and 0.55 g/cm^3 to give a smooth curve for a plot of $\Delta\rho/\Delta p$ versus $\bar{p}$. This is estimated to involve an error in K of ± 1 percent at $\rho = 0.40$ and 0.55 g/cm^3, of ± 2 percent at $\rho = 0.45$ and 0.50 g/cm^3, and of ± 3 percent at $\rho = 0.476$ g/cm^3.

The inset of figure 4, an isometric of 10^5K versus t for $\rho = 0.474$ g/cm^3, suggests an extremely high value of K at the critical point itself.

At high density, over a limited temperature range at least, the thermal conductivity of CO_2 appears to be nearly constant at a given density. Thus 10^5K for $CO_{2(l)}$ at 26.00 °C and $\rho = 0.76$ g/cm^3 is 20.4 and for $CO_{2(g)}$ at 75.26 °C and $\rho = 0.77$ is 20.8. For $\rho \geq 0.74$ g/cm^3, all points of K versus ρ plot smoothly on a single curve regardless of temperature.

Any additional increment of thermal conductivity at the critical density has nearly vanished at 75 °C, and is <25 percent for 40 °C. The effect lies almost entirely between $\rho = 0.30$ and $\rho = 0.60$ g/cm^3, which at 32.054 °C is between $p = 72.51$ and 75.90 atmospheres. Consequently, most investigations which "cover" the critical region in fact skip it, so that no unusual behavior is observed.

It is not unusual to assume that the density and temperature to which a measurement of the thermal conductivity corresponds is the average density and average temperature of the gas. Rigorously, the thermal conductivity should be defined as the limit of measurements at an average gas temperature and an average density, extrapolated to zero temperature difference. There will be no significant difference if K may be satisfactorily represented as a linear function of T and ρ, provided significant convection is absent. However, in the critical region, K is not linearly, or even monotonically varying with T and ρ, so that for reliability, K should be extrapolated versus Δt to zero temperature difference, even in the absence of convection.

The cell used in these measurements was designed to give high accuracy under conditions of low transport of heat by convection, a requirement in effect that the conductivity gap be large enough to minimize the error of the cell constant.

It would enhance the reliability of the results in the critical region if the conductivity gap were reduced to about one-third that used. Correspondingly, the ratio of K conv/K gas would be reduced to one eighty-first of what was observed. However, the merit of the equipment used is manifested in the accuracy of the thermal conductivity at low and high densities.

7. Comparison With Other Results

Recently Sengers and Michels [13] have published a preliminary paper where measurements of the thermal conductivity of CO_2 in the critical region are reported. The agreement between the results presented in this paper and the new work is satisfactory in the regions $0 < \rho < 0.20$ g/cm^3 and $\rho \geq 0.65$ g/cm^3 at all temperatures, and at all densities for $t \geq 40$ °C. In the same units of K, Sengers and Michels show a value of $10^5K = 21$ for $\rho = 0.466$ g/cm^3 and $t = 34.8$ °C, and a value of $10^5K = 33$ for $\rho = 0.466$ g/cm^3 and $t = 32.1$ °C. In addition, they have a 31.2 °C isotherm, with $10^5K = 81$ at $\rho = 0.466$ g/cm^3. Therefore, the results of Sengers and Michels show a marked increase of the thermal conductivity of CO_2 near the critical point, but less than that reported in this paper.

8. Conclusions

The thermal conductivity of carbon dioxide increases rapidly at the critical density as the critical temperature is approached from higher temperatures. Relatively large increases were observed only at temperatures less than 10 °C above the critical temperature, and over a density range between 0.30 to 0.60 g/cm^3. The corresponding pressure change is 3.4 atm at 32.054 °C. Thus most prior measurements have not included much of the region where the phenomenon occurs.

The transport of heat by convection was very high for the measurements near the critical density at 32.054 °C. However, the limiting temperature difference for the transition to turbulent flow is high enough that extrapolation procedures should be valid.

It is estimated that the thermal conductivity values at low and high densities have high accuracy. At low densities, the values have the sort of temperature dependence that is regarded as typical of the thermal conductivities of dilute gases. However at densities above $\rho = 0.74$ g/cm^3, essentially no temperature dependence is manifested from 3.66 to 75.26 °C.

9. References

[1] S. Naldrett and O. Maass, Can. J. Research **18B,** 322 (1940).

[2] A. Michels, A. Botzen, and W. Schuurman, Physica **23,** 95 (1957).

[3] W. Sellschopp, Forsch. Gebiete Ingenieurw, **5B,** 162 (1934).

[4] L. M. Lenoir and E. W. Comings, Chem. Eng. Prog. **47,** 223 (1951).
[5] D. L. Timrot and V. G. Oskolkova, Izvestia V. T. I., No. 4 (1949).
[6] L. A. Guildner, J. Research NBS, **66A** (Phys. and Chem.), No. 4, p. 333 (1962).
[7] S. C. Collins, Rev. Sci. Inst. **7,** 502 (1936).
[8] A. W. Hull, Gen. Elec. Rev. **32,** 390 (1929).
[9] O. C. Bridgeman, J. Am. Chem. Soc. **49,** 1174 (1927).
[10] A. Michels and C. Michels, Proc. Roy. Soc. (London) **A153,** 201 (1935).
[11] A. Michels, B. Blaisse, and C. Michels, Proc. Roy. Soc. (London) **A160,** 358 (1937).
[12] R. Wentorf, Jr., J. Chem. Phys. **24,** 607 (1956).
[13] J. V. Sengers and A. Michels, Prog. in Int. Res. on Thermodynamics and Transport Properties 434, ASME, Academic Press 1962, New York, N.Y.

(Paper 66A4–169)

JOURNAL OF RESEARCH of the National Bureau of Standards—A. Physics and Chemistry
Vol. 66A, No. 4, July–August 1962

Derivation of the Relaxation Spectrum Representation of the Mechanical Response Function

Robert S. Marvin*

(April 3, 1962)

Relaxation spectra have been used in both the presentation and interpretation of measurements of the mechanical properties of rubberlike polymers.

Relaxation spectra have been widely used in both the presentation and interpretation of measurements of the mechanical properties of rubberlike polymers. They are generally introduced in terms of a more or less specific model representing linear viscoelastic behavior, since the a priori assumption of a spectrum of a certain form is equivalent to assuming a certain model representation for mechanical response.

Ordinarily the derivation of such functions is based on the assumed equivalence of the mechanical response of a material to the response of an assembly of ideal springs and dashpots. And indeed it can be shown rigorously that any linear response is equivalent to the response of some such array if one admits certain limiting cases analogous to the familiar electrical cable with distributed resistance and capacitance. However, the proper form for the spectrum, whether it should be an integral or a sum, is not determined by this approach, but is arbitrarily assumed depending on the type of analysis preferred.

This ambiguity is not particularly serious for any practical application, since our experimental measurements are seldom precise or extensive enough to permit us to distinguish experimentally between the two forms. It is, however, quite possible to define the spectra unambiguously in terms of a relation between the transient and steady-state functions which must hold whenever the behavior is linear and the Boltzmann superposition principle applies. Moreover, this development automatically determines the nature of the spectrum in terms of the singularities of the steady-state response function, and yields directly an algebraic relation giving the spectrum exactly if the response function is known or assumed in analytic form.

The basic definition of the mechanical response function of a material is considered here to be that obtained from experimental observation. For a linear passive material either the response to a force which is a unit step function of time, $G(t)$, or the steady-state response to sinusoidal force, $G^*(i\omega) \equiv G'(\omega)+i\,G''(\omega)$, will completely define the response in shear. In principle $G(t)$, $G'(\omega)$, and $G''(\omega)$ can be measured for all real positive times, t, or frequencies, ω, and we shall assume that both functions are known, are bounded, and are reasonably smooth. Since we are considering relaxation-type behavior, we shall further assume that $G(t)$ is monotonic nonincreasing and contains no oscillatory terms which would characterize resonance- or damped resonance-type response.

We define a function $G^*(p)$, with $p=s+i\omega$, by analytic extension of $G^*(i\omega)$ from its line of definition. By a somewhat lengthy argument involving energy considerations it can be shown that the singularities of $G^*(p)$ are confined to the negative real axis including the origin. This same conclusion can be reached from a consideration of the relation between $G^*(p)$ and $G(t)$, established through the Carson transformation

$$G^*(p)=p\int_0^\infty G(t)\,\exp\,(-pt)dt$$

and its inverse

$$G(t)=\frac{1}{2\pi i}\int_{c-i\infty}^{c+i\infty}[G^*(p)/p]\,\exp\,(pt)\,dp. \qquad (1)$$

Since $G(t)$ is defined for all real $t\geq 0$, and has been assumed to have the character of a relaxation-type response, the singularities of $G^*(p)/p$ must be confined to the negative real axis, including the origin. Moreover, if these singularities are poles they must be of first order, since any higher order poles would lead to terms in $G(t)$ of the form $t^b e^{at}$, inconsistent with relaxation-type behavior. If these singularities are simple poles, $G(t)$ will be given by a sum of terms of the form $r_n \exp\,(s_n t)$, $s_n \leq 0$, where the sum may be either finite or infinite. This may be written in terms of a relaxation spectrum, $h(\lambda)$, as

$$G(t)=\int_0^\infty h(\lambda)\,\exp\,(-\lambda t)d\lambda \qquad (2)$$

if we take

$$h(\lambda)=\sum_n r_n\delta(\lambda+s_n). \qquad (3)$$

The various molecular theories of viscoelastic behavior yield expressions of this form. However, a continuous spectrum is consistent with our assumptions, and will be found if $G^*(p)$ is characterized not by poles but by a branch cut along a portion or the whole of the negative real axis. Since the various approximation methods for obtaining a spectrum

*Present address: Department of Polymer Chemistry, Kyoto University, Kyoto, Japan.

from the measured response functions ordinarily yield a continuous spectrum, it is of interest to see how this can be derived.

If $G^*(p)$ contains a branch cut, the contour of eq (1) may be deformed and the integral written as

$$G(t)=(1/2\pi i)\lim_{\rho\to 0}\lim_{\epsilon\to 0}\left\{\int_{-\infty}^{-\sqrt{\rho^2-\epsilon^2}}[G^*(s-i\epsilon)/(s-i\epsilon)]\exp[(s-i\epsilon)t]ds+i\int_{-a}^{a}G^*(\rho e^{i\varphi})\exp(\rho t e^{i\varphi})d\varphi+\int_{-\sqrt{\rho^2-\epsilon^2}}^{-\infty}[G^*(s+i\epsilon)/(s+i\epsilon)]\exp(s+i\epsilon)t]ds\right\} \quad (4)$$

where $a=(\pi/2)+\cos^{-1}(\epsilon/\rho)$.

The second term of (4) yields $G^*(0)=G(\infty)$. The first and third terms can be combined, using the fact that G^* of p-conjugate equals the conjugate of $G^*(p)$, to give:

$$G(t)-G(\infty)=(1/\pi)\int_0^{-\infty}ds(e^{st}/s)\lim_{\epsilon\to 0}\operatorname{Im}G^*(s+i\epsilon)=\int_0^{\infty}d\lambda\exp(-\lambda t)h(\lambda), \quad (5)$$

where

$$h(\lambda)=\pm(1/\pi\lambda)\lim_{\epsilon\to 0}\operatorname{Im}G^*(-\lambda\pm i\epsilon). \quad (6)$$

This will be a continuous function of λ over the region of the branch cut. If applied to a function characterized by simple poles it will yield zero for $h(\lambda)$ except at the poles where Im $G^*(p)$ goes to infinity.

The same procedure can be used to define the retardation spectrum from the relation between $j(\infty)-j(t)$ and its transform, where $j(t)$ is the recoverable part of the creep function $J(t)$.

The algebraic relation (6) was derived by Gross [1] by a less direct method starting from the integral giving $G^*(i\omega)$ in terms of $h(\lambda)$.

[1] Bernhard Gross, Mathematical Structure of the Theories of Viscoelasticity. pp. 31-33 Hermann and Cie, Paris (1953).

(Paper 66A4-170)

JOURNAL OF RESEARCH of the National Bureau of Standards—A. Physics and Chemistry
Vol. 66A, No. 4, July–August 1962

Intermediate Phases in Superconducting Niobium-Tin Alloys

L. L. Wyman, J. R. Cuthill, G. A. Moore, J. J. Park, and H. Yakowitz

(April 13, 1962)

In attempting to produce superconducting wire of the niobium sheath Nb_3Sn core type, it became apparent that results were generally unpredictable. Metallographic examination showed that such materials are heterogeneous and contain a number of intermediate phases. Detailed metallographic studies were made on diffusion zones in which tin had been allowed to react with porous niobium blocks, with fused niobium rod, and with niobium wires, and on a number of reacted powder mixtures.

The phases produced were identified by anodizing to characteristic colors and by microspot analysis, supplemented by some hot-stage microscope and thermal analysis tests. On the basis of these observations, a tentative revised diagram is offered to illustrate the types of reactions which occur in the system.

The presumably desired phase, Nb_3Sn, is found to lie between the more easily formed phases Nb_6Sn and Nb_2Sn_3, which are stable to temperatures well above the peritectoid decomposition of the Nb_3Sn. At lower temperatures the compound Nb_2Sn is formed. It is indicated that the high-temperature treatment to react niobium and tin should be followed either by very slow cooling or by an anneal in the 600 to 700 °C range to form Nb_3Sn.

1. Introduction

When the results from the initial investigations of the superconducting properties of the niobium-tin alloy "Nb_3Sn" were first disclosed, the Chemical Metallurgy Section was requested by the NBS Cryogenic Engineering Laboratory at Boulder, Colo., to produce some of this material. This was accomplished in a manner subsequently revealed in the initial report of Kunzler et al., [1] [1] concerning the properties of this material. The outstanding performance of this NBS-produced wire was disclosed by Arp, Kropschot, and Wilson [2].

Although the original objective had been the attainment of an alloy, or rather an intermetallic compound of "β-Tungsten" structure, having the composition Nb_3Sn, the actual result of the processing of the material was shown by preliminary metallurgical investigations to be something quite different. The fact that the alloys prepared by any of several methods consisted of from four to six or seven different metallurgical constituents has been known and privately reported by this and other metallurgical laboratories.

This disclosure has profound significance in several areas. It must be recognized that we have not been dealing with a directly formed homogeneous material. Also, if it is correct to assume that only the Nb_3Sn phase has the desired superconducting properties, a minimum requirement is to achieve a continuity of this phase throughout the length of the conductor. A simplified "filament" or "thread" hypothesis, which tacitly assumes that when the resistivity is zero an infinitely small conducting path can carry an infinitely large current, is not sufficient to characterize a practical superconductor; it does not take into account the concept of "quality," whereby one specimen can carry more current, or resist a higher magnetic field, than can another specimen of the same size. Nevertheless, one can presume that any superconducting alloy wire does not necessarily need to be homogeneous, but does at least require one or more continuous paths of the desired superconducting constituent throughout the length of the conductor.

Initially, the superconductor, Nb_3Sn, was prepared by Matthias [3] who described its electrical properties. At a later date, Kunzler [1] arrived at several modes of Nb—Sn alloy preparations and treatments. However, the metallurgist realized, from previous experience with other systems, that treatment of niobium, with its extremely high melting point, and of tin, with its extremely low melting point, at temperatures far from the melting point of either could only result in extreme heterogeneity.

Experience in other laboratories had shown that, not infrequently, wires produced in the manner suggested by Kunzler failed to show the desired superconducting properties. As a consequence of all of these factors, it became evident that the physical metallurgy of this alloy formation would need to be carefully investigated if the process were to be adequately controlled. Previous to the interest in its superconducting properties, this alloy system had received but little metallurgical attention. A constitutional diagram of the binary Nb—Sn system was proposed by Savitskii et al. [4], figure 1. The only constituent shown, other than the terminal phases of the component metals, is the intermetallic compound Nb_3Sn, which is indicated as having been

[1] Figures in brackets indicate the literature references at the end of this paper.

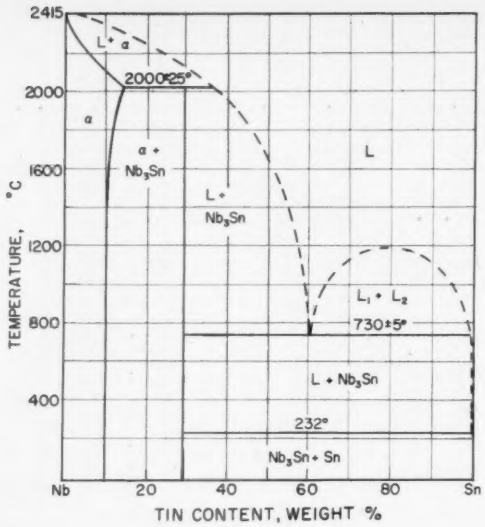

FIGURE 1. *Constitution diagram of the niobium-tin system according to Savitskii et al., [4].*

formed by a peritectic reaction near 2000 °C. These authors detected a reaction horizontal near 730 °C which they attribute to the presence of a monotectic between two tin-rich liquids.

The Savitskii diagram is certainly not compatible with the large number of phases which have been observed by microexamination of the alloy wires. Thus, the system must be further studied in order to identify positively the various phases and to establish the conditions for their formation.

2. Experimental Procedure

Rather than endeavoring to use the extremely fine wires prepared for superconducting experiments as subjects of metallurgical study, it was decided to use massive specimens. Diffusion studies were conducted using semi-sintered bars made from rather coarse-grained niobium powder.[2] These were partially immersed in baths of molten tin for periods of from 4 to 400 hr at temperatures ranging from 700 to 1,200 °C. Also, in each bath was placed a specimen of 1/4-in.-diam wrought electron-beam melted niobium.[3]

The choice of the porous niobium bar was fortuitous because it provided two simultaneous experiments. First, by capillary action the molten tin was drawn up to fill all of the interstices in the niobium; thus the upper part of the bar represented conditions in the system where the amount of tin was limited. Second, the bottom of the specimen and the surfaces of both the porous bar and the wrought rod represented the tin-rich side of the system. In addition to these diffusion specimens, other specimens were prepared by compressing and sintering mixed powders and by fusion of the components. All of the resulting structures were heterogeneous.

The metallographic study of these materials was greatly facilitated by the use of anodic oxidation techniques suggested by Dr. M. L. Picklesimer of the ORNL. This procedure is an adaptation of a method first used for the study of zirconium hydrides [5]. Application of this technique imparts distinctive colors to the various microconstituents. These colors are uniform for each constituent for a single specimen and anodizing condition, but can be varied considerably by changes in the anodizing conditions. To prevent confusion in phase identification, the anodizing must be accurately controlled.

To eliminate polemic discussion between different observers examining the same or different microsections, it was decided to standardize the anodization of the present group of specimens so that niobium metal assumes a "Light Beryl Blue" coloration. To avoid use of multiple names for similar colors, it was agreed that the colors obtained under these conditions best match the colors in the Maerz and Paul Dictionary of Color [6] as follows:

Nb	Light Beryl Blue	Plate 33, E–1
Nb_4Sn	Calamine Blue	Plate 33, J–2
Nb_3Sn	Orient	Plate 36, D–11
Nb_2Sn	Purple Aster	Plate 43, J–7
Nb_2Sn_3	Burnt Sienna	Plate 5, F–12
Sn	Chrome Lemon	Plate 9, K–2
Impurity	Wistaria	Plate 41, E–8

In order to verify the chemical compositions of the observed phases, numerous areas were subjected to microspot analysis on the NBS electron probe, a description of which is currently in preparation [7].

A number of the microstructures resulting from the reaction of powder mixtures of known composition are the subject of a concurrent quantitative metallographic analysis by means of a digital computer. These methods have recently been outlined by Moore, Wyman, and Joseph [8]. In this current work, color separation prints, showing each phase separately, are made from color photomicrographs, or alternately from color separation negatives made directly on the microscope. Each phase separation print is then scanned into the computer and analyzed for the total amount of that particular phase, the continuity or connectivity of the phase, and the mean free path for linear motion within the phase areas. Details of this effort will be described in another report. Some preliminary results of this quantitative metallographic study have been drawn upon in estimating the probable position of some of the phase boundaries indicated in this paper.

It may be of interest to note here that one such analysis was made on a color micrograph, furnished by Dr. Picklesimer, representing a selected "bad" section of a commercial Nb sheathed "Nb_3Sn" powder process wire. This section had been given a minimal reaction treatment prior to showing poor electrical properties, but other sections of the same

[2] NBS spectrochemical analysis indicated the following impurity elements: 0.01–0.1% Fe, Si; 0.001–0.01% Al, Ca, Cr, Cu, Mg, Ni; less than 0.001% Ag, B, Mn, Pb, Pt, Ta, Ti.

[3] NBS spectrochemical analysis indicated the following impurity elements: 0.01–0.1% none; 0.001–0.01% Cr, Fe, Mg, Si; less than 0.001% Ag, B, Ca, Cu, Ni, Pt.

wire, given a more complete reaction, showed a normal superconducting quality. The "bad" area was found to contain 70 volume percent of the Nb_3Sn phase, of which at least 99 percent is interconnected by one or more circuitous paths, at least within the area of the micrograph. However, the mean free path within the Nb_3Sn phase, in a direction parallel to the axis of the wire, is only 0.027 mm. These results appear to indicate that the existence of a threadlike continuous path of convoluted shape is not in itself sufficient to guarantee useful superconducting properties; it would rather appear highly desirable to obtain wires so processed as to maximize the proportion of Nb_3Sn in the structure and produce a high level of simple linear connectivity between the particles of this phase.

3. Results

Due to the fact that these initial experiments were conducted for the purpose of simulating thermal treatments which had previously produced good superconductor wire, the subsequent observations must be considered from this viewpoint, that is, as but preliminary results.

The diffusion studies have shown that the niobium-rich side of the system quite readily forms the intermetallic compound Nb_4Sn, whereas the tin-rich side of the system forms the compound Nb_2Sn_3. Between these two compounds, one finds the compounds Nb_3Sn and Nb_2Sn. Additionally, there is a eutectic between Nb_2Sn_3 and the Sn-rich terminal phase occuring at about 215 °C and near 83 percent[4] Sn.

3.1. Nature of the Nb_4Sn Phase

Preliminary studies of the melting of a specimen previously identified as consisting predominantly of Nb_4Sn revealed partial fusion at $1{,}950 \pm 50$ °C as determined with an optical pyrometer. Due to thermal gradients in the specimen, some portions were probably somewhat hotter, and in such an area subsequent microscopic examination revealed dendritic structure interspersed with small amounts of eutectic structure (fig. 5).

These observations lead to the conclusion that the compound Nb_4Sn melts congruently near 2,050 °C and that it forms a eutectic with the niobium terminal solid solution; the eutectic composition presumably is located near to that of the compound.

3.2. Electron-Probe Microanalyzer Measurements

The identification of the phases in the system was carried out primarily with the NBS electron-probe. After the specimens had been subjected to the anodic oxidation technique, the composition of each "color" was determined. The results are listed in table 1. Column 3 shows the actual probe results and their average, while column 4 shows the phase assigned to the color.

3.3. Metallographic Evidence for a Continuous Nb_3Sn Filament

In general, when a niobium block is immersed in molten tin and then slowly cooled from above 700 °C the surface becomes converted to Nb_4Sn, which gradually and uniformly penetrates the block. As the process continues, there is an irregular outward growth into the Sn. Upon cooling, the tin-rich areas of this zone transform to Nb_3Sn. Additionally, the tips of the fingerlike Nb_3Sn areas show the Nb_2Sn_3 phases growing crystals into the molten tin. Also, discrete crystals of Nb_2Sn_3 can be observed dispersed in the last areas to freeze.

If a continuous "filament" of Nb_3Sn is essential for superconductivity, conditions for its proper formation must be such that there are enough niobium particles in the mass to permit their surfaces to react, forming Nb_3Sn, and that these surface layers must form mutual contact in order to attain continuity throughout a wire length.

[4] All percentages in this paper are atomic percentages.

TABLE 1. *Results obtained by means of electron-probe microanalysis*

Treatment	Color analyzed	Results (atomic percent Sn)	Phase
34 hr at 1,200 °C+W.Q.	Calamine blue	22.3; 21.5; 19.4; 21.0→Av 21.0	Nb_4Sn
	Impurity	0 (60-70 Atomic percent Nb)	Nb_2N (?)
8 hr at 1,200 °C+S.C.	Eutectic in Sn	83.6; 83.3→Av 83.4	
8 hr at 1,000 °C+S.C. (wire in tube)	Offshore needles in Sn (fig. 10)	22.6	Nb_4Sn
Reaction tube held at 800 °C+W.Q. Nominal 25% Sn.	Calamine blue (matrix)	17.0; 23.2; 24.4; 18.5;→Av 20.8	Nb_4Sn
32 hr at 900 °C+S.C.	Orient	24.7; 28.5; 27.1→Av 26.8	Nb_3Sn
	Burnt sienna	58.7	Nb_2Sn_3
400 hr at 750 °C+S.C.	Orient	26.5	Nb_3Sn
	Burnt sienna	59.0	Nb_2Sn_3
200 hr at 700 °C+S.C. [Run (1)]	Burnt sienna	60.4; 61.6; 61.0; 62.1; 59.7→Av 61.0	Nb_2Sn_3
200 hr at 700 °C+S.C. [Run (2)]	Burnt sienna	59.3; 58.3; 60.5; 58.0; 60.5→Av 59.3	Nb_2Sn_3
Reaction tube held at 600 °C+S.C. Nominal 35% Sn.	Purple aster	29.9; 29.3; 29.2; 30.2; 32.3→Av 30.2	Nb_3Sn
	Calamine blue (matrix)	21.8; 21.1; 18.6; 19.5→Av 20.6	Nb_4Sn
	Orient	25.1	Nb_3Sn

The interiors of many of the porous bars were replete with examples of this action. However, the most striking example was one in which the periphery of a ¼-in.-diam rod specimen became united with the flat surface of a porous bar during a 16 hr treatment at 1,200 °C, with subsequent furnace cooling. In this specimen the tangential interface was mainly Nb_3Sn, with thin layers of underlying Nb_4Sn on each of the niobium bodies (fig. 6). Progressing away from the tangent area into the "V's" showing remaining Sn, the layers on each niobium piece retained both the Nb_4Sn and Nb_3Sn and also revealed Nb_2Sn_3 needles forming on the Nb_3Sn and growing into the Sn.

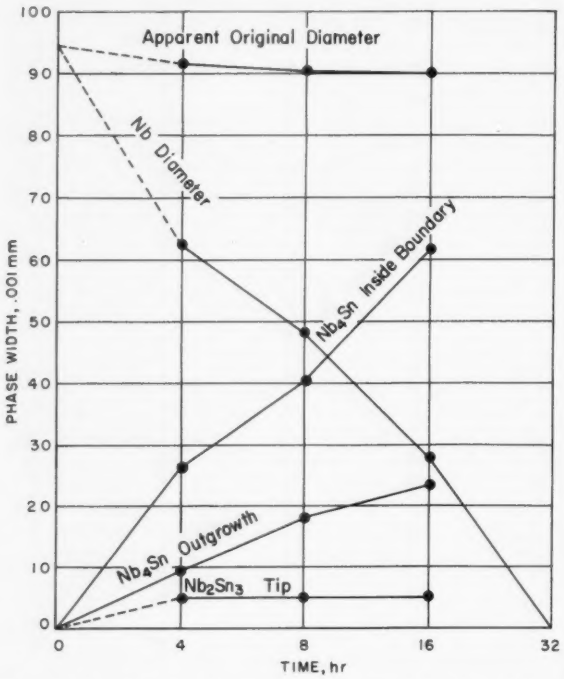

FIGURE 2. *Growth of reaction layers on 0.004-in. niobium wires versus time in molten tin at 1,000 °C followed by furnace cooling.*

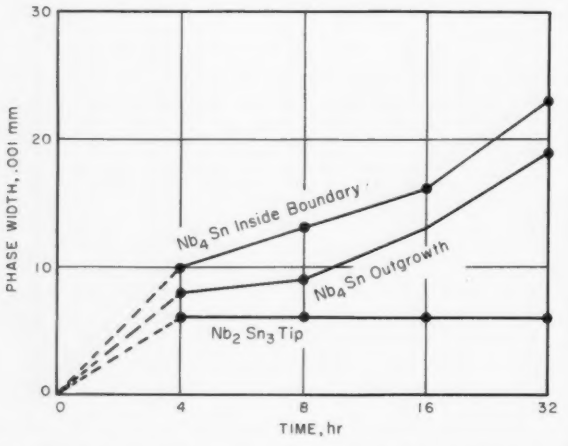

FIGURE 3. *Reaction depths on the interior of the niobium shell versus time in molten tin at 1,000 °C followed by furnace cooling.*

3.4. Reaction of Niobium Wires in a Bath of Tin at 1,000 °C

In another set of experiments, small niobium wires were threaded into a ⅛-in.-I.D. niobium tube and the tube then filled with Sn. These specimens were treated for periods of 4, 8, 16, and 32 hr at 1,000 °C, the latter being water quenched, and the others furnace cooled.

The alloying in these specimens progressed in quite the same manner as that previously described. In addition, the Nb_4Sn "grew" out beyond the limits of the original niobium wire area and in turn developed the Nb_3Sn and Nb_2Sn_3 layers (fig. 7).

The 32-hr water quenched specimen revealed a completely new condition because from 43 wires originally within the tube, there remained but one very small speck of niobium surrounded by a few islands of Nb_4Sn.

Rough measurements were made of the progress of the reaction layers in this series of treatments, the results being shown graphically in figure 2. Similar measurements of reaction depths on the interior of the niobium tube are shown in figure 3. The extent of the Nb_3Sn layer could not be measured due to the quite irregular nature of the surface. However, this phase was observed to be present in the 4-, 8-, and 16-hr specimens as a narrow zone of variable thickness lying between the overlying Nb_2Sn_3 crystals and the underlying Nb_4Sn.

This wires-in-tube experiment points out the possibility of a new means of fabricating the Nb-Sn complex in such manner as to more completely insure a continuity of the Nb_3Sn phase throughout the entire length of the wire.

3.5. Diffusion Studies

The diffusion specimen which was water quenched after 32 hr at 1,200 °C (fig. 9) showed quite large amounts of Nb_4Sn in the reaction zones, together with infrequent crystal tips of Nb_2Sn_3, but no Nb_3Sn or Nb_2Sn. In contrast to this, the furnace cooled specimen had a reaction zone predominantly Nb_3Sn with frequent Nb_2Sn_3 tips (fig. 8).

In most of the slow-cooled specimens from the initial 700 to 1,200 °C diffusion series there was a distinct but very narrow band of precipitate in the tin at a short distance from the Nb-Sn reaction surface. At the higher treatment temperatures, distinct needles were observed in this band. From their position, these needles were at first expected to be a high tin phase, but they were subsequently identified by color comparison in normal and in polarized light, and by electron probe analysis, as being composed of Nb_4Sn (fig. 10).

Previous mention was made of the observation that the water-quenched wire-in-tube specimen

treated 32 hr at 1,000 °C revealed only a trace of niobium together with small particles of Nb_4Sn. No Nb_3Sn was in evidence. Similarly, in the diffusion series held at 1,000 °C, the 4-, 8-, and 16-hr slow-cooled specimens displayed islands of Nb_3Sn and a bit of Nb_2Sn_3 in the Nb_4Sn bands (fig. 8).

After studying the microsections from the various diffusion experiments, the fact became evident that the Nb_3Sn phase can form quite readily from the Nb_4Sn phase on slow cooling. Quenched specimens retain only the Nb_4Sn.

As compared with the long diffusion times required to convert niobium particles or wires to Nb_4Sn, the conversion of Nb_4Sn to Nb_3Sn appears to proceed too rapidly to allow the diffusion of an additional 5 percent of tin into the converted areas. Such a difference might be expected if the Nb_4Sn phase dissolves excess tin, and thus approaches the Nb_3Sn composition.

Evidence of width for the Nb_4Sn phase was obtained by making electron-probe traverses across Nb_4Sn areas on a specimen quenched from 1,200 °C. The analytical values so obtained indicated a composition gradient of about 6 percent within the Nb_4Sn areas. This would place the tentative limits of the Nb_4Sn phase region at 17 and 23 percent at 1,200 °C, and confirm that only a small amount of additional tin is required for conversion to the Nb_3Sn phase.

3.6. Thermal Analysis

A specimen of nominal "Nb_2Sn_3" composition was subjected to thermal analysis (direct time versus temperature). This powder mixture had been pressed at 150 °C and 100,000 psi prior to loading into the furnace. The sample gave reproducible thermal arrests on three separate but continuous heating and cooling runs at 3 °C/min. Two thermal arrests on cooling occurred at 922 ±5 °C and at 863 ±5 °C and were easily detected from the temperature recording. The sample was later prepared for metallographic observation and it exhibited the Nb, Nb_4Sn, Nb_3Sn, Nb_2Sn_3 phases in an excess of Sn (figs. 11, 12).

Additional thermal analyses were run on pressed pellets of "Nb_3Sn" composition, but, in general, no strong arrests were noted. However, in one instance in which the sample was being held at a steady temperature near 1,150 °C, the furnace winding burned out and consequently the specimen cooled more quickly than the usual rate. During this cooling, the temperature record showed a definite arrest at 743 °C.

TABLE 2. *Results of thermal analysis*

Sample	Cooling rate	Arrest Temperature	
Compressed "Nb_2Sn_3" mixture	3 °C/min	917 °C	858 °C
		927	867
		924	867
Compressed "Nb_3Sn" mixture	4 °C/min	743	

The thermal analysis data have been interpreted to assign the 863 ° C temperature as the peritectic temperature of the Nb_2Sn_3 compound and the 922 °C temperature as the liquidus for this composition. The 743 °C arrest on a quick cool is probably near the peritectoid temperature of the Nb_3Sn compound. The results are shown in table 2.

3.7. High-Temperature Metallography

In a further attempt to reveal the reactions occurring in this system, a microsection containing a wide vein of Nb_2Sn_3 with side veins of Nb_4Sn and Nb_3Sn was removed from the diffusion specimen treated for 200 hr at 700 °C. This section was mounted in the high-temperature stage of a metallurgical microscope in a purified argon atmosphere and kept under observation during a 3-hr heating to an indicated 930 °C.

No significant changes were observed up to 450 °C. However, from this temperature up to 693 °C there were grain-boundary changes in the Nb_2Sn_3, and some changes in the Nb_4Sn and Nb_3Sn side veins. At 693 °C the narrow band ($Nb_3Sn + Nb_4Sn$) between the Nb_2Sn_3 and the niobium appeared to be more clearly defined and slightly wider. Between 693 and 735 °C a new phase believed to be Nb_3Sn had made its appearance at the Nb—Nb_2Sn_3 interface and had grown slightly into both phases. During the course of the heating, the noble-metal thermocouple, located adjacent to the specimen, indicated a brief arrest at 863 °C. As heating continued, this new phase grew until, at 930 °C, it had gradually covered the entire field of view.

At this point, the specimen was given a "gas-quench," resulting in a fairly rapid drop in temperature, probably of the order of 400 °C the first minute.

Microscopic examination of the specimen after removal from the furnace failed to provide further information, due to surface roughness. Also, the usual anodizing procedure failed to give response. As a consequence, the specimen was remounted, very lightly repolished, and then anodized. The structure then revealed a mixture of Nb_4Sn and Nb_3Sn scattered through the niobium grains, with the original vein of solid Nb_2Sn_3 terminating as a heavily voided area of dendritic appearance.

3.8. General Nature of the System

During the course of these investigations, several generalities have evolved which indicate the type of system under study, as well as some of the difficulties to be anticipated in finally determining the facts concerning the several reactions and their rates. For example, there is considerable evidence that the formation of Nb_3Sn, Nb_2Sn, and Nb_2Sn_3 is a function of the rate of cooling from temperatures above the decomposition temperatures for these compounds. As a consequence, it is essential to the controlled formation of Nb_3Sn that the characteristics of the decomposition reactions be determined.

In this connection, accumulated observations made during the course of these investigations give some indications as to the nature of these reactions. Thus, the unexpected and repeated observance of three or four phases after long-term thermal treatments clearly reveals the sluggishness of some of these reactions. Furthermore, this offers a significant

reason for the observation that the reaction horizontals are difficult to detect by thermal analysis.

The original series of diffusion experiments revealed limited ranges of stability for Nb_2Sn_3, Nb_2Sn, and Nb_3Sn. The Nb_2Sn_3 phase, appearing as a band at the reaction interface, is much more abundant at 700 °C than at higher temperatures. In the range from 750 to 900 °C this layer becomes thinner and discontinuous. In slowly cooled specimens from the higher temperatures, Nb_2Sn_3 is usually found only at the tips of Nb_3Sn protuberances extending into the tin-rich liquid, or in pockets where tin has been trapped between niobium particles. These structures can be explained if Nb_2Sn_3 decomposes thermally at some temperature below 900 °C, and if, at lower temperatures, it reacts with niobium or Nb_4Sn to yield Nb_3Sn and Nb_2Sn.

The Nb_3Sn phase, in turn, while generally present in significant amounts in the reaction layers of slowly cooled specimens, was essentially absent from all of the quenched specimens. Specimens which originally contained identified Nb_3Sn, including a special powder mixture prepared for this purpose, contained extensive areas of Nb_3Sn after heating to temperatures as high as 1,000 °C and quenching from 800 °C or higher. These observations appear to contain numerous contradictions and leave the true decomposition temperature of Nb_3Sn most uncertain.

3.9. Reacted Stoichiometric Mixtures of Niobium and Tin

In an effort to fix more firmly the position of the lines defining the interactions of Nb_4Sn, Nb_3Sn, Nb_2Sn, and Nb_2Sn_3, a series of specimens of accurately predetermined composition were prepared for quantitative metallographic measurement by the digital computer [8]. Mixtures of niobium and tin powders, covering the range from 10 to 60 percent tin, were hot pressed into pellets and then pressed into niobium tubes. The mixtures were reacted at 1,000 °C, cooled to low temperatures to establish a new equilibrium, and then water quenched. Preliminary examinations of these series may be summarized as follows:

Specimens water quenched from 1,000 °C contained *only* niobium, Nb_4Sn, and a quenched liquid, not Nb_2Sn_3 crystals. The quenched liquid, by a preliminary material balance, appears to lie closer to 50 than to 60 percent Sn.

Specimens quenched from 800 °C were originally similar to the 1,000 °C specimens, with a few very small particles of Nb_3Sn mixed in with the particles of high tin material. Critical examination of the specimen containing 60 percent tin, made some weeks after quenching, showed large amounts of Nb_2Sn_3, which apparently was stable at 800 °C. In the lower tin ranges, residual particles of Nb_2Sn_3 or quenched liquid apparently had reacted with Nb_4Sn and niobium to form additional particles of Nb_3Sn.

Specimens quenched after 21 hr at 700 °C all showed considerable amounts of Nb_3Sn, which, however, had not yet replaced Nb_4Sn as the continuous phase. Thus these specimens were reacted *below* the decomposition temperature of Nb_3Sn, but as the reaction was proceeding slowly, it may be presumed that 700 °C is only slightly below this critical temperature.

Specimens slowly cooled after 18 hr at 600 °C showed both Nb_2Sn and Nb_3Sn in a matrix of Nb_4Sn. There were also a few particles of unreacted niobium. The identity of the Nb_2Sn phase was confirmed in this group of specimens by means of the electron-probe microanalyzer. These results are summarized in table 3.

TABLE 3. *Phases observed in reacted powder mixtures*

Mixtures pressed, reacted at 1,000 °C, and finished by final reaction listed

Final treatment		Nb	Nb_4Sn	Nb_3Sn	Nb_2Sn	Nb_2Sn_3	Quenched liquid
Temp.	Cooled	L. blue	C. blue	Orient	Aster	Sienna	
°C							
1,000	WQ	+	++	(n)	–	–	+
800	WQ	+	++	(n)	–	+	–
740	Q(1)	+	+	tr	–	+	–
715	Q(1)	+	+	++	–	tr	–
700	WQ	+	+	+	–	+	–
680	Q(1)	+	+	+	+	tr	–
600	F.C.	+	+	+	+	+	–

(1) Single small pieces of a thermal analysis specimen at 75% Nb, 25% Sn, water quenched. All others are summation of observations on 9 compositions.
(n) Some specimens, particulary these near 35% Sn, showed a few small spots of Nb_3Sn when first examined. Over several weeks, additional particles of Nb_3Sn grew at the interfaces between Nb_4Sn and Nb_2Sn_3.
+ Indicates presence.
++ Indicates presence in large amount.
tr Indicates trace.
– Indicates absence.

Thus, the decomposition temperature of Nb_2Sn_3 lies between 800 and 1,000 °C, and must of necessity be of the peritectic form, while the decomposition of the desired Nb_3Sn phase lies below 800 °C and can be associated with earlier evidences of changes near 730 °C. The reaction observed in this temperature range is now seen to be due to the peritectoid decomposition of Nb_3Sn into Nb_4Sn and Nb_2Sn_3, and not to a monotectic at higher tin composition as originally presumed by Savitskii et al.

One additional observation on the pressed powder specimens is significant to the present discussion. After the specimens quenched from 800 °C had been stored for some weeks, all of the residual niobium particles could be seen to contain a barely resolvable Widmanstatten structure covering all of the central areas and extending to within a short distance (around 0.002 mm) from the surface (which is generally in contact with Nb_4Sn). This structure indicates that Savitskii's estimate of relatively extensive tin solubility in the terminal niobium phase should be accepted for the high-temperature range. However, the solubility limit must retreat at lower temperatures in the manner of a typical precipitation hardening solution.

3.10. Friability in the Observed Intermetallic Phases

The hardness values for the three identifiable compounds have not as yet been determined. However, it was initially recognized by the early experimenters with Nb_3Sn that this compound was extremely brittle[1]. In fact, this brittleness is

highly detrimental to the processing of the wire into magnet windings because the slightest bending of a heat-treated wire will fracture the superconducting core. As a consequence, heat treatment *must follow* the coil forming.

Metallographic examination fully confirms this occurrence for it may be noted that areas of Nb_3Sn frequently abound with cracks. In addition to this, it was also noted that too much haste in specimen grinding resulted in the chipping out of Nb_3Sn areas.

The Nb_2Sn_3 phase exhibits a rather unusual friability. This phase is usually observed to form by outward growth into areas of the Sn-rich phase. In addition, individual crystals may be found in the Sn, adjacent to a reaction interface. The unusual feature to be noted is that both the "growing" crystals and the "free" crystals usually display severe cracking.

In contrast to these observations, the Nb_4Sn phase does not exhibit cracking, nor does it readily chip out during metallographic specimen preparation.

3.11. Impurity Inclusion in the Porous Niobium Bar

In addition to the phases so far identified, several of the diffusion couples have shown, in the porous niobium bar only, a streamerlike structure. These streamers appear as a wistaria color (fig. 9) when subjected to the anodic oxidation technique.

An attempt to determine the composition of these streamers was made by means of the electron-probe. The results showed that they contained no tin and about 60 to 70 percent Nb. Based on these data, it is felt that the streamers are extraneous to the binary system Nb-Sn. Furthermore, the wrought electron-beam melted niobium rod never showed these streamers or a phase of a color approximating wistaria. It is suggested that the probable identity of the streamers may be Nb_2N.

As the result of the investigations of the Nb-Sn binary system thus far conducted, the evidence clearly shows that the prior constitutional diagram is most incomplete. The tentative diagram shown in figure 4 is offered in its place as indicating the salient features of the system as shown by the investigations carried out to date.

4. Discussion

The present investigations have revealed several factors which are pertinent to any attempt to understand the physical metallurgy of the composite Nb—"Nb_3Sn" wires which have displayed such outstanding superconducting properties. Furthermore, the complete story of the physical metallurgy is essential to the process metallurgist in order that he may best fabricate this material, and to the physicist as a basis for further theoretical studies of superconductivity.

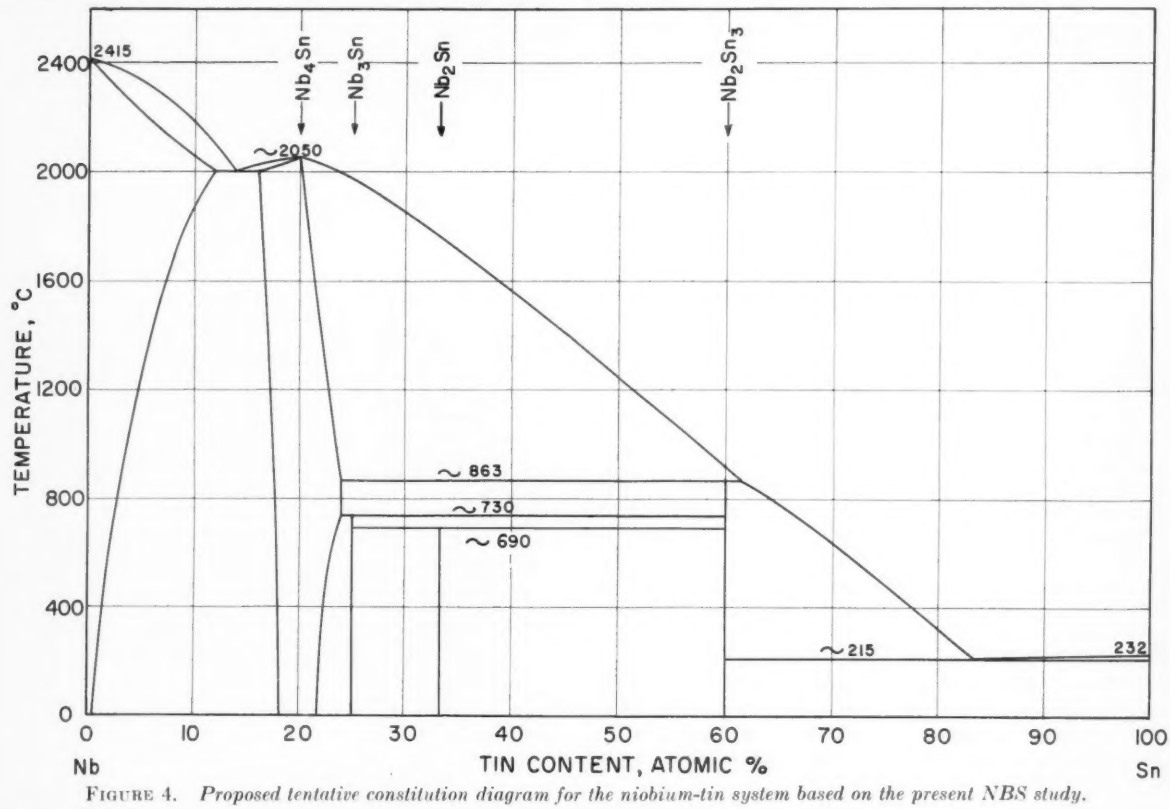

FIGURE 4. *Proposed tentative constitution diagram for the niobium-tin system based on the present NBS study.*

637358—62——7

Niobium and tin react quite readily to form Nb_4Sn at temperatures far below the melting point of the compound. On the other hand, practical experience has shown that the direct formation of the compound Nb_3Sn either by diffusion of tin into solid niobium or by fusion of the components, seldom meets with material success.

In diffusion experiments near 800 °C, Nb_2Sn_3 appears to form quite readily in layers at the Nb_4Sn—Sn interface, with crystals of Nb_2Sn_3 growing out into the tin and occasionally becoming detached. By contrast, the Nb_3Sn phase appears only as much thinner layers and is usually discontinuous.

This configuration can be expected when one realizes that the Nb_3Sn phase itself is not stable in this temperature range, and hence that the observed layer is found, on cooling, only in those areas where the composition is very close to 25 percent tin.

The extent of the areas which can transform directly to Nb_3Sn on cooling can be increased by control of the configuration of the niobium particles and of the degree to which the reaction with tin is allowed to progress. This control must prevent either excessive reaction with tin, which will produce reaction layers predominantly of Nb_2Sn_3, or excessive reaction of niobium, which will produce mainly Nb_4Sn. A diffusion reaction at or below 700 °C should avoid these undesirable reactions, but probably would require a very much longer reaction time than would be acceptable.

The problem of producing a homogeneous core of Nb_3Sn, either by fusion methods or by complete interaction of niobium and tin powders, involves first forming a mixture of Nb_4Sn and Nb_2Sn_3, followed by a peritectoid reaction between these products to form the Nb_3Sn.

The application of these phenomena to practical wire fabrication could take two distinct forms. If a continuous network of Nb_3Sn is sufficient to meet the requirements for superconductivity, niobium particles, preferably of elongated or fine niobium wires, may in effect be cemented together by a continuous film of Nb_3Sn. If the reaction is operated near 1,000 °C, the reaction time must be closely controlled in order to stop the reaction when material containing 25 percent Sn is most abundant. The amount of tin to be used in this case will be dictated in part by packing considerations, and might be well below 25 percent if much of the niobium is to remain unreacted.

If homogeneous Nb_3Sn must be produced, a mixture containing 25 percent tin may be reacted at or above 1,000 °C until the core is completely converted to Nb_4Sn and residual liquid. This mixture may then subsequently be annealed in the range 600 to 700 °C until the peritectoid conversion to Nb_3Sn is complete.

Probably the most significant practical result of this investigation will be to clarify the fact that the desired Nb_3Sn phase does not exist at the reaction temperatures normally employed in producing the superconducting complex. Thus, regardless of other details of fabrication, the attainment of a satisfactory superconducting structure will be directly associated with the rate of cooling from the reaction temperature; and, specifically, with the time that the material remains in the 600 to 700 °C range.

5. Conclusions

Current investigations of Nb—Sn superconducting materials have shown thus far that the Nb—Sn binary alloy system is much more complicated than had previously been assumed. A new constitutional diagram is proposed predicated from the results thus far obtained in the current investigations.

The intermetallic compound Nb_3Sn, which appears to be the desirable constituent for superconducting purposes, occurs between the compounds Nb_4Sn and Nb_2Sn_3, which are stable to considerably higher temperatures. At lower temperatures, the system is further complicated by the formation of Nb_2Sn.

This seriously complicates the problem of attaining either a continuous body of homogeneous Nb_3Sn throughout a conductor, or of obtaining a controlled type of heterogeneous structure which will give a continuously interconnected network of the superconductor. The successful preparation of either type of structure will require critical control of the preparation and heat treatment of the material in order to overcome the inherent difficulty in forming the desired phase.

The previously described investigations were instigated and were conducted under the auspices of the Cryogenic Engineering Section of the NBS Boulder Laboratories, R. B. Scott, Chief. The advice and assistance rendered by Messrs. Arp, Corruccini, and Kropschot of this group is most deeply appreciated. Thanks are also extended to Messrs. C. A. Owens, W. J. Hall, and B. T. Sanderson of this laboratory for the preparation of specimens.

6. References

[1] J. E. Kunzler, E. Buehler, F. S. L. Hso, and J. H. Wernick, Superconductivity in Nb_3Sn at high current density in a magnetic field of 88 Kgauss, Phys. Rev. Letters **6**, 89, (1961).

[2] V. D. Arp, R. H. Kropschot, and J. H. Wilson, Superconductivity of Nb_3Sn in pulsed fields of 185 kilogauss, Phys. Rev. Letters **6** (9), 452, (1961).

[3] B. T. Matthias, T. H. Geballe, S. Geller, and E. Corenzwit, Superconductivity of Nb_3Sn, Phys. Rev. **95**, 1435, (1954).

[4] E. M. Savitskii, M. I. Agafona, and V. V. Baron, The structure and properties of niobium-tin alloys, Izvest. Akad. Nauk S.S.S.R. Met. i Toplivo (Teklin) **1959** (5) 138–141 (in Russian).

[5] M. L. Picklesimer, Anodizing as a metallographic technique for zirconium base alloys, United States Atomic Energy Commission ORNL—2296, 13pp., (1957).

[6] A. Maerz and M. R. Paul, Dictionary of Color, McGraw-Hill Book Company, Inc., New York, New York (1930).

[7] J. R. Cuthill, L. L. Wyman, and H. Yakowitz, Metallurgical microanalysis by means of the electron probe, (in preparation).

[8] G. A. Moore, L. L. Wyman, and H. M. Joseph, Comments on the possibilities of performing quantitative metallographic analysis with a digital computer. Ch. from Quantitative Metallography, F. N. Rhines Ed. McGraw-Hill Co., in Press.

LEGEND

PHASE	DESIGNATION[+]	LOCATION	COLOR
Nb	Light Beryl Blue	Plate 33; E-1	
Nb_4Sn	Calamine Blue	Plate 33; J-2	
Nb_3Sn	Orient	Plate 36; D-11	
Nb_2Sn	Purple Aster	Plate 43; J-7	
Nb_2Sn_3	Burnt Sienna	Plate 5; F-12	
Sn	Chrome Lemon	Plate 9; K-2	
Impurity	Wistaria	Plate 41; E-8	

[+]See ref. 6

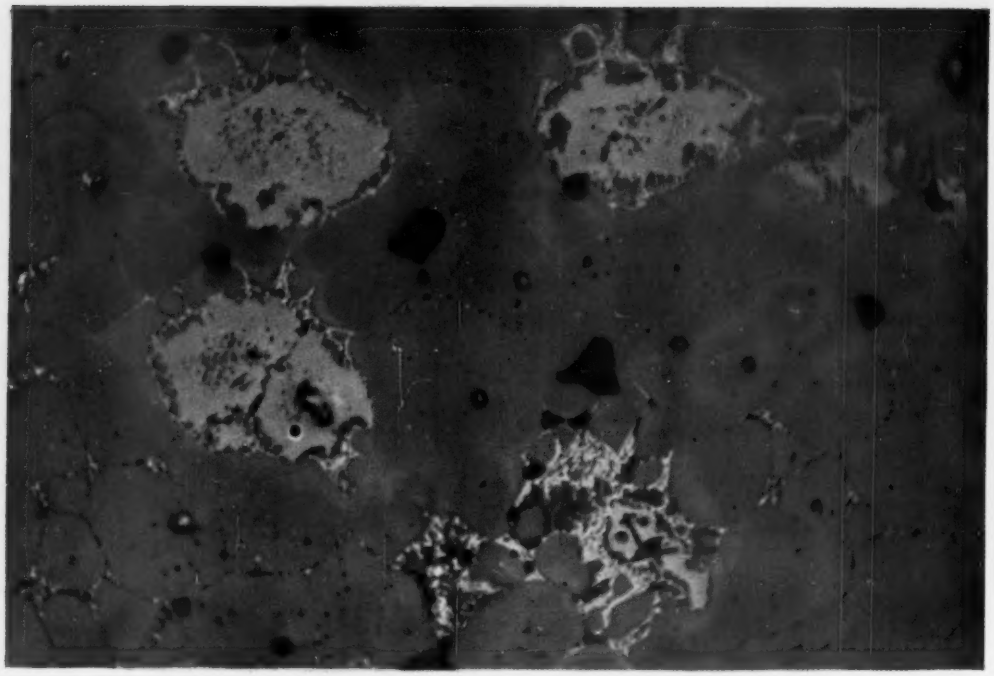

FIGURE 5. *Eutectic type structure developed between some free niobium and* Nb_4Sn *after reheating a specimen of nominal 80%* Nb—*20%* Sn *composition quenched from 800, to about 1,850 °C.*

The matrix is Nb_4Sn. X1000.

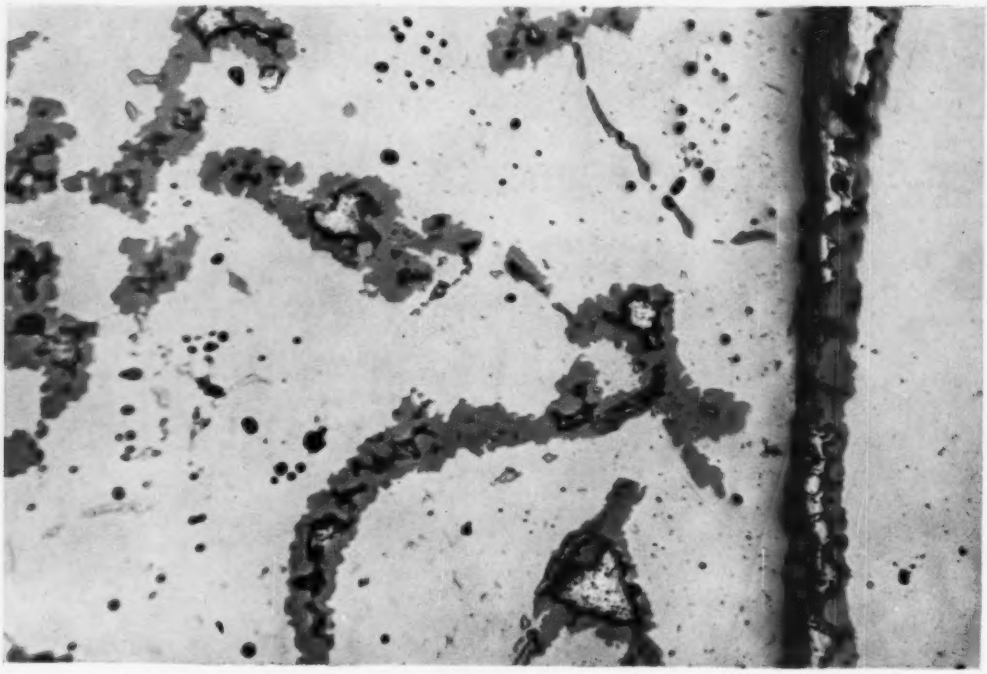

FIGURE 6. *Joint developed between the porous niobium bar (left) and the electron beam melted niobium rod (right).*

X100.

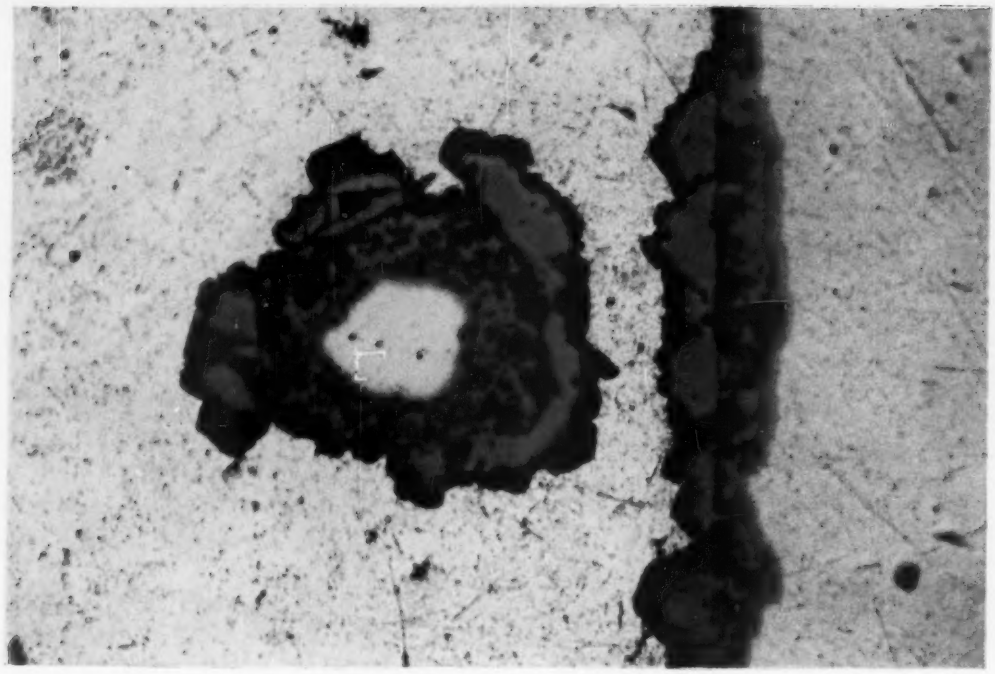

FIGURE 7. *Cross section of a nominal 0.004-in. niobium wire heated for 8 hr at 1,000 °C in a bath of molten tin and furnace cooled.*

The niobium shell is at the right. X500.

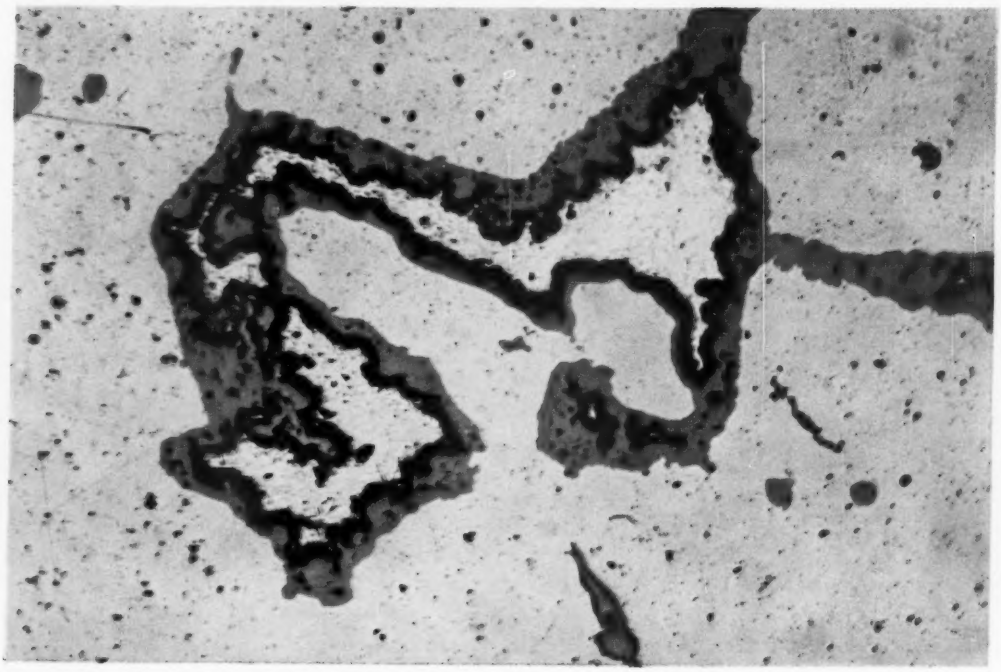

FIGURE 8. *Interior of porous niobium bar after diffusion in a bath of molten tin for 16 hr at 1,000 °C followed by furnace cooling.*

X200.

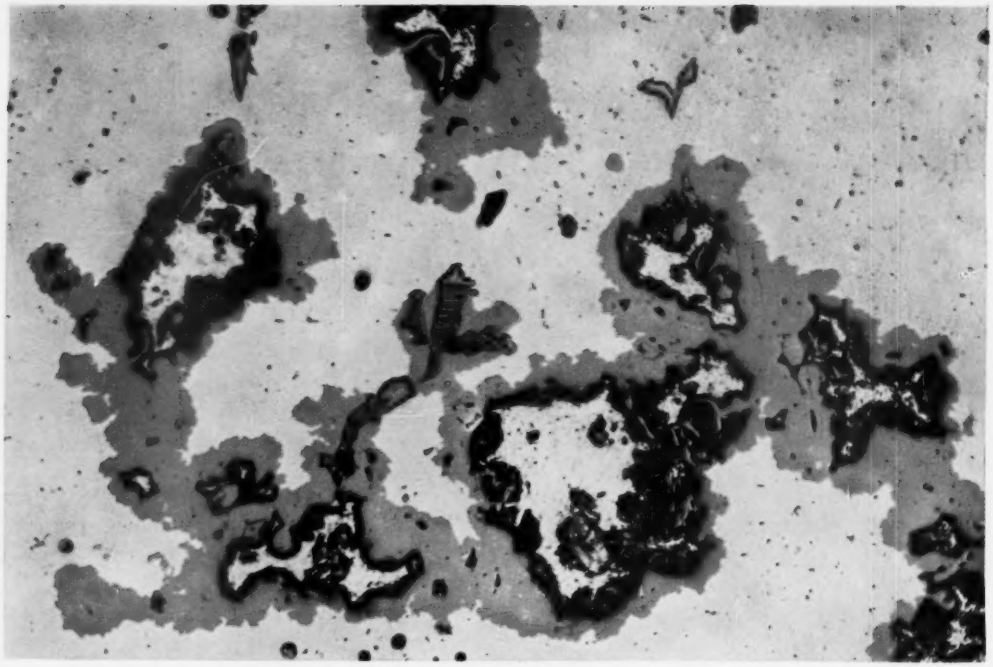

FIGURE 9. *Interior of porous niobium bar after diffusion in a bath of molten tin for 32 hr at 1,200 °C followed by water quench.*

X200.

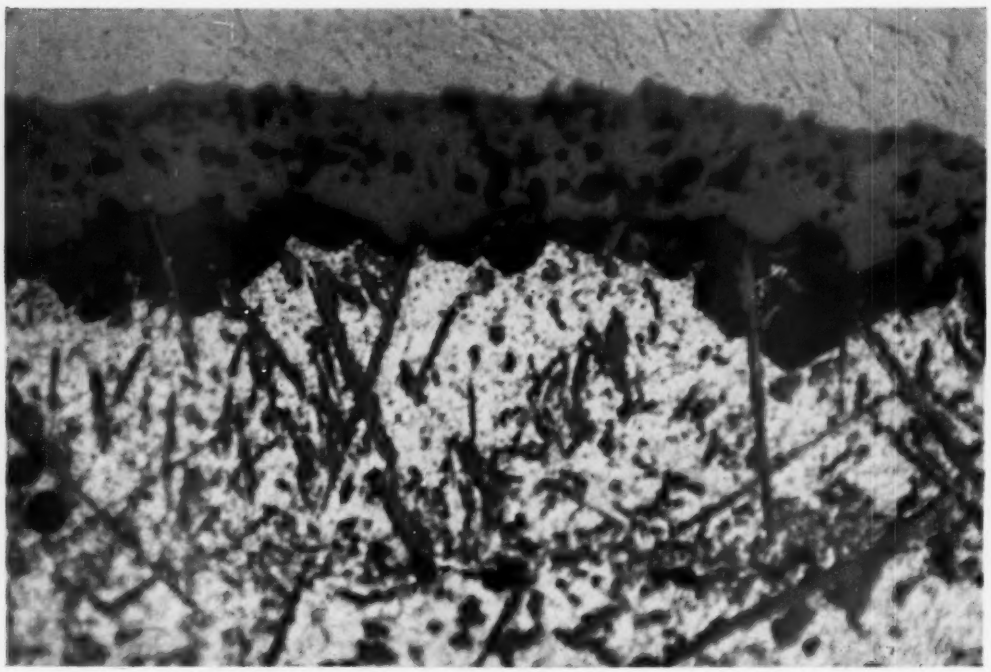

FIGURE 10. *Exterior of niobium shell after diffusion in a bath of molten tin for 8 hr at 1,000 °C followed by furnace cooling.*

The needles are Nb_3Sn. X1000.

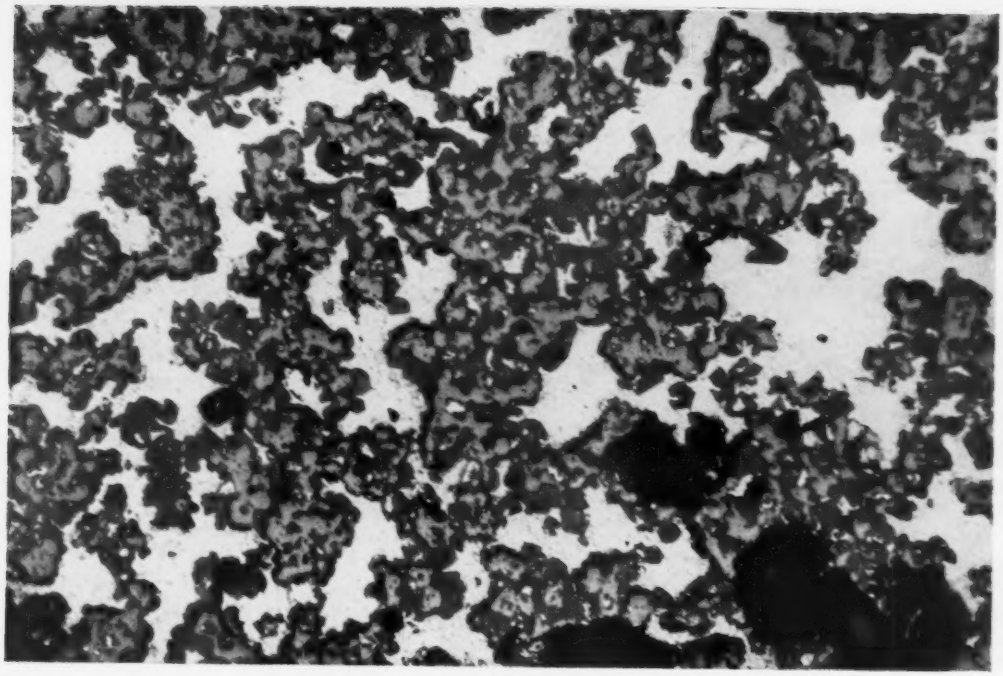

FIGURE 11. *Interior of thermal analysis specimen (nominal Nb_2Sn_3 hot pressed pellet) after heating to 1050 °C at 3 °C/min followed by cooling to room temperature also at 3 °C/min.*

X200.

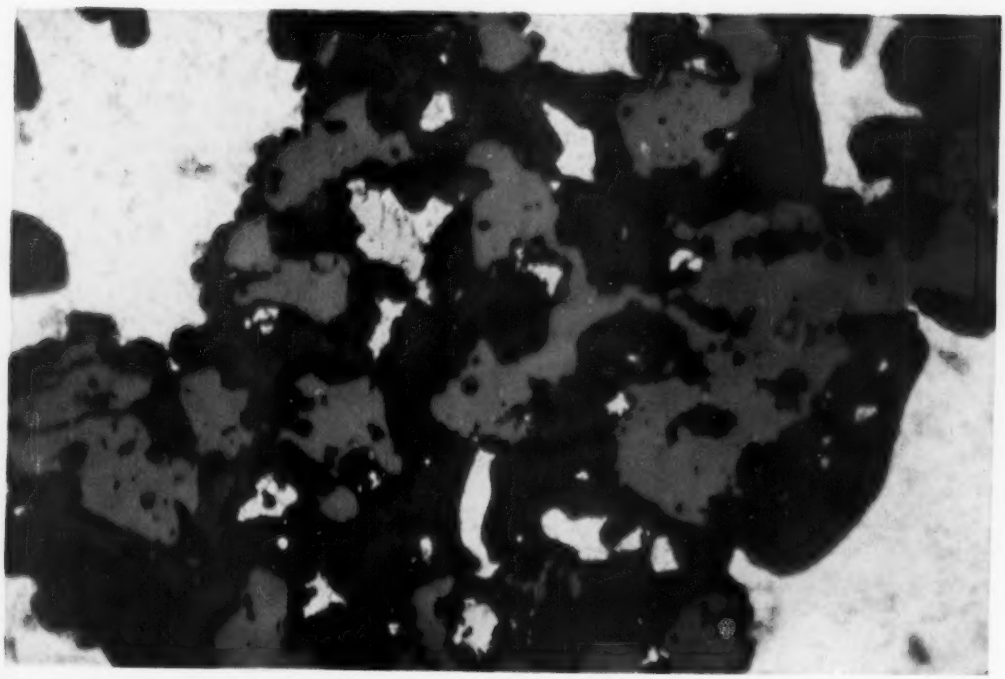

FIGURE 12. *Interior of thermal analysis specimen (nominal Nb_2Sn_3 hot pressed pellet) after heating to 1,050 °C at 3 °C/min followed by cooling to room temperature also at 3 °C/min.*

X1000.

(Paper 66A4–171)

JOURNAL OF RESEARCH of the National Bureau of Standards—A. Physics and Chemistry
Vol. 66A, No. 4, July–August 1962

Publications of the National Bureau of Standards*

Selected Abstracts

The interaction between an obliquely incident plane electromagnetic wave and an electron beam in the presence of a static magnetic field of arbitrary strength, K. H. B. Wilhelmsson, *J. Research NBS* **66D** (*Radio Prop.*) *No. 4, (July–August 1962).*
The purpose of the paper is to study theoretically the interaction between an obliquely incident plane electromagnetic wave and an electron beam. We assume that a static magnetic field of arbitrary strength is present in the axial direction. Machine computations made for the case of a cylindrical electron plasma show that resonances occur in the backscattering cross section as a function of the angle of incidence of the plane wave. The dependence of the resonance angles on the plasma frequency for fixed gyrofrequency suggests a possibility to utilize the results of the investigation for diagnostics of a cylindrical plasma.

Magnetotelluric fields in the frequency range 0.03 to 7 cycles per kilosecond: Part I. Power spectra, C. W. Horton and A. A. J. Hoffman, *J. Research NBS* **66D** (*Radio Prop.*) *No. 4 (July–August 1962).*
Power spectra of the horizontal components of the magnetic field and the telluric field are computed for data recorded on 1 and 2 September 1957 at the Soviet Magnetic Observatory in Tbilisi. Power spectra of the East-West telluric field component are computed for 20 September 1957 for Soviet stations located at Lvov, Tbilisi, and Ashkhabad. All analyses are based on microfilm copies furnished by the IGY World Data Center A. Each power spectrum shows a frequency dependence over a frequency range of 0.03 to 7 c/ks of the form $P_0 f^{-n}$ where n varies from 1.1 to 2.5. The coherency between orthogonal components of the telluric and magnetic fields is computed for the data from Tbilisi. Magnetotelluric power spectra from USSR, Canada, Texas, and Massachusetts are plotted on a common graph to show the frequency dependence over the range 0.03 to 400 c/ks.

Magnetotelluric fields in the frequency range 0.03 to 7 cycles per kilosecond: Part II. Geophysical interpretation, C. W. Horton and A. A. J. Hoffman, *J. Research NBS* **66D** (*Radio Prop.*) *No. 4 (July–August 1962).*
The power spectra computed in Part I for Tbilisi, USSR are used to compute apparent resistivity in accordance with a formula developed by Cagniard. It is found that both components of the telluric field yield a value of 6 ohmmeters for the apparent electrical resistivity of the earth. The data do not extend over a sufficiently wide range of frequency to permit conclusions about the stratification. There is no evidence of horizontal anisotropy of the earth's resistivity.
The magnetic power spectrum for the earth's ambient field is corrected for the tranmission losses in the ionosphere to yield the power spectrum of the magnetic field incident on the earth. The major part of the variation with frequency is eliminated by this correction.

Standard X-ray diffraction powder patterns, H. E. Swanson, M. C. Morris, R. P. Stinchfield, and E. H. Evans, *NBS Mono. 25—Section 1 (March 9, 1962) 40 cents.*
Forty-six standard X-ray diffraction powder patterns are presented. Fourteen are to replace twelve patterns already given in the X-ray Powder Data File, and thirty-four are for substances not previously included. The X-ray Powder Data File is a compilation of diffraction patterns from many sources and is used for the identification of unknown crystalline materials by matching spacing and intensity measurements. The patterns were made with a Geiger counter X-ray diffractometer, using samples of high purity. The *d*-values were assigned Miller indices determined by comparison with calculated interplanar spacings and from space group considerations. The densities and lattice constants were calculated, and the refractive indices were measured whenever possible.
Included are X-ray data for the following forty-six substances: $(NH_4)_2OsCl_6$, $Al_2SiO_4(F,OH)_2$, topaz, BiF_3, $CeCl_3$, $CeVO_4$, $CsClO_4$, $CsV(SO_4)_2 \cdot 12H_2O$, $Er_3Ga_2(GaO_4)_3$, $EuCl_3$, EuOCl, GdF_3, GdOCl, Gd_2O_3, $Ho[C_2H_5)SO_4]_3 \cdot 9H_2O$, FeAs, $LaBO_3$, $LaCl_3$, $La_2Mg_3(NO_3)_{12} \cdot 24H_2O$, Li_2MoO_4, Li_2O, Li_2WO_4, Lu_2O_3, $Mg_2Al_4Si_5O_{18}$ (low-cordierite), $Mg_2Al_4Si_5O_{18}$ (high-cordierite), $3Mg_2SiO_4 \cdot MgF_2$ (humite), $NdBO_3$, $NdCl_3$, $Nd_3GA_2(GaO_4)_3$, NiAsS (gersdorffite), $NiCO_3$, NiS, millerite, KH_2AsO_4, $PrCl_3$, $SmCl_3$, SmF_3, $Sm_3Ga_2(GaO_4)_3$, SmOCl, Ag_2CO_3, Ag_2O, Na_2MoO_4, Na_2WO_4, Tl_2WO_4, $Yb_3Ga_2(GaO_4)_3$, $Y_3Ga_2(GaO_4)_3$, YOCl, $Zr(IO_3)_4$.

Theory and methods of optical pyrometry, H. J. Kostkowski and R. D. Lee, *NBS Mono. 41 (March 1, 1962) 25 cents.*
A detailed review of the theoretical methods of optical pyrometry and the application of these methods at the National Bureau of Standards in realizing, maintaining, and distributing the International Practical Temperature Scale above 1063 °C is presented. In the theoretical presentation, the concepts of effective and mean effective wavelengths are introduced, and various equations relating these parameters to each other and other physical quantities are derived. The important features of precision visual optical pyrometers are discussed and a number of blackbody sources and tungstrip lamps described. Detailed experimental procedures and results of primary and secondary calibrations of optical pyrometers at NBS are given. Finally, recommendations for achieving high precision and accuracy and the fundamental limitations in visual optical pyrometry are presented.

Standard materials issued by the National Bureau of Standards. A descriptive list with prices, *NBS Misc. Publ. 241 (March 12, 1962) Supersedes C 552, 3d edition, 30 cents.*
A descriptive listing of the various Standard Materials issued by the National Bureau of Standards is given. A schedule of fees and weights, as well as directions for ordering, is included. Summarized tables of analyses are presented, to indicate the type of standards of composition presently available. Announcements of new standards will be made in the Federal Register, in scientific and trade journals, and in the Standard Materials column of the National Bureau of Standards Technical News Bulletin. The current status of the various standards will be indicated by an *insert sheet* available from the Bureau.

A tabulation of the thermodynamic properties of normal hydrogen from low temperatures to 300 °K and from 1 to 100 atmospheres, J. W. Dean, *NBS Tech. Note 120 (Pb161621) (1961) $1.75.*
Pressure, volume, temperature, internal energy, enthalpy, and entropy of normal hydrogen gas have been tabulated along isobars in 1 °K temperature steps. The range covered is from the saturation temperature to 300 °K and from a pressure of 1 to 100 atmospheres. The source of data is the Research Paper 1932 of the National Bureau of Standards Journal of Research. The method is described by which the data presented in Research Paper 1932 is reduced to properties directly useful for engineering calculations. A method is also described for estimating the effect of ortho-para compositions upon the tabulated properties.
Tabular values are presented in the dimensional units of the metric system. The tabulations are also available in the dimensional units of the British system as Technical Note No. 120, Supplement A.

A survey of the literature on heat transfer form solid surfaces to cryogenic fluids, R. J. Richards, W. G. Steward, and R. B. Jacobs, *NBS Tech. Note 122 (PB 161623) (1961) $1.25.*
A bibliography of 156 references on heat transfer from solid surfaces to fluids and related phenomena is presented. Heat transfer data obtained from experimental work on cryogenic fluids are presented in graphical form. The theoretical and

empirical formulations appearing in the references are presented. In those cases where sufficient information is available to make numerical computations, the formulations are presented graphically to permit comparison with the results of the experimental work.

Functional and design problems of the NBS RF voltage bridge, L. F. Behrent, *NBS Tech. Note 123* (*PB161624*) (*1961*) *$1.00.* A detailed presentation is given of the practical solutions to the design and operating problems encountered in constructing a Thermistor Bridge similar to that used by the NBS for RF Voltage Standaridization. Measurement and operating techniques, critical structural features, as well as the proper use of available components are discussed.

Provisional thermodynamic functions for para-hydrogen, H. M. Roder and R. D. Goodwin, *NBS Tech. Note 130* (*PB161631*) (*1961*) *$3.00.*
New PVT data recently obtained at this laboratory were used to compute tabular values of internal energy, enthalpy, and entropy of para-hydrogen. These properties, together with specific volume, are presented here as functions of temperature and pressure. The new data encompassed the temperature range 20° to 100 °K at pressures up to 340 atm. Earlier data were used to extend the tables to 300 °K. Above 100 °K the upper limit of pressure is 100 atm. The information is also presented in the form of thermodynamic charts. In supplement A to this report the thermodynamic tables and charts are presented in units of: psia, degrees Rankine, BTU pounds, and cubic feet.

Photoionization of atoms and molecules, F. L. Mohler, *NBS Tech. Note 131* (*PB161632*) (*1962*) *$1.25.*
This is a review of experimental results on photoionization of atoms and some molecules. There are some quantitative data on all the alkalies, magnesium, calcium, and thallium and all rare gases except xenon. Results are given for the common gases; hydrogen, nitrogen, oxygen, CO, CO_2, NO, K_2O, NO_2, H_2O, and CH_4. Autoionization, excitation to a state above the ionization threshold followed by transition to the ionized state, can be an important factor. Often the broad autoionization lines mask the true continuum. There are some mass spectrometric measurements of photoionization products for most of these molecules.

Low temperature thermometry, R. P. Hudson, *Experimental Cryophys. p. 214–253* (*1961*).
A discussion is given of apparatus and methods for thermometry in the range 1°–100° K in a style and brevity suited to an entry in a scientific encyclopaedia.

Photolysis of acetone-d_6 in the presence of propane-2, 2-d_2. Decomposition of the *n*-propyl radical, W. M. Jackson and J. R. McNesby, *J. Am. Chem. Soc.* **83,** *4891–4896* (*1961*).
Methyl-d_3 radicals generated by photolysis of acetone-d_6 react with acetone-d_6 and propane-2, 2-d_2 producing methane by the following reactions

(1) $CD_3+CD_3COCD_3 \rightarrow CD_4+CD_2COCD_3$
(2) $CD_3+CH_3CD_2CH_3 \rightarrow CD_4+CH_3CDCH_3$
(3) $CD_3+CH_3CD_2CH_3 \rightarrow CH_3H+CH_2CD_2CH_3$

Ratios of rate constants obtained are approximately temperature independent and

$k_1/k_3=1.10$
$k_2/k_3=0.58$

Analogous ratios for CH_3 radicals are indistinguishable from those for the CD_3 species. Decomposition of *n*-propyl to H and propylene is found to proceed at a much lower rate than suggested by Kerr and Trotman-Dickenson.
Consideration of kinetic and thermochemical evidence suggests the best value for the rate constants k_{5a} and k_{4a} are:

(5a) $CH_3CH_2CH_2 \rightarrow H+CH_3CH=CH_2$
(4a) $CH_3CH_2CH_2 \rightarrow CH_3+CH_2=CH_2$

$k_{5a}=10^{14.1}\ \exp\ (-37{,}000/RT)\ \text{sec}^{-1}$, $k_{4a}=10^{13.9}\ \exp\ (-31{,}000/RT)\ \text{sec}^{-1}$

Analysis of the absorption spectrum of $YbCl_3 \cdot 6H_2O$, J. C. Eisenstein, *J. Chem. Phys.* **35,** *No. 6, 2097–2100* (*Dec. 1961*).
The measurements of Dieke and Crosswhite on the absorption spectrum of $YbCl_3 \cdot 6H_2O$ are discussed. Their interpretation of the spectrum is extended by the identification of two of the weaker lines. The entire spectrum is considered on the basis of crystal field theory, and the possibility of determining the parameters of the crystal field potential is assessed. It is concluded that the terms in the potential with axial symmetry are small, and that additional small terms with twofold symmetry are present. The spin-orbit coupling constant is determined to be $-2924\ \text{cm}^{-1}$.

A lattice with an unusual frequency spectrum, R. J. Rubin and R. Zwanzig, *J. Math. Phys.* **2,** *No. 6, 861–864* (*Nov.–Dec. 1961*).
The lattice is a special rooted Cayley tree, generated by N successive m fold branchings. With each point of the tree are associated a mass M and a position coordinate χ_i. All end points are held fixed at $\chi_i=0$. The potential energy is $V=\frac{1}{2}\Sigma_{i,j}K_{ij}(\chi_i-\chi_j)^2$, where $K_{ij}=K$ if i and j are connected neighbors and neither is an end point, $K_{ij}=\alpha K$ if i and j are connected neighbors and either is a branch tip point, and $K_{ij}=0$ if i and j are not connected neighbors. The allowed frequencies of vibration are obtained for two different cases: In the first case all springs are identical ($\alpha=1$), and in the second case the springs connecting interior points to the branch tips are cut ($\alpha=0$). In the case in which all force constants are the same, the allowed frequencies of vibration, in the limit of infinite N, are given by $\omega(r)=(K/M)^{\frac{1}{2}}[m+1-2m^{\frac{1}{2}}\cos r\pi]^{\frac{1}{2}}$, where r is any rational number between zero and one. The fraction of all normal modes having precisely the value $\omega(r)$ is $\rho[\omega(r)]=(m-1)^2/(m^q-1)$, where r is expressed as the ratio $r=p/q$ of relatively prime integers p and q. The frequency spectrum is dense within the interval $(m^{\frac{1}{2}}-1, m^{\frac{1}{2}}+1)$; and $\rho[\omega]$ is discontinuous at every ω for which it does not vanish.

Net heat of combustion and other properties of kerosine and related fuels, G. T. Armstrong, L. Fano, R. S. Jessup, S. Marantz, T. W. Mears, and J. A. Walker, *J. Chem. Eng. Data* **7,** *No. 1, 107–116* (*Jan. 1962*).
Data are reported on the net heat of combustion (Q_p[net]), API Gravity (G), aniline point (A), hydrogen, carbon, and sulfur content, composition in terms of hydrocarbon types, and density of 139 fuels. These fuels are mainly petroleum-distillate kerosines of varying degrees of refinement or alkylates boiling in the kerosine range and represent the production of a large number of refineries. The remaining fuels are special formulations developed for the Wright Air Development Center.
Equations have been derived to represent Q_p(net) as a function of $(A\times G)$, and of hydrocarbon-type composition for the 110 petroleum-distillate kerosines. The net heat of combustion can be represented by a linear function of $(A\times G)$ with a standard deviation of 22 Btu/lb (0.12%) and a maximum deviation of +80 Btu/lb (0.43%) for a large range of values of $(A\times G)$. The equations relating Q_p(net) to the hydrocarbon-type composition give a larger standard deviation than the $(A\times G)$ equation when applied to the same 110 fuels. The results calculated from any of these equations for fuels classes other than that used in their derivation are not satisfactory.

On the thermodynamic properties of fluids, E. H. Brown, *Inst. Intern. Du Froid, Intern. Inst. of Refrigeration, Commission* **1,** *169–178* (*1960*).
Methods for determining the general behaviour of the thermodynamic properties of fluids over the entire pressure-temperature domain, including models of ideal fluids and condensing fluids and descriptions of the most important "characteristic curves" (curves on which the compressibility factor or its derivatives become zero), are outlined. Some of the results are applied to specific problems, such as furnishing some means of judging between conflicting sets of data on the shape and location of the Joule-Thomson inversion curve of hydrogen.

Double probe measurements of ionization in active nitrogen, H. P. Broida and I. Tanaka, *J. Chem. Phys.* **36,** *No. 1, 236–238* (*Jan. 1962*).
Electron temperatures and ion densities have been measured in nitrogen afterglows in a flow system at short times after the discharge. In pure nitrogen a maximum occurs in the

ionization density and in the electron temperature at 5 to 10 msec after the discharge. The position of this maximum coincides with the visible short-duration nitrogen afterglow in which N_2^+ emission is prominent. Small amounts of added impurity decrease this ion density but cause an increase in the ion density at longer times, reaching a second maximum at 80 to 100 msec after the discharge. These results show that ions and electrons are being produced continuously in nitrogen afterglows and that the rate of production is affected strongly by impurities.

Intramolecular rearrangements. III. Formation of 1-methylcyclobutanol in the photolysis of 2-pentanone, P. Ausloos and R. E. Rebbert, *J. Am. Chem. Soc.* **83,** *4897–4899 (1961).*
1-Methyl cyclobutanol has been isolated as a product in the vapor-phase photolysis of 2-pentanone. The yield of the alcohol diminishes with decrease in pressure and wavelength. Oxygen and nitric oxide reduce the yields of acetone, ethylene, and 1-methyl cyclobutanol. In the photo-chemical decomposition of the liquid phase, the ratio: acetone/1-methyl cyclobutanol is independent of wavelength and only slightly dependent on temperature.

Re-examination of the polymorphism of dicalcium silicate, D.K. Smith, A. J. Majumdar, and F. Ordway, *J. Am. Ceram. Soc.* **44,** *No. 8, 405–411 (Aug. 1961).*
Samples of Ca_2SiO_4 have been prepared by three different methods. These samples were examined by differential thermal analysis, high-temperature X-ray diffraction, and air quenching of pellets. It was found that the β modification, on cooling, converts completely and rapidly to the γ modification and dusts only if it has been heated above 1420° ±10° C. If the sample was not heated above this critical temperature, a mixture of the β and γ forms always resulted at room temperature.
The addition of 0.5 percent of CaO, SiO_2, Al_2O_3, Fe_2O_3, or MgO showed no effect on the sequence of phases for samples cooled from above the critical temperature. However, when these same samples were cooled from below 1410° C, the final room temperature product was not the same for all samples. On the other hand, the additional 0.5 percent of Na_2O, K_2O, Cr_2O_3, and B_2O_3 prevented the formation of the γ modification regardless of the temperature from which the sample was cooled.
The critical temperature correlates with the transformation temperature for the α–α' inversion. A theory relating this inversion to the completeness of $\beta \rightarrow \gamma$ transformation is presented.

Fluorine flame calorimetry, G. T. Armstrong, Books, *Experimental Thermochemistry* **II,** *Ch. 7, 129–145 (Interscience Publ., London, England, 1962).*
The necessity for flame calorimetry with elemental fluorine for determining heats of formation of fluorocarbons, hydrofluorocarbons and other fluorine compounds is justified on the grounds that elemental fluorine must be used in some reactions under any circumstance, that less ambiguity in the heat measurement is encountered if no additional elements are introduced into reactions of the compounds of interest, and that it is also desirable to check the results obtained by other calorimetric methods. A flame calorimeter has been developed at the National Bureau of Standards and used for measurements of heats of reaction of ammonia and methane with fluorine. The amounts of reaction determined by weighing the methane introduced and hydrogen fluoride formed have a mean difference of 0.13 per cent. Enthalpy correction for hydrogen fluoride imperfections are tabulated over the pressure range 0.1 to 0.5 atm at 26°, 32°, 38°, 44°, and 56°. The accuracy of measurements of heat of reaction is about 0.3 per cent (standard deviation of the mean). Revisions of the heats of formation of HF and CF_4 are suggested.

Polymorphism in monobromoacetic acid and the diagram of state of dichloroacetic acid at elevated pressures, A. R. Glasgow and J. Timmermans, *Bull. Soc. Chim. Belges* **70.** *623–641 (1961).*
Piezometric measurements to 5000 atmospheres have shown that dichloroacetic acid occurs in only one crystalline form; monobromoacetic acid exists in three forms with triple points at about 50.5° C and 120 kg/cm² (liq, C I, C II) and 53° C and 260 kg/cm$_2$ (liq, C II, C III). The transitions C I to CII and CII to C III have negative temperature-pressure coefficients (dT/dP) and occur only at elevated pressures. No example has been previously reported of an organic compound which has two successive solid transitions with negative dT/dP coefficients such as were observed for monobromoacetic acid.
Values of dT/dP, ΔH, and ΔS, calculated from the piezometric data, are given for the fusion of dichloroacetic acid and for the two solid transitions and the fusion (C III. liq) of monobromoacetic acid. An evaluation of purity of the acids from time-pressure data is discussed.

Superconducting magnets, R. H. Kropschot and V. Arp, *Cryogenics* **2,** *No. 1, 1-15 (Sept. 1961).*
The abrupt and total disappearance of electrical resistivity of certain metals at liquid helium temperatures is known as superconductivity. The use of superconductors for electromagnet windings eliminates the totally wasted Joule heating of conventional electromagnets and hence results in important power savings. However, electrical resistance is restored by magnetic fields greater than a certain critical value which depends upon the physical properties of the particular superconductor.
Certain alloys appear to have critical fields of 100 kgauss or greater, and theory indicates that very thin films of some of the more common metals may have critical fileds of about this same magnitude. Small size superconducting magnets producing up to 15 kgauss have been made. Large size magnets using the high field superconductors to produce fields up to 100 kgauss appear feasible with present technology.
The operating cost of a large, 100 kgauss superconducting magnet and its associated refrigeration system is 10^2 to 10^4 times less than the conventional magnet it replaces; it is expected that this will have an important effect on nuclear physics and plasma physics research.

An introduction to flame photometry and a review of recent studies, M. Margoshes, Book, **Physical Techniques in Biological Research,** W. L. Mastok, Ed., **IV,** *215–260 (Academic Press, New York, N.Y., 1962).*
Accurate and precise analysis with the flame photometer requires knowledge of the basic principles of instrumentation, excitation in the flame, preparation of standards and samples, and possible sources of error. This chapter is intended to provide such information, primarily to biologists and biochemists.
A brief historical introduction is followed by discussion of the chemical and physical processes involved in the introduction of the sample into the flame and the subsequent excitation of atomic and molecular spectra. The other components of the flame photometer, the monochromator and the detecting and measuring systems, are then considered. A summary of areas of application of flame photometry is followed by an extensive discussion of major causes of error in flame photometric analysis, including possible errors in the preparation of samples and standards, and those arising in the vaporization and excitation steps and in the components of the instrument. Some means of recognizing and circumventing these sources of error are mentioned.
The chapter concludes with a discussion of some recent developments in flame photometry, including the use of high-temperature flames as sources, the application of organic solvents (particularly in connection with liquid-liquid extraction), and atomic absorption spectroscopy.

The ionization constant of *o*-nitrophenol from 0 to 60°, G. F. Allen, R. A. Robinson, and V. E. Bower, *J. Phys. Chem.* **66,** *No. 1, 171–172 (1962).*
The spectrophotometric method has been used to measure the dissociation constant of *p*-nitrophenol in aqueous solution from 0 to 60 °C. The dissociation constant, K_a, is 7.03×10^{-8} at 25 °C. It is given as a function of the absolute temperature (T) by

$$-\log K_a = \frac{2186.53}{T} - 4.0475 - 0.01298\,T.$$

The thermodynamic quantity, $\Delta H°$, is computed as 4.725 cal. mole^{-1} at 25 °C and compared with 4,700 cal. mole^{-1} determined by direct calorimetric measurement by Fernandez and Hepler.

Oscillator models in unimolecular reactions, M. L. Vestal and H. M. Rosenstock, *J. Chem. Phys.* **35,** *No. 6, 2008–2016 (Dec. 1961).*
The absolute reaction rate theory for the unimolecular decomposition of isolated excited molecules is applied to two models. The first considers the molecule as a set of harmonic oscillators in which only a finite amount of energy may be stored in a particular degree of freedom. In the second model the spacing between adjacent levels is assumed to decrease exponentially. The first leads to a decrease in the lifetime above that calculated for the conventional harmonic oscillator model for short-lived molecules. The second produces an increase depending directly on the rate of change of the level spacing. The effect of anharmonicity on rates is discussed.

Some physical properties of monochloro-, dichloro, and monobromoacetic acids at 1 atmosphere, A. R. Glasgow and J. Timmermans, *Bull. Soc. Chim. Belges* **70,** *599–622 (1961).*
Monochloro-, dichloro-, and monobromoacetic acids (99.8 mole percent or better) have been prepared. The following physical properties have been determined: melting point (monobromo and dichloro acids), dielectric constants of liquid and solid (monochloro and dichloro), specific heat of solid (monobromo and dichloro), and heat of fusion (dichloro). Thermal analysis of solutions of the monobromo and dichloro acids with each other, with monochloro acid, and with water was used to obtain the phase diagrams. Three polymorphic forms of monochloroacetic acid were found at normal pressures; no polymorphs were found for the dichloro and monobromo acids. Formation of a continuous series of solid solutions between monobromoacetic acid and the mastastable β-form of monochloroacetic acid suggests that this matastable form and the monobromo acid have the same crystal structure.

Intramolecular rearrangements. IV. Photolysis of 2-pentanone-4, 5, 5-d_3, R. P. Borkowski and P. Ausloss, *J. Phys. Chem.* **65,** *2257–2260 (1961).*
The photolysis of 2-pentanone-4,5,5-d_3 in the vapor and liquid-states yields $D_2C{=}CHD$ and $DHC{=}CHD$. These ethylenes are formed by intramolecular rearrangements in which either an H or a D-atom is transferred to the carbonyl group.

$$CH_3COCH_2CHDCD_2H + h\nu \rightarrow \begin{cases} D_2C{=}CHD + CH_3COCH_3 & \text{(I)} \\ DHC{=}CHD + CH_3COCH_2D & \text{(II)} \end{cases}$$

In the vapor phase the quantum yield of ethylene is independent of concentration, temperature, and intensity, whereas it decreases with increasing wavelength and oxygen pressure. The effect of oxygen is more pronounced at the longer wavelength and lower temperature which indicates that oxygen interacts only with molecules excited to a low vibrational level. The ratio $C_2D_3H/C_2H_2D_2$ is independent of intensity, but increases with increasing wavelength and ketone concentration, and diminishes with increasing temperature and oxygen pressure. These effects may be explained qualitatively in terms of the difference in the bond strength of C—D and C—H.
In the liquid phase the quantum yield of ethylene increases, and the ratio $C_2D_3H/C_2H_2D_2$ decreases with increasing temperature. A difference of activation energy of about 1 kcal/mole was obtained for D and H transfer in the intramolecular rearrangement.

Electrophoretic mobilities and surface adsorption in the polystyrene latex-aliphatic soap system, C. L. Sieglaff and J. Mazur, *J. Colloid Sci.* **17,** No. 1, 66–85 (Jan. 1962).
The electrophoretic mobilities of a polystyrene latex stabilized by straight chain aliphatic soaps were measured as a function of soap and salt concentrations. The soaps employed were alkali salts of fatty acids ranging from C_8 (caprylic) soap to C_{16} (palmitic) soap. The salts employed were potassium and sodium choride. The results are explained by a modification of the Stern localized adsorption model which takes into account the effect of the ionic strength of the system on the rate of adsorption of soap anions by the latex particle.
It has been postulated, on the basis of these experimental data, that the chloride ions are preferably adsorbed by the latex particle, in addition to the soap ions. This requires an extension of the Stern-Langmuir adsorption isotherm into a two-component adsorption of ions of the same sign, but with different effective areas and adsorption potentials.
From the maxima in the curves representing mobilities versus soap concentration, the dependence of adsorption potential and of effective area of soap ion on the number of CH_2 groups in the aliphatic chain was obtained. It was observed that within the limitations of the theoretical model employed the adsorption potential increases by approximately 600 cal/mole for each additional —CH_2— group in the soap molecule.

An equation of state for calculating the thermodynamic properties of helium at low temperatures, R. D. McCamy and R. B. Stewart **(1962 2d Symp. Thermophysical Properties, January 24-26, 1962, Princeton University, Princeton, New Jersey), Progress in International Research on Thermodynamics and Transport Properties,** *Am. Soc. Mech. Engrs. (New York, N.Y.), p. 107 (1962).*
A new equation of state for helium gas with six adjustable constants is presented. This relation is adequate for the representation of the P-V-T data and for the calculation of the entropy and enthalpy for a range of temperatures from 20 to 300 K, with pressures to 100 atm. A comparison of calculated volumes with the original data indicates an average arithmetic deviation of 0.07 percent and maximum deviations of 0.5 percent. A comparison of calculated pressures with original data indicates about the same average and maximum deviations. A temperature-entropy chart and a compressibility factor chart have been prepared from values calculated by this equation of state. Values of density, enthalpy and entropy, are tabulated with temperature and pressure as independent arguments.

Journal of Research 66B (Math. and Math. Phys.) No. 2, (Apr.–June 1962) 75 cents.
Hindsight technique in machine translation of natural languages. I. Rhodes and F. L. Alt.
An extension of Jensen's theorem for the derivative of a polynomial and for infrapolynomials. O. Shisha.
Two matrix eigenvalue inequalities. S. Haber.
Graphs for determining the power of Student's *t*-test. M. C. Croarkin.

Journal of Research 66D (Radio Prop.) No. 4, (July–Aug. 1962) 70 cents.
Propagation problems with space radio communications. K. Rawer.
On the absolute intensity of incoherent scatter echoes from the ionosphere. K. L. Bowles, G. R. Ochs, and J. L. Green.
On the forward scattering of radio waves in the lower ionosphere. T. Hagfors.
The representation of diurnal and geographic variations of ionospheric data by numerical methods. W. B. Jones and R. M. Gallet.
The interaction between an obliquely incident plane electromagnetic wave and an electron beam in the presence of a static magnetic field of arbitrary strength. K. H. B. Wilhelmsson. (See above abstract.)
An analysis of VLF mode propagation for a variable ionospheric height. J. R. Wait.
A method for the determination of lower inonsphere properties by means of field measurements on sferics. F. B. Harris, Jr., and R. L. Tanner.
Defocusing of radio rays by the troposphere. R. E. Wilkerson.
Magnetotelluric fields in the frequency range 0.03 to 7 cycles per kilosecond: Part I. Power spectra. C. W. Horton and A. A. J. Hoffman. (See above abstract.)
Magnetotelluric fields in the frequency range 0.03 to 7 cycles per kilosecond: Part II. Geophysical interpretation. C. W. Horton and A. A. J. Hoffman. (See above abstract.)
The impedance of a circular loop in an infinite conducting medium. M. B. Kraichman.

Calibration procedures for direct-current resistance apparatus, P. P. B. Brooks, NBS Mono. 39 (Mar. 1962), 40 cents.

Thermocouple materials, F. R. Caldwell, NBS Mono. 40 (Mar. 1962) 30 cents.

Evaluation of convolution integrals occurring in the theory of mixed path propagation, J. R. Johler and C. M. Lilley, NBS Tech. Note 132 (PB161633) (1961) $1.00.

Historical survey of fading at medium high radio frequencies, R. K. Salaman, NBS Tech. Note 133 (PB161634) (1962) 75 cents.

A study of *F*2-layer effects as observed with a Doppler technique, K. Davies, J. M. Watts, and D. H. Zacharisen, J. Geophys. Research **67,** 601–609 (Feb. 1962).

Ionospheric effects associated with the solar flare of September 28, 1961, K. Davies, Nature Letter 193, 763–764 (Feb. 24, 1962).

Sferic observations of the severe weather on May 19, 1960, C. A. Samson and R. F. Linfield, J. Geophys, Research 67, 627–635 (Feb. 1962).

On the mean temporal variations of electron density at a fixed height in the *F* region, A. J. Hirsh and R. W. Knecht, J. Geophys. Research **67,** No. 2, 595–600 (Feb. 1962).

Displacement and strain-energy distribution in a longitudinally vibrating cylindrical rod with a viscoelastic coating, P. Hertelendy, J. Appl. Mechanics, No. 61–WA–30 (1962).

Comparison of United States and Canadian free-air ionization chambers, J. H. Aitken, L. De LaVergne, W. H. Henry and T. P. Loftus, Brit. J. Radiol. 35, No. 409, 65–70 (Jan. 1962).

Statistical problems arising in the establishment of physical standards, W. J. Youden, Proc. Fourth Berkeley Symp. on Math. Statistics and Probability III, 321–335 (1961).

National Bureau of Standards, Washington, D. C. and Boulder, Colorado, C. E. Moore, Astron. J. **66,** No. 10 (Dec. 1961).

Rapid method for interpolating refractive index measurements, O. N. Stavroudis and L. E. Sutton, J. Opt. Soc. Am. **51,** No. 3, 368–370 (Mar. 1961).

The three-dimensional nature of boundary-layer instablitity, P. S. Klebanoff, K. D. Tidstrom, and L. M. Sargent, J. Fluid Mechanics **12,** Pt. 1, 1–34 (1962).

A specimen for use in investigating the stress-corrosion cracking of matals at elevated temperatures, H. L. Logan, Materials Research and Standards (ASTM Bull.) **2,** No. 2, 98–100 (Feb. 1962).

Dynamic behavior of a simple pneumatic pressure reducer, D. H. Tasai and E. C. Cassidy, J. Basic Eng., 253–264 (June 1961).

Effect of porosity on Young's modulus of alumina, F. P. Knudsen, J. Am. Chem. Soc. **45,** No. 2, 94–95 (Feb. 1962).

Characteristic electron energy loss measurement at low temperatures, E. M. Horl and J. A. Suddeth, J. Appl. Phys. **32,** No. 12, 2521–2525 (Dec. 1961).

A new approach to the mechanical syntactic analysis of Russian, I. I. Rhodes, Mech. Transl. **6,** 33–50 (Nov. 1961).

A string language for symbol manipulation based on ALGOL 60, J. H. Wegstein and W. W. Youden, Commun. ACM **5,** No. 1, 54–61 (Jan. 1962).

Ray-tracing formulas for uniaxial crystals, O. N. Stavroudis, J. Opt. Soc. Am. **52,** No. 2, 187–191 (Feb. 1962).

Doppler studies of the ionosphere with vertical incidence, K. Davies, Proc. IRE **50,** No. 1, 94 (Jan. 1962).

Parametric behavior of an ideal two-frequency varactor, G. F. Montgomery, Proc. IRE **50,** No. 1, 78–80 (1962).

Auroral zone geomagnetic micropulsations with periods of 5 to 30 seconds, W. H. Campbell and S. Matsushita, J. Geophys. Research **67,** 555–573 (Feb. 1962).

On the interpretation of prominence spectra. V. The emission lines in quiescent prominences, J. T. Jefferies and F. Q. Orrall, Astrophys. J. **135,** 109–121 (Jan. 1962).

Design of retarding field energy analyzers, J. A. Simpson, Rev. Sci. Instr. **22,** No. 12, 1283–1293 (Dec. 1961).

Stress-strain relationships in yarns subjected to rapid impact loading. Part VIII: Shock waves, limiting breaking velocities, and critical velocities, J. C. Smith, J. M. Blandford, and K. M. Towne, Textile Research J. **32,** No. 1, 67–76 (Jan. 1962).

The standards challenge, A. H. Scott, Insulation **8,** No. 2, 48–50 (Feb. 1962). Average decay laws for VLF fields, J. R. Wait, Proc. IRE **50,** No. 1, 53–56 (Jan. 1962).

Radiation beam mapping with photographic film, W. L. McLaughlin, Radiology **78,** No. 1, 119–120 (Jan. 1962).

Fitting refractive index data by least squares, L. E. Sutton and O. N. Stavroudis, J. Opt. Soc. Am. **51,** No. 8, 901–905 (Aug. 1961).

Compton scattering by *K*-shell electrons, J. W. Motz and G. Missoni, Phys. Rev. **124,** No. 5, 1458–1468 (Dec. 1961).

Current-limited rectifiers, G. F. Montgomery, *Proc. IRS* **50,** *No. 2, 190–193 (Feb. 1962).*

**Publications for which a price is indicated (except for Technical Notes) are available only from the Superintendent of Documents, U.S. Government Printing Office, Washington 25, D.C. (foreign postage, one-fourth additional). Technical Notes are available only from the Office of Technical Services, U.S. Department of Commerce, Washington 25, D.C. (order by PB number). Reprints from outside journals and the NBS Journal of Research may often be obtained directly from the authors.*

U. S. GOVERNMENT PRINTING OFFICE: 1962

UNIVERSITY MICROFILMS INC
EDITORIAL DEPARTMENT
313 NORTH FIRST ST
ANN ARBOR MICH
S-JR-A OCT
...VERSITY OF MICHIGAN

UNITED
GOVERNMENT P
DIVISION OF PU
WASHINGTON 25, D.C.

OFFICIAL BUSINESS

PENALTY FOR PRIVATE USE TO AVOID
PAYMENT OF POSTAGE, $300
(GPO)

JOURNAL OF RESEARCH of the National Bureau of Standards Vol. 66A, No. 4 July–August 1962
A. Physics and Chemistry

Contents

Page

Dielectric properties of semicrystalline polychlorotrifluoroethylene. Arnold H. Scott, Donald J. Scheiber, Alexander J. Curtis, John I. Lauritzen, Jr., and John D. Hoffman. 269

Thermal degradation of fractionated high and low molecular weight polystyrenes. S. L. Madorsky, D. McIntyre, J. H. O'Mara, and S. Straus. 307

Synthesis of 2-propoxy-5-methylbenzoic acid. Gerhard M. Brauer and Lester Simon. 313

The gamma-ray distribution from oriented cerium-141. J. F. Schooley, D. D. Hoppes, and A. T. Hirshfeld. 317

Light source for producing self-reversed spectral lines. Jack Sugar. 321

A diamond cell for X-ray diffraction studies at high pressures. G. J. Piermarini and C. E. Weir. 325

Thermal conductivity of gases. I. The coaxial cylinder cell. Leslie A. Guildner. 333

Thermal conductivity of gases. II. Thermal conductivity of carbon dioxide near the critical point. Leslie A. Guildner. 341

Derivation of the relaxation spectrum representation of the mechanical response function. Robert S. Marvin. 349

Intermediate phases in superconducting niobium-tin alloys. L. L. Wyman, J. R. Cuthill, G. A. Moore, J. J. Park, and H. Yakowitz. 351

Publications of the National Bureau of Standards. 365

For sale by the Superintendent of Documents, U.S. Government Printing Office, Washington 25, D.C. Price 70 cents (single copy). Subscription price: $4 a year, 75 cents additional for foreign mailing.

UNITED STATES GOVERNMENT PRINTING OFFICE, WASHINGTON : 1962